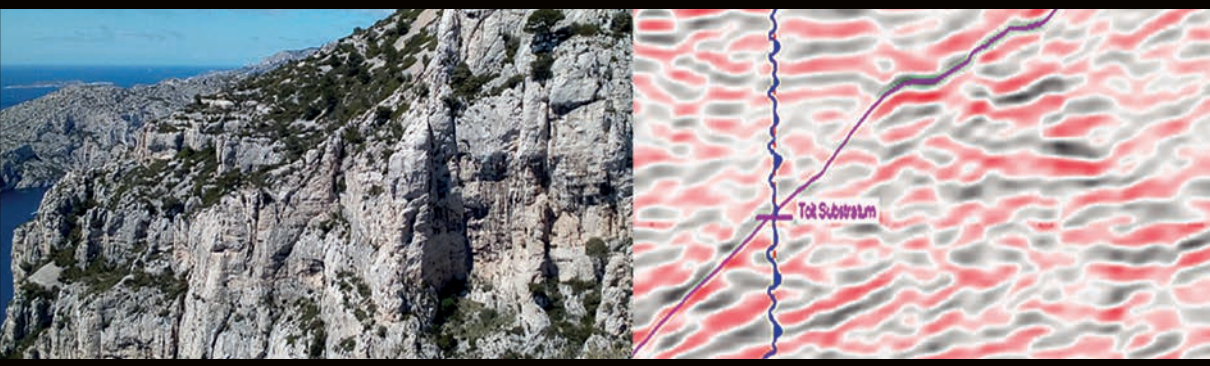

PROfile

Seismic imaging: a practical approach

Jean-Luc Mari and Manuela Mendes

edp sciences

agap QUALITÉ GÉOPHYSIQUE APPLIQUÉE

Seismic Imaging

A practical approach

Seismic Imaging

A practical approach

Jean-Luc Mari
Manuela Mendes

edp sciences

DOI: 10.1051/978-2-7598-2351-2
ISBN(ebook) : 978-2-7598-2351-2

Contents

Foreword

J.-L. Mari, M. Mendes

Based on their experience in geophysics as applied to the oil and gas industry, and in the geotechnical field, the authors have set out to explain how conventional seismic methods used in deep exploration geophysics for imaging can be applied to certain geotechnical and hydrogeological surveys, and to site characterizations in the framework of seismic hazard studies. After reviewing the current state of knowledge in seismic wave propagation, refraction and reflection seismic methods, the book aims to describe how seismic tomography and full waveform inversion methods can be used to obtain seismic images of the subsurface. The book highlights the benefit of combining different seismic methods through various synthetic and field examples. In addition to these examples, the authors provide readers with guidelines to carry out these operations, in terms of acquisition, as well as processing and interpretation.

The authors thank Hervé Chauris, Béatrice Yven and Michel Hayet for their contributions to this book.

Many thanks to Jim Johnson and Katell Guernic from Tamarin (www.tamarin-text.com) for the English revision of the book.

DOI: 10.1051/978-2-7598-2351-2.c001

The authors

Jean-Luc Mari

A graduate of the *Institut Physique du Globe Strasbourg* and the IFP School (petroleum geosciences, major in geophysics in 1978), Jean-Luc Mari was employed by IFP *Energies Nouvelles* in 1979 as a research engineer in the Geophysics Department. Here he worked on several research projects, such as high-resolution seismic surveying, reservoir monitoring, and the development of borehole tools, in collaboration with industrial partners GdF-Suez, CGG, Total and ELF Aquitaine.

In 1986, he was seconded to ELF Aquitaine where he worked on reservoir geophysics. He joined IFPEN in 1987 and was seconded to the Reservoir Department, where he studied, in particular, the benefits of using geophysical methods in horizontal wells. In 1994 he was appointed to the IFP School as a professor and obtained the accreditation to supervise earth science research (HDR). He was an expert in geophysics for IFP *Energies Nouvelles*.

Jean-Luc was a member of the EAGE and an associate editor for *Near Surface Geophysics*. Currently retired from IFP *Energies Nouvelles*, Jean-Luc is an independent researcher and consultant in geophysics. He is a member of the board and of the accreditation committee for the Association for Quality in Applied Geophysics (AGAP - *Association pour la Qualité en Géophysique Appliquée*).

An author and co-author of patents and numerous scientific articles, Jean-Luc Mari has also contributed to educational scientific books and has been involved in the design and development of online learning modules, tutorials and e-books. In 2010, he received a Knighthood from the *Ordre des Palmes Académiques.*

Email: jeanluc90.mari@gmail.com

Manuela Mendes

Since 1990, Manuela Mendes has been an assistant professor at the *Instituto Superior Técnico*, Portugal. She received an MSc. (1986) in Geophysics and a PhD. (1989) in Earth Sciences from the University of Paris VII.

During 1977-1978 she worked as a geophysicist at the Institute of Geosciences, Azores Island.

In 1989 Manuela worked as a researcher at the *Compagnie Générale de Géophysique* (CGG), France, and participated

in several seismic imaging research projects during 1998-1999 and 2003-2004 at the *Institut Français du Pétrole* (IFP), France.

She contributes regularly to peer reviewing, academic committees and is an expert-evaluator for the European Commission. Her main research interests are seismic-volcanic risk and seismic imaging applications for the oil industry, the environment and culture heritage.

Manuela Mendes is a member of EAGE.

Email: d1865mm@gmail.com

Hervé Chauris

Hervé Chauris graduated in 1996 from the *École des Mines de Paris* (Paris School of Mines, France), as a civil engineer. After a research master in Geophysics, he attained a PhD in Geophysics from the *École des Mines de Paris*. He then worked for Shell in Rijswijk, The Netherlands, between 2000 and 2005, within the seismic imaging R&D department. He became an associate professor at MINES ParisTech in 2006, before taking on a full professor position at the same institute in 2011.

Hervé completed his accreditation to supervise research in earth sciences (HDR) in 2010, on the theme "seismic imaging from locally coherent events". His main research interests are related to the development of new algorithms for quantitative seismic imaging. Coherent events refer to the fact that seismic waves have an intrinsic spatial size. He has developed a large number of imaging algorithms in the context of Migration Velocity Analysis, a focusing technique to evaluate the quality of a given velocity model through the consistency between independent seismic images. The main applications have been developed in the context of exploration geophysics and near surface characterization.

Since 2006, Hervé Chauris has supervised 12 PhD students, 5 post-docs and 15 masters students. He has published more than 30 articles and is a co-author of 100 conference presentations. He is a member of EAGE, SEG and SIAM, a reviewer for Geophysics among other journals, and is associate editor for Geophysical Journal International and Geophysical Prospecting. He is also responsible for Geosciences education for civil engineer students at MINES ParisTech, and head of the geophysical team within the Geosciences department.

Email: herve.chauris@mines-paristech.fr

Béatrice Yven

Béatrice Yven studied at the University of Paris Diderot where she received her PhD in Geophysics in 2001. Her research work focused on the characterization of the petrological and petrophysical properties of 3,000 m of volcanic deposits in a high-energy geothermal field. She performed a wide variety of laboratory experiments on core samples and analysed them with well logging data to extrapolate acoustic and thermal properties at the site scale.

Béatrice joined the French National Agency for Radioactive Waste Management (Andra) in 2002 where she is in charge of the 3D modelling for thermal, hydraulic and mechanical properties of the site expected to host the radioactive waste disposal. She has participated in several major R&D programmes and reference documents.

From 2014, Béatrice Yven has been working on the monitoring of geological disposal facilities. Since 2017 she has been responsible for the monitoring team and has supervised the R&D programme to ensure that reliable, durable, metrological qualified and tested monitoring systems will be available at the time of repository construction to respond to monitoring objectives.

Email: beayven@gmail.com; beatrice.yven@andra.fr

Michel Hayet

Graduating from the *École Nationale Supérieure de Géologie Appliquée de Nancy* in 1984, Michel Hayet was employed by CGG as a seismologist, party chief, area manager and area geophysicist, mainly in land and shallow water seismic acquisition. In 2009, he joined the *Agence nationale pour la gestion des déchets radioactifs (Andra)*, responsible for high-resolution 3D seismic surveying. Michel is the current chairman of AGAP, Association for Quality in Applied Geophysics (*Association pour la Qualité en Géophysique Appliquée*).

Email: michelhayet@hotmail.fr

Introduction

J.-L. Mari, M. Mendes

In the geophysics of oil exploration and reservoir studies, the surface seismic method is the most commonly used method to obtain a subsurface model in 2 or 3 dimensions. This method plays an increasingly important role in soil investigations for geotechnical, hydrogeological and site characterization studies regarding seismic hazard issues.

This book is neither a basic introduction nor a theoretical study of seismic imaging. Its goal is to provide a practical guide, through the use of examples from the field, to the application of seismic methods to surface imaging.

After reviewing the current state of knowledge in seismic propagation, refraction and reflection seismic methods, the book aims to describe how seismic tomography and full waveform inversion methods can be used to obtain seismic images of the subsurface. The book highlights the benefit of combining different seismic methods through various synthetic and field examples.

DOI: 10.1051/978-2-7598-2351-2.c002

The tomographic approach is well adapted to seismic data imaging. The main focus of seismic tomography is to explore the sensitivity of selected seismic phases to different geological structures to obtain high quality depth or time images of the subsurface. Traditionally, depending on the input data, seismic tomographies fall into three main categories: transmission tomography, reflection tomography and diffraction tomography. The results of seismic tomography, known as tomograms, may even provide useful input data for further processing as pre or post-stack seismic migrations or inversion techniques. Here, the seismic tomography tools are efficiently used for processing multiple marine and land field datasets, acquired with different types of geometry: surface, cross-hole and vertical seismic profile (VSP). This diversity of field examples, in terms of scales and geometries, helps to show the application of seismic tomography in wide near-surface studies such as geotechnics, hydrogeology or site characterization.

Full Waveform Inversion (FWI) is an advanced seismic imaging method. The technique is simple: the objective is to obtain a model (velocity, density, and possibly anisotropy and attenuation) of the subsurface in which the synthetic shot gathers best fit the observed data. The results are quantitative in the sense that, for example, the velocity images are expressed in m/s. Beyond the apparent simplicity there are a number of challenges regarding the applicability of the method. The objectives of the chapter are (1) to provide the main elements of the formalism and (2) to indicate the applicability of the method as well as the strategy to be developed for successful results. The method is illustrated using 2D synthetic data in a geotechnical context, demonstrating that the practical aspects are essential. Two real data examples extracted from the literature are used to illustrate the value of the approach. We give particular attention to understanding the challenges raised by FWI.

With field data targeting shallow structures, we show how more accurate geophysical models can be obtained by combining different datasets: refracted waves with reflected waves, and body waves with surface waves. The proposed hybrid methods investigate the sensitivity of more than one type of wave to different geological structures or mechanical properties, benefiting from the advantage of several existing types of waves, in the same data set. This strategy is shown to be of interest, since it can be implemented without increasing the cost of seismic data acquisition, and the seismic data can be processed using standard procedures. A first example refers to a refraction-reflection imaging strategy with the capability to evaluate reflectivity information starting from the surface. One drawback of reflection processing is that the reflectivity model starts a few meters below the surface, depending on the first offset. The upper region can be modeled through the use of refraction data velocity models. A next step is to build continuous and accurate extended reflectivity information putting together both images. Thus, this hybrid tool is very useful for providing information about the reflectivity for targets located in the near and/or very near surface. A second field example proposes a strategy for imaging with refraction and surface waves. This hybrid seismic method combines knowledge about the P-wave velocity provided by the refraction arrivals and the S-wave velocity

distribution through the surface wave data. The distributions of both velocities allow a better definition of a hydrothermal system, such as subsurface gas pathways consistent with degassing.

Finally, we show how the integration of seismic data (3D survey and VSP), logging data (acoustic logging) and core measurements, combined with a succession of specific and advanced processing techniques, enables the development of a 3D high resolution geological model in depth.

1

Wave propagation

J.-L. Mari

Seismic prospecting consists of the generation of very low-amplitude artificial earthquakes at predetermined times and positions. The seismic disturbances generated by a seismic source are recorded by a seismic receiver spread. The acquisition geometry is defined by the distribution of the source spread and the receiver spread.

The following elements are needed to observe the propagation of seismic, acoustic or elastic waves:

1. A source spread. The source is a device capable of producing a deformation in a medium. In land acquisition, it can be an explosive charge (dynamite), a weight dropper or a vibrator. In marine acquisition, it can be an air gun, a sparker or a vibrator. Seismic energy radiated by the source is split between body waves (compressional and shear waves) and surface waves.
2. A physical medium defined by its geometric and mechanical characteristics. Here we consider the geological formations defined by the following mechanical properties:
   - Propagation velocity of the compressional *P*-waves in the rock: V_P (expressed in m/s),

DOI: 10.1051/978-2-7598-2351-2.c003

- Propagation velocity of the shear *S*-waves in the rock: V_S (expressed in m/s),
- Density ρ (expressed in g/cm^3 or kg/m^3),
- Quality factor Q which characterizes the ability of the rock to absorb seismic energy: a higher value indicates lower absorption of seismic energy. Sedimentary rocks have a Q value ranging from about 10 to several hundred.

3. An elastic deformation of the medium after the initial shaking caused by the source. A deformation is considered elastic when the medium returns to its original state after the causes of deformation have disappeared, i.e. when the medium has not been damaged by the wave passing through it.
4. A receiver spread. Which must be capable of recording the deformations generated by the source after propagation in the geological medium:
   - Either by variations in the displacement, velocity or acceleration of particles (geophones, accelerometers),
   - Or by pressure variations (hydrophones).

Table 1.1 *Seismic velocities and densities, and mechanical moduli (after Lavergne, 1989).*

Type of rock or medium	***P*-velocity** V_P (m/s)	***S*-velocity** V_S (m/s)	**Density** ρ (g/cm^3)
Weathered rocks	300 – 700	100 – 300	1.7 – 2.4
Dry sands	400 – 1200	100 – 500	1.5 – 1.7
Wet sands	1500 – 4000	400 – 1200	1.9 – 2.1
Clay	1100 – 2500	200 – 800	2.0 – 2.4
Marl/shale	2000 – 3000	750 – 1500	2.1 – 2.6
Sandstone	3000 – 4500	1200 – 2800	2.1 – 2.4
Limestone	3500 – 6000	2000 – 3300	2.4 – 2.7
Chalk	2300 – 2600	1100 – 1300	1.8 – 2.3
Salt	4500 – 5500	2500 – 3100	2.1 – 2.3
Anhydrite	4000 – 5500	2200 – 3100	2.9 – 3.0
Dolomite	3500 – 6500	1900 – 3600	2.5 – 2.9
Granite	4500 – 6000	2500 – 3300	2.5 – 2.7
Basalt	5000 – 6000	2800 – 3400	2.7 – 3.1
Coal	2200 – 2700	1000 – 1400	1.3 – 1.8
Water	1450 – 1500	–	1
Ice	3400 – 3800	1700 – 1900	0.9
Oil	1200 – 1250	–	0.6 – 0.9

First Lamé parameter $\lambda = \rho\left(V_P^2 - 2V_S^2\right)$

Shear modulus (or second Lamé parameter) $\mu = \rho V_S^2$

Poisson's coefficient $\sigma = \dfrac{\gamma^2 - 2}{2\left(\gamma^2 - 1\right)}$ where $\gamma = \dfrac{V_P}{V_S}$

Young's modulus $E = \rho V_P^2 \dfrac{(1-2\sigma)(1+\sigma)}{1-\sigma}$

Bulk modulus $K = \rho\left(V_P^2 - \dfrac{4}{3}V_S^2\right)$

Table 1 shows the range of values of propagation velocities, V_P and V_S, and the densities of principal rock types. It also gives the expressions of the main mechanical modules (Poisson's coefficient, Young's modulus…).

1.1 Seismic wave equation

In seismic prospecting, the energy generated by the seismic source is relatively weak and the medium can be considered as elastic, obeying Hooke's laws. For small deformations, each stress tensor ($\sigma_{i,j}$) is a linear combination of the elements of the deformation tensor ($\varepsilon_{i,j}$). The constants of proportionality for a homogeneous and isotropic medium are Lamé's constants λ and μ. The parameter μ is termed the shear modulus. The displacements U_i (components of the displacement vector) that are observable at all points within the medium and, particularly, on the surface are solutions to the wave equation. In a three-dimensional rectilinear frame of reference (x_i, i=1 to 3) the wave propagation in the x-direction is written as:

$$\rho \frac{\partial^2 U_i}{\partial t^2} = \sum_{j=1}^{3} \frac{\partial}{\partial x_j}\left(\sigma_{i,j}\right)$$

with:

$$\sigma_{i,j} = \lambda\left(\sum_{k=1}^{3} \varepsilon_{k,k}\right)\left(\delta_{i,j}\right) + 2\mu\left(\varepsilon_{i,j}\right) \qquad \text{stress}$$

$$\varepsilon_{i,j} = \frac{1}{2}\left(\frac{\partial U_i}{\partial x_j} + \frac{\partial U_j}{\partial x_i}\right) \qquad \text{strain}$$

where $\delta_{i,j}$ are the Kronecker symbols:

$$\delta_{i,j} = \begin{cases} 1 & i = j \\ 0 & i \neq j \end{cases}$$

For each element of the stress tensor ($\sigma_{i,j}$) the first index i indicates the stress component in the reference system (x_i, i=1 to 3); the second index j is the surface undergoing the stress, the surface being defined by its normal in the reference system.

All waves (body waves and surface waves) are solutions to the wave equation. The compressional *P*-waves correspond to longitudinal vibrations which, at every point in the medium, have a particle motion parallel to the direction of propagation (Figure 1.1-a). The propagation velocity for compressional waves is equal to:

$$V_P^2 = (\lambda + 2\mu)/\rho$$

The shear *S*-waves correspond to transverse vibrations which, at every point in the medium, have a particle motion perpendicular to the direction of propagation (Figure 1.1-b and c). The propagation velocity for shear waves is equal to:

$$V_S^2 = \mu/\rho$$

A

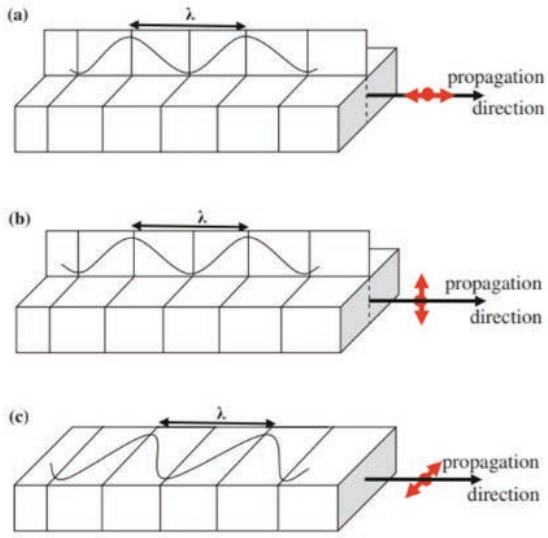

B

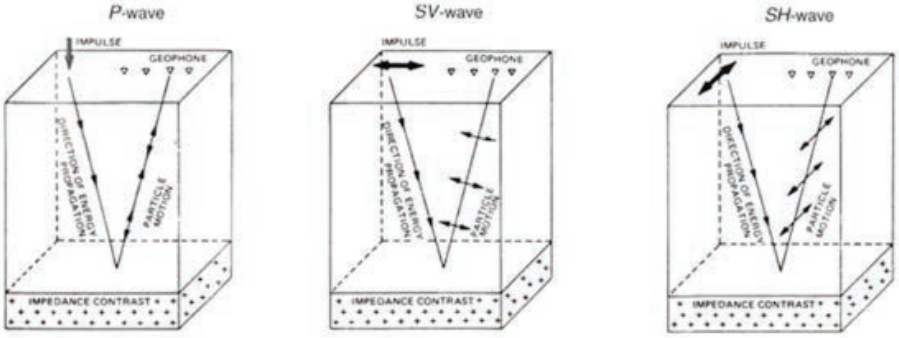

Figure 1.1 *Schematic representation of the particle displacement induced by body-waves traveling in a solid medium, (λ) is the wavelength: A – plane body-wave (a) P-wave, (b) SV-wave, (c) SH-wave. (Adapted from Alsadi, 2017); B – propagation and vibration directions for body waves (a) P-wave, (b) SV-wave, (c) SH-wave (after Ensley, 1985).*

Shear waves do not propagate in fluids. The ratio V_P/V_S is independent of the formation density so allows the calculation of Poisson's ratio which is used to differentiate unconsolidated rocks (Poisson's > 0.35) from consolidated rocks (Figure 1.2).

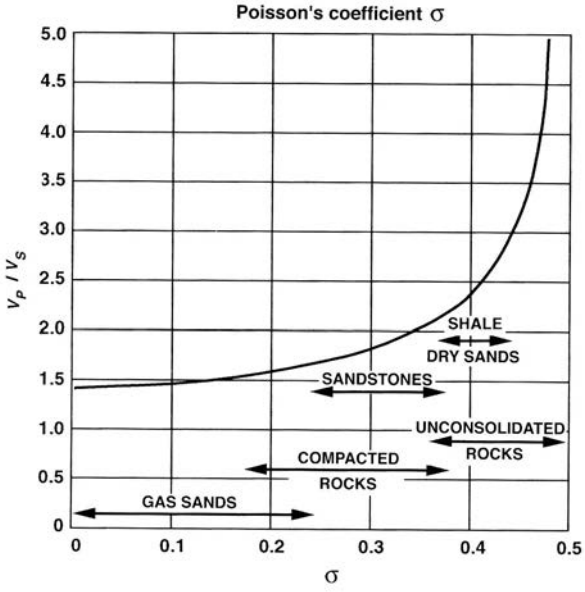

Figure 1.2 *Poisson's ratio.*

In the three-dimensional reference system (x, y, z), the x-direction (horizontal) and the z-direction (vertical) represent the vertical plane of the acquisition profile, which contains the source and the receivers and is oriented perpendicular to the main axis of the structure. If the structure has no lateral variation in the y-direction, the structure is said to be cylindrical; variations in displacements along y are zero. On the assumption of a cylindrical structure, the propagation directions of all waves are contained within the plane of the acquisition profile. Particle displacements of the *P*-waves are in the (x, z) plane. *S*-wave particle motions are either in the plane of the profile – called *SV*-waves (vibrations in the vertical plane) – or perpendicular to the plane of the profile, called *SH*-waves (vibrations in the horizontal plane). The vibration and propagation directions of the various wave types, *P, SV* and *SH*-waves, are illustrated in Figure 1.1-B.

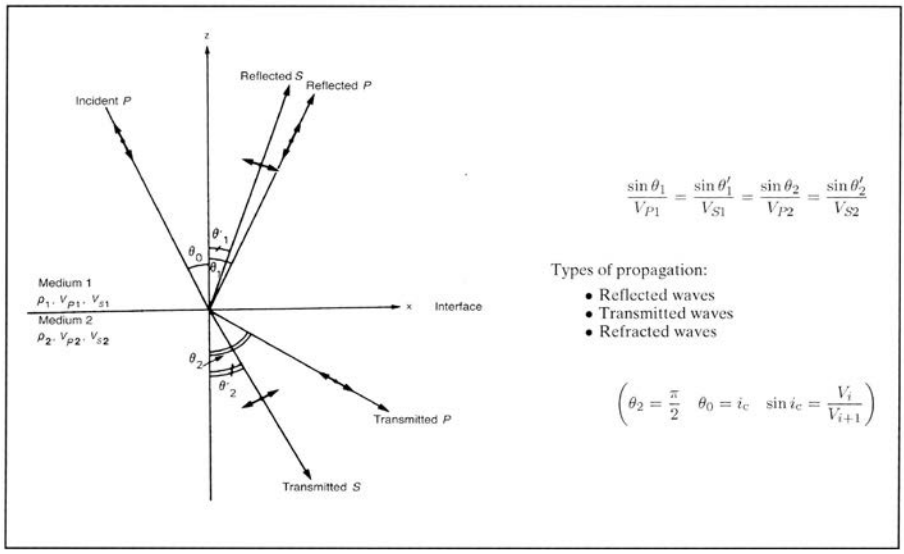

Box 1.1 *Snell's law. Angular relationships between incident, reflected and transmitted rays for the various wave types in the case of an incident compressional wave with a wave-front perpendicular to the plane of the diagram. Particle motion is represented schematically (after Lavergne, 1989).*

When a *P* or *SV*-wave strikes an interface at an angle of incidence not equal to zero, four waves are generated: two transmitted (one *P* and one *SV*-wave) and two reflected (again, one *P* and one *SV*-wave). The angular relationships between the propagation directions of each of these waves are given by Snell's law (Box 1.1).

The creation of an *S*-wave from a *P*-wave, or vice versa, is a phenomenon called mode conversion. For cylindrical structures, *SH*-waves propagate without mode conversion. Box 1.2 gives the wave equations associated with particle displacements (u, v, w) observed in the (x, y, z) directions for a seismic profile oriented in the x-direction and perpendicular to the axis of a cylindrical structure on the y-axis.

Particle movements in the y-direction, associated with *SH*-waves, are governed by a simple equation involving only the displacement v along y and the velocity V_S, hence there can be no mode conversion (Box 1.2, Eq. (2)). Equations are more complex for the u and v displacements associated with the propagation of *P* and *SV*-waves (Box 1.2, Eq. (1)).

The wave equation may be used to calculate synthetic seismograms that are the response of the subsurface to an excitation. For a distribution of velocities (V_P and V_S) and densities ρ, a synthetic seismogram can be calculated for a given acquisition geometry. The synthetic seismogram can be compared with an actual field record registered with the same geometric parameters (source and receiver positions). The distribution of velocities and densities can be updated so that an

optimum fit between the synthetic and the field data is obtained. This procedure is called full waveform inversion (FWI). FWI is discussed in a specific chapter (chapter 5). The wave equation is used in specific processing procedures such as tomography and migration.

Notation: $U_1 = u(//x) \quad U_2 = v(//y) \quad U_3 = w(//z) \qquad \frac{\partial}{\partial y} = 0$

$$\frac{\partial^2 w}{\partial t^2} = \frac{\partial}{\partial x}\left(V_S^2\left(\frac{\partial w}{\partial x} + \frac{\partial u}{\partial z}\right)\right) + \frac{\partial}{\partial z}\left(V_P^2\left(\frac{\partial u}{\partial x} + \frac{\partial w}{\partial z}\right)\right) - 2\frac{\partial}{\partial z}\left(V_S^2\frac{\partial u}{\partial x}\right) \quad (1)$$

$$\frac{\partial^2 v}{\partial t^2} = \frac{\partial}{\partial x}\left(V_S^2\frac{\partial v}{\partial x}\right) + \frac{\partial}{\partial z}\left(V_S^2\frac{\partial v}{\partial z}\right) \quad (2)$$

Equation (1): P- and SV-waves with mode conversion

Equation (2): SH-waves no mode conversion

Velocity : $V = \sqrt{\frac{\text{Elasticity}}{\text{Density}}} = \sqrt{\frac{E}{\rho}}$ $\quad E = \lambda + 2\mu$ P-wave $\quad E = \mu$ S-wave

Box 1.2 *Wave equation for a 2D seismic profile.*

Works such as Achenbach (1973), Dobrin (1988) and Quiblier (1997) should be consulted for more complete information on synthetic seismogram calculation.

1.2 Seismic methods

When P or S-waves strike the interface at the critical angle i_c, head waves or refracted waves are generated. This only occurs when a wave perturbation passes from a medium with velocity V_i to another with velocity V_{i+1} which is greater than V_i and at the critical angle given by $sin(i_c) = V_i / V_{i+1}$.

The critical angle i_c is the criterion for differentiating the various seismic methods associated to body wave propagation (Box 1.3):

- $i<i_c$: the method is seismic reflection
- $i=i_c$: the method is seismic refraction
- $i>i_c$: the method is wide angle reflection. In wide angle reflection there is no transmitted energy, only reflected.

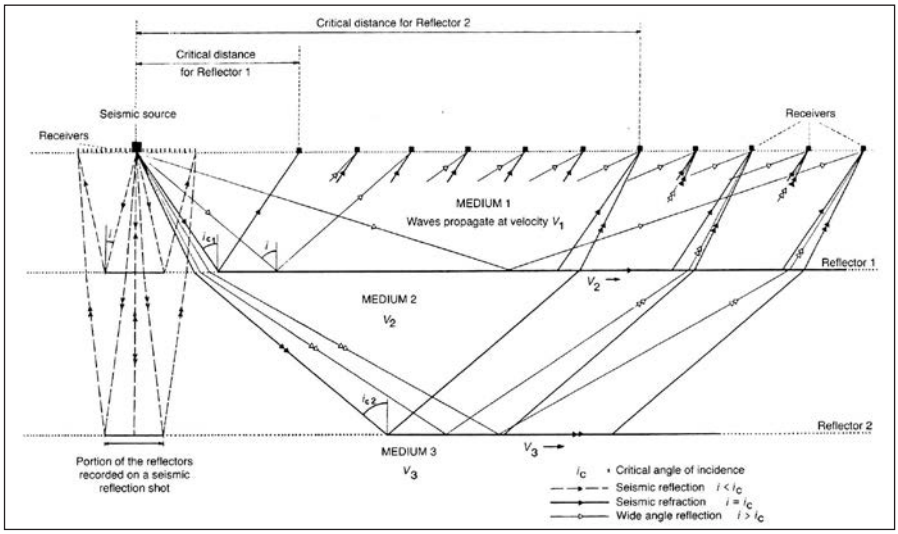

Box 1.3 *The various types of seismic surveying. At distances equal or greater than the critical distance, refracted waves or wide-angle reflections can be captured from the reflector.*

In addition to the body waves generated by a surface seismic source, which propagate through the subsurface, surface waves also propagate through the earth with their energy concentrated near to the surface. Surface waves, which are mainly sensitive to the shear modulus, do not represent a new wave type; they are interference phenomena resulting from body waves (Figures 1.3-a, b). Travelling only within a few seismic wavelengths from the surface of a solid, the lower the frequency of a surface wave, the deeper its penetration depth into the earth. Therefore, in the same medium, waves of different wavelengths affect different depths (Figure 1.3-c).

These waves, which usually exhibit larger amplitudes and lower frequencies than body waves, are used in civil engineering to determine the mechanical parameters (shear velocity and shear modulus) of the first tens of meters below the ground surface.

Among surface waves, which are the main component of ground roll, there are two classes of great interest to characterize the shallow near surface:

a) Rayleigh waves, (R-waves) – travel on the free surface of a semi-infinite solid medium. They are generated from the interference of multiple reflections of *P* and *SV*-waves. The particle motion has a retrograde elliptical orbit travelling in a vertical plane parallel to the propagation direction, this is polarized in a vertical plane through the propagation direction. The minor axis of the ellipse is parallel to the wave motion direction and equal to two-thirds of its major axis (Figure 1.3-a). On the surface of a solid medium with a Poisson's ratio of $\nu = 0.25$, the Rayleigh waves travel with a velocity V_R, which is slightly lower than shear wave velocity V_S, $V_R = 0.92V_S$.

If the semi-infinite medium is overlain by a low-velocity surface layer, as occurs in the field where a weathered layer is present, the elastic constants change with depth, and long wavelengths travel faster than short wavelengths, depending on the elastic properties at greater depths. Such conditions alter some of the wave characteristics and the surface wave is referred to as a pseudo-Rayleigh wave. In this case, the harmonic components of longer wavelengths (lower frequencies) travel faster, and different wavelengths sample different depths in the earth and the propagation velocity can be strongly frequency-dependent (dispersion). The degree of dispersion is a measure of seismic wave velocity as a function of depth and can be used to calculate the thickness of surface layers.

b) Love waves, (L-waves) – develop only if a horizontal low-velocity layer lies over a solid elastic semi-infinite medium. These waves consist of multiples reflections of *SH*-waves while trapped in the horizontal layer. Particle motion is transverse and horizontally polarized (Figure 1.3-b). Since the vertical component does not exist, Love waves are not detected by the vertical geophones. Velocity is close to *S*-wave velocity in the subsurface medium for very long wavelengths; and close to that of the surface layer for short wavelengths. Therefore, these waves always exhibit dispersion and the propagation velocity increases with the period of the harmonic component.

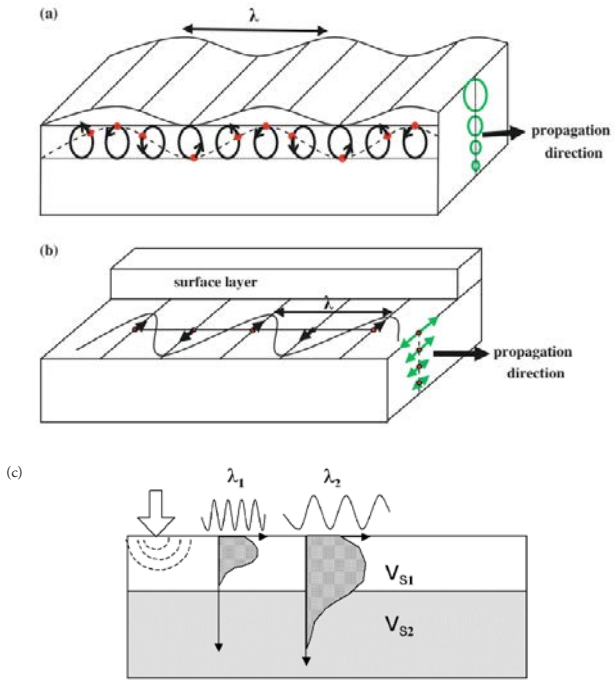

Figure 1.3 *A depiction of the displacement induced by plane surface waves. Wavelength (λ): (a) Rayleigh waves; and (b) Love waves (adapted from Alsadi, 2017); (c) geometrical dispersion of Rayleigh waves associated with short (λ_1) and long (λ_2) wavelengths. (Adapted from Socco and Strobia, 2004).*

The processing classically applied to surface waves is based on spectral analysis and involves two steps. The first step is the construction of a dispersion curve (a plot of phase-velocity against frequency). A large number of techniques are available, which can be classified into two main classes: frequency–wavenumber or spatial auto-correlation. The next step aims to obtain shear wave velocity (i.e. stiffness) profiles as a function of depth and horizontal position along the seismic survey line. The profiles are calculated using one of the two iterative purposes: matching the experimental dispersion curves to a theoretical curve derived from forward analytical modeling or an automatic least-squares approach.

A field example of surface waves processing is provided in chapter 6.

1.3 Example of field records

A seismic spread is composed of a source spread and a receiver spread. In 2D seismic surveys, the sources and receivers are located on the same line which defines a 2D seismic profile. In 3D seismic surveys, the sources and receivers are usually located on 2 orthogonal lines: a line of sources and a line of receivers.

The relative positions of the sources and receivers define the acquisition geometry.

A seismic record is a set of seismic traces recorded at different receiver positions. The seismic trace represents the vibrations of the ground due to wave propagation generated by a seismic source. A geophysicist is able to identify the different seismic waves from a field record. For a simple geological model (a single horizontal layer over an infinite substratum), the arrival times T of the different body waves observed at a distance X from the source are given by simple T-X equations (T-X curves). Figure 1.4-a shows, for a line of receivers, different possible locations of source points. The distance between 2 geophones on the seismic line is 2 m. If the source point (green dots) is located at the extremities of the receiver spread, the spread is called an end-on spread and the shot is an in-line shot (2D). If the source point (yellow dots) is located on a line perpendicular to the receiver line, the spread is called a cross-spread and the shot is a cross-line shot (3D). The distance between the source position and the receiver position is called the Offset X. An offset can be decomposed in an in-line offset x, and a cross-line offset y, such that:

$$X^2 = x^2 + y^2$$

If y = 0, and if x = 0 corresponds to the middle of the line of receivers, the spread is called a split-dip spread, and the shot is a split-dip in-line shot (2D).

Body waves can be differentiated by their T-X curves. Figure 1.4-b shows the ray paths and the T-X curves associated to the direct wave, refracted wave and the reflected wave. The arrival times of a surface wave are locally approximated by linear equations. Figure 1.4-c shows an in-line shot obtained with an end-on spread with the identification of the different waves. Figure 1.5 shows a cross-line shot obtained

with a cross-line spread. In this figure, the horizontal axis represents the in line offset x, consequently the waves appear with a hyperbolic shape on the T-X diagram.

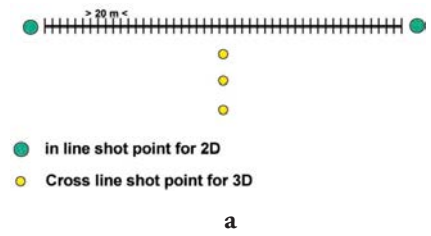

a

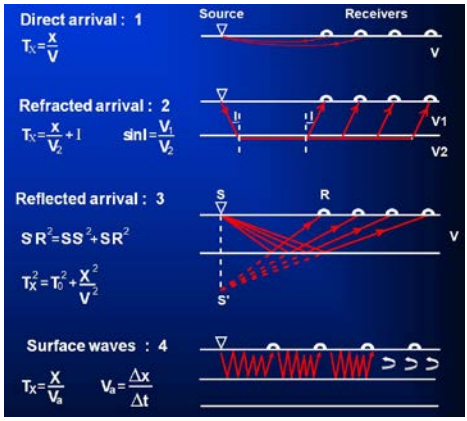

b

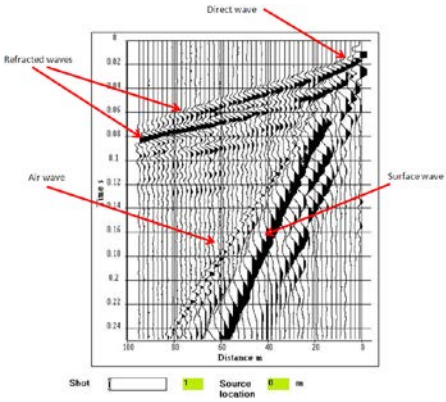

c

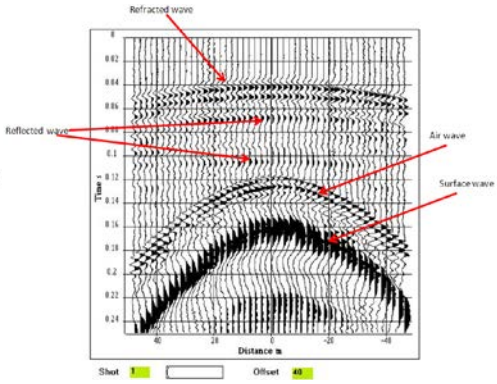

d

Figure 1.4 *Seismic spreads (a), T-X curves (b), In-line shot (c), Cross-line shot (d).*

Figure 1.5 shows examples of 2D shot points with split-dip spreads (top) and end-on spreads (bottom). For the end-on spread, the 2 shots are obtained with the source located at the 2 extremities of the receiver line. One shot is called a direct shot, the other a reverse shot.

Figure 1.6 shows examples of 3D shot points with cross spread, the cross-line offset varying between 0 and 40 m. With a lateral offset of 40 m, reflected events are clearly visible, as indicated on Figure 1.4-d.

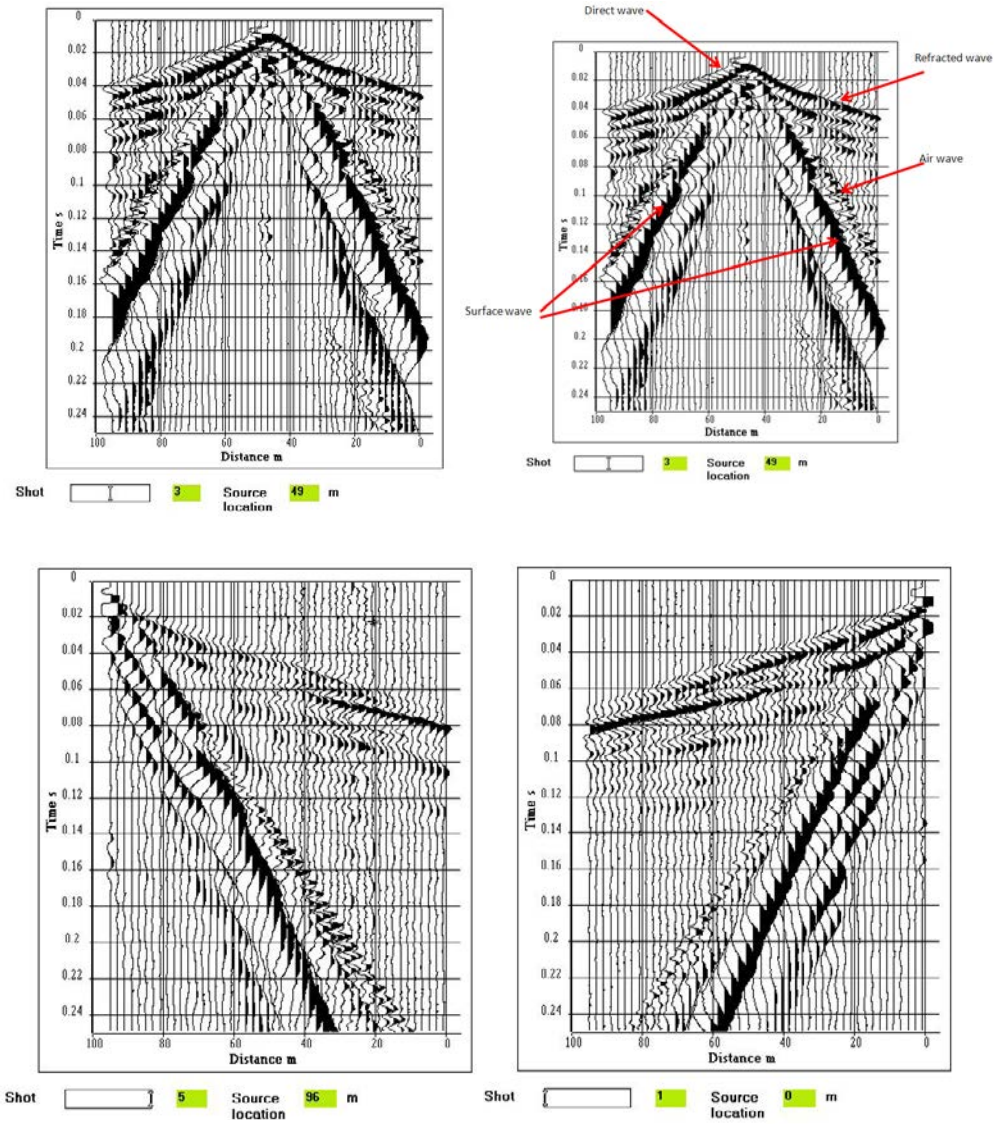

Figure 1.5 *2D shot points (top: split dip spread, bottom: direct and reverse end-on spreads).*

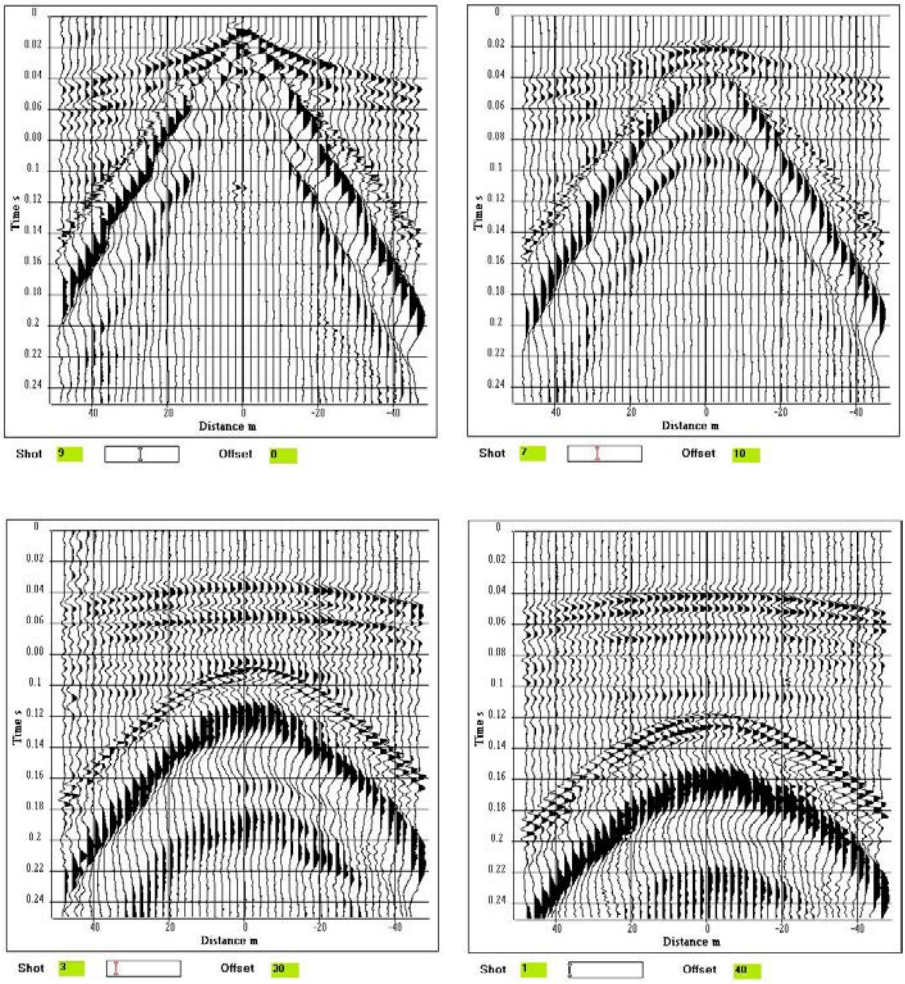

Figure 1.6 *3D shot points (cross-spread with cross-line offset ranging from 0 to 40 m).*

In marine surveys, raw data can be presented in shot point gathers as for land acquisition. Another method of viewing the data is the constant offset section. For each shot, a trace at a given offset is selected. The set of constant offset traces is called a constant offset section. Figure 1.7 is an example of a constant offset section. The first event, named Primary, is the sea bottom reflected wave. The water bottom generates a very characteristic multiple, called a water-bottom multiple (labeled 'Multiple' on the Figure). A multiple reflection is an arrival that has been reflected several times (generally an odd number of times) during its travel path in the subsurface.

Multiple reflections are produced within the rock layers due to laminations of the rock formations, giving rise to internal multiples.

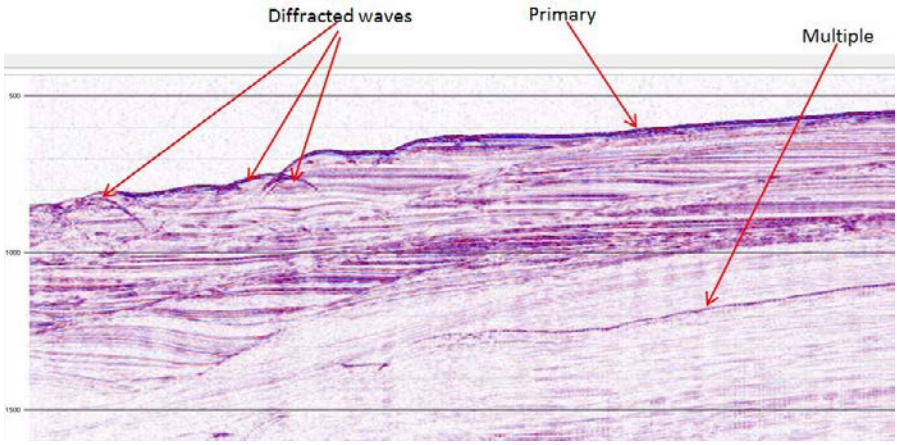

Figure 1.7 *Marine constant offset section (data provided courtesy of Craig Fullthorpe, University of Texas).*

Other notable spurious arrivals on the records are diffractions. A seismic diffraction is produced when the seismic wave impinges on an angular point or heterogeneity of a size that is less than the wavelength of the incident wave. The heterogeneity or point diffractor radiates energy in all directions. On a seismic record, the point diffractor appears across different traces as a hyperbolic alignment. Figure 1.7 shows diffracted waves due to the heterogeneity of the sea bottom.

1.4 Wave separation

Direct and refracted arrivals have linear time-distance curves, reflection events are hyperbolas to a first approximation (Figure 1.4-b). The time-distance curves of surface waves can be treated as locally straight lines. Diffractions have a hyperbolic time-distance curve.

Locally a wave can be characterized by its:

- period T expressed in s or ms,
- apparent velocity $Va = \Delta x / \Delta t$. The quantity Δt is the difference in arrival times of the wave at various receivers at a distance Δx apart.

The wave can be characterized equally well by its:

- frequency f, expressed in Hz (or in cycles/second),
- Wavelength λ, expressed in m, and
- Wavenumber k, expressed in cycles/meter (c/m).

Frequency is the reciprocal of the period T ($f = 1/T$). Wavelength is the distance traveled by a wavefront during a time equal to the period T ($\lambda = VT = V/f$, V being the propagation velocity). Wavenumber k is related to the wavelength λ in the same way that frequency f is related to the period T ($k = 1/\lambda$).

Velocity V can be expressed in the time-distance domain (t, x) or in the frequency – wavenumber domain (f, k): $V = x/t = f/k$.

The translation from the (t, x) domain to the (f, k) domain and vice versa is accomplished by the forward and inverse Fourier transforms. The amplitude representation of a (t, x) record in the (f, k) domain is called a two–dimensional amplitude spectrum.

Waves can be separated by different filters (Mari, 2015) such as:

- Frequency filter (f),
- Wavenumber filter (k),
- Apparent velocity filter in the (f, k) domain ($Va = f/k$).

Other filters can also be used, such as:

- SVD (Singular Value Decomposition) filter,
- polarization filter,
- …

Figure 1.8 shows an example of an in-line shot point obtained with an impulse source. The receiver spread is composed of 48 single geophones. The distance between 2 adjacent geophones is 5 m. The time sampling interval is 0.25 ms and the recording length is 0.5 s. The data are presented both in the time distance domain and in the frequency - wavenumber domain. The wave separation is done in the (f, k) domain by apparent velocity filters.

The 2D amplitude spectrum of the raw data (Figure 1.8-a) shows that some of the energy is located in the negative wavenumbers. The waves associated with this energy propagate with negative apparent velocities.

The main energetic wave fields are the direct waves, and the low and high apparent velocity pseudo-Rayleigh waves (Figures 1.8-b and c). Figure 1.8-d shows the wavefield associated with negative wavenumbers. These waves are converted refracted waves. The refracted wave is shown in Figure 1.8-e. The reflected waves, shown in Figure 1.8-f, are characterized by small wavenumbers and, consequently, very high apparent velocities.

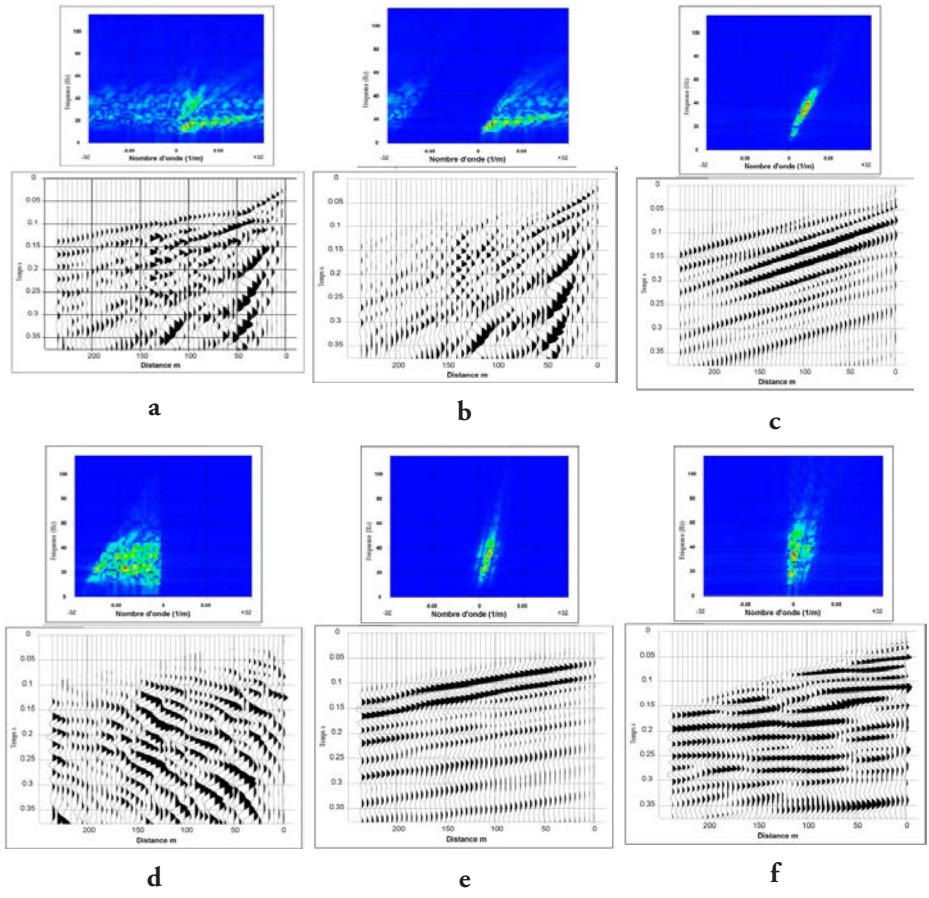

Figure 1.8 *wave separation - In line shot point (a) raw data, (b) direct wave and slow Rayleigh wave, (c) fast Rayleigh wave, (d) converted refracted waves, (e) refracted wave, (f) reflected waves (Normalised displays).*

Figure 1.9 is an example of wave separation by wavenumber filters. The example shown is based on a VSP (Vertical Seismic Profile; Mari and Vergniault, 2018) data set. From top to bottom, this figure shows:

- Raw data,
- Downgoing wavefield associated with positive wavenumbers,
- Upgoing wavefield associated with negative wavenumbers.

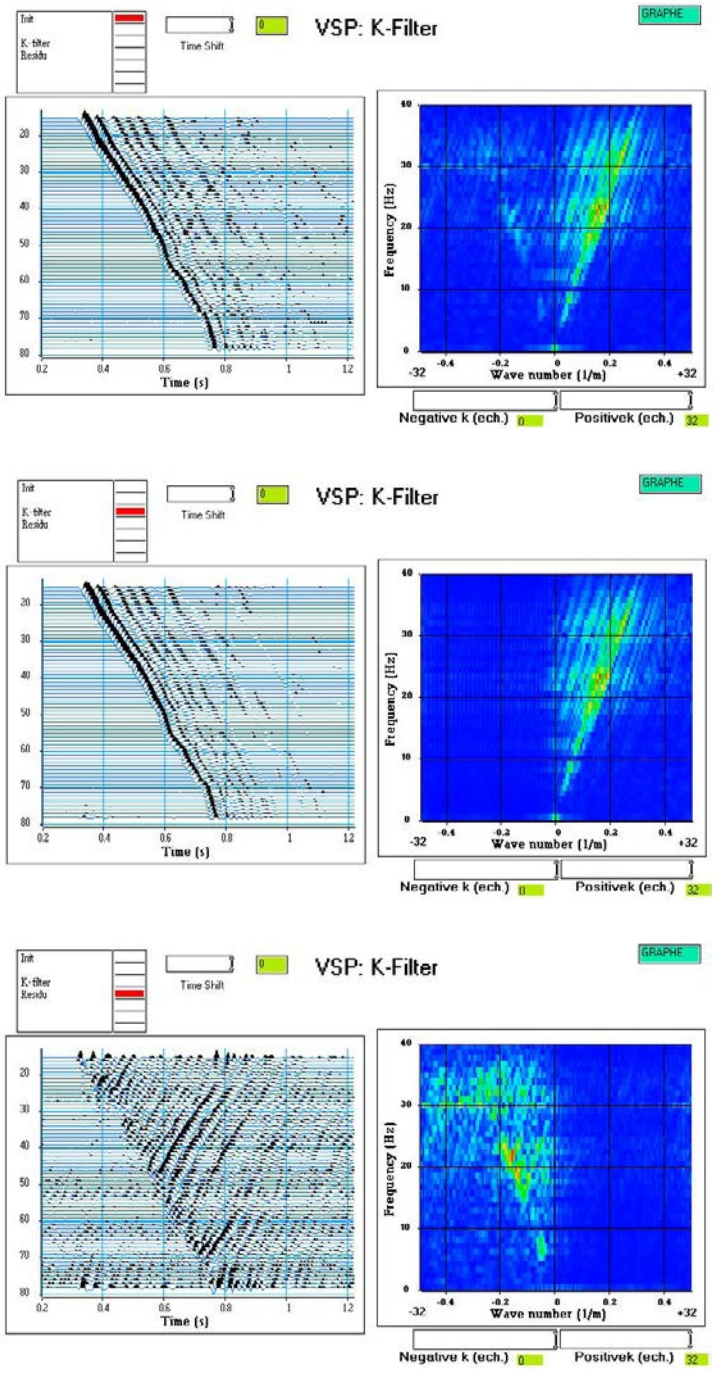

Figure 1.9 *wave separation - VSP data. From top to bottom: raw data, downgoing wavefield, upgoing wavefield.*

1.5 Conclusion

In summary, a seismic record contains:

- direct arrivals,
- refracted waves,
- surface waves,
- reflected waves,
- diffractions,
- multiples, and
- noise unrelated to the seismic shot.

The various waves can be categorized according to their characteristic properties. One of the most distinguishing properties is a wave's time-distance curve. The acquisition geometry and the type of seismic survey must be taken into consideration. The waves can be separated by filters such as (f, k) filters in the (f, k) domain.

References

Achenbach J.D., 1973, *Wave propagation in Elastic solids*, North Holland Publishing Company, 3rd Ed.

Alsadi H.N., 2017, *Seismic hydrocarbon exploration, 2D and 3D techniques*. Springer, ISBN: 978-3-319-40435-6. http://www.springer.com/978-3-319-40435-6.

Dobrin M.B., Savit C.H., 1988, *Introduction to Geophysical Prospecting*, 4th edition McGraw-Hill Book Co., 867 p.

Ensley R., 1985, Evaluation of direct hydrocarbon indicators through comparison of compressional- and shear-wave seismic data: a case study of the Myrnam gas field, Alberta, *January Geophysics* 50(1), DOI: 10.1190/1.1441834.

Lavergne M., 1989, *Seismic methods*, Éditions Technip, Paris, ISBN: 2-7108-0552-9.

Mari J.L., 2015, *Signal processing for geologists & geophysicists*, e-book, DOI:10.2516/ifpen/2011002. http://books.ifpenergiesnouvelles.fr/ebooks/signal-processing/

Mari J.L., Vergniault C., 2018, *Well seismic surveying and acoustic logging*, EDP Sciences, DOI: 10.10051/978-2-7598-2263-8, ISBN (ebook): 978-2-7598-2263-8. https://www.edp-open.org/well-seismic-surveying-and-acoustic-logging

Socco L.V., Strobbia C., 2004, Surface-wave method for near-surface characterization: a tutorial, *Near Surface Geophysics*, 165-185.

Quiblier J., 1997, *Propagation des ondes en géophysique et en géotechnique. Modélisation par méthodes de Fourier*, Éditions Technip, Paris.

2

Refraction surveying

J.-L. Mari

Seismic refraction was the first technique used in oil exploration. During the 1920-1960s, the refraction method allowed the detection of salt domes in the United States, the mapping of large extend structures in Iran, and oil field discoveries in the Algerian Sahara. However, from the 1930s seismic reflection became the predominant seismic method and the refraction method was used for the computation of static corrections.

Today, the refraction method provides a quick reconnaissance-mapping tool for delineating near-surface velocity structures and/or their associated static corrections. It requires only the measurement of the arrival times of first arrival waves (direct and refracted waves) to provide a geological model, whereas the reflection method requires a complete processing of the recorded wavefield. The picking of first arrivals is much easier than the identification and picking of other events.

DOI: 10.1051/978-2-7598-2351-2.c004

Seismic refraction is currently used in civil engineering and hydrogeology for targeted depths of less than 300 m (Mari *et al.*, 1999). The method is particularly suited for the following studies:

In civil engineering:

- Preliminary studies for construction sites,
- Determination of the near surface structures,
- Rock mechanics (rippability, Poisson's ratio),
- Search for cavities.

In hydrogeology:

- Highlighting channels carved in bedrock,
- Highlighting fractured areas in bedrock,
- Measurement of water table depth.

2.1 Refraction surveying: Plus-Minus and GRM methods

Refraction-based velocity estimation of the subsurface is conventionally carried out using well-known methods, such as the Hagedoorn's Plus-Minus method (1959) or the generalized reciprocal method (GRM) proposed by Palmer (1986), which provides simple models of the subsurface defined by refractors with simple geometry and a relatively constant velocity distribution. The GRM method is widely used in refraction prospecting (Ge *et al.*, 2010). It assumes that first arrivals only originate from critical refraction and lateral continuous refractors with relatively simple velocity distributions. The method becomes less accurate as subsurface variability increases. It is used for shallow investigations and to determine weathering corrections in refraction and reflection surveys.

Refraction imaging of the subsurface is based on the analysis of refraction time-distance curves. The arrival time t(x) of the refracted wave is given by the following relationship:

$$t(x) = x.\cos(\varphi)/ VR + \delta(0) + \delta(x) \quad (2.1)$$

- x: source – receiver distance
- φ: dip of refractor over spread length
- VR: refractor velocity
- δ(0): delay time at source point
- δ(x): delay time at receiver point

Equation (2.1) can be rewritten as follows:

$$t(x) - x.\cos(\varphi)/ VR = \delta(0) + \delta(x) \quad (2.2)$$

Equation (2.2) is called the T – X/V curve.

To obtain the true velocity of each marker, its dip and thickness, time-distance curves in both directions are required, i.e. up-dip shooting and down-dip shooting (direct and reverse shots), as shown in Figure 2.1. This requires recordings where geophones are aligned with shot points. Such an implementation makes it possible to measure two apparent velocities Va1 and Va2 and two intercept times I1 and I2 on time-distance curves associated with the refractor.

For shot 1 (up-dip), the following relationships apply:

$$t(x) = x/Va1 + I1 \text{ with } V1/Va1 = \sin(i_c + \varphi) \text{ and } I1 = 2H1.\cos(i_c)/V1$$

For shot 2 (down-dip), the following relationships apply:

$$t(x) = x/Va2 + I2 \text{ with } V1/Va2 = \sin(i_c - \varphi) \text{ and } I2 = 2H2.\cos(i_c)/V1$$

The measurements of the two apparent velocities Va1 and Va2 of the refraction time-distance curves, and the velocity V1 of the direct wave in the first layer, enable the determination of the critical angle i_c, the refractor velocity VR ($V1/VR = \sin(i_c)$), its dip φ, and the thicknesses (H1 and H2) of the layer at the vertical of the two shot points.

The method, known as the intercept-time method, is illustrated in Figure 2.1 for a single layer over a substratum. It can be extended to multilayer models (Palmer, 1986).

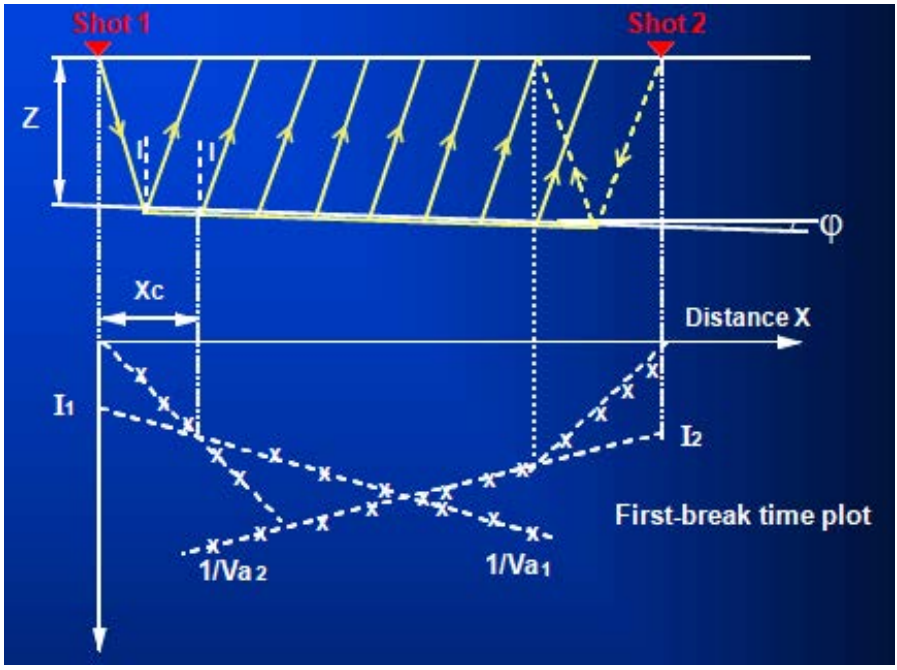

Figure 2.1 *Intercept-time method.*

The direct and reverse shots allow the differentiation between anomalies due to the topography and anomalies associated with the refractors, as shown in Figure 2.2. In the synthetic example, the model is a single layer over a substratum. The waves are refracted by the substratum. The topography is flat with a small rectangular horst. The substratum is flat, with a vertical fault. This Figure shows, from top to bottom:

- Time-distance curves for the arrival times of the waves refracted from the substratum. The red curve corresponds to a direct shot located on the left; the blue curve corresponds to a reverse shot located on the right. It can be seen that the anomaly due to the topography is located on the T-X curves at the same abscissas X.
- The geological model. The raypaths associated with the direct and reverse shots (red and blue lines) are shown within the model.
- T-X/V curves. On the T-X/V curves, the anomalies due to the topography are in phase; the anomalies due to the substratum are shifted laterally in distance. The distance between the anomalies of the 2 curves is the double offset or critical distance (X_c = 2h. tg(i_c)). The two T-X/V curves must be shifted in opposite directions towards their associated shot point to put in phase the anomalies due to the substratum (fault) at the location of the geological feature (fault). The distance of the shift is the single offset (half the critical distance).

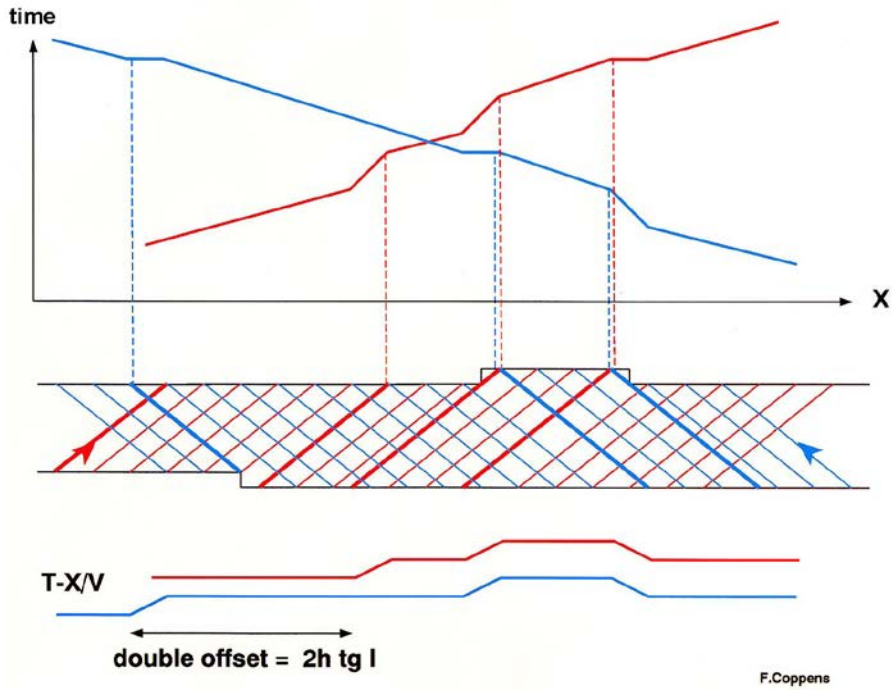

Figure 2.2 *Seismic anomalies on T-X curves.*

Picked times of direct and reverse shot points (Figure 2.3) give access to the t^+ and t^- curves which allow the computation of the refractor velocity analysis function, t_V and the generalized time-depth or delay time, t_G respectively. The analysis of the travel time data proceeds in two stages, with the computation of seismic velocities followed by the depth computations.

Formulae for the computation of the velocity analysis function t_V and time-depths t_G are given in Chapter 8 of "Refraction seismics", (Palmer, 1986). The symbols used are defined in Figure 2.3.

The refractor velocity analysis function, t_V at position G (Figure 2.3-a), is defined by the equation:

$$t_V = \frac{1}{2} t_G^- = \frac{1}{2}\left(t_{AY} - t_{BX} + t_{AB}\right) \tag{2.3}$$

This function is computed for each pair of forward and reverse arrival times, t_{AY} and t_{BX} and the reciprocal time, t_{AB}. The value of the function is referenced to G, which is midway between X and Y, and it is plotted as a function of the distance AG. Equation (2.3) is a linear relation between t_V and the distance AG. Considering a multi-layer model with a plane dipping interface, the slope or gradient of this equation is taken as the inverse of an apparent velocity, V_n', where:

$$\frac{d}{dx} \cdot t_V = 1 / V_n'$$

If dip angles are reasonable, and appear planar over a Fresnel zone, the relation between the true refractor velocity V_n and the apparent velocity, V_n', is:

$$V_n \approx V_n' \cos\theta_{n-1} \text{ with } \theta_{n-1} \text{ the true dip angle of layer } n\text{–}1$$

In general, V_n' is usually taken as the true refractor velocity.

The generalized time-depth, t_G at position G (Figure A1-b), is defined by:

$$t_G = \frac{1}{2} t_G^+ = \frac{1}{2}\left(t_{AY} + t_{BX} - \left(t_{AB} + XY / V_n'\right)\right) \tag{2.4}$$

The relationship between layer thicknesses and the generalized time-depth is:

$$t_G = \sum_{j=1}^{n-1} Z_{jG}\left(\cos\alpha_{jn} + \cos\beta_{jn}\right) / 2V_j \tag{2.5}$$

where α_{jn}, β_{jn} are the ray path angles of incidence at interface j, V_j is the interval velocity of layer j, and Z_{jG} is the thickness of layer j at surface position G.

The depth conversion can be conveniently approximated with the zero-dip expression:

$$t_G = \sum_{j=1}^{n-1} Z_{jG}\left(\cos\phi_{jn}\right) / V_j \text{ with } \sin\left(\phi_{jn}\right) = V_j / V_n \tag{2.6}$$

where ϕ_{jn} are the ray path angles of incidence at interface j if the dip angle θ_j of layer j is 0.

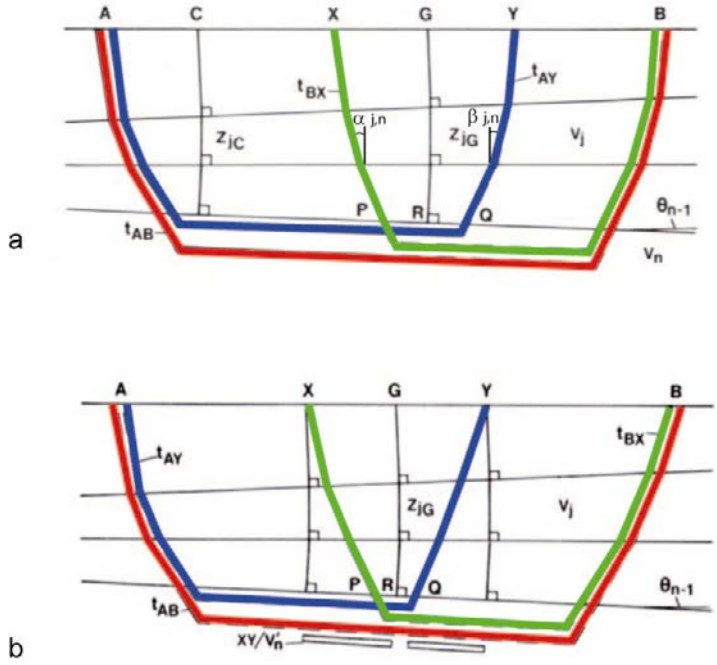

Figure 2.3 *GRM method.*

Figures 2.3-a and b are schematics of the ray paths used in the calculation of both the velocity and the shape of the refractor. For a value of XY such that the forward and reverse rays emerge from nearly the same point on the refractor, i.e. P, R and Q coincide, as shown in Figure 2.3, a result similar to the mean of the migrated forward and reverse delay times is obtained. At the optimum value of XY (P and Q are coincident), accurate velocities can be measured with deep or irregular refractors and the maximum definition of the refractor can be recovered from the travel time data (Palmer, 1986). The Plus-Minus method (a simplified version of the GRM method with XY=0) assumes that first arrivals only originate from critical refraction and laterally continuous refractors with relatively simple velocity distributions.

Figure 2.4 is an example of a refraction survey. The refraction line is rectilinear. In the acquisition of data, a 48-channel recorder was used. An explosive source (25 g) was detonated and a single geophone (10 Hz) per trace was deployed. Such a source makes it easy to identify and pick first arrivals. The distance between two adjacent geophones was 5 m. A direct shot and a reverse shot were recorded (Figure 2.4, top). To obtain the velocity of the refractor (top of the reservoir) and its depth, the Plus-Minus method was used. This method requires geophones to be aligned with shot points. The arrival times of the direct and refracted waves have been picked on the two in-line shots. The picked times from the in-line shots (direct and reverse) have been used to compute the t^- and the t^+ curves to obtain the velocity V2 of the

refractor and the generalized time-depth curve. The t^- curve (Figure 2.4, bottom) can be approximated by a straight line, the slope of which gives the velocity of the refractor, which was found to be 3,350 m/s. The slope of the direct wave gives the velocity V1 of the medium situated above the refractor. The medium situated above the refractor is defined as the weathering zone (Wz). Its velocity was found to be 850 m/s. The generalized time-depth, t_G, also called delay time, shows the shape in time of the refractor (Figure 2.4, bottom).

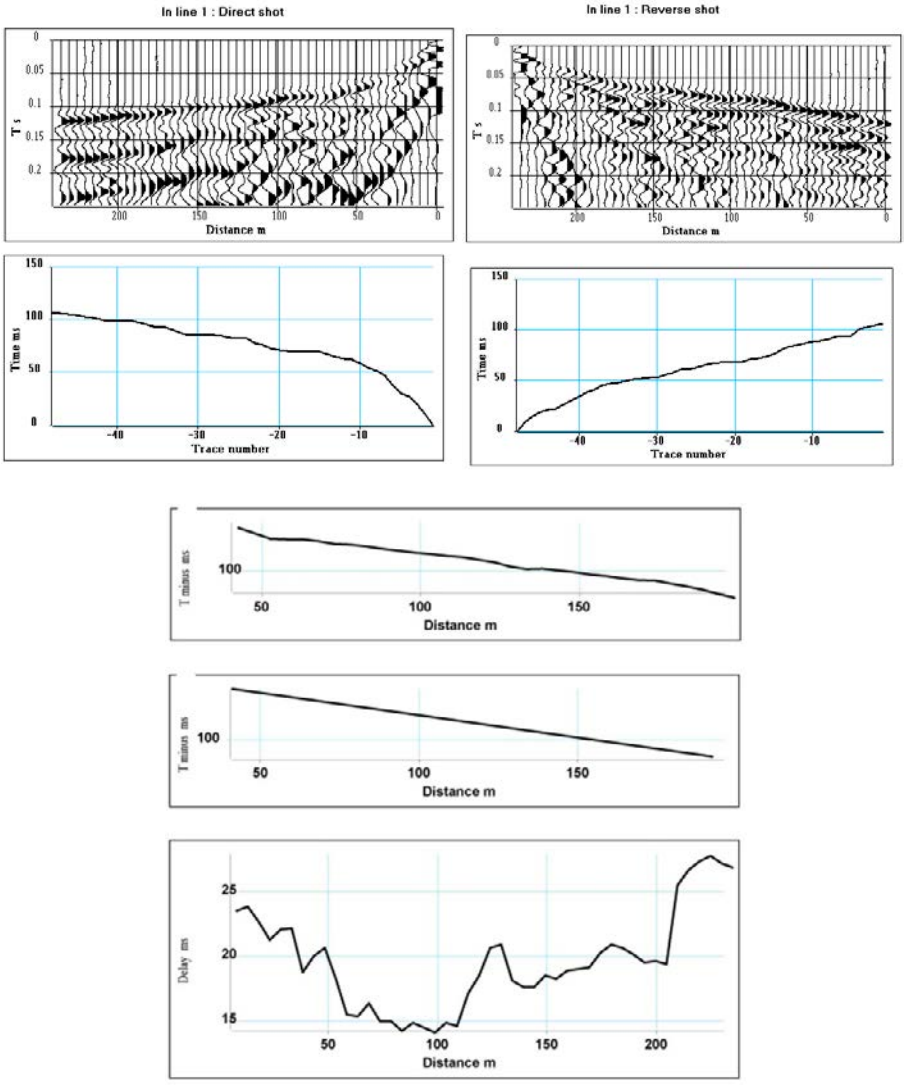

Figure 2.4 *Example of a refraction survey with the Plus-Minus method.*

2.2 Amplitudes of refracted waves

Amplitudes of refracted waves, also called head waves, are not commonly used in seismic refraction studies. Nikrouz (2016) has conducted an interesting synthesis of the relationship between head wave amplitudes and seismic refraction velocities, showing through field studies that variations in amplitudes are associated with velocity changes in the refractor: the higher the contrast in the refractor wave velocity, the lower the head wave amplitude and vice versa (Palmer, 2001). Heelan (1953) and Werth (1967) have shown that the amplitude of a head wave for a thick reflector with a plane horizontal interface is K.G.F(t) where:

- K is the head coefficient which is a function of seismic velocities and densities in the upper layer and the refractor. Werth (1967) expressed K as:

$$K = \frac{2\rho\chi\gamma\left[\lambda_1\left(1+2m\gamma^2\right)+\lambda_2\left(\rho-2m\gamma^2\right)\right]^2}{\left(1-\gamma^2\right)^{1/2}\left[\gamma^2\left(1+2m\gamma^2-\rho\right)+\rho\chi\lambda_2+\chi\lambda_1\left(1+2m\gamma^2\right)^2\right]^2}$$

$$\gamma = V_{P1}/V_{P2}$$

$$\rho = \rho_1/\rho_2$$

$$m = \rho\left(V_{S1}^2/V_{P1}^2\right)-\left(V_{S2}^2/V_{P1}^2\right)$$

$$\chi = \left(1-\gamma^2\right)^{1/2}$$

$$\lambda_1 = \left(V_{P1}^2/V_{S1}^2-\gamma^2\right)^{1/2}$$

$$\lambda_2 = \left(V_{P1}^2/V_{S2}^2-\gamma^2\right)^{1/2}$$

  where V_{P1}, V_{S1} and ρ_1 are, respectively, the P-wave velocity, the S-wave velocity and the density in the upper medium 1; and V_{P1}, V_{S2} and ρ_2 are, respectively, the P-wave velocity, the S-wave velocity and the density in the lower medium 2. The variations of K for a set of elastic parameters can be decreased as the contrast in velocities V_{P2} / V_{P1} is increased (Figure 2.4-a). Figures 4-b to d show variations of K versus V_{S2} / V_{S1} for V_{P2} / V_{P1} ranging from 1.1 to 2, in 3 cases: V_{P1} = 1,700 m/s and V_{S1} = 500 m/s, V_{P1} = 2,000 m/s and V_{S1} = 1,000 m/s, V_{P1} = 2,400 m/s and V_{S1} = 1,600 m/s.
- G is the geometric spreading component given by $1/((rL^3)^{1/2})$ where r is the shot-receiver distance and L is the distance the wave has travelled within the refractor. The geometric spreading component is the major contributor of head wave amplitude.
- F(t) is the displacement potential of the incident pulse.

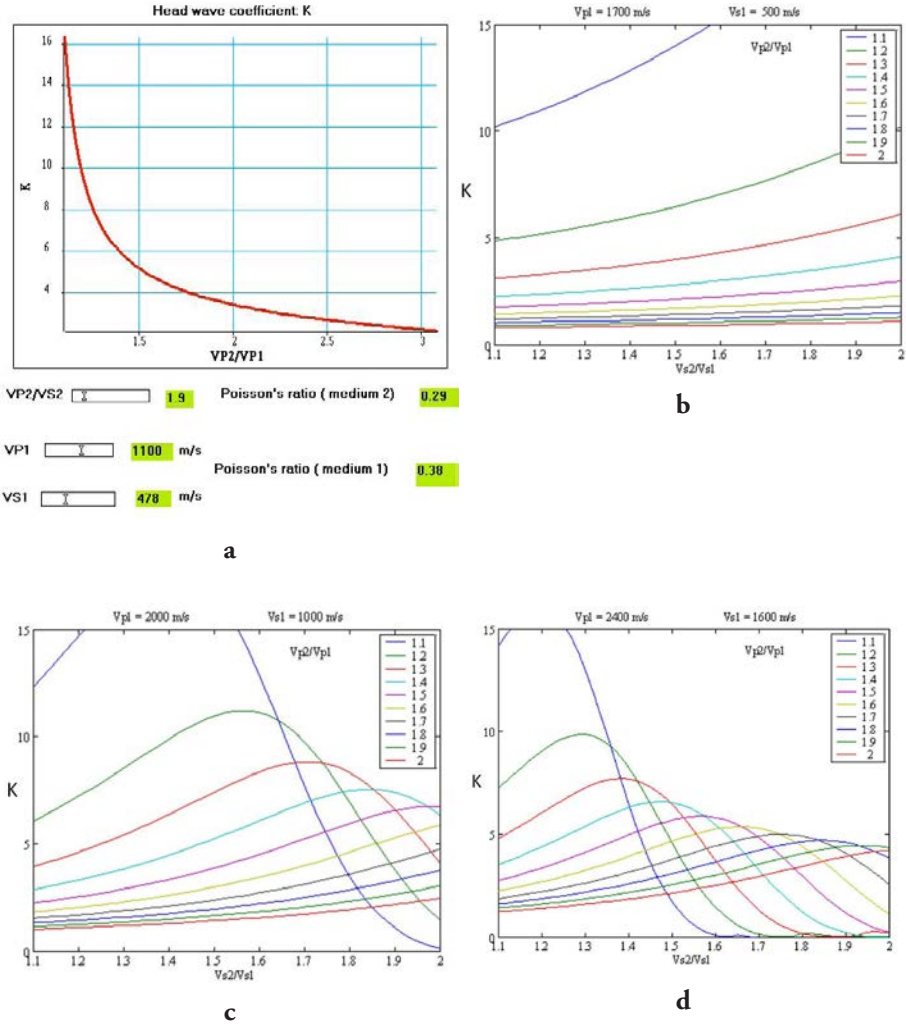

Figure 2.5 *Head wave coefficient.*

The geometric spreading component G must be removed to detect the amplitude variations related to changes in the refractor. In the case of an irregular interface, the refracted wave can be corrupted by converted or diffracted waves, which introduce distortions of the refracted signal. The distortion of the refracted P-wave can be measured by a qualitative dimensionless attribute known as the Shape Index (Ic), which is given by the ratio A2+A3 to A1 where A1, A2 and A3 are the amplitudes of the first three picks of the refraction wavelet. Use of the Shape Index

for acoustic logging was introduced in the 1980s (Lebreton and Morlier, 1983) and then extended to near surface refraction data, as shown in the hydrogeology field case.

2.3 Recommendations for refraction surveying

For refraction surveying, the most favorable conditions are:

- Layer velocity must increase with depth,
- Limited number of markers,
- Weak dips,
- Mostly homogeneous overburden,
- Limited lateral velocity variation.

The choice of implementation parameters (minimum offset, distance between traces, and length of receiver spread) is made by recording refraction shots in the field with a large number of traces covering a wide range of offsets. Analysis of the refraction shot T-X curves enables the definition of the implementation parameters to track a refractor and to predict the modifications of the refraction spread as a function of refractor depth.

The targeted depth defines the minimum offset, it also conditions the receiver spread length. The refraction method is only usable if the refractor velocity (V_R) is clearly discernable from the velocity of the overlying or surrounding layer ($V_R > V_M$). For an accurate measurement of the velocity of the first layer, the distance between the geophones can be reduced (by 1 or 2m) close to the shot point.

To obtain an accurate T-X curve, the refractor must be tracked over a sufficiently large range of offsets. In practice, with a targeted depth h, the total spread length must be 3 to 5 times the depth h. However, if the refractor is a thin bed, the portion of the T-X curve associated with it will not be detected. The seismic refraction method is then “blind”. Another problem that limits the use of refraction seismic surveying is the presence of velocity inversions. For example, for a four-layer model with velocity distributions of: V1<V2>V3<V4, the V3 layer would not appear on the T-X curve. The result of this phenomenon would be an overestimation of depths for the top of layer V4. In the case of lateral velocity variations, the T-X curve can be very complex and difficult to interpret. For the surface detection of a buried structure, the a/h ratio between the size and the depth of the buried structure must be between 2 and 3.

Seismic lines must be laid out in order to facilitate the interpretation of the T-X curves as much as possible. Refraction lines must be rectilinear to avoid errors in the interpretation of the T-X curves. If possible, the receiver spread must be laid out on a plane surface to avoid topographic effects (Figure 2.2).

Refraction seismic surveying is widely used for near surface applications and can be carried out with light field equipment (Figure 2.6):

- A seismic recorder (48 to 96 channels),
- A set of sensors (geophones, hydrophones for marine surveys),
- Cables or streamers,
- Seismic sources (explosive, hammer, weight drop…).

a

b

c

d

e

f

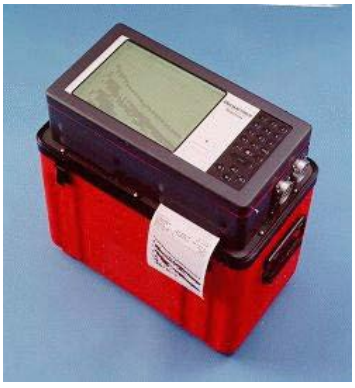

g

h

Figure 2.6 *Field equipment. Source: explosive, gun, weight drop (a, b, c: Apec document); sensors: vertical and horizontal geophones (d, e: IFPEN document), cables (f: IFPEN document); recorders: Geometrics Strataview (g: IFPEN document), Geometrics geode (h: GEO2X document).*

2.4 First example of a seismic refraction application: static corrections

In land seismic acquisition, the elevation differences added to lateral variations in the velocities of the shallow layers cause delays in the arrival times, which vary from trace to trace. Given that these delays are constant with time, the corrections calculated to compensate for them are referred to as "static corrections".

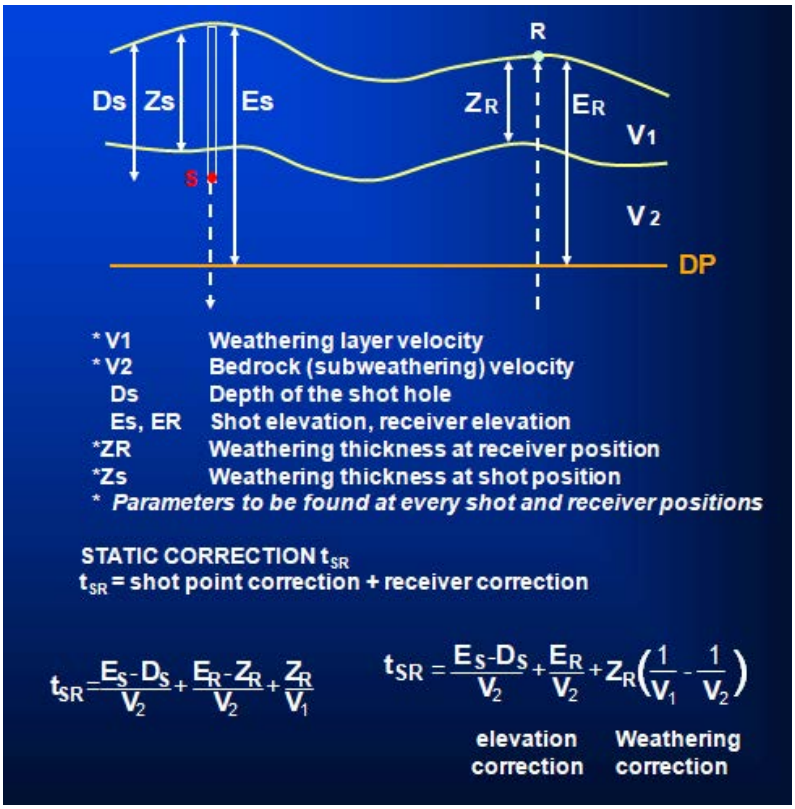

Figure 2.7 *Static corrections. Compensation for delays caused by surface weathering.*

On a seismic record, the event corresponding to a reflection on a seismic horizon no longer forms a hyperbola. The associated t, x (time - distance) curve is distorted due to the surface effects. The surface layer with a variable velocity along the seismic profile is known as the WZ layer, the weathered zone or weathering (Figure 2.7).

The objective of calculating static corrections is to adjust the times of the various traces to simulate the situation where the shots and receivers are on the same surface plane, below which the velocity is constant along the profile. This surface is called the "reference plane" or the "datum plane", abbreviated as DP.

In calculating static corrections, the assumption is that the emergence angle is very small, i.e. the raypaths in the weathered zone (and in practice above the DP) are vertical. The static correction for a given trace is then only a function of the geographical position of the source and receiver and is independent of the source-receiver offset. In some cases this assumption may not be correct: if the emergence angles are not very small, then offset-dependent static corrections must be applied.

Various data are used for the computation of static corrections depending on the location of the line and the land acquisition technique, such as:

- Up-hole or down-hole surveys (Mari and Vergniault, 2018) to obtain the velocity distribution versus depth (Figure 2.8). An up-hole survey gives the absolute static correction at the borehole location. The borehole must be deep enough to reach below the weathering layer. The distance between up-hole surveys on a profile should be less than the spread length to correctly determine long wavelength statics. In practice, close up-hole surveys (more than 2 up-hole surveys per spread length) are needed to make correct correlations between borehole locations. This method, despite the expense due to the need to drill holes, is the best method to use if all the recommendations are followed.
- Weathering shots which are special recordings using a refraction spread designed to determine the thickness and velocity of the weathering layer (Figures 2.1 and 2.4).
- Seismic reflection records. Depending on the geometry designed for the acquisition, the picking of first arrival times (direct and refracted arrivals) provide velocity and delay values (Figure 2.10). If the sources are buried charges, the vertical time VT, also called up-hole time, provides the travel time from the bottom of the borehole.

The total static correction applied to a trace is the sum of the static correction at the source position and the static correction at the receiver position. Determination of the static correction time t_{SR} requires that the elevation, weathered thickness, plus velocities in and below the weathering are known at every point, as illustrated in Figure 2.7.

Below we briefly present the Chronos method, developed by F. Coppens (1985), which provides a set of basic static corrections using constant offset sections and automatic picking. For more details on the Chronos method, the reader should refer to the article by Coppens published in Geophysical prospecting (1985).

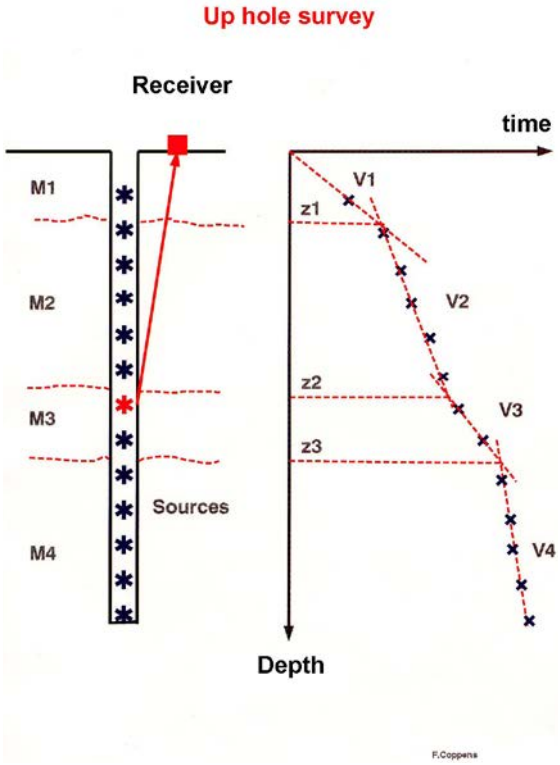

Figure 2.8 *Up-hole survey.*

The calculation of static corrections is based on the measurement of first arrival times. The geophysicist's task is made easier with the use of automatic picking algorithms (Hatherly, 1982; Gelchinsky and Shtivelman, 1983; Coppens, 1985).

Figure 2.9-a shows a seismic record and the 255 m constant offset section, the arrow on the shot point indicating the selected trace. The seismic source is a weight drop. On the constant offset section, the refracted signal evolves very little from trace to trace, which helps with the identification of first arrivals.

The Chronos method is based on the criterion of a sudden energy increase associated with the arrival of a refracted wave. Each seismic trace is transformed into an energy trace representing the ratio between the energy contained in a small sliding window W_2, and the cumulative energy contained in a window W_1, which starts at time zero and ends at the end of window W_2 (Figure 2.9-b). The abscissa τ_0 of the maximum of the energy function gives the approximate time of the refracted arrival. The exact time is then accurately determined by picking the extreme (peak or trough) closest to τ_0 (Figure 2.9-b). If it is an impulsive source, the measured time is reduced by the rise time.

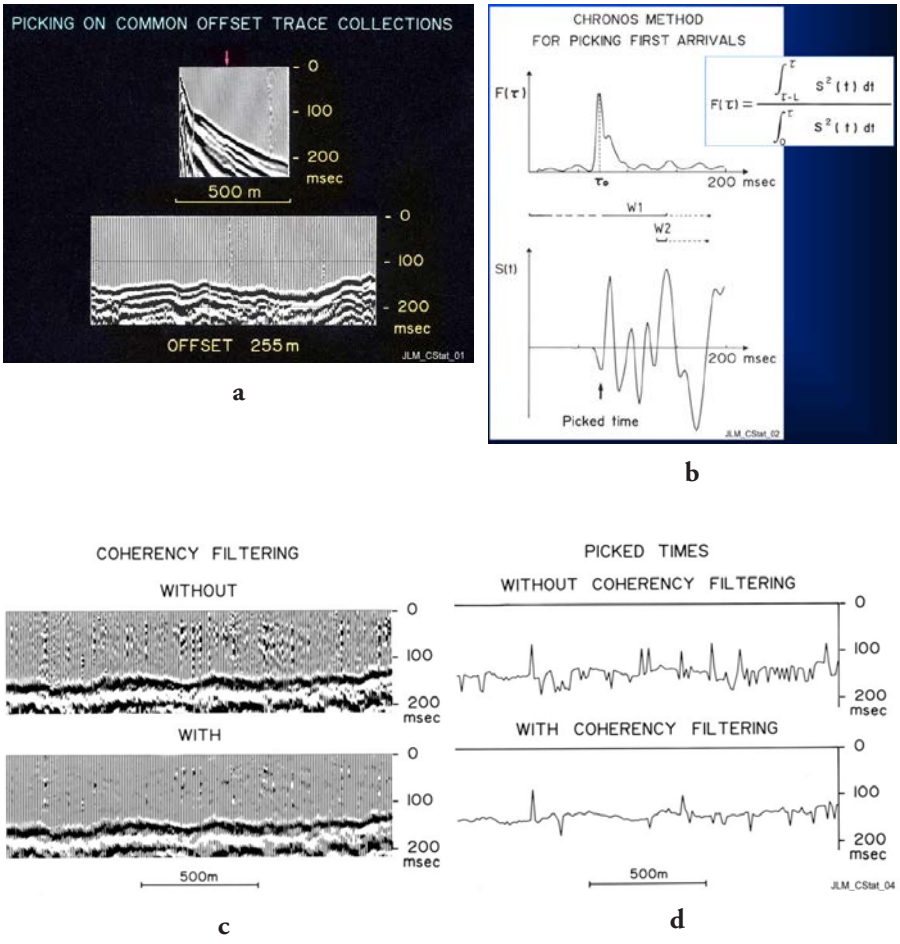

Figure 2.9 *Automatic process for first arrival picking (Coppens, 1985).*

To improve the picking in noisy traces, it is recommended that a spatial coherency filter is applied to seismic traces sorted in constant – offset gathers. Figure 2.9-c shows the efficiency of the coherency filtering on a noisy constant – offset section. The associated picked times are shown in Figure 2.9-d. The number of erroneous picks was considerably reduced. The remaining erroneous values can be edited manually or filtered by a median filter (Mari *et al.*, 1999, 2015).

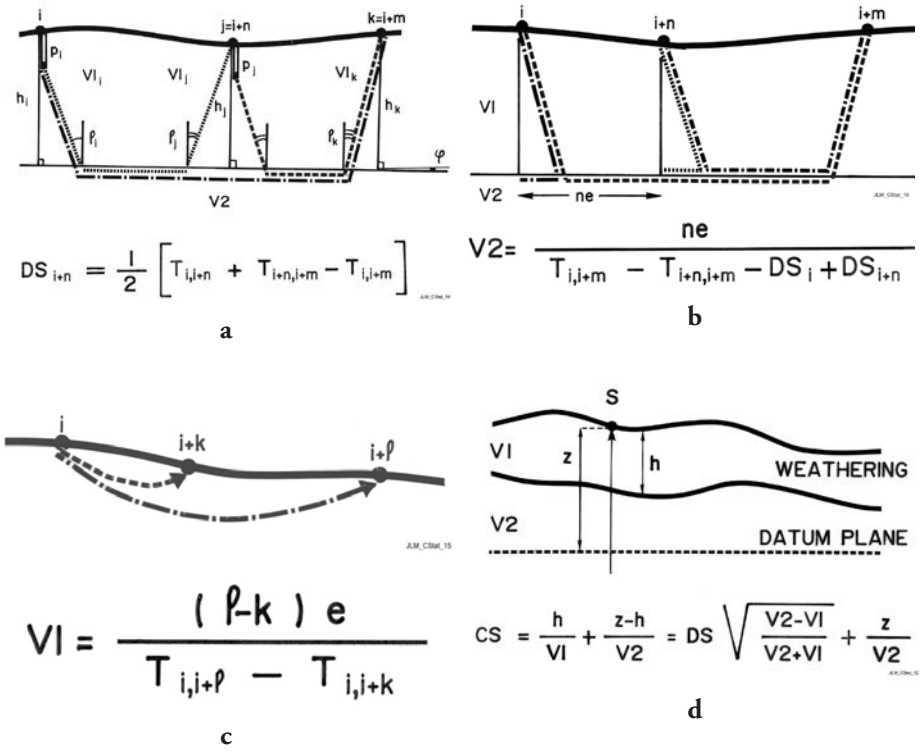

$$DS_{i+n} = \frac{1}{2}\left[T_{i,i+n} + T_{i+n,i+m} - T_{i,i+m}\right]$$

$$V2 = \frac{ne}{T_{i,i+m} - T_{i+n,i+m} - DS_i + DS_{i+n}}$$

$$VI = \frac{(\ell - k)\, e}{T_{i,i+\ell} - T_{i,i+k}}$$

$$CS = \frac{h}{VI} + \frac{z-h}{V2} = DS\sqrt{\frac{V2-VI}{V2+VI}} + \frac{z}{V2}$$

Figure 2.10 *Chronos method (Coppens, 1985).*

Coppens showed that picking two traces per shot, i.e. two constant-offset sections on a seismic profile, is sufficient to determine the delay time for each source or receiver location. This method is well adapted to end-on spreads (Figure 2.10). The two constant offsets must be chosen to ensure that the first arrival times on the two selected traces originate from the same refractor as shown in Figure 2.10-a:

- $T_{i,i+n}$ is the arrival time of the refracted wave with the source located at position i and the receiver at position j= i + n, the source receiver distance being n (near offset).
- $T_{i,i+m}$ is the arrival time of the refracted wave with the source located at position i and the receiver at position i + m, the source receiver distance being m (far offset).
- $T_{i+n,i+m}$ is the arrival time of the refracted wave with the source located at position i + n and the receiver at position i + m, the source receiver distance being m -n (near offset). Consequently, the far offset (m=2n) is the double of the near offset (n).
- The arrival times $T_{i,i+n}$, $T_{i,i+m}$ and $T_{i+n,i+m}$ are used to calculate the delay DS_{i+n} at position j= i + n.

Determining the delay times, and the arrival times of the refracted wave picked on the two constant-offset sections, enables the calculation of the refractor velocity at any point (Figure 2.10-b).

Picking the direct arrival on geophones close to the shot point provides the weathered zone velocity (Figure 2.10-c). Determining the delay, the refractor velocity and the velocity of the weathered layer enables the calculation of the static correction at any point (Figure 2.10-d).

Figure 2.11 and 2.12 are an example of the results obtained using the Chronos method. Figure 2.11 shows, from top to bottom, the variation of velocity V1 of the weathered zone along the line, the variation of the refractor velocity, the delay time curve, the topography and the static correction curve. The static correction curve shows an anomaly between shot points 60 and 110. Figure 2.12 shows the seismic section processed with the static corrections presented in Figure 2.11.

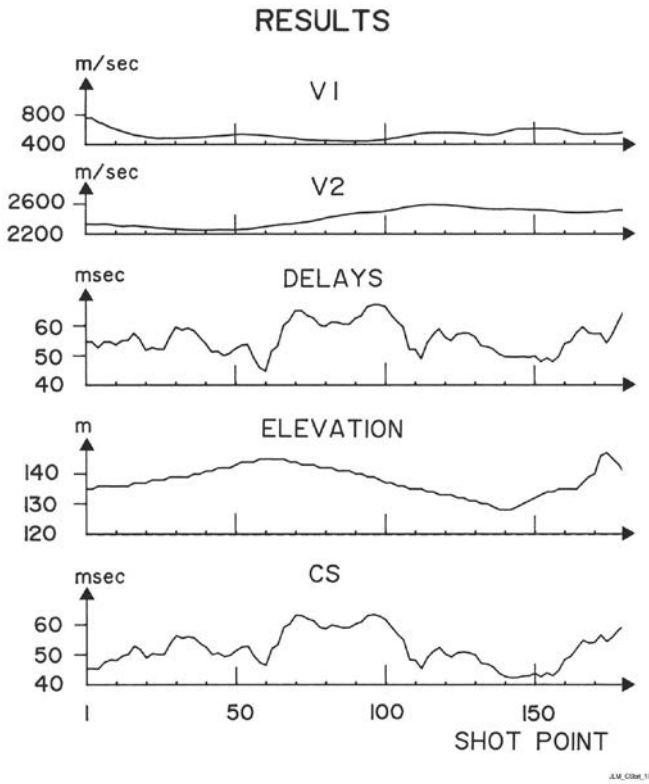

Figure 2.11 *Static corrections with the Chronos method (Coppens, 1985).*

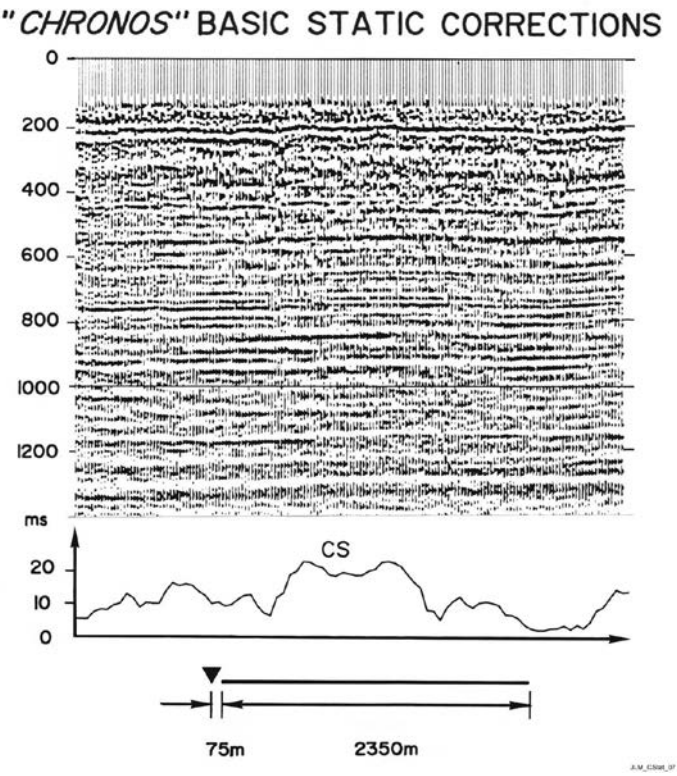

Figure 2.12 *Seismic section processed with static corrections computed by the Chronos method (Coppens, 1985).*

2.5 Second example of a seismic refraction application: Hydrogeology

The University of Poitiers (France) has a Hydrogeological Experimental Site (HES) built near the campus for the sole purpose of providing facilities to develop long-term monitoring and experiments for a better understanding of fluid flow and transfers in fractured rocks (Bernard *et al.*, 2006; Kaczmaryk and Delay 2007; Bourbiaux *et al.*, 2007). The aquifer concerned, 20 to 130 m in depth, consists of tight karstic carbonates of Middle Jurassic age, and lies on the borderline, named the "Poitou threshold", between the Paris and the Aquitaine sedimentary basins (Figure 2.13-a), covering an area of 12 hectares. The top of the reservoir was initially flat and horizontal, 150 million years ago, but has been eroded and weathered since,

during the Cretaceous and Tertiary ages. It is shaped today as hollows and bumps with a relief reaching up to 35 m. Refraction seismic surveying, described in detail by Mari and Porel (2007), has been used to map the irregular shape of the top of the karstic reservoir.

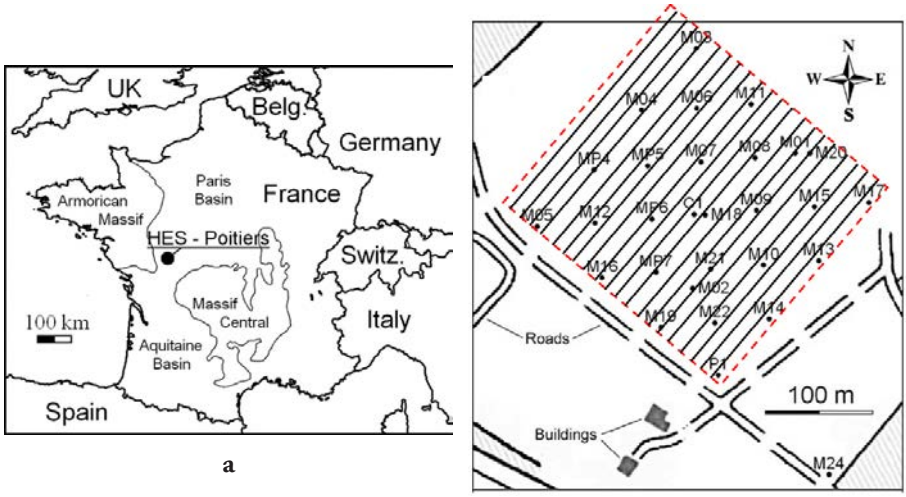

Figure 2.13 *Hydrogeological experimental site in Poitiers. a) location map; b) seismic line implementation.*

Due to the limitations of the area, the length of the seismic line could not exceed 250 m in the in-line direction. In the cross-line direction, the extension of the area does not exceed 300 m. As a result, 20 receiver lines have been implemented, with a 15 m distance between adjacent lines. Figure 2.13-b shows the map locating the seismic lines. A 48-channel recorder was used for the data acquisition. An explosive source (25 g) was detonated and a single geophone (10 Hz) per trace was deployed. The use of this type of source makes it easy to identify and pick first arrivals. A 5 m distance between two adjacent geophones was selected to avoid spatial aliasing.

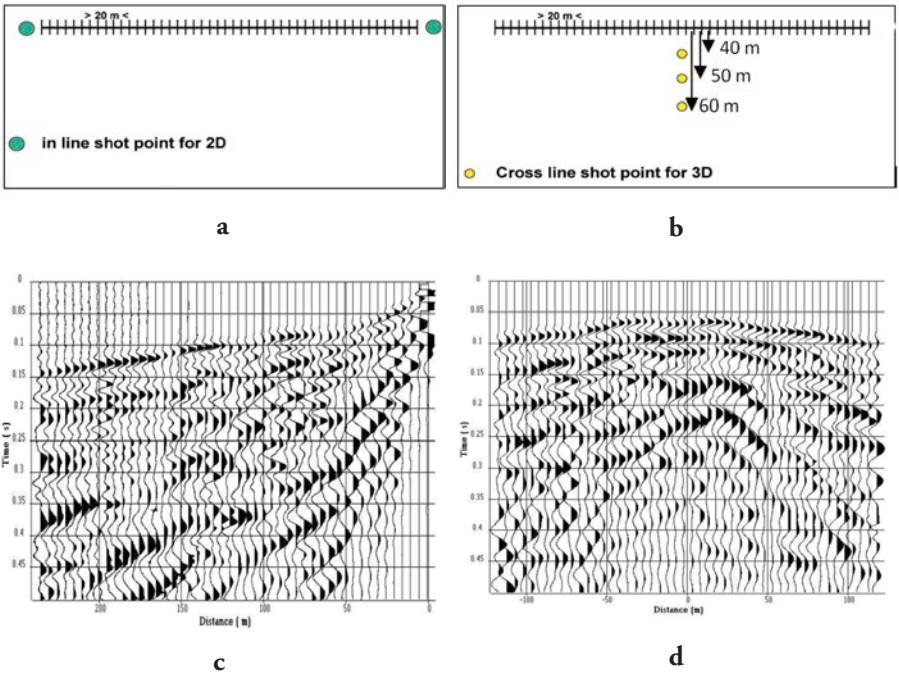

Figure 2.14 *Seismic acquisition. a) 2D in line acquisition geometry, b) 3D cross-line acquisition geometry, c) Example of in-line shot gather, d) Example of cross-line shot gather with 60 m of lateral offset.*

A direct and a reverse shot were recorded per receiver line (Figure 2.14-a). Three shot points in the cross-line direction were fired at distances of 40, 50 and 60 m from the receiver line under consideration (Figure 2.14-b). Figure 2.14-c shows an example of an in-line shot gather and Figure 2.14-d a cross-line shot gather with a lateral offset of 60 m. The range of offsets was selected to optimize the quality of the seismic image over the reservoir depth interval, between 40 and 130 m. The minimum offset distance was chosen as 40 m to reduce the influence of surface waves. The time sampling interval was 0.25 ms and the recording length was 0.5 s.

To obtain the velocity of the refractor (top of the reservoir) and its depth, the Plus–Minus method was used. To apply this method the recordings must be carried out where geophones are aligned with shot points. The arrival times of the direct and refracted waves were picked on all the in-line shots. The picked times from the in-line shots (direct and reverse) were used to compute the t^- and the t^+ curves to obtain the velocity V2 of the refractor and the delay time curve. Figure 2.4 shows the results obtained on line 9. It shows the direct and reverse shot points, the raw t^- curve

and its associated straight-line curve, and the delay time curve. The procedure was applied on each line independently. To obtain a map with a homogeneous sampling interval in both cross-line and in-line directions, the delay time curves were interpolated by kriging with an omni-directional variogram model composed of a nugget effect, a cubic structure with a range of 55 m and a long-scale spherical structure with a range of 145 m (Bourges *et al.*, 2012). Finally, a kriging with the model described above, and a filtering of the nugget effect (random acquisition noise) were performed to obtain the filtered delay time map on a grid 2.5 m x 5m (Figure 2.15-a).

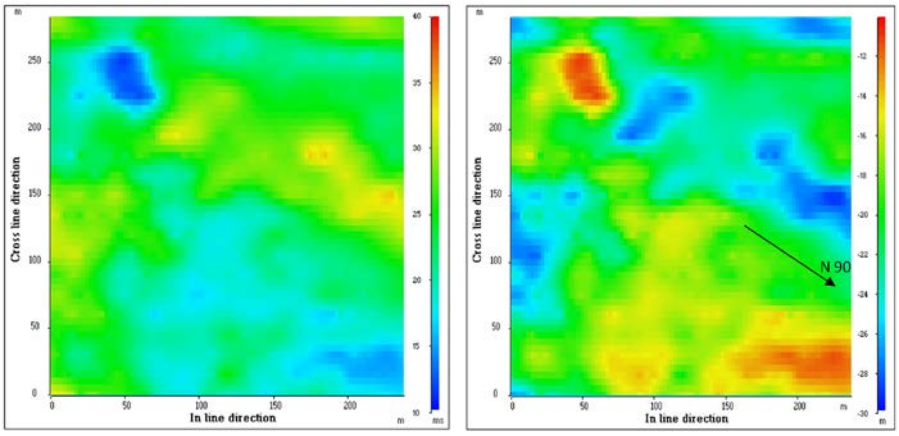

Figure 2.15 *Plus – minus method. a) Delay time map, b) Wz depth map.*

To perform the depth conversion, the velocity of the medium situated above the refractor must be known. Here, it is given by the slope of the direct wave. The medium situated above the refractor is defined as the weathering zone (Wz). In the area, the velocity V_2 of the refractor was found to be 3,350 m/s (from interpretation of the t^- curves), and the velocity of the Wz to be 850 m/s. On the Wz depth map (Figure 2.15-b), the arrow indicates the direction N 90° which corresponds to the main orientation of fracture corridors.

The picked times of the first seismic arrivals on all shots (in-line and cross-line shots), the Wz depth map and the velocity model obtained by the Plus–Minus method are input data for the inversion procedure, called tomography, which can be used to obtain the velocity distribution in depth (Mari and Mendes, 2012). More information on tomography is provided in the following chapter, and readers should also refer to the article by Mari and Mendes published in Near Surface Geophysics (2012).

Figure 2.16 shows the velocity distribution at different depths (15 and 20 m), the 2,500 m/s iso-velocity depth map, and a 3D block with vertical velocity sections located at distances of 0 m, 60 m and 180 m in the cross-line direction and a velocity map located at 20 m in depth. A strong correlation can be seen between the 2,500 m/s iso-velocity depth map (Figure 2.16-c) and the Wz depth map (Figure 2.15-b). The correlation coefficient reaches 0.96.

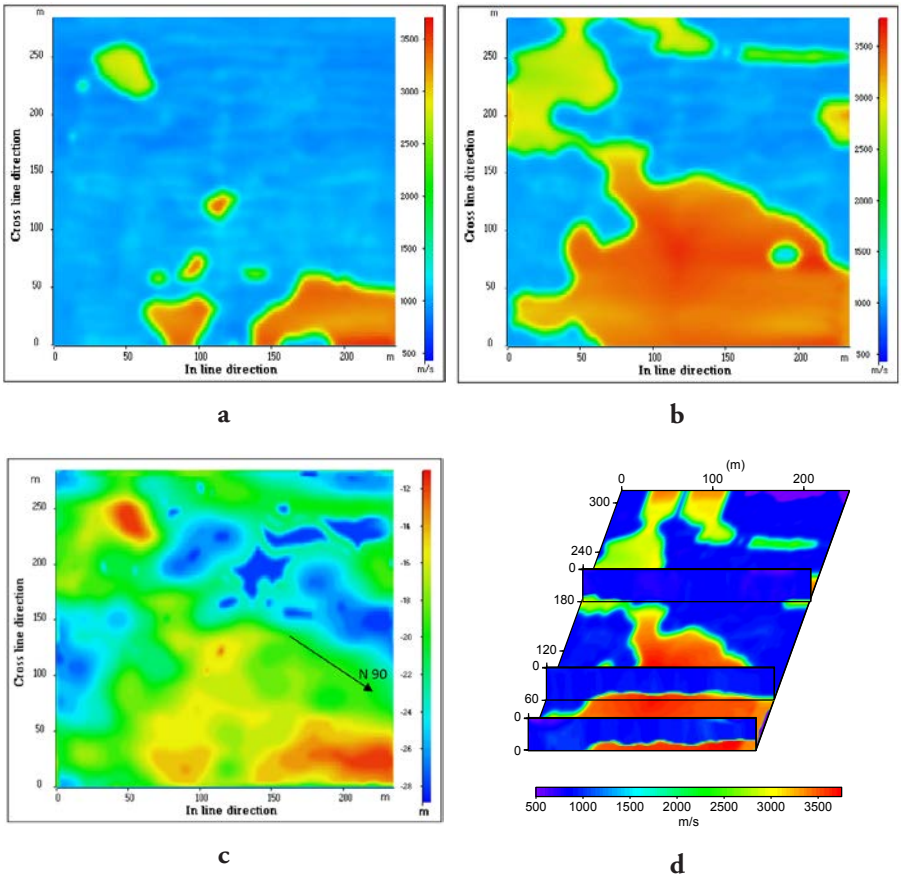

Figure 2.16 *Results of 3D tomography. a) Velocity distribution at 15 m in depth, b) Velocity distribution at 20 m in depth, c) 2,500 m/s iso velocity depth map, d) 3D block with vertical velocity sections located at distances of 0 m, 60 m and 180 m in the cross-line direction and a velocity map located at 20 m in depth.*

The results obtained by the Plus-Minus tomographic inversion joint method can also be used effectively to compute the static corrections in 3D. For that purpose, the thickness H of the weathering zone is given by the 2,500 m/s iso-velocity depth

map. The average velocity V1 in the weathering zone is computed from the velocity distribution obtained by the inversion procedure in the 0-H depth interval. The V2 velocity of the refractor is computed from the velocity distribution obtained by inversion in a narrow depth bandwidth (3 m) situated below the interface located at the depth H. The application to the 3D data is shown in Figure 2.17.

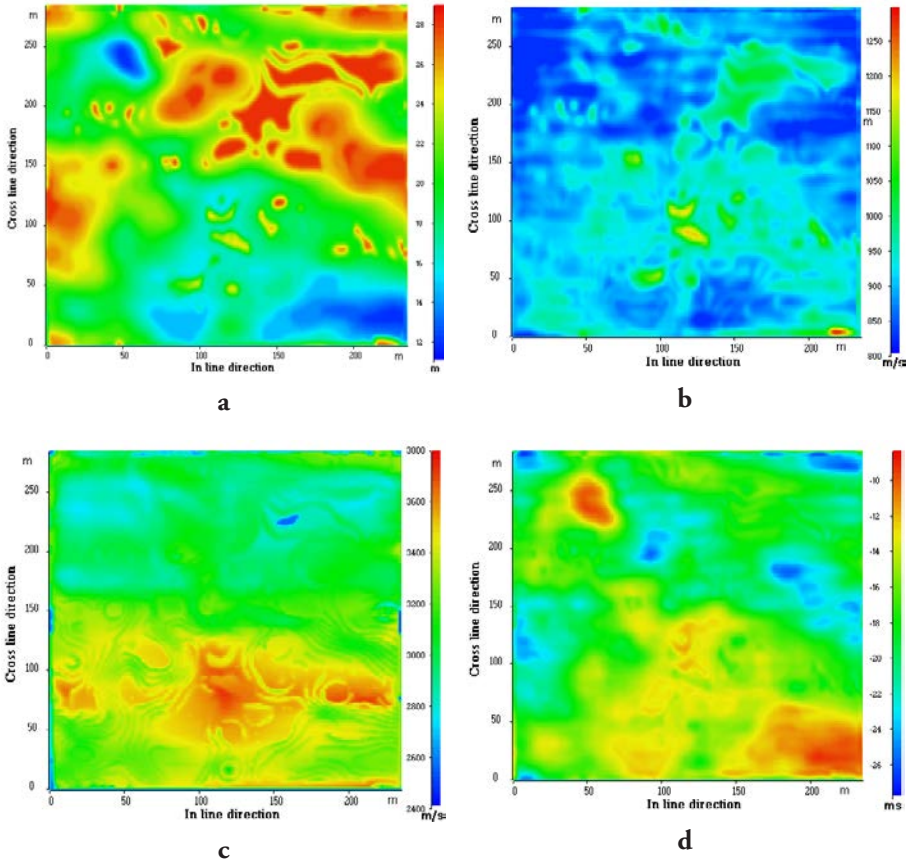

Figure 2.17 *3D static corrections from 3D tomographic inversion. (a) Thickness H of the weathering zone. (b) Average velocity V1 in the weathering zone. (c) Velocity V2 below the weathering zone. (d) 3D static correction map (-H/V1 + H/V2).*

The picked times of the refracted waves were able to provide both a map of the reservoir top (using the T plus –T minus method) and a map of the shape index. Figure 2.18 shows an example of a shot point oriented in the in-line direction before and after the filtering of direct and surface waves. After filtering, a refracted wave is clearly visible, along with interference from refracted – reflected events.

These events are due to heterogeneities and fractures in the bedrock. The shape index map highlights the geological features with an N90 orientation associated with a corridor of fractures (Mari *et al.*, 2018).

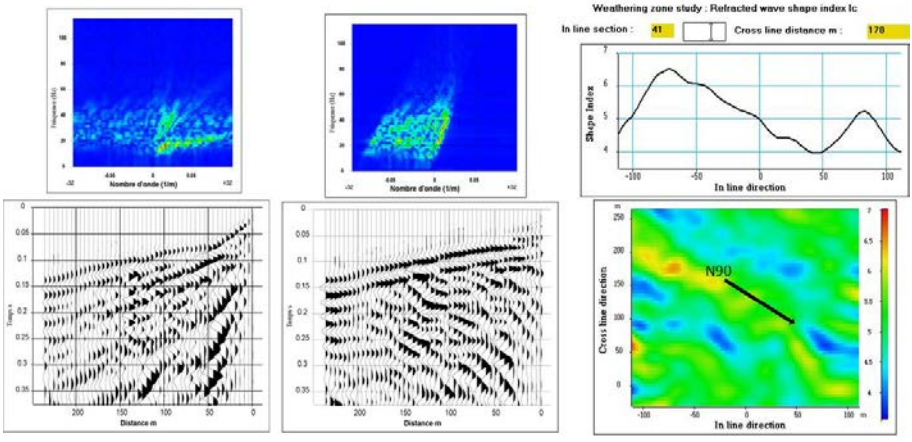

Figure 2.18 *refraction survey: shots before and after the filtering of direct and surface waves, and a shape index map.*

The proposed inversion procedure applied to the field data enables:

- a complete velocity model of the first 35m to be obtained;
- the top of the karstic reservoir to be mapped;
- the detection of the main corridor of fractures, highlighted by a shape index map;
- the calculation of static corrections.

2.6 Conclusion

Seismic refraction can be used for investigations at all depths, but for various technical reasons it is mostly used to study the first 300 meters of the subsurface (spread length, importance of source energy…).

Refracted P-waves are currently used to obtain a velocity model of the near surface by combining conventional methods such as the T plus – T minus method, the GRM method, and tomography. The refraction method is currently used in hydrogeology and civil engineering.

We presented two applications of the refraction method:

- the computation of static corrections,
- the characterization of a near surface karstic reservoir.

For conventional studies, the refraction method only requires the measurement of arrival times of the first arrival waves (direct and refracted waves) to provide a geological model. Amplitudes are not commonly used in seismic refraction studies. A detailed analysis of head wave amplitudes did not generate useful results, however, the fact that head wave amplitude is a function of densities and of seismic velocities suggests that the joint inversion of seismic refraction travel times and head wave amplitudes should facilitate the determination of both seismic velocity and density models (Nikrouz, 2016). Where irregular interface occurs, the analysis of the distortion of the head wave arrival allows the detection of wave interferences, which can be associated with the presence of fractures (second field example).

Seismic refraction is widely used for the study of near-surface layers. Its advantages are:

- only simple equipment required,
- good determination of velocities,
- rapid depth determination.

Unfortunately, it also presents several drawbacks:

- Layer velocity must increase with depth; which is not always the case when dealing with compacted formations;
- A particularly thin layer may completely evade detection; which is even more possible if the velocity contrast is insufficient. In such cases, the determined depths would be incorrect;
- The method is unable to provide highly detailed mapping of structures.

References

Bernard S., Delay F., Porel G., 2006, A new method of data inversion for the identification of fractal characteristics and homogenization scale from hydraulic pumping tests in fractured aquifers, *Journal of Hydrology*, 328, 647-658.

Bourbiaux B., Callot J.P., Doligez B., Fleury M., Gaumet F., Guiton M., Lenormand R., Mari J.L., Pourpak H., 2007, Multi-Scale Characterization of a Heterogeneous Aquifer Through the Integration of Geological, Geophysical and Flow Data: A Case Study, *Oil and Gas Science and Technology, Rev IFP*, 62, 347-373.

Bourges M., Mari J.L., Jeannee N., 2012, A practical review of geostatistical processing applied to geophysical data: methods and applications, *Geophysical prospecting,* 60, 400-412.

Coppens F., 1985, First arrival picking on common offset trace collection for automatic estimation of static corrections, *Geophysical Prospecting*, 33, 1212-1231.

Ge J., Magnani M., Waldron B., 2010, Imaging a shallow aquitard with seismic reflection data in Memphis, Tennessee, USA, Part I: source comparison walk-away tests and the plus-minus method, *Near Surface Geophysics*, 8, 331-340.

Gelchinsky B., Shtivelman V., 1983, Automatic picking of first arrivals and parameterization of travel time curves, *Geophysical Prospecting*, 31, 915-928.

Hagedoorn G.J., 1959, The Plus–Minus method of interpreting seismic refraction sections, *Geophysical Prospecting* 7, 158- 182.

Hatherly P.J., 1982, A computer method for determining seismic first arrival times, *Geophysics*, 47, 1431-1436.

Heelan P.A., 1953, On the theory of head waves, *Geophysics*, 18, 871-893.

Kaczmaryk A., Delay F., 2007, Interference pumping tests in a fractured limestone (Poitiers - France): Inversion of data by means of dual-medium approaches, *Journal of Hydrology* 337, 133-146.

Lebreton F., Morlier P., 1983, Une diagraphie de perméabilité par méthode acoustique, *Bulletin of the International Association of Engineering geology*, n° 26-27.

Mari J.L., Arens G., Chapellier D., Gaudiani P., 1999, *Geophysics of reservoir and civil engineering*, Éditions Technip, Paris, ISBN 2-7108-0757-2.

Mari J.L., Glangeaud F., Coppens F., 1999, *Signal processing for geologists and geophysicists*, Editions Technip, Paris, ISBN 2-7108-0752-1.

Mari J.L., Porel G., 2007, 3D seismic imaging of a near-surface heterogeneous aquifer: a case study, *Oil and Gas Science and Technology, Rev IFP* 63, 179-201, Published online: DOI: 10.2516/ogst/2007077.

Mari J.L., 2015, *Signal processing for geologists & geophysicists*, e-book, DOI: 10.2516/ifpen/2011002, http://books.ifpenergiesnouvelles.fr/ebooks/signal-processing/

Mari J.L. and Vergniault C., 2018, Well seismic surveying and acoustic logging, EDP-Sciences, Les Ulis, DOI: 10.1051/978-2-7598-2263-8, ISBN (eBook): 978-2-7598-2263-8, https://www.edp-open.org/well-seismic-surveying-and-acoustic-logging

Mari J.L., Mendes M., 2012, High resolution 3D near surface imaging of fracture corridors and cavities by combining Plus-Minus method and refraction tomography, *Near Surface Geophysics*, 10, DOI: 10.3997/1873-0604.2011052.

Mari J.L., Lopez A.I, Benjuma B., Garcia-Lobon J.L., 2018, Shape index: a refraction attribute to detect fractures and permeable bodies, paper Th J 12, 80th EAGE annual conference, Copenhagen, Denmark.

Mendes M., 2009, A hybrid fast algorithm for first arrivals tomography, *Geophysical Prospecting*, 57, 803-809. DOI: 10.1111/j.1365-2478.2008.00755.x

Nikrouz R., 2016, Relationship between head wave amplitudes and seismic refraction velocities to detect lateral variation in the refractor, *Journal of the Earth and Space Physics*, 4, 69-76.

Palmer D., 1986, Refraction seismics, *Geophysical Press*, 13.

Palmer D., 2001, Resolving refractor ambiguities with amplitudes, *Geophysics*, 66, 1590-1593.

Palmer D., 2008, Is it time to re-engineer geotechnical seismic refraction methods? *First Break* 26, 69-77.

Werth G.A., 1967, *Method for calculating the amplitude of the refraction arrival*, in: Musgrave A.W. (Ed), seismic refraction prospecting, Society of Exploration Geophysics, 119-137.

3

Seismic tomography

M. Mendes

According to Wikipedia, "tomography is imaging by sections or sectioning, through the use of any kind of penetrating wave". The apparatus applied in tomography is called a tomograph, while the image revealing the internal structure of an unknown property of the object under study is a tomogram.

Tomography was originally developed in medical research to produce images of tissue density (Hounsfield, 1973). In this type of tomography, the object (the patient) is moved through a large donut-shaped machine, where an X-ray beam and a set of electronic X-ray detectors are located opposite each other. The source and detectors are rotated around the target region, collecting the amount of radiation being absorbed throughout the patient's body at many different angles (Goldman, 2007) (Figure 3.1).

DOI: 10.1051/978-2-7598-2351-2.c005

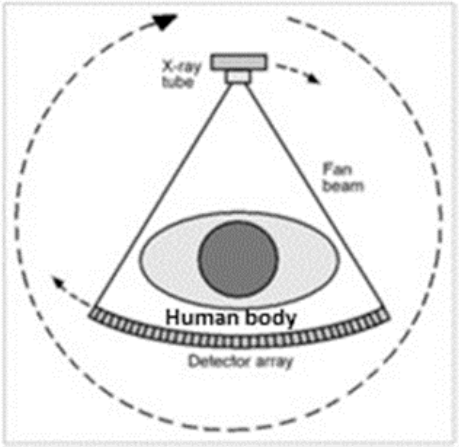

Figure 3.1 *Geometry of a computed tomography scanner apparatus (third-generation). The emission of a large X-ray beam encompasses the entire patient's width and the array of detectors measures the amount of radiation being absorbed throughout the patient's body. X-ray tube and detectors were rigidly linked and underwent single rotational motion. Adapted from Goldman (2007).*

The method has been successfully employed in many other scientific fields, such as biology, astrophysics, materials science and geophysics. In geophysics, seismic tomography is an effective technique for 2D, 3D and 4D reconstructions of the Earth's subsurface, exploiting the properties of seismic wave energy after it has travelled through the ground. Such properties include travel time, ray paths and amplitude, which are an important key to reveal information about seismic velocity, density, and absorption or the Q-factor attenuation of geological formations (Padina *et al.*, 2006; Brzostowski and McMechan, 1992; Spakman *et al.*, 1993; Witten *et al.*, 1992).

Currently, seismic tomography is widely applied on a variety of scales and geometries:

- On regional and global scales, tomography inverts the seismic records generated by passive sources, such as natural or induced earthquakes, and those received by the seismograph network located around the world. Historically, seismic tomography was first applied to global scale data to study crustal velocity anomalies (Aki and Lee, 1976). The irregularity in time and space distribution presented by this type of source, along with the incomplete coverage of recording stations, leads to significant gaps in the data and limits the spatial resolution of global tomography to 100 - 200 Km.
- On the local scale, tomography is convenient for environmental or civil engineering investigations, economic exploration and archaeological research. The versatility of applying this technique to surface, vertical seismic profile (VSP) or cross-hole data makes it very popular, gaining widespread acceptance as a viable

tool to generate detailed geophysical models of the subsurface. However, higher spatial resolution requires greater computational effort, therefore, tomograms with high spatial resolution are limited to smaller scale data acquisitions, such as VSP and cross-hole, where the spatial resolution may reach less than 1 m.

Classically, depending on the input data, seismic tomographies fall into three main categories:

- transmission tomography using P or S first arrivals, i.e., direct, diving and refracted waves;
- reflection tomography using P or S reflection waves;
- diffraction tomography using P or S scattered waves (e.g., diffractions, reflections, and converted transmissions).

In the following sections, we present some field study examples of each tomography category to show the adaptability of the technique to provide subsurface images in different applications. The intention here is not to describe the field cases in detail, but to provide some background information and the main model features identified from the tomography.

The authors emphasize that although a different type of acquisition geometry was chosen for almost every tomography category described below, this by no means implies that these geometries are restricted only to these acquisition types.

3.1 Transmission tomography example: surface seismic field data

Transmission tomography is an appropriate technique to define:

- horizontal layering structures;
- regions exhibiting low complexity velocity distributions.

This section shows:

- how to obtain a P-wave velocity model from first arrival times;
- how to evaluate the spatial (horizontal and vertical) resolution for the tomograms.

A transmission tomographic technique was used to invert a 3D seismic data set, part of a more comprehensive geophysical survey conducted in a karstified dolostone region, to provide information about the upper epikarst structure. The selected field example comes from Galibert *et al.* (2014).

3.1.1 *Geophysical survey*

The acquisition procedures were optimized to obtain the best results with a high acquisition speed and a high resolution. For a seismic survey this involves high folds and wide azimuthal coverage.

A three-member crew was required, working for two and a half days, to acquire:

- 3D surface seismic survey, extended for about 120 × 100 m;
- 2D surface seismic line, 235 m long;
- Walkaway VSP, 50 m depth;
- GPS surveying.

The 3D surface seismic acquisition was performed using an orthogonal geometry, shot lines were perpendicular to receiver lines, with two overlapping swaths (Figure 3.2).

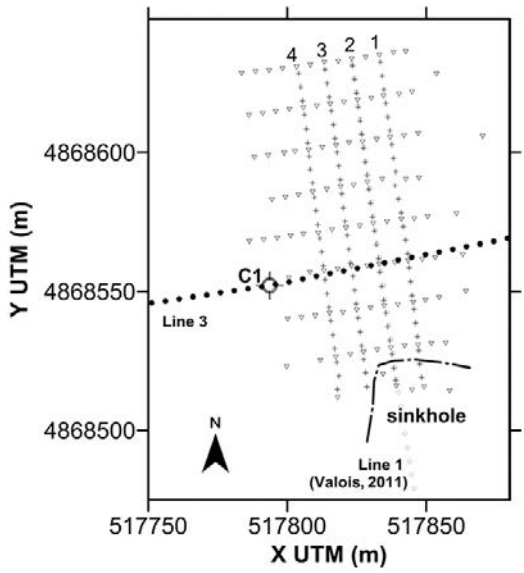

Figure 3.2 *Plan view of the survey area. 3D orthogonal geometry was used for the seismic survey, C1 shows the position of borehole. Receiver (crosses) and shot point (triangles) positions are shown. Line 3 is an additional 2D shot included in the 3D tomographic inversion. Line 1, obtained from previous data acquisition, is included for reference purposes only. Receiver lines are numbered 1 to 4. The UTM coordinate zone is 31. Adapted from Galibert* et al. *(2014).*

The main acquisition parameters are as follows:

- Source: sledgehammer, with 5 m spacing, and 15 m source line spacing;
- Number of shots: 154;

- Receiver: vertical geophone, Oyo GS-14 Hz, with 5 m spacing, and 10 m receiver line spacing;
- Number of receiver lines: 3;
- Seismograph: 96 channels;
- Record length: 1 second;
- Swaths: 1 using receiver lines 1-3; 2 using receiver lines 2-4.

3.1.2 *Tomographic methodology*

Figure 3.3 provides the workflow for the transmission tomography algorithm of Mendes (Mendes, 2009) used to produce tomographic images of the subsurface, enabling a structural evaluation of the upper epikarst.

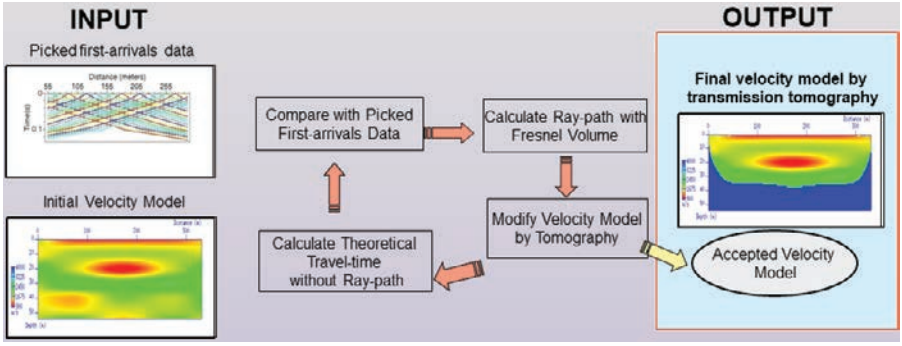

Figure 3.3 *Simplified workflow of the global inversion scheme. The transmission tomography methodology utilizes the picking times of first arrivals and a simplified initial velocity model to produce a more detailed velocity model for the epikarst region.*

The basic features of this algorithm are:

- gridded model;
- SIRT back-projection technique for iterative inversion;
- Fresnel volume: which is the area formed by the points around the geometric ray delayed by less than half of the period of the dominant wave;
- fat-ray: represents the wave path from source to receiver, with a width defined by the points belonging to the Fresnel volume.

The choice of the most appropriate dominant period of the input wave, not only depends on the characteristic period of the source wavelet, but also on the scale of the experiment. A useful "rule of thumb" for choosing the input period, T, suggested by Jordi *et al.* (2016) is estimated by the ratio $T = 0.1 \times H/V$, where H is the target depth of the survey and V the average of the expected subsurface velocities.

3.1.3 *Data pre-processing*

Typical shot-gathers and first arrival picking is shown in Figure 3.4.

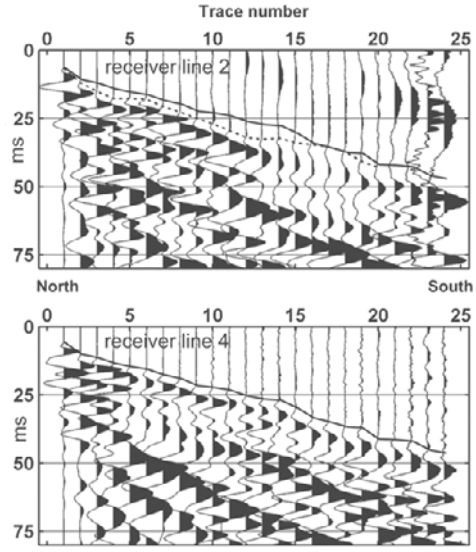

Figure 3.4 *Example of two parallel shot-gathers. The picked first arrivals at receiver line 2 are marked with a dashed line, and at receiver line 4 with a solid line.*

The first-break times were picked manually, and their reliability was carefully analyzed for plausibility and erroneous travel times.

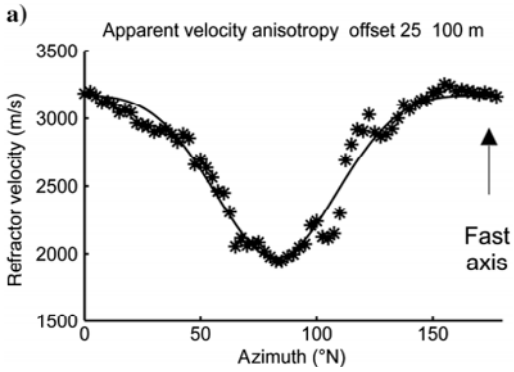

Figure 3.5 *Travel time azimuthal variations. Estimated refractor velocity at the base of the epikarst from surface receivers; the solid line is the fitted azimuthal model. Adapted from Galibert* et al. *(2014).*

The picked travel times were used to compute the refractor velocity at the base of the epikarst. It was noted that the values change between 2,000 m/s and 3,200 m/s, with a clear azimuthal variation, being the strike of the fast axis around 175°N (Figure 3.5).

Despite the azimuthal variation of velocity, for simplicity, an initial 1D velocity model, with linear velocity gradients, was considered adequate for the tomographic inversion.

Then, the input data were:

- 7,813 first-break times;
- 1D model with 2 linear vertical velocity gradients;
- 100 Hz central signal frequency.

3.1.4 *Results and discussion*

The processing of seismic data led to a 3D velocity block. The inversion scheme was stopped after 10 iterations, when the misfit function reached 1.69 *ms* for the root-mean-squared (*rms*) error, i.e., the squared difference between measured and calculated travel times. An example describing the quality control of the inversion results is specified for shot number 83. Figure 3.6 shows three travel time sets: a) the picked times of field data; b) computed times for the initial model; and the times for the best model provided by the tomographic inversion. The evolution of travel time residues, during velocity model building, is illustrated in Figure 3.7. Note the significant reduction of travel time differences, showing a good tie between the picked and best model data. This provides assurance that the final model accurately reflects the field data.

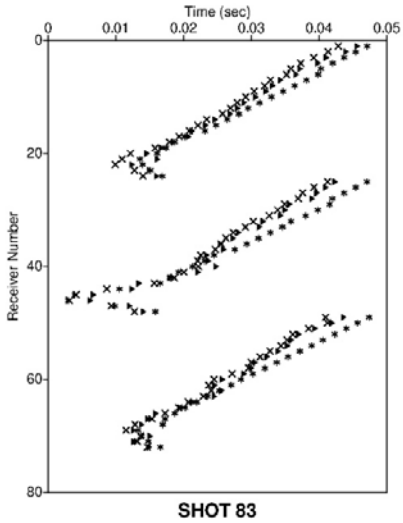

Figure 3.6 *Diagrams of travel times for shot number 83. The picked times of field data (black triangles), travel times for initial model (asterisks) and travel times for a model provided by iteration 10 (crosses).*

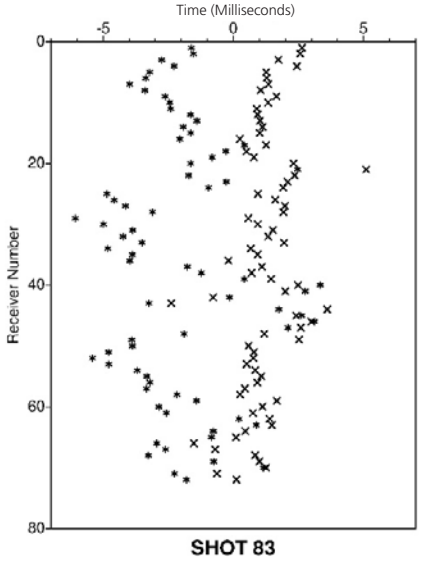

Figure 3.7 *Diagrams of travel time residues for shot number 83. For the initial model, the travel time residues show high values (asterisks) and in the case of the final model the travel time residues (crosses) have a significant reduction. The good fit provides assurance that the final model accurately reflects the picked data.*

Next, for structure interpretation, a horizontal slice analysis was applied to the 3D depth velocity output model. An example of a horizontal slice at 7 m depth, cut through the velocity model is shown in Figure 3.8-a. This shallow slice corresponds to the base of the epikarst, reported in the boreholes available in the region. Clear patterns of elongated high-low velocity anomalies were identified, probably corresponding to a succession of ridges and furrows, which is consistent with the aforementioned 175°N trend. However, the transmission tomography was unable to determine the deeper structure, as shown by the horizontal slice at 28 m depth, corresponding to the water level (Figure 3.8-b).

The tomography of first arrival times picked from surface data provides images that are low resolution at depth, due to the limited azimuthal coverage. Therefore, a new tomographic inversion combining the surface data with an additional VSP data set available at the region, proved to be an effective and reliable tool for the detection of deeper structures. For details see Annex 3-A.

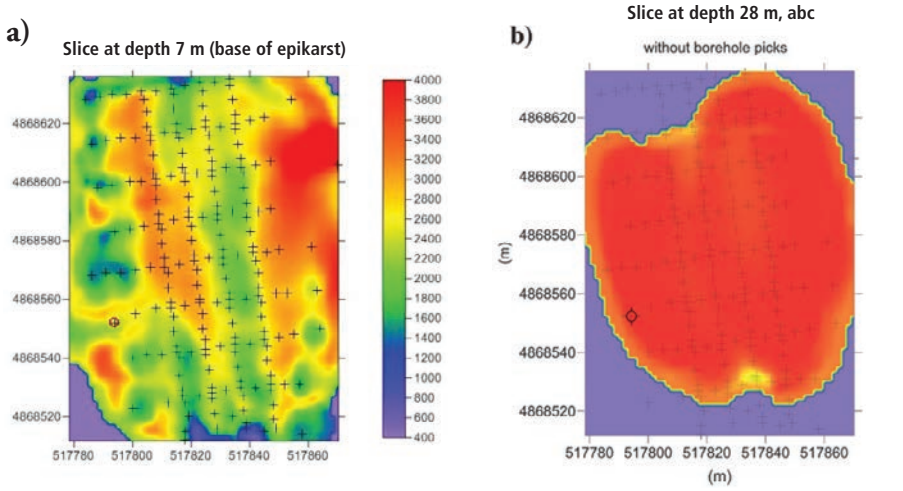

Figure 3.8 *Constant-depth velocity slices from 3D tomography output, presenting noticeable differences: (a) The depth-slice at 7 m, corresponding to the base of the epikarst, exhibits high-low elongated patterns in 175°N; (b) The depth-slice at 28 m, contrasting with the shallow complexity, is characterized by a very poor resolution (high and homogeneous velocity). Adapted from Galibert* et al. *(2014).*

3.1.5 *Conclusions*

This example showed the successful application of a transmission tomography algorithm to uncover the shallow complex structures at a karst region. A set of elongated furrows incised at the base of the epikarst, along a strike of 175°, were revealed. The limited azimuthal coverage obtained from the surface acquisition data limited the depth of the investigation. To increase the depth of the analysis, a combination of borehole acquisitions is suggested.

In general, transmission tomography enables the velocity of subsurface structures to be obtained, containing smooth information on a large scale, which is an essential component for pre or post-stack seismic migrations or inversion techniques.

Annex 3-A

The limits of spatial resolution can be estimated according to the formula suggested by Sheng and Schuster (2003)

$$\Delta x_i\,(\mathrm{p}) \approx \frac{\pi}{max_{\eta,f}\,(k_{xi})}, \tag{3.1}$$

$$\text{with}\;\; k_{xi} = \omega\left[\left|\nabla_{xi}\tau\,(s,p) + \nabla_{xi}\tau\,(p,r)\right|\right], \tag{3.2}$$

where $\Delta x_i(\mathrm{p})$ indicates the resolution limit for the direction i, k_{xi} denotes the horizontal wavenumber at maximum frequency f, $\nabla_{xi}\tau(\mathrm{r1},\mathrm{r2})$ is the horizontal gradient

of travel time from point r1 to point r2, and η stands for the set of suitable rays selected from all available shots.

In the example presented here, only the horizontal resolution is considered and discussed.

Our first step was the analysis of the Fresnel zone for a frequency of 120 Hz, with a surface acquisition and velocity gradient model characteristic of the karst region (Figure 3.A.1-a).

We noted that:

- in the shallow area - wave paths are nearly vertical and provide large horizontal wavenumbers, by combining neighbouring shots, leading to small Δx values => high horizontal resolution (≈ 1.5 m);
- in the deeper area - wave paths are nearly horizontal and provide small horizontal wavenumbers for all shots, leading to large Δx values => low horizontal resolution (≈ 10 m).

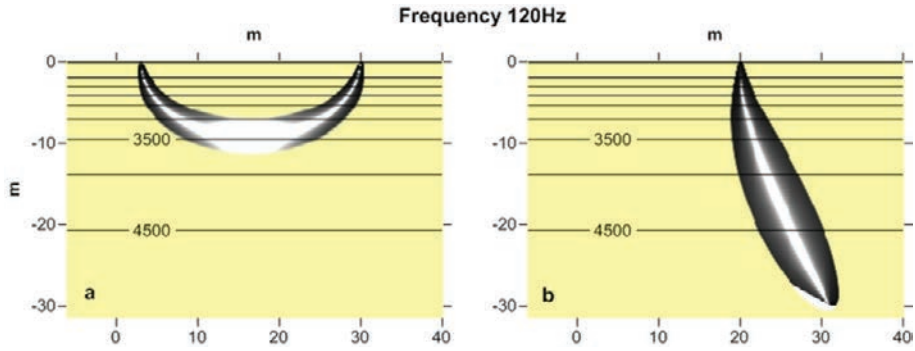

Figure 3.A.1 *Horizontal resolution Δx of band limited travel time tomography: (a) for surface acquisition, (b) for borehole acquisition. The contours represent the background velocity gradient. Inside the Fresnel volume, there is no resolution at all along the geometrical ray (white area), according to wave path theory. Resolution increases toward the fringes (dark area). Adapted from Galibert* et al. *(2014).*

These very different limits of spatial resolution demonstrate the capacity of the technique, as shown by the surface acquisition data, for investigating the upper epikarst; but its unsuitability for the underlying low-permeability region.

To overcome this issue, an additional VSP acquisition was suggested to increase the azimuthal coverage with depth. Under such acquisition conditions, the analysis of the Fresnel zone (Figure 3.A.1- b) illustrates how the wave path is nearly vertical and the horizontal cross width of the low-sensitivity region becomes narrow. Therefore, in situations where it is possible to combine surface and borehole acquisitions, the tomographic resolution should be substantially improved.

For this reason, we repeated the tomographic inversion using both surface and VSP data. The result presented in Figure 3.A.2 revealed some significant velocity anomalies, which can be compared with the homogenous velocity presented in Figure 3.8-b.

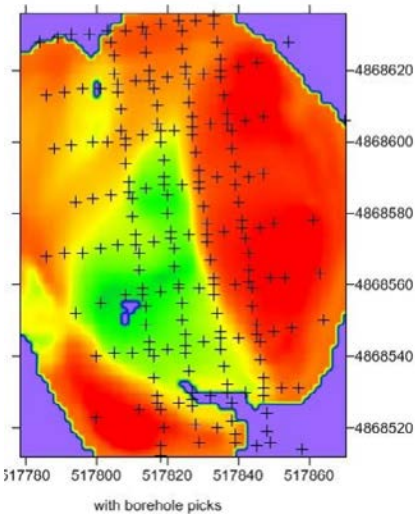

Figure 3.A.2 *A horizontal slice at 28 m depth taken at the 3D velocity cube produced by tomography when combining seismic surface and VSP data. Now, the model is characterized by velocity anomalies contrasting with the high homogeneous velocity and very poor resolution produced by the tomographic inversion of the surface data (Figure 3.8-b). Adapted from Galibert* et al. *(2014).*

3.2 Reflection tomography example: cross-hole field data

It has been demonstrated that reflection tomography is an appropriate technique for building a good velocity model of subsurface structures based on multichannel seismic data.

This section describes the use of a reflection tomography procedure to image a limestone reservoir at a depth of about 1,850 m, utilizing the information present in the travel time of reflected S-waves. These data were recorded during a cross-hole seismic experiment, carried out in the Paris basin. The data processing sequence is detailed in Becquey *et al.* (1992).

3.2.1 *Seismic survey*

In general, a typical cross-hole seismic profile has sources situated in one borehole and receivers in another, with the source and receiver boreholes being separated by a distance of up to 1 km.

For this study, the seismic source was wall-clamped in a vertical borehole and the receivers in a deviated borehole. The distance between the two boreholes increased from 30 m at the surface to 380 m at the reservoir level, located at a depth of 1,850 m. Both boreholes were cased with a 7-inch casing.

The total recording time was 40 hours and the whole operation, which involved more than 3,000 shots and the removal and resetting of the tubing, took one week.

The principal parameters of this data acquisition were:

- Source: S-wave weight-drop, releasing ≈ 2,000 joules/shot, 4 m spacing between 1,314 - 1,916 m in vertical depth;
- 8 shots/position;
- 400 shot positions;
- Receiver: Multilock™ tool with 4 levels and triaxial geophones, 4 m spacing between 1,620 - 1,916 m in logging depth.

For promoting the S-wave conversions two conditions were combined:

- source directivity pattern diagram with a strong S lobe perpendicular to the borehole;
- acquisition geometry designed to explore the wide angles of incidence.

Figure 3.9 shows the multicomponent raw data with complex arrivals.

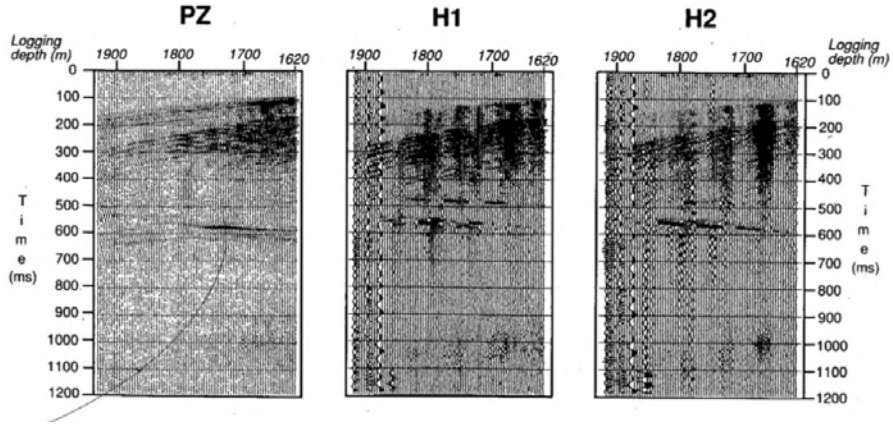

Figure 3.9 *Raw data. PZ component along the borehole axis. H1 and H2 perpendicular to the borehole axis. Adapted from Becquey* et al. *(1992).*

3.2.2 *Data processing*

Only two preprocessing steps were applied to the multicomponent data set, namely:

- a bandpass filter (20-120 Hz);
- a re-orientation following the projection along the source-receiver direction R, its normal in the source-receiver plane N and the binormal B, orthogonal to the source-receiver plane.

We noted that the component R (Figure 3.10) contains clear direct down-going P-waves, followed by up-going S-wave reflections. The component N has obvious down-going S waves, appearing as a train of quasi-parallel events spread over about 150 ms.

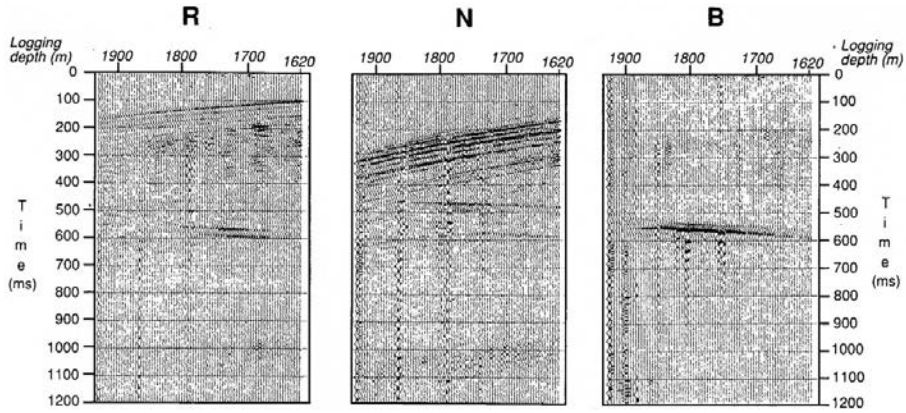

Figure 3.10 *Filtered and reoriented data. R component along the source-receiver direction; N component perpendicular to R, in the source-receiver plane; B component, orthogonal to R and N, so normal to the source-receiver plane. Adapted from Becquey* et al. *(1992).*

The imaging from the cross-hole data set was inspired from a traditional offset VSP. Therefore, based on other previous VSP data acquisitions of P and S-waves at the vertical borehole, a velocity-depth model was built and used by the VSP-CDP time technique to transform the S-S reflected data (Figure 3.11). More details on the VSP-CDP time technique are available in chapter 2 of "*Well seismic surveying and acoustic logging*" (J.-L. Mari and C. Vergniault, 2018).

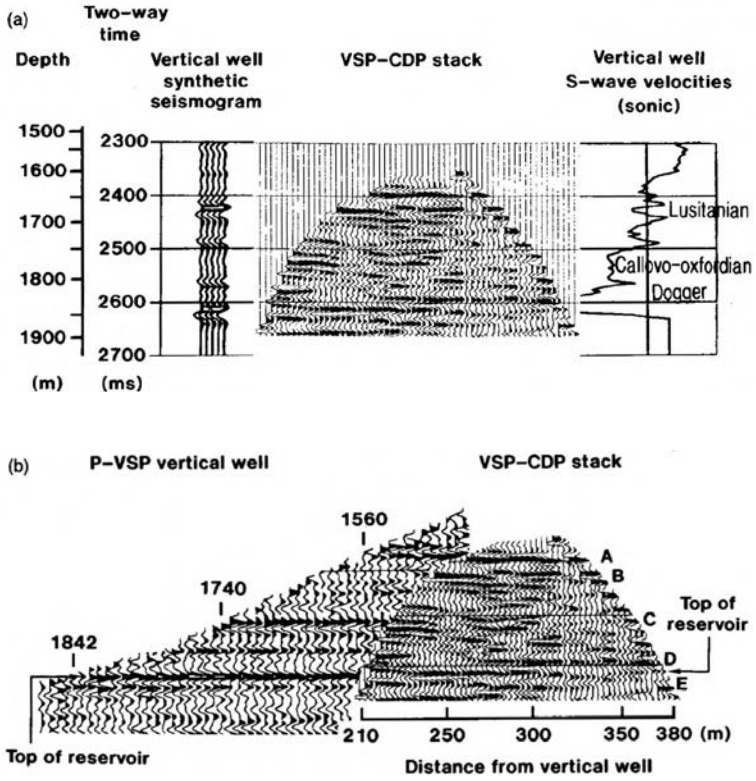

Figure 3.11 *(a) S-wave VSP-CDP time transformation compared with S-wave sonic log and synthetic seismogram; (b) S-wave VSP-CDP time transformation compared with P-wave VSP data. Adapted from Becquey* et al. *(1992).*

3.2.3 *General interpretation*

An analysis of the S-wave VSP-CDP image in Figure 3.11 shows, that three main events correlate well with the S-wave sonic log from the vertical borehole:

- 1,580 to 1,745 m: Lusitanian marl and limestone layers, giving rise to internal impedance contrasts;
- 1,745 to 1,851 m: Callovo-Oxfordian marls;
- 1,851 m to the bottom: Limestone reservoir.

The S-wave VSP-CDP stack was compared with the P-wave VSP acquired at the vertical borehole and the synthetic seismograms produced by the S-wave sonic log convolved with a characteristic signal with the same bandwidth as the VSP-CDP image. The improvement in the vertical resolution of the S-wave VSP-CDP image is significant, compared to the conventional P-wave VSP (Figure 3.11b).

3.2.4 *Conclusions*

A good agreement was obtained between the S-wave image and the S-wave sonic log, furthermore the enhanced S-wave reflection image revealed high vertical resolution, approximately 5 m, and allowed imaging of the region between two boreholes, nearly 400 m away from the borehole.

This field experiment also demonstrated that the conventional borehole seismic receiver tools and the low-energy sources are well suited to obtain high-resolution lithological structure delineation.

3.3 Diffraction tomography example: Borehole field data

Exploiting amplitude information in addition to arrival times, the diffraction tomography schemes are the most suitable to interpret the propagation of recorded seismic data through complex velocity structures.

Diffraction tomography algorithms are available:

- in the spatial domain and based on the Born approximation, most suited for the primary reflected or diffracted part of the wave field;
- in the wavenumber domain and based on the Rytov approximation, most suited for the transmitted wave field.

This section shows:

- how to obtain elastic depth images (P and S-wave velocities and density) from P-P or S-S and P-S or S-P reflected and diffracted waves;
- how to evaluate the elastic image confidence.

We adopted the diffraction tomography algorithm developed by Beydoun and Mendes (1989) for the following depth imaging examples. This imaging technique, based on the Born approximation, uses a one-step conditioned gradient technique for optimization and is equivalent to an elastic pre-stack migration.

The procedure requires the following input data:

- gridded model defined for 3 elastic parameters (P and S-wave velocities and density), close to the actual medium;
- elastic ray-Born approximation;
- multi-component field data, with scattered waves (diffracted and reflected body waves).

And the provided output data are:

- quantitative elastic depth images.

3.3.1 *Vertical seismic profile (VSP) field data*

This example describes the processing of a multicomponent offset VSP dataset, collected in the North Sea. The purpose of this survey was to detect fault blocks at the deep Brent reservoir formation, thicker than 150 m. The reservoir is located in the Middle Jurassic Brent formation, positioned under the Cimmerian unconformity (3,558 m) at the boundary between the base of the Lower Cretaceous and the top of the Upper Jurassic. An analysis of the VSP tomograms enabled the delineation of the reservoir and the identification of at least two faults. Beydoun *et al.* (1990), provide details of this application.

3.3.1.1 Seismic data acquisition

Surface seismic data acquisition carried out previously in this area had failed to provide good quality imaging of the Brent reservoir. In particular, the strong multiples generated at the Cimmerian unconformity masked the weak primary reflections from the reservoir. To improve the quality of the seismic results and considering the surface data information, a multi-component offset VSP set up was performed with the following characteristics:

Source:

- 2 x 200 in^2 Bolt air guns (on a supply boat);
- depth 7 m;
- offset: 1,200 m;
- 6 shots per level (i.e., at each receiver location).

Receiver:

- 3 component Geolock H3 hydraulic tool (from CGG);
- Geophones:15 Hz;
- sampled rate: 2 ms;
- station interval: 25 m;
- depth range: 600 – 4,140 m;
- number of depth levels: 129.

A zero offset VSP was simultaneously acquired, shooting alternatively from the supply boat and from the rig, which had a 550 in^2 Bolt air gun attached.

The VSP survey recording time was 27 hours, while rig down time was 28 hours.

3.3.1.2 Data Processing

The main focus of data preprocessing was to preserve the seismic wave amplitude. For such preprocessing, it was sufficient to only apply a few steps, which were:

- the reorientation of the three-component data along Z the vertical axis, X the axis in the plane of propagation, and Y the transverse (out of plane) horizontal axis;

- the separation of up-going and down-going P-waves and S-waves;
- the recombination of P-P and P-S up-going waves for the X and Z-components.

The following points were noted after the analysis of the processed data (Figure 3.12):

- Y-component data present very weak energy compared with that of X and Z-components. For simplicity, this component was disregarded in further processing;
- weak up-going S-P and S-S waves;
- strong reflected P-P and P-S waves;
- some hyperbolic-shaped arrivals, probably due to fault diffractions (see at 4,000 m; 1,700 ms).

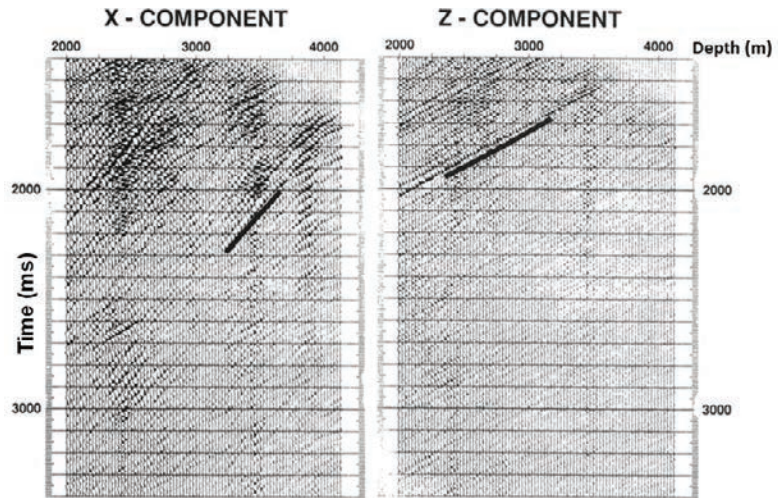

Figure 3.12 *Two-component (X, Z) VSP field data input to diffraction tomography. The Y-component was disregarded due to its weak energy. Adapted from Beydoun* et al. *(1990).*

3.3.1.3 Diffraction tomography processing

In this example, the imaging technique deals with the processed *X* and *Z*-components of the data, mainly consisting of up-going P-P and P-S waves. The 1D initial elastic model (P and S-wave velocities and density) was created by the combination of geological and geophysical information available for the region.

The target zone, covering the reservoir area, is a rectangle extending from 50 m to 550 m east of the borehole with depths from 3,400 m to 4,400 m, discretized by a uniform square grid of 10 x 10 m.

The selected field data were 86 VSP levels, ranging from depths of 2,000 – 4,150 m within a time window of 1,400 – 3,400 ms.

3.3.1.4 Depth elastic images and general discussion

The diffraction tomography provided an estimation of the elastic parameters, P and S-wave velocities, and density, as illustrated in Figure 3.13. These results enabled the identification of several interesting features that were interpreted as:

- the top of the Brent reservoir, which can be delineated and described continuously away from the borehole;
- tilted panels under the Cretaceous base discordance - Cimmerian unconformity, at depth of 3,558 m.
- a reverse fault at 250 m east of the borehole, with an apparent throw < 30 m, unclear whether it reaches the reservoir;
- a normal fault about 450 m east of the borehole with an apparent throw ≈ 60 m, intersects the reservoir at about 350 m offset;
- an event at depth ≈ 3,850 m, slightly dipping to the west, which was interpreted to be the Heather sandy claystone formation.

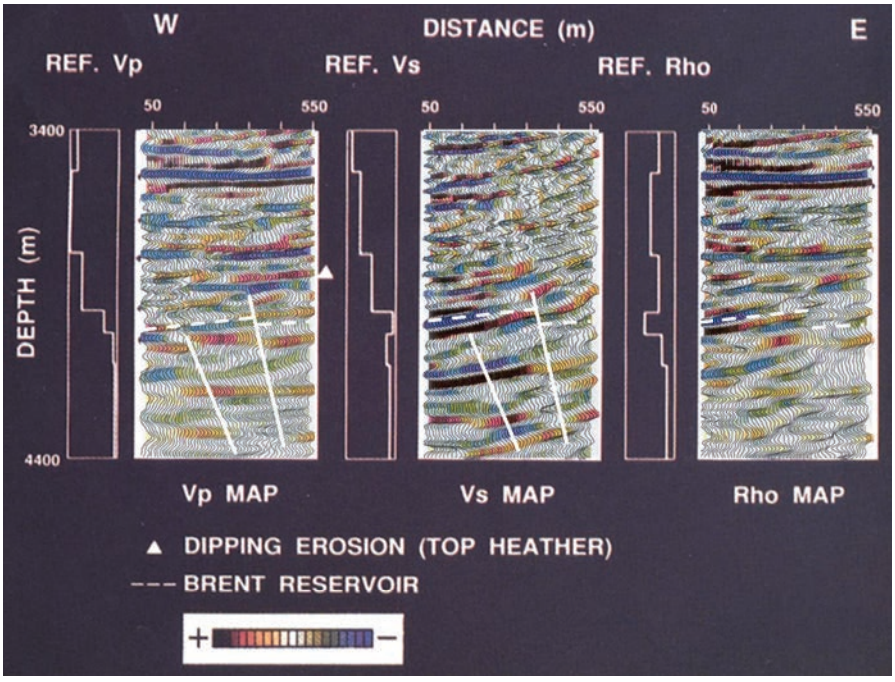

Figure 3.13 *Elastic depth images (P and S-wave velocities and density) of VSP field data of Figure 3.12. The initial input model is at the left of each image. The Brent reservoir and two fault locations were successfully interpreted. Adapted from Beydoun* et al. *(1990).*

The quality control of the elastic depth images is given by the goodness of fit between synthetic and field data sets. Therefore, Figure 3.14 illustrates the synthetic

seismograms computed with the elastic images provided by the tomography, and in Figure 3.15 the residual data, i.e. the difference between field and computed seismograms. There is observable evidence of some major P-P and P-S events in the field data also present in the synthetic seismograms. The underlined P upgoing arrival (on the Z-component) and S upgoing arrival (on the X-component) are particularly recognizable, see Figures 3.12 and 3.15.

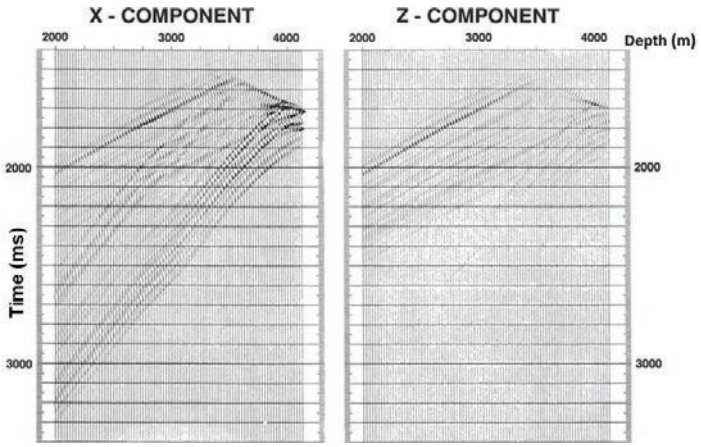

Figure 3.14 *Two-component (X, Z) synthetic VSP using P-P and P-S scattered waves from elastic images in Figure 3.13. Adapted from Beydoun* et al. *(1990).*

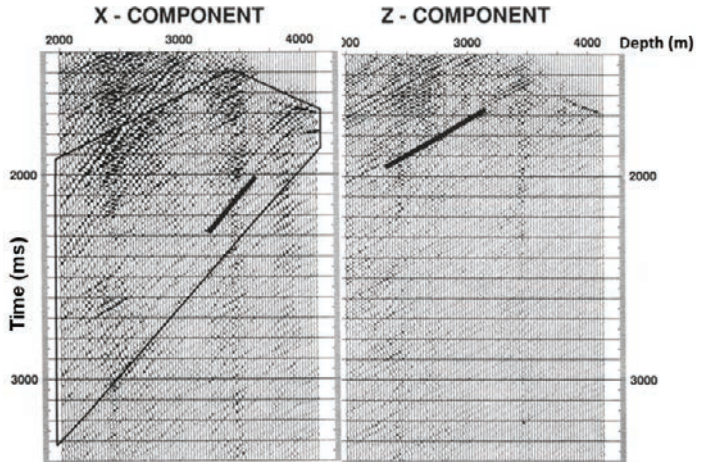

Figure 3.15 *Residual data (i.e., the difference between the data in Figures 3.12 and 3.14). The box represents the part of the data covered by the rectangular area under study. The comparison between the black underlined P upgoing arrival (on the Z-component) along with the S upgoing arrival (on the X-component) in Figure 3.12, with those of this figure confirms the high quality of the tomography. Adapted from Beydoun* et al. *(1990).*

3.3.1.5 Conclusions

This diffraction tomography approach produced high-resolution 2D depth elastic models from offset VSP data, collected in the North Sea. The images reveal several geological and geomorphological features that had previously been undetected or poorly mapped by other surface seismic acquisitions.

The study has shown that the diffraction tomography technique is practical, efficient and particularly suitable for depth imaging of complex geological systems.

3.3.2 *Cross-hole field data*

The second diffraction tomography example is aimed at handling acoustic and multicomponent borehole data collected at two different boreholes, located in the Paris basin. High-resolution tomograms were produced, allowing the identification of three near-surface hydrocarbon reservoirs with thicknesses of between 2–5 m. The reservoirs are separated by a set of north-south faults with east dips and throws in the order of 30-40 m, consisting of three sand levels imbedded in shales, and depths of between 575-600 m.

Beydoun provides a more detailed processing and interpretation of these data (Beydoun *et al.*, 1989).

3.3.2.1 Field parameters

An oil field test site was constructed in the Paris basin, an area in which the geology is well known from previous well logs and seismic studies.

The test site has several boreholes with inter-well distances ranging between small offsets (80-100 m) and large offsets (600-800 m), making it favorable for cross-hole seismic research, such as downhole source prototypes.

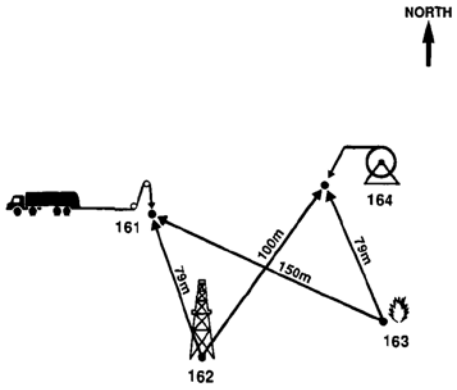

Figure 3.16 *Cross-hole test site. Source/receiver setup. Adapted from Beydoun* et al. *(1989).* **161***: Geolock recorder;* **162***: Downhole seismic source: sparker/weight-drop;* **163***: Dynamite source;* **164***: Downhole streamer.*

For the purposes of this study, four cased 7-inch diameter boreholes were available (Figure 3.16) and a prototype weight drop downhole source was tested, designed at the Institut Français du Pétrole (IFP). A diagram showing the principle and mechanism of this downhole weight-drop source, which generates P and S-waves, is shown in Figure 3.17.

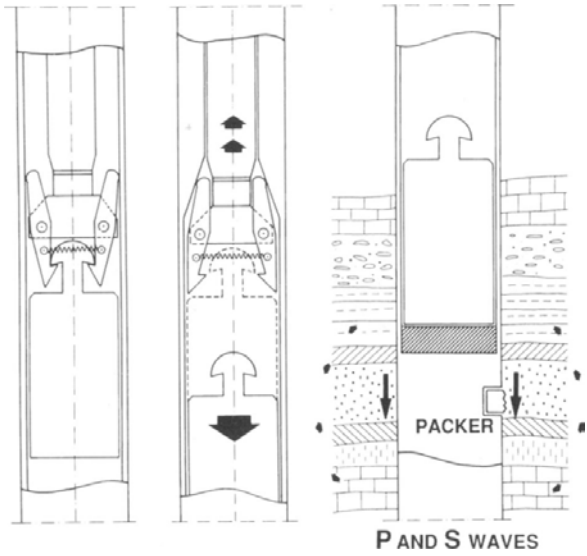

Figure 3.17 *Principle and mechanism of the downhole weight-drop source developed at the Institut Français du Pétrole (IFP). Adapted from Beydoun* et al. *(1989).*

The seismic source was deployed with drill strings in borehole 162 and wall-clamped at depth 455 m, the firing position, with a packer (Brown 7 inches, type MI) which locked and unlocked to the hole through the tool's rotation. The loading of the source (lifting of the mass) is carried out with the drill strings, the weight is then dropped automatically, hitting an anvil bound to the packer.

The seismic data were recorded simultaneously in borehole 164 with a vertical hydrophone streamer and in borehole 161 with a three-component geophone tool.

The basic acquisition tools were as follows:

– Source in borehole 162:
  - weight-drop, generating mainly S-waves perpendicular to the borehole;
  - 3,000 joules/shot;
  - 2 shots/minute capability;
  - depth = 455 m;
– Receivers in borehole 164:
  - vertical hydrophone streamer not anchored, thus highly sensitive to tube waves;
  - band range 10-5,000 Hz;

- 48 channels;
- 1 m spacing.

– Receivers in borehole 161:
  - triaxial geophone tool (Geolock H, CGG VSP tool) anchored, thus less sensitive to tube waves;
  - band range 10-150 Hz.

3.3.2.2 Seismic data

It should be noted that the hydrophones recorded the pressure disturbance in the borehole fluid and the geophones the vector wave field at the borehole wall, since the shot was simultaneously recorded by two receiver tools with sensitivity to different physical quantities.

Figure 3.18 (a) shows the hydrophone data, dominated by down-going S waves, S-S and S-P reflections; while P-P and P-S reflections are absent.

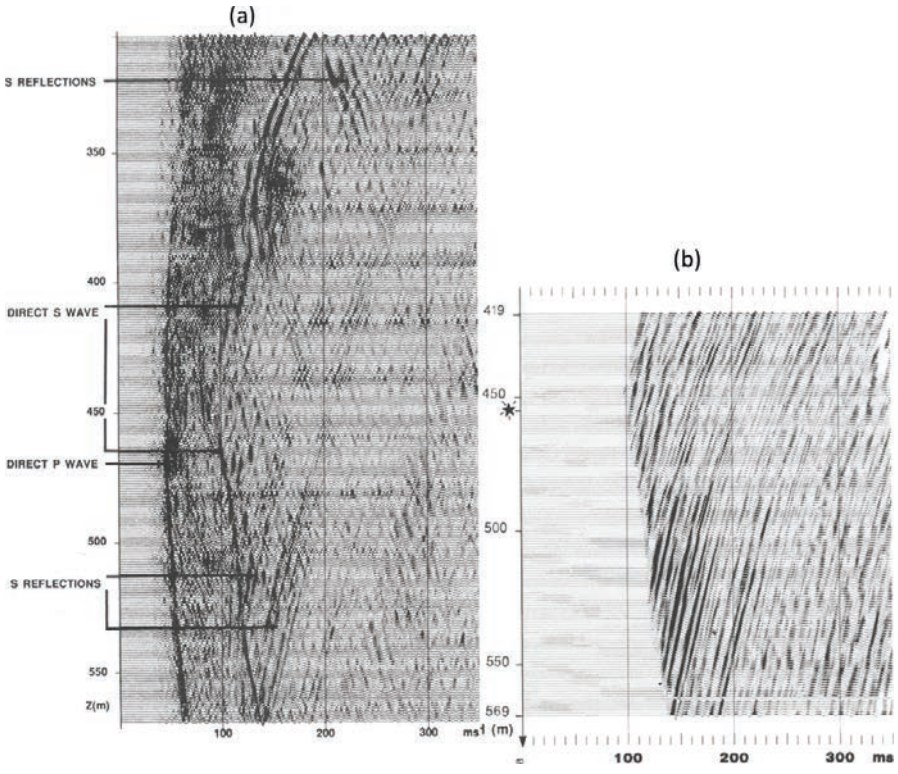

Figure 3.18 *Hydrophone data. (a) Showing the different seismic arrivals in the raw data after tube-wave filtering. Note the absence of P-P and P-S reflections and the presence of strong down-going S-wave arrivals. (b) Subset data used as input data for the tomography. Adapted from Beydoun* et al. *(1989).*

This is due to:

- the pattern radiation of the source having a strong S lobe perpendicular to the borehole;
- the acquisition geometry with large angles of incidence, favouring the shear-wave conversions.

The acquired data were processed with tube-wave filter removal, down-wave field separation and band-pass filters (40-60-300-450) Hz. Figure 3.18 (b) shows a subset of processed data.

Figure 3.19 shows the raw geophone data after rotation from (H1, H2) directions to (X, Y) directions, where X is the horizontal axis in the acquisition plane and Y is the transverse (out-of-plane) direction.

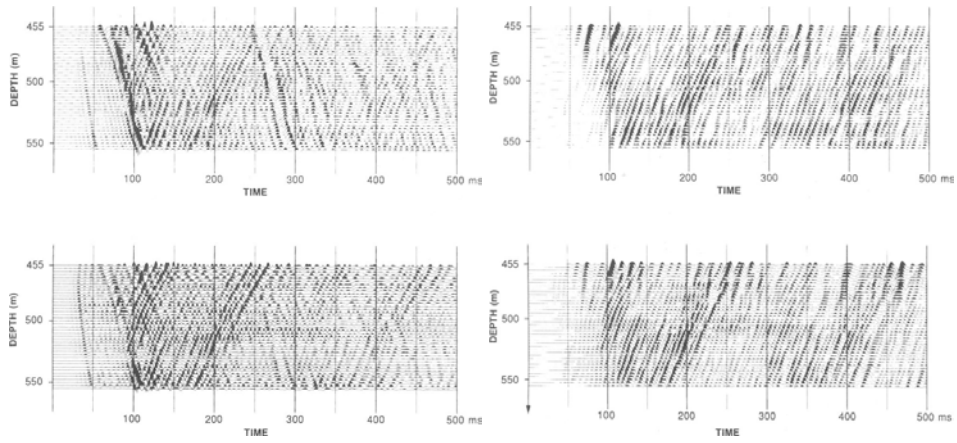

Figure 3.19 *Geophone data: Z-component (upper) and X-component (lower). (a) Raw data after reorientation (X, Y). (b) After down-wave field separation and used as input data for the tomography. Adapted from Beydoun* et al. *(1989).*

Given that seismic wave amplitude and travel time information are both used in the inversion algorithm, for a successful solution it is fundamental that careful data pre-processing is carried out to preserve both amplitude and travel time parameters.

The pre-processing steps for both datasets were similar:

- least-squares approach in the frequency and depth domains to estimate simultaneously the up and down-going tube waves by minimizing the separation residual;
- residual waves were filtered by similar processing to eliminate only down-going P and S-waves;
- only upgoing S-S and S-P reflected events are used for the tomography;

- band-pass filtered; hydrophone data (40-60-300-450) Hz; geophone data (6-12-150-200) Hz;
- no deconvolution;
- 3D to 2D amplitude correction, i.e., $\sqrt{t}$ multiplicative amplitude correction to compensate for the transverse (out of plane) spreading.

3.3.2.3 Initial model

The starting model for the tomographic inversion was defined by integrating cross-hole data with log information from the three holes, and VSP information on P and S-waves in borehole 161. Unfortunately, a shear-wave sonic log was not available, because S-waves, being slower than Stoneley waves, were masked. The density information was obtained from a compensated formation density (FDC) log in borehole 164. An elastic 1D velocity-depth model was used as background (Figure 3.20) with the P/S-wave velocity ratio constant (equal to 1.9) at the reservoir area**.**

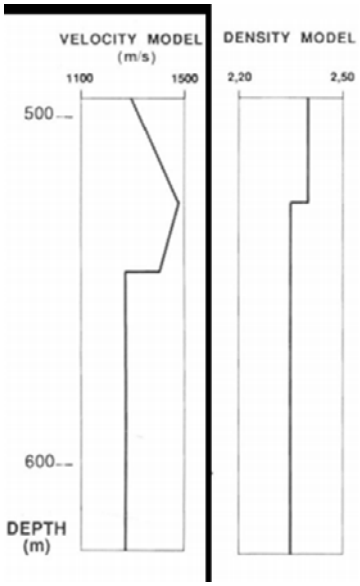

Figure 3.20 *Initial elastic 1D model. Adapted from Beydoun* et al. *(1989).*

3.3.2.4 Depth elastic images: comparison with density log

In this field example, given that P-P scattered waves are not visible in the data and only up-going S-S and S-P scattered waves have enough energy, then P-wave imaging is not possible and only two images, S-wave velocity and density images, could be generated.

The diffraction tomography applied to the single-shot geophone data has a target zone, which encloses the reservoir area near the receiver borehole (161), and is defined as follows:

- from 40 to 75 m away from the emitter borehole (162) to the receiver borehole (161);
- depth interval 475-625 m.

Since the tomography technique produces reliable estimates of changes in elastic parameters only when the source and receiver coverage is satisfactory, then the upper part of the elastic images (above 560 m) should not be interpreted due to insufficient coverage (Figure 3.21). In the lower right portion of the images (below 560 m), source and receiver coverage is very good (maximum coverage), so a confidence region can be defined here in the target zone.

The target zone for the single-shot hydrophone data, which encloses the reservoir area near the receiver borehole (164), is defined as follows:

- from 50 and 86 m away from the emitter borehole (162) to the receiver borehole (164);
- depth interval 500-650 m.

In spite of the different nature of both geophone and hydrophone data (particle velocity and pressure), in coupling with the formation (clamped geophone versus hydrophone string), and spatially (holes 161 and 164), a good correlation between the images is observed. Furthermore, the three reservoir levels, R3=575 m, R2=583 m, and R1=600 m, can be identified.

In both boreholes, the density tomograms were assessed in a practical manner, by carrying out a comparison between the density images with a pseudo-density log. The density logs were convolved with a characteristic signal matching the frequency bandwidth of the density tomogram. Therefore, the results could be compared directly to identify similarities and differences to aid in interpretation.

In borehole 164, an FDC log was used, which verifies a good correlation between the two independent sets of density information.

In borehole 161, a density log was generated from a combination of gamma-ray, neutron-porosity, and the sonic logs from this borehole, and the density log of borehole 164.

The tomography of hydrophone data produced a better and cleaner density tomogram than the geophone data image. Comparison of the images from both data sets revealed a vertical resolution of the geophone data image that is lower than that of the hydrophone data. This also fits with differences in signal bandwidth, 150 Hz versus 350 Hz. However, the fit at the Lower Hauterivian level, around R1= 600 m, seems reasonable.

Since the thicknesses of these reservoirs are of the order $\approx$ 3 m, the very limit of seismic resolution, it is difficult and delicate to attempt any detailed interpretation within each reservoir level, especially with only one-shot record.

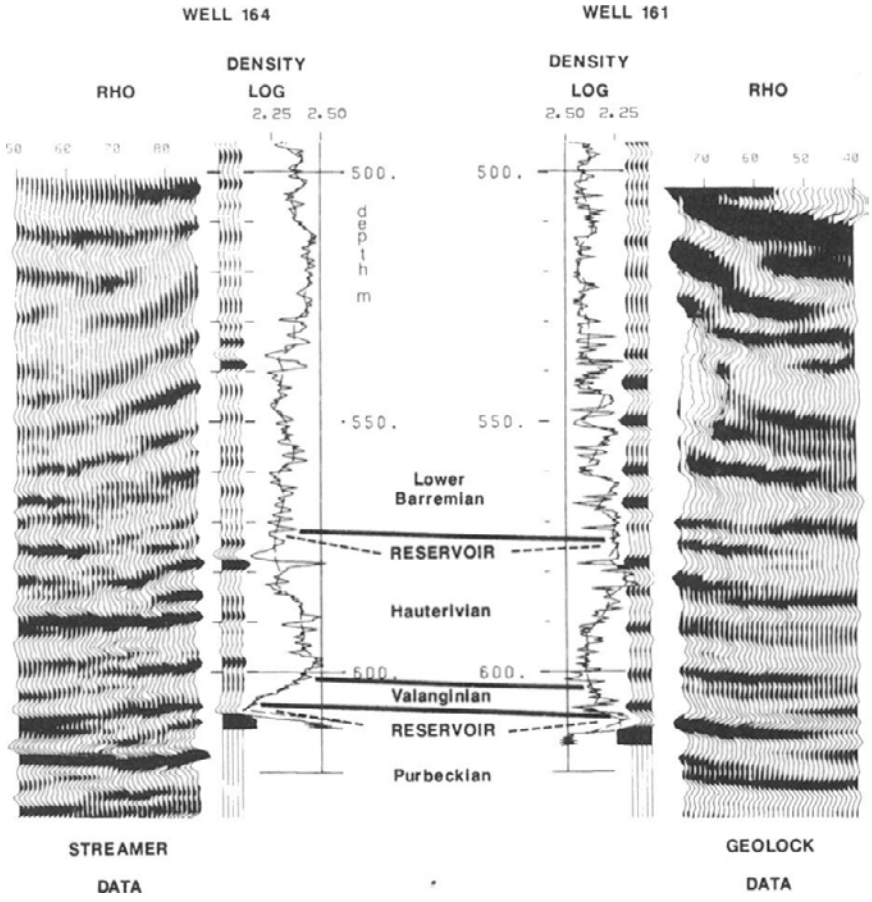

Figure 3.21 *Density logs, band-pass filtered density logs, and elastic depth migration images (density) of geophone and hydrophone data. Note the strong and different image artifacts on the upper portion of both images (above 560 m) due to insufficient source and receiver coverage of this region. Within the reservoir area, the density image from the hydrophone data corresponds closely to the filtered log from borehole 164. Adapted from Beydoun* et al. *(1989).*

3.3.2.5 Conclusions

The diffraction tomography approach, even using only a one-shot cross-hole acoustic (hydrophone) dataset, or a multicomponent (geophone) field dataset, proved successful in producing high-resolution (≈ 3-5 m) density tomograms for the interwell region. These tomograms are in close agreement with regional geology and density borehole logs.

3.4 General conclusion

This chapter, supported by several seismic field data examples, demonstrates the possibility of imaging the subsurface structures with seismic tomography.

Seismic tomography is able:

- to handle acquisitions of various scales and geometries;
- to handle single or multi-component data;
- to handle direct, reflected or diffracted P or S-body waves;
- to produce high-resolution depth or time images;
- to provide confidence criteria for the resulting tomogram.

The main requirements for seismic tomography to build reliable images are:

- high fold coverage;
- large azimuthal coverage;
- data that preserves travel times and amplitudes;
- an initial model (P and/or S-wave velocity and density) that adequately represents the main subsurface features.
- low or moderate computational effort.

These tomograms may provide useful input data for further processing as pre or post-stack seismic migrations or for full waveform inversion techniques.

References

Aki K., Lee W.H.K., 1976, Determination of the three-dimensional velocity anomalies under a seismic array using first P arrival times from local earthquakes 1. A homogeneous initial model, *J. Geophys. Res*. 81, 4381-4399.

Becquey M., Bernet-Rollande J.O., Laurent J., Noual G., 1992, Imaging reservoirs - a crosswell seismic experiment, *First Break*, 10 (9), 337.

Beydoun W.B., Mendes M., Blanco J., Tarantola A., 1990, North Sea reservoir description: Benefits of an elastic migration/inversion applied to multicomponent vertical seismic profile data, *Geophysics*, 55 (2), 209-217.

Beydoun W.B., Mendes M., 1989, Elastic ray-Born K2-migration/inversion, *Geophys. J*. 97, 151-160.

Beydoun W.B., Delvaux J., Mendes M., Noual G., Tarantola A., 1989, Practical aspects of an elastic migration/inversion of crosshole data for reservoir characterization: A Paris basin example, *Geophysics*, 54 (12), 1587-1595.

Brzostowski, M.A. and McMechan G. A., 1992, 3-D tomographic imaging of near-surface seismic velocity and attenuation, *Geophysics*, 57 (3), 396-403, https://doi.org/10.1190/1.1443254.

Galibert P.-Y., Valois R., Mendes M., Guérin R., 2014, Seismic study of the low-permeability volume in southern France karst systems, *Geophysics*, 79 (1), EN1-EN13, http://dx.doi.org/10.1190/geo2013-0120.1.

Goldman L.W., 2007, *J. Nucl. Med. Technol.*, 35 (3), 115-128, DOI: 10.2967/jnmt.107.042978 http://tech.snmjournals.org/content/35/3/115.full.

Hounsfield G.N., 1973, Computerized transverse axial scanning (tomography): Part 1. Description of system. The British Institute of Radiology Central Research Laboratories of EMI Limited, Hayes, Middlesex, 1973, https://doi.org/10.1259/0007-1285-46-552-1016.

Jordi C., Schmelzbach C., Greenhalgh S., 2016, Frequency-dependent travel-time tomography using fat rays: application to near-surface seismic imaging, *Journal of Applied Geophysics* 131, 202-213, http://dx.doi.org/10.1016/j.jappgeo.2016.06.002.

Mari J.L., Vergniault C., 2018, *Well seismic surveying and acoustic logging*, EDP Sciences, DOI: 10.10051/978-2-7598-2263-8, ISBN (ebook): 978-2-7598-2263-8. https://www.edp-open.org/well-seismic-surveying-and-acoustic-logging

Mendes, M., 2009, A hybrid fast algorithm for first arrivals tomography, *Geophysical Prospecting*, 57, 803–809, doi: 10.1111/j.1365-2478.2008.00755.x.

Padina S., Churchill D., Bording R.P., 2006, Travel time inversion in seismic tomography. Available from http://webdocs.cs.ualberta.ca/~cdavid/pdf/HPCSPaper.pdf

Sheng J., Schuster G.T., 2003, Finite-frequency resolution limits of wave path travel-time tomography for smoothly varying velocity models, *Geophysical Journal International*, 152, 669–676, doi: 10.1046/j.1365-246X.2003.01878.x.

Spakman W., Van der Lee S., Van der Hilst R., 1993, Travel-time tomography of the European-Mediterranean mantle down to 1400 km, *Physics of the Earth and Planetary Interiors*, 79 (1–2), 3-74.

Witten A., Gillette A. A., Sypniewski J., King W.C., 1992, Geophysical Diffraction Tomography at a Dinosaur site, *Geophysics*, 57, 187-195.

4

Near-surface reflection surveying

J.-L. Mari

Seismic reflection is the most widely used seismic technique. It has the advantage of being able to provide a picture of the subsurface in two or three dimensions (2D or 3D) in a regular grid (Figure 4.1).

For the last two decades there has been significant progress in 3D seismic technology. Between 1990 and 1996 there was an exponential increase in the number of 3D seismic surveys carried out by many major oil companies to cover their offshore fields. Today, 3D land seismic acquisition is also developing very rapidly. The technology has reduced many uncertainties in oil and gas exploration and production, and it benefits greatly from developments in other fields such as computing, GPS positioning, an increased number of channels in instrument recording, improvements in processing software, etc. 3D data are now increasingly used for field development and production and not only as an exploration tool. Pre-planning of

DOI: 10.1051/978-2-7598-2351-2.c006

3D surveys has become a fundamental step to ensure that the 3D data quality meets structural, stratigraphical and lithological requirements. Pre-planning includes the evaluation of both geophysical and non-geophysical parameters such as environmental considerations, health and safety requirements, etc. Specific pre-planning tools (Cordsen A., Galbraith M., Peirce J., 2000) have been developed to estimate all acquisition characteristics such as offset, fold and azimuth distributions, effects of surface obstacles, etc. Pre-planning steps aim to define the geological targets of the 3D survey, with the associated geophysical parameters, design and costs.

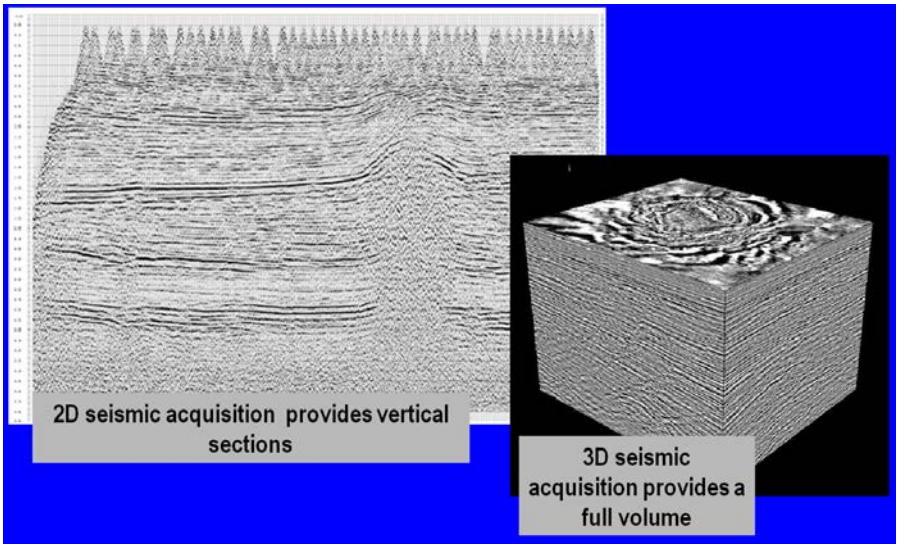

Figure 4.1 *2D and 3D seismic imaging (after J. Meunier, 2004, IFP School course).*

In 2D acquisition, the image obtained after processing is a vertical seismic section. The horizontal axis of the section represents the geographical abscissa of subsurface points along the acquisition profile, and the vertical axis represents the record time. The seismic events that appear on the records correspond to the arrivals of waves reflected at normal incidence on the seismic horizons. The seismic horizons correspond to discontinuities of acoustic impedance; their picks provide a structural image of the subsurface.

3D seismic acquisition provides full volume interpretation, consisting of a collection of sections parallel to each other. Surface seismic has vertical and horizontal resolutions measured in tens of meters with lateral investigation distances only limited by the size of the area investigated by the seismic surveys.

This chapter is neither a basic introduction nor a theoretical study of seismic acquisition and processing; its goal is to show, through the use of field examples, the contribution of seismic reflection to near-surface imaging, and to hydrogeological

studies. For each field example we have described the survey design (acquisition parameters) and the applied processing sequence.

The reader will find more information about acquisition and survey design in Galbraith (2000), Lansley (2000), Mayne (1962), Meunier and Gillot (2000), Meunier (2011), Monk and Yates (2000), Musser (2000), Vermeer and Hornman (2000), and Chaouch and Mari (2006); more about signal processing in Mari *et al.* (1999, 2015); and more on seismic processing in Yilmaz (1987), and Robein (2003).

4.1 General notes about acquisition and survey design

2D seismic acquisition is achieved with either end-on (also called off-end) or split dip spreads (Figure 4.2-a).

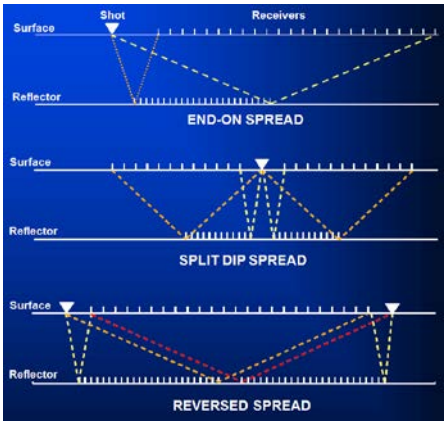

a

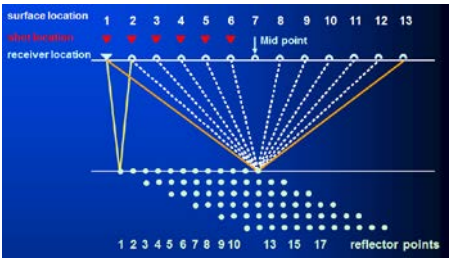

b

Figure 4.2 *2D land seismic acquisition: (a) seismic spreads, (b) stacking fold.*

The individual shot element is defined by the distance between the source and the first receiver, the number of receivers and the distance between two adjacent receivers. A receiver can be a single sensor (geophone for land acquisition) or an array of sensors. If the receiver is a single sensor, the interval between two receivers is of several meters, if it is an array, the interval is of several tens of meters. The maximum source-receiver offset to the far receiver is about the same as the maximum depth of the geological objective. The near receiver offset is chosen to minimize interference between ground roll (surface waves) and reflection arrivals. The distance between reflection points, assumed to be midpoints, is equal to half the receiver interval. For a receiver spread of length L, the length of the reflector illuminated is equal to half

the length of the spread (L/2). If the entire spread (source and receiver spreads) is shifted by L/2 then the reflection zone illuminated by the current shot adjoins that illuminated by the previous shot. Where there is no overlap between the successive reflection zones, the coverage is called single fold coverage.

If the distance between shots is m/2 times the receiver interval, where m is a submultiple of the number of receivers N, then there is an overlap between the reflection zones illuminated by successive shots; the reflection coverage is then termed multiple coverage, with the fold coverage being equal to N/m. Figure 4.2-b is an example of multiple coverage. A 12-receiver spread (N=12) is moved up by one receiver interval (m=2) to provide 6-fold coverage. The fold of coverage corresponds to the number of traces having the same common midpoint (CMP).

The distribution of offsets is regular in 2D surveys; the azimuth (angle between the theoretical direction of the seismic line and the straight line joining the source and the receiver) is constant (0° for end-on shooting, and 0° and 180° for split spread shooting).

Acquisition is more complex for 3D land surveys. Source and receiver lines are laid out to provide the most homogeneous coverage. The most conventional implementation is the cross-spread design with lines of sources perpendicular to lines of receivers (Figure 4.3).

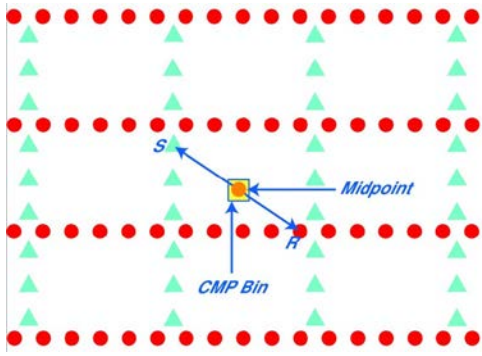

Figure 4.3 *Cross-spread design: Lines of sources (green triangles) perpendicular to lines of receivers (red dots).*

In 3D acquisition, the CMP is replaced by a cell or bin, the size of which being the product of half the source interval and half the receiver interval. Traces contributing to the same CMP bin have irregularly distributed azimuths and offsets. Implementation is optimized to ensure the most regular azimuth and offset distribution possible. Figure 4.4-a shows a single fold 3D subset, obtained with an elementary cross spread for which source positions belong to the same source line, and receiver positions belong to the same receiver line. The stacking fold is the number of overlapping elementary cross spreads (Figure 4.4-b).

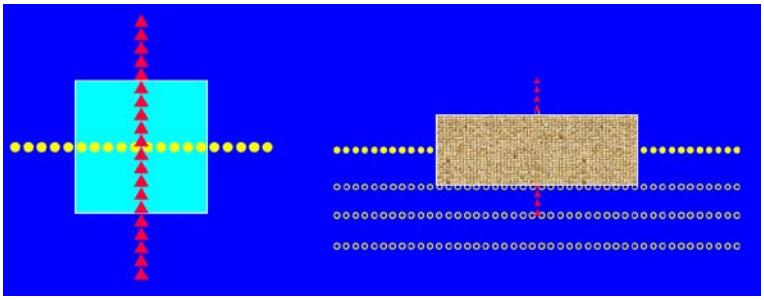

a

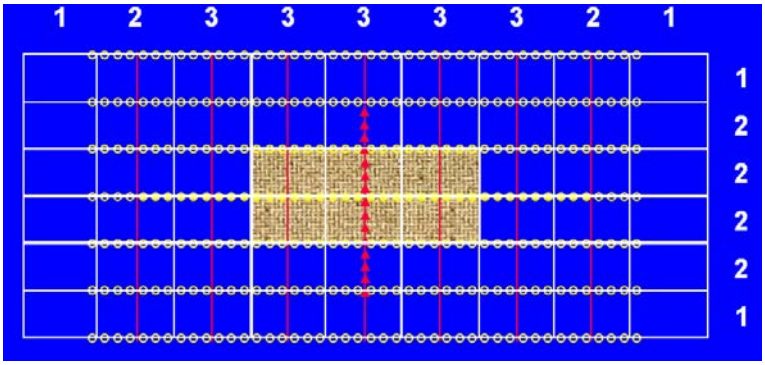

b

Figure 4.4 *3D land seismic acquisition (after J. Meunier, 2004, IFP School course). (a) Cross-spread build up: Cross-spread set of seismograms for which source positions belong to the same source line, and receiver positions belong to the same receiver line. (b) Stacking fold: number of overlapping cross-spreads (G. Vermeer).*

The data are correctly sampled if the geophone interval **i** is sufficiently small (several meters) to avoid spatial aliasing. In 3D acquisition, it is necessary to use telemetric recording systems to simultaneously record several thousands of traces (an elementary shot being composed of several lines of receivers and several hundred receivers per line). The undersampling in distance can be done by applying a wave number filter in processing. Another solution is to use field arrays of sensors and a specific acquisition design called stacked array geometry introduced by Anstey (1986).

For 2D surveys, a common midpoint can be viewed as a spatial filter, which is the convolution of a receiver array and a stack array. The geometry of acquisition must respect the following rules (Figure 4.5):

- Shot points (SP) should be recorded with a symmetric split dip spread,
- Source and receiver intervals should be the same,

- The SP should be located halfway between receivers,
- The receiver interval **e** should be **n** (number of sensors) times the sensor interval **i** (**e=ni**).

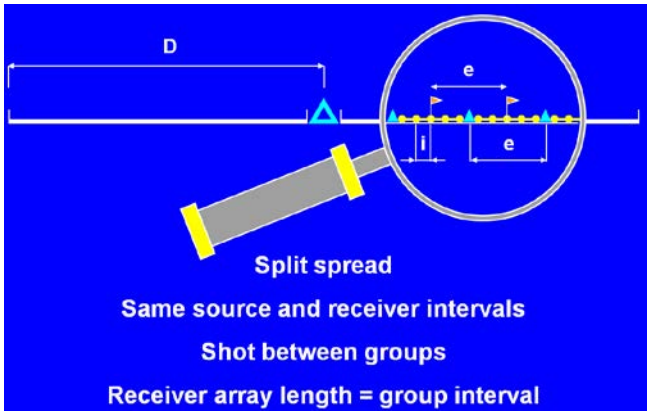

a

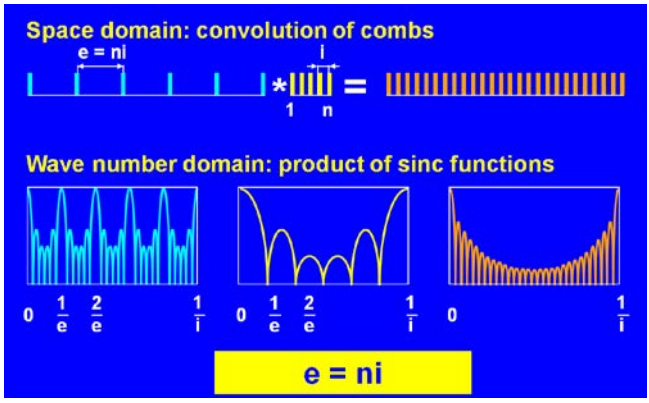

b

Figure 4.5 *2D stack array geometry (after J. Meunier, 2004, IFP School course); (a) 2D stack array rules; (b) convolution of 2 combs representing a receiver array and a stack array. Some wave numbers of the stack response are zeroed by notches of the receiver response, resulting in an unaliased combined response (from Meunier, 1998).*

The extension of the 2D stack array theory to 3D acquisition is not straightforward. Source and receiver lines become source and receiver grids (x, y) and 1D arrays (combs) become 2D arrays (brushes).

The geometry of acquisition (Figure 4.6) must respect the following rules (Meunier, 1999):

- Same source and same receiver interval **e** in x and y (full grid),
- Receiver–array size $\mathbf{n^2i^2}$ is equal to source and receiver intervals $\mathbf{e^2}$,
- Source and receiver grids are shifted by half an interval **e/2** in both directions.

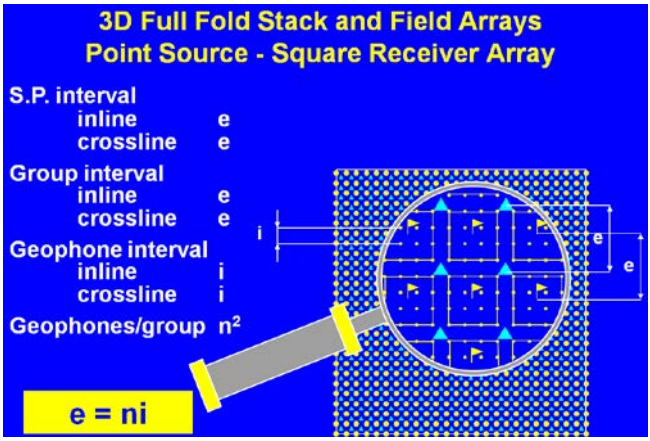

a

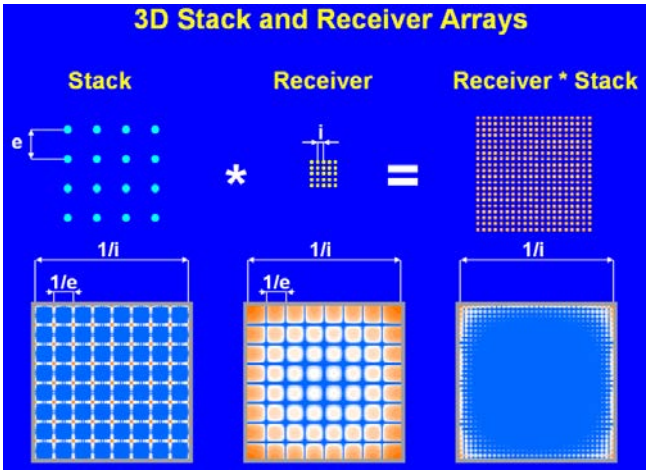

b

Figure 4.6 *3D stack array geometry (after J. Meunier, 2004, IFP School course). (a) 3D stack array rules; (b) convolution of the 3D receiver and stack arrays (Meunier, 1998).*

4.2 Comments on the reflection seismic processing sequence

The classical approach to seismic processing can be summarized in two main steps.

The first step includes pre-processing of the data and the application of static corrections. The purpose of pre-processing is to extract reflected waves from individual shots, by filtering out the parasitic events created by direct and refracted arrivals, surface waves, converted waves, multiples and noise. It is intended to compensate for amplitude losses related to propagation. Deconvolution operators are applied to improve resolution and harmonize records by taking into account source efficiency variations and eventual disparities between receivers. Any deconvolution is sensitive to noise. A classically used method that is relatively robust to noise is deconvolution with the Wiener filter. The Wiener filter allows the processing of a measured signal to obtain a desired signal. It minimizes (least squares conditions) the difference between the desired signal and the signal estimated by the filter. The desired signal can be a Dirac impulsion. In this case, spiking deconvolution is necessary. Static corrections, which are specific to land seismic surveys, are intended to compensate for weathered zone and topographic effects. Seismic records are sorted in common midpoint gathers or common offset gathers.

The second processing step is the conversion of common midpoint gathers or common offset gathers into time or depth migrated seismic sections. This second step includes the determination of the velocity model, with the use of stacking velocity analyses, or tomography methods. The role of migration is to place events in their proper location and increase lateral resolution, in particular by collapsing diffraction hyperbolas at their apex. Proper migration requires the definition of a coherent velocity field, which must be a field of actual geologic velocities in migrated positions. Determination of the velocity field is the most critical aspect of migration.

In near-surface experimentation, the separation of interfering wavefields is a crucial step to enhance reflected waves. To achieve this, wave separation filters such as F-K filters or SVD (Singular Value Decomposition) filters should be used.

4.3 Near-surface imaging

An experimental site at Vesdun (situated in the Cher region in central France) has been developed to train IFP School and university students, along with professionals. The geophysics training relates to the acquisition and processing of surface seismic data in 2D or 3D. A borehole has been drilled on site. It allows the acquisition of well seismic data such as vertical seismic profiles (VSP), and logging data such as full waveform acoustic data. The site is also used for experimental studies in near-surface geophysics.

Shot points recorded for near-surface seismic surveys are usually corrupted by surface waves such as pseudo-Rayleigh waves. For seismic imaging based on reflected waves, it is necessary to be able to separate weak reflected events from high energy surface waves. Wave separation is a crucial step in the processing sequence. We describe here the benefit of combining two different wave separation methods to remove the energetic wavefield. The conventional F-K method is used to filter surface waves and converted refracted waves. The SVD method (Singular Value Decomposition) is then used to extract refracted waves. The different steps of the processing sequence are: amplitude recovery, deconvolution by spectrum equalization, wave separation by SVD and F-K filters, normal moveout (NMO) with constant velocity for quality control.

The shot point presented here is an end-on spread shot composed of 96 traces. The distance between 2 adjacent geophones was 1 m. The source was a weight dropper (see Figure 2.6-c in the "Refraction surveying" chapter). There was no data filtering at the acquisition, consequently the shot was highly corrupted by surface waves (pseudo Rayleigh modes). This shot type is often called a noise profile. It can be used for the analysis of surface waves and also to define the acquisition parameters for near-surface 3D acquisition.

Figures 4.7 to 4.8 show the step-by-step processing sequence of the noise profile. At each stage the data are shown both in the time-distance domain, and in the frequency-wavenumber domain (f-k domain).

Figure 4.7-a shows the raw shot. The seismic trace close to the source is saturated. We observed a very strong attenuation of seismic amplitudes with the offset. After amplitude compensation (Figure 4.7-b), the direct wave, refracted waves, air wave and surface waves were clearly visible. The f-k amplitude spectrum shows that most of the energy is limited in wave number up to 0.25 c/m. Consequently, a geophone interval of 2m allowed the data to be recorded without spatial aliasing. A deconvolution process was applied to the data to increase the vertical resolution by spectral balancing and to facilitate the wave separation (Figure 4-d). The wave separation process involves the extraction of a wave by an apparent velocity filter defined in the f-k domain and then the subtraction of the estimated wave from the dataset to obtain a residual section. The process is carried out iteratively for different waves or seismic events. Figure 4.7-d shows the estimation of the air wave and the Rayleigh wave.

The associated residual section is shown in Figure 4.8-a. On the 2D amplitude spectrum, we note that the energy is concentrated in the 0 to 0.2 c/m wave number interval. It is also possible to see that the air wave is aliased for frequencies larger than 200 Hz and appears with negative apparent velocities. The events with negative apparent velocities are shown in Figure 4.8-b, while the associated residual section (Figure 4.8-c) mainly contains the refracted events (Figure 4.8-d). The residual section associated with the refracted events shows events of very weak amplitude with high apparent velocities in the 60 to 150 ms time interval (Figure 4.9-a). These events are reflected events. On the same section, we can observe low apparent velocity events which are residues of direct waves and air waves (Figure 4.9-b). The residual section associated with the low apparent velocity events shows reflected events (Figure 4.9-c), which are flattened after NMO corrections (Figure 4.9-d).

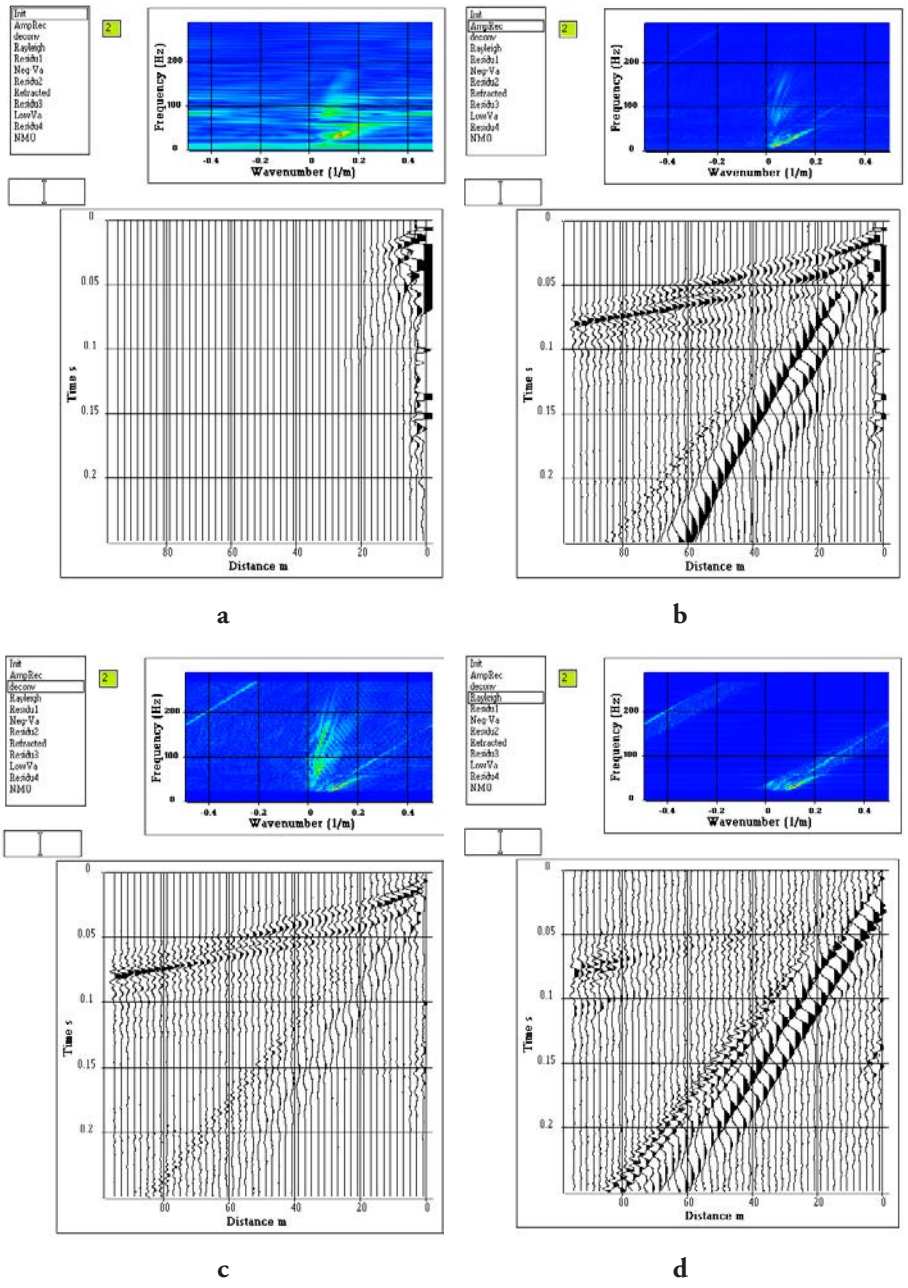

Figure 4.7 *Noise profile processing: (a) raw shot, (b) amplitude compensation, (c) deconvolution, (d) extraction of air wave and surface waves.*

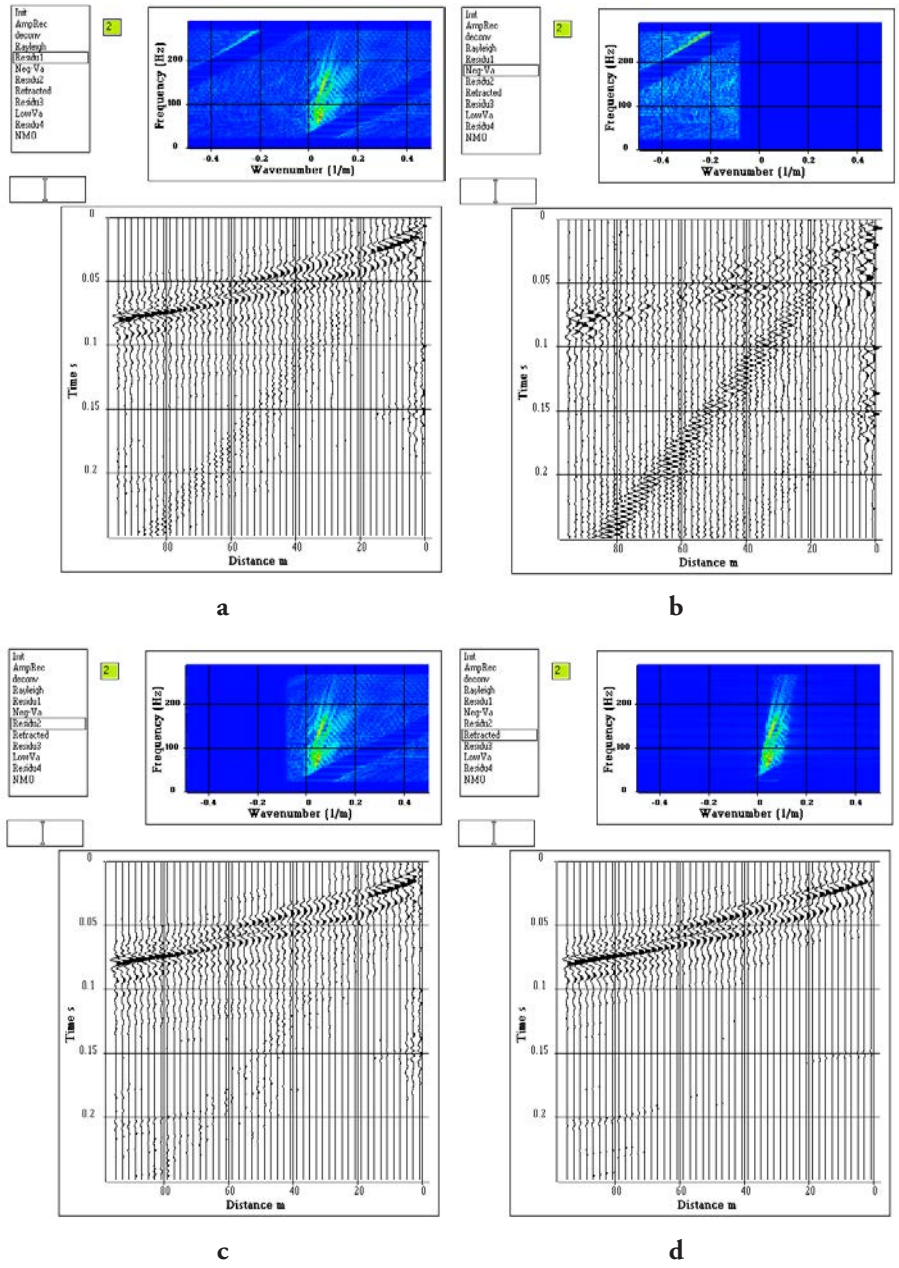

Figure 4.8 *Noise profile processing: (a) first residual section, (b) seismic events with negative apparent velocities, (c) second residual section, (d) direct and refracted waves.*

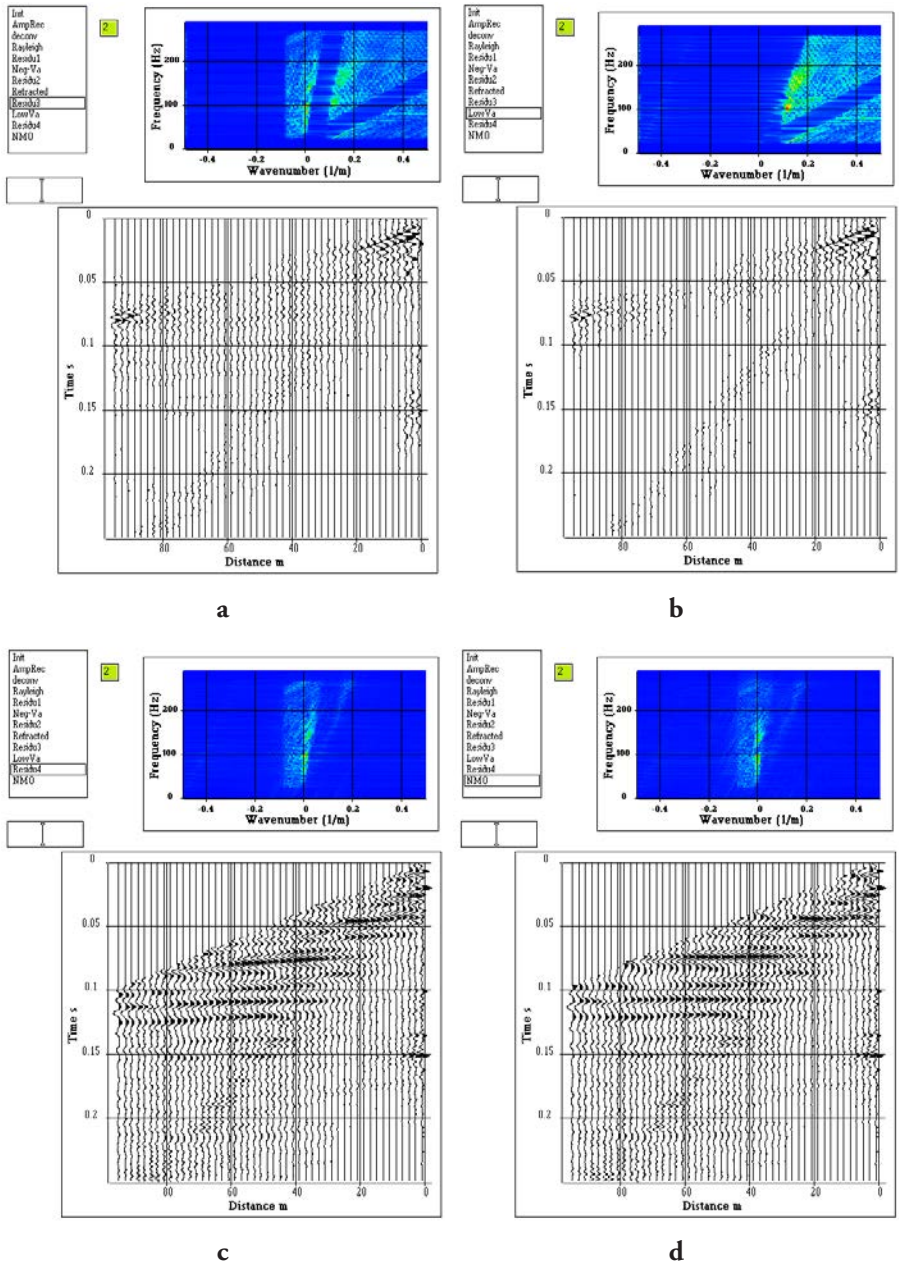

Figure 4.9 *Noise profile processing: (a) third residual section, (b) low apparent velocity events, (c) fourth residual section, (d) reflected waves after NMO corrections.*

The analysis of the noise profile shows that a seismic acquisition with a minimum offset of 40 m and a geophone interval of 2 m can be implemented to obtain reflected events in the 60 to 150 ms time interval. These parameters were checked in a 3D configuration, with an elementary cross-spread composed of 48 geophones (Figure 4.10-a). The distance between 2 adjacent geophones was 2 m. The source was a weight dropper situated in the middle of the recording, with a lateral offset of 45 m. Figures 4.10 to 4.12 illustrate the step-by-step processing sequence.

Step 1: Display of the shot point before and after band pass filtering (Figure 4.10-b). In the upper part, we can see the refracted wave, the high frequency air wave and the low frequency surface wave. In the lower part, after filtering the air waves and surface waves are attenuated.

Step 2: Display of the shot point after amplitude recovery and band pass filtering (Figure 4.10-c): refracted waves can be seen in the first arrivals, and a reflected wave can be hypothesized after 0.1s.

Step 3: Display of the shot point after amplitude recovery, band pass filtering and deconvolution (Figure 4.10-d). The deconvolution increases the vertical resolution and facilitates wave separation.

Step 4: Extraction of refracted waves by SVD filter (Figure 4.11-a).

Step 5: Calculation of the first residual section: in the F-K diagram one can see events with wave numbers close to 0, and frequencies ranging between 50 Hz up to 200 Hz (Figure 4.11-b). Events with low frequencies and wave numbers ranging between -0.1 and 0.1 c/m can also be seen.

Step 6: Extraction of seismic waves with low apparent velocities by F-K filter (Figure 4.11-c).

Step 7: Calculation of the second residual section (Figure 4.11-d): one can mainly see reflected waves.

Step 8: Reflected waves after static corrections (Figure 4.12-a)

Step 9: Time variant velocity model used for the NMO correction (Figure 4.12-b)

Step 10: NMO correction with time variant velocity model. The reflected waves are flattened (Figure 4.12-c). Seismic horizons between 0.04 and 0.12 s can be seen.

Step 11: Time to depth conversion of the seismic section (Figure 4.12-d). The upper part of the figure shows the depth versus time law. On the seismic section, a continuous layer can be seen above 60 m. The layers below 60 m are situated in the bedrock.

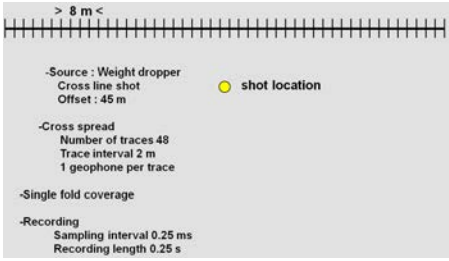

a

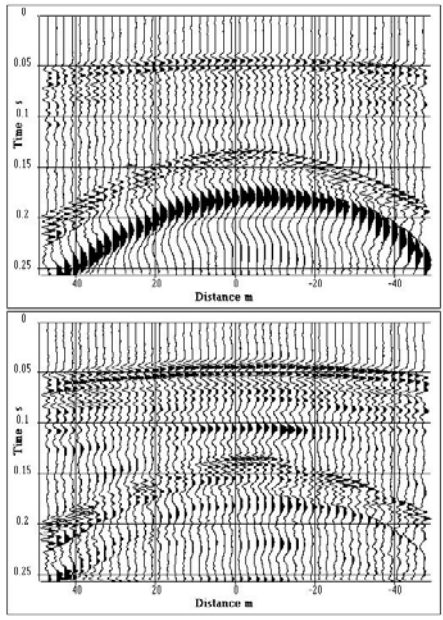

b

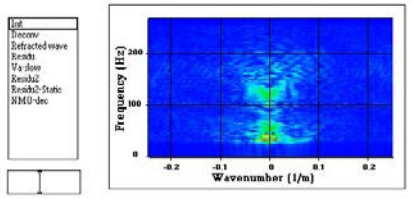

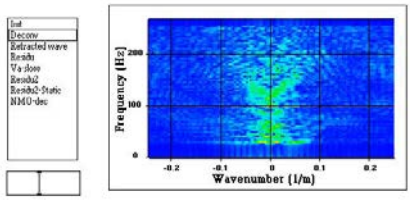

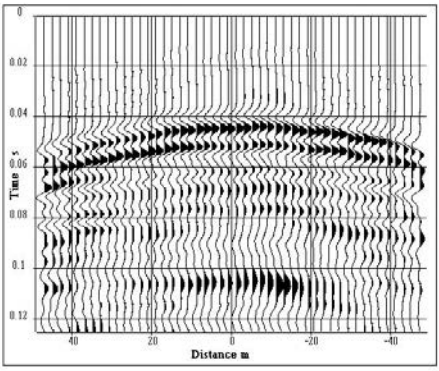

c

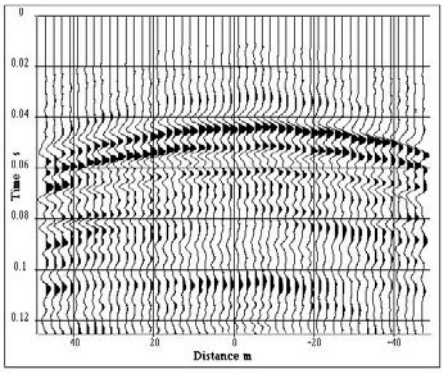

d

Figure 4.10 *Elementary cross-spread shot: (a) acquisition spread, (b) raw shot before and after filtering, (c) amplitude compensation, (d) deconvolution.*

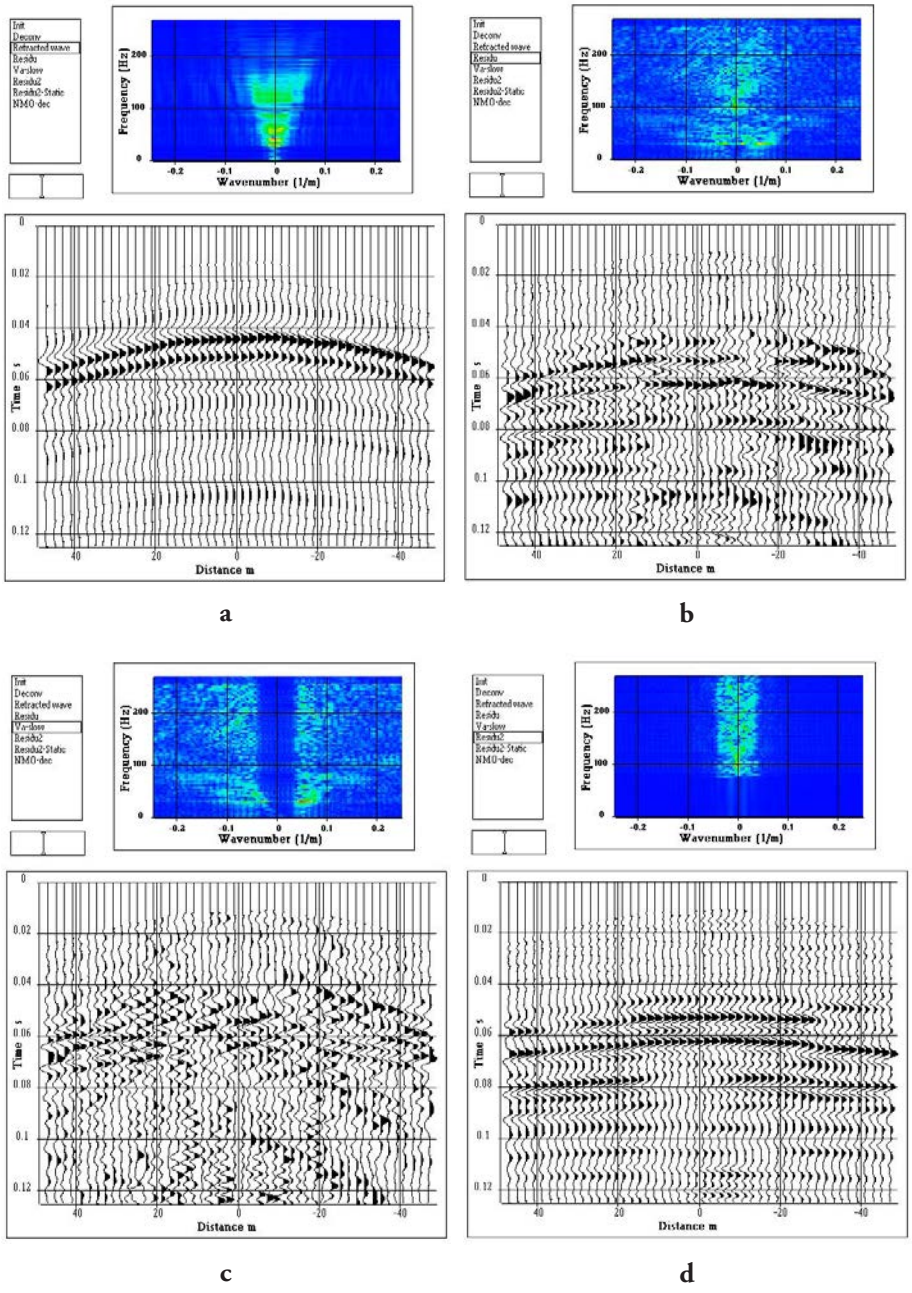

Figure 4.11 *Elementary cross-spread shot: (a) refracted wave, (b) first residual section, (c) low apparent velocity events, (d) Second residual section.*

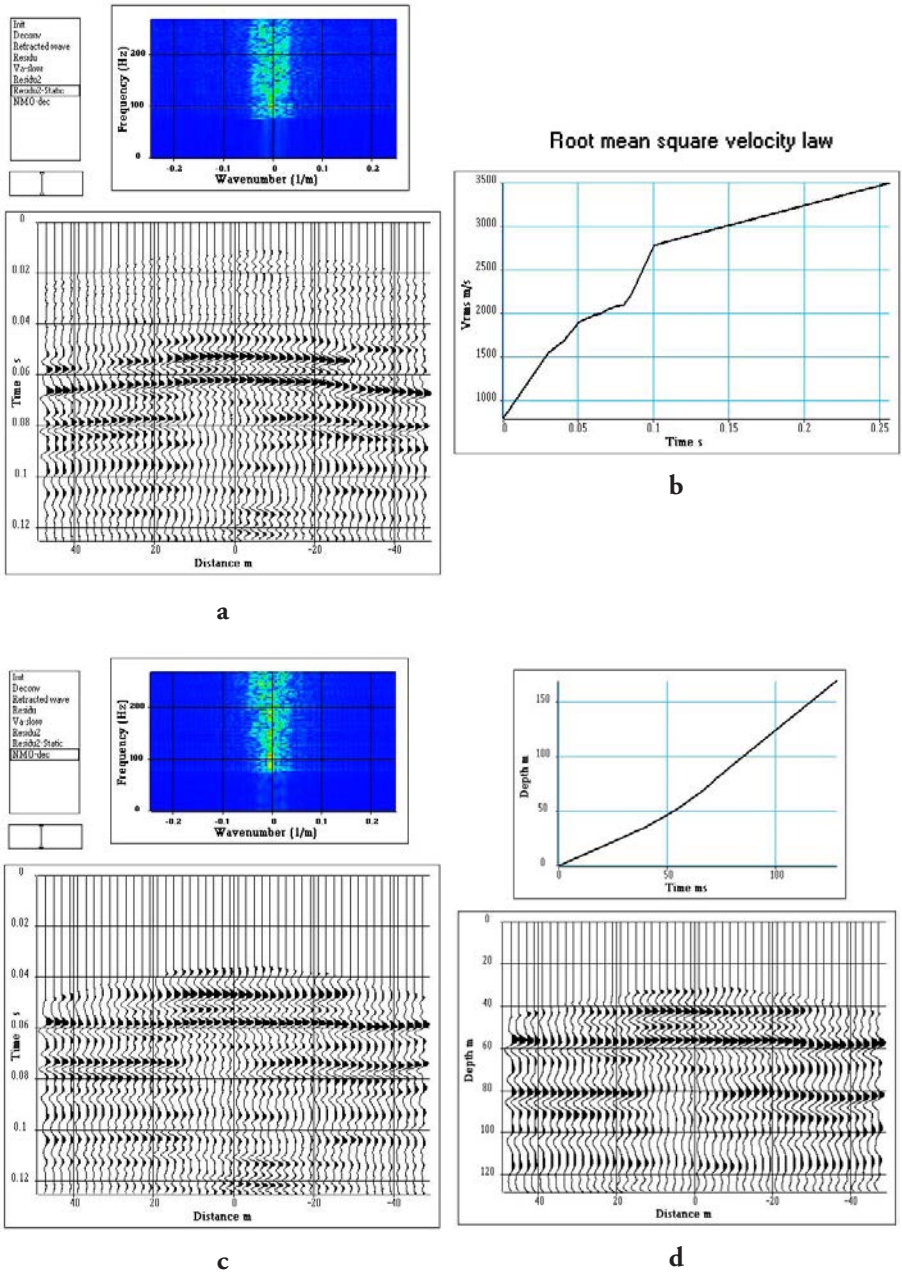

Figure 4.12 *Elementary cross-spread shot: (a) second residual section after static corrections, (b) Rms velocity model, (c) section after NMO correction, (d) section in depth.*

The results obtained by the analysis of the noise profile and the elementary cross-spread enabled the acquisition parameters for a 3D survey and processing flow to be defined, to obtain a significant 3D cube in multiple fold (up to 22).

The seismic spread was composed of a receiver spread and a source spread. The receiver spread, shown in green, had 2 receiver lines. The receiver line direction is known as the in-line direction. The distance between the receiver lines was 4 m. There were 24 geophones per line. The distance between the geophones was 2 m.

The source spread, shown in yellow, was composed of 11 source lines oriented perpendicular to the receiver lines. 11 shots were fired per line. The distance between the shots was 2 m. The distance between the source lines was 4 m. The source lines and the receiver lines were perpendicular.

The distance between the receiver spread and the source spread was 4 m. There was no overlap between the source and the receiver spread.

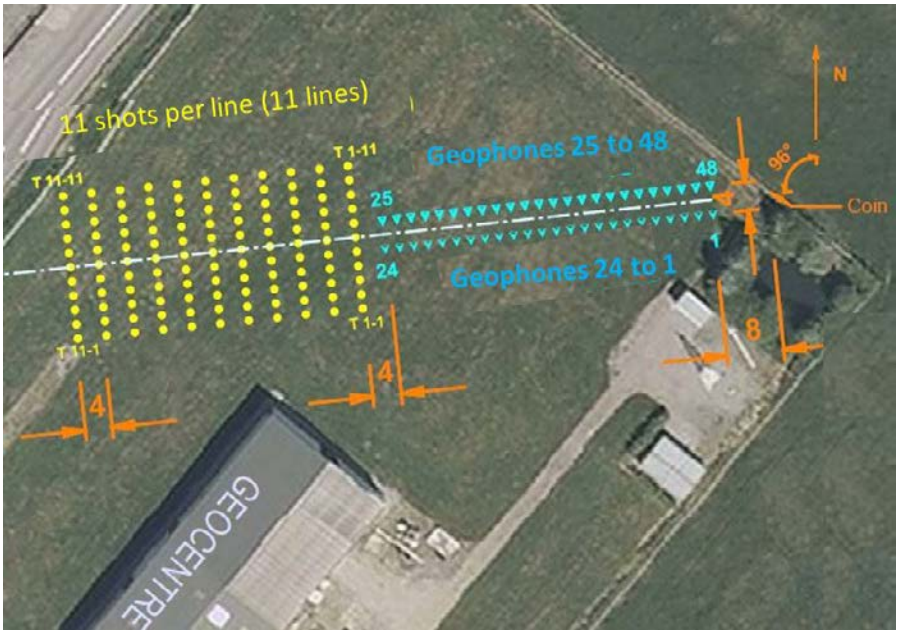

Figure 4.13 *3D Seismic spread.*

Due to the geometry of acquisition, the geometric fold was symmetric. Figure 4.14 shows the fold variation, which varied from 0 to 22.

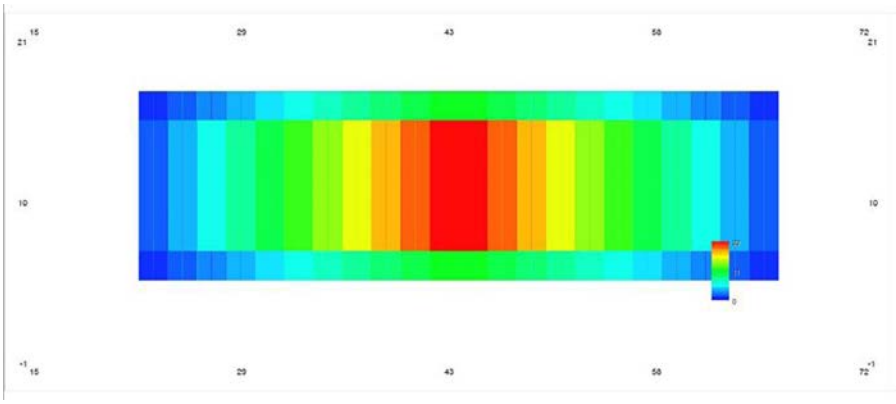

Figure 4.14 *Fold variation. Variation was from 0 to 22. The horizontal axis in the figure is the in-line direction. The vertical axis is the cross-line direction.*

The processing was carried out with the SPW software developed by Parallel Geoscience (Mari and Herold, 2015). The listening time was limited to 250 ms, the sampling time interval was 0.5 ms. Figure 4.15 shows a shot point example.

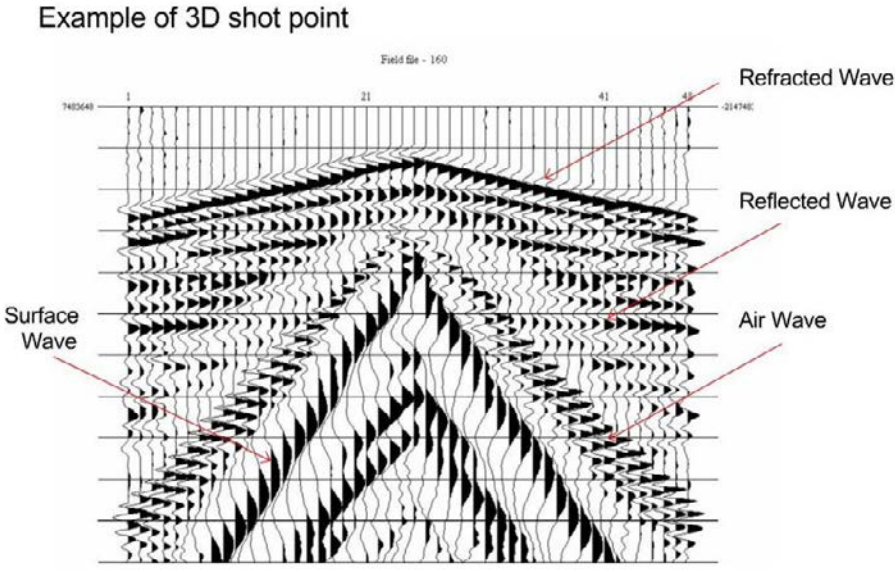

Figure 4.15 *Example of a 3D shot point. It is possible to identify the refracted wave, reflected wave, air wave and surface wave. The air wave is aliased.*

The processing sequence of each shot includes: amplitude recovery, deconvolution in the 15-150 Hz frequency bandwidth, tail mute, and static corrections (Figure 4.16). The deconvolution was carried out to increase the resolution and attenuate the surface waves. A tail mute was used to eliminate air waves and surface waves. The static corrections were performed to compensate the effects of the weathering zone. In the example, the 3D static corrections are very weak.

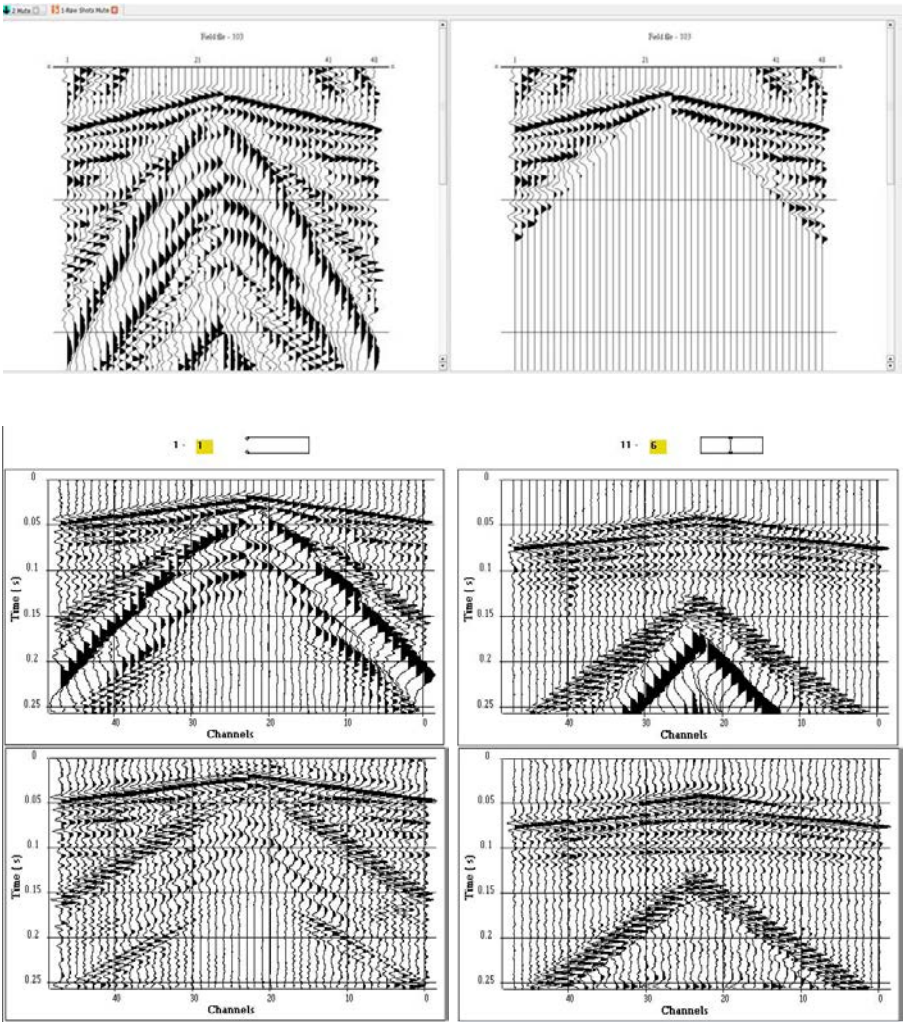

Figure 4.16 *Some processing steps. Top: example of a raw shot before and after tail mute; bottom: example of 3D shot point before and after deconvolution; left: near offset 3D shot point. The shot point is shot number 1 on line 1; right: far offset 3D shot point. The shot point is shot number 6 on line 11. A reflected event is clearly visible at 100 ms, after deconvolution.*

The data were sorted in common midpoint (CMP) gathers. NMO corrections were carried out with a stacking velocity model obtained by velocity analysis. Surface consistent residual statics were calculated to enhance the signal to noise ratio and preserve the high resolution of the data in the CMP stack procedure.

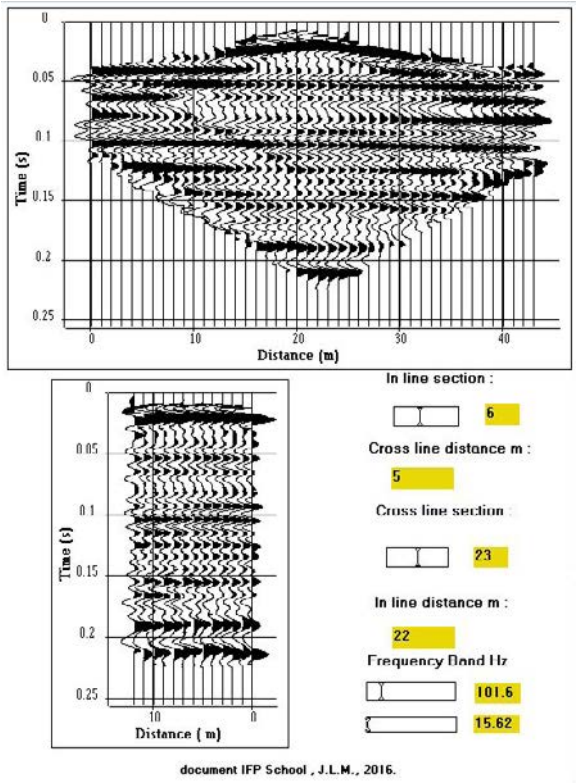

Figure 4.17 *CMP stacked sections. The high-resolution 3D cube revealed near-surface seismic horizons between 50 and 200 ms.*

The 3D block is composed of 13 in-line sections 1 m apart. Each section is composed of 44 CMP points 1 m apart. Figure 4.17 shows an example of in-line and cross-line seismic sections extracted from the 3D block. The two sections presented (section 6 in the in-line direction, and section 23 in the cross-line direction) intersect in the middle of the 3D block. They have been filtered in the 15-150 Hz bandwidth, which provides an excellent signal-to-noise ratio. The CMP point located at the intersection of the in-line seismic section No. 3 and cross-line No. 6 is located about twenty meters from a borehole in which a vertical seismic profile (VSP) was recorded. The VSP (Figure 4.18, top) was used to obtain an interval velocity model and a time versus depth law, which was used to perform the time to depth conversion of the 3D block (Figure 4.18, bottom).

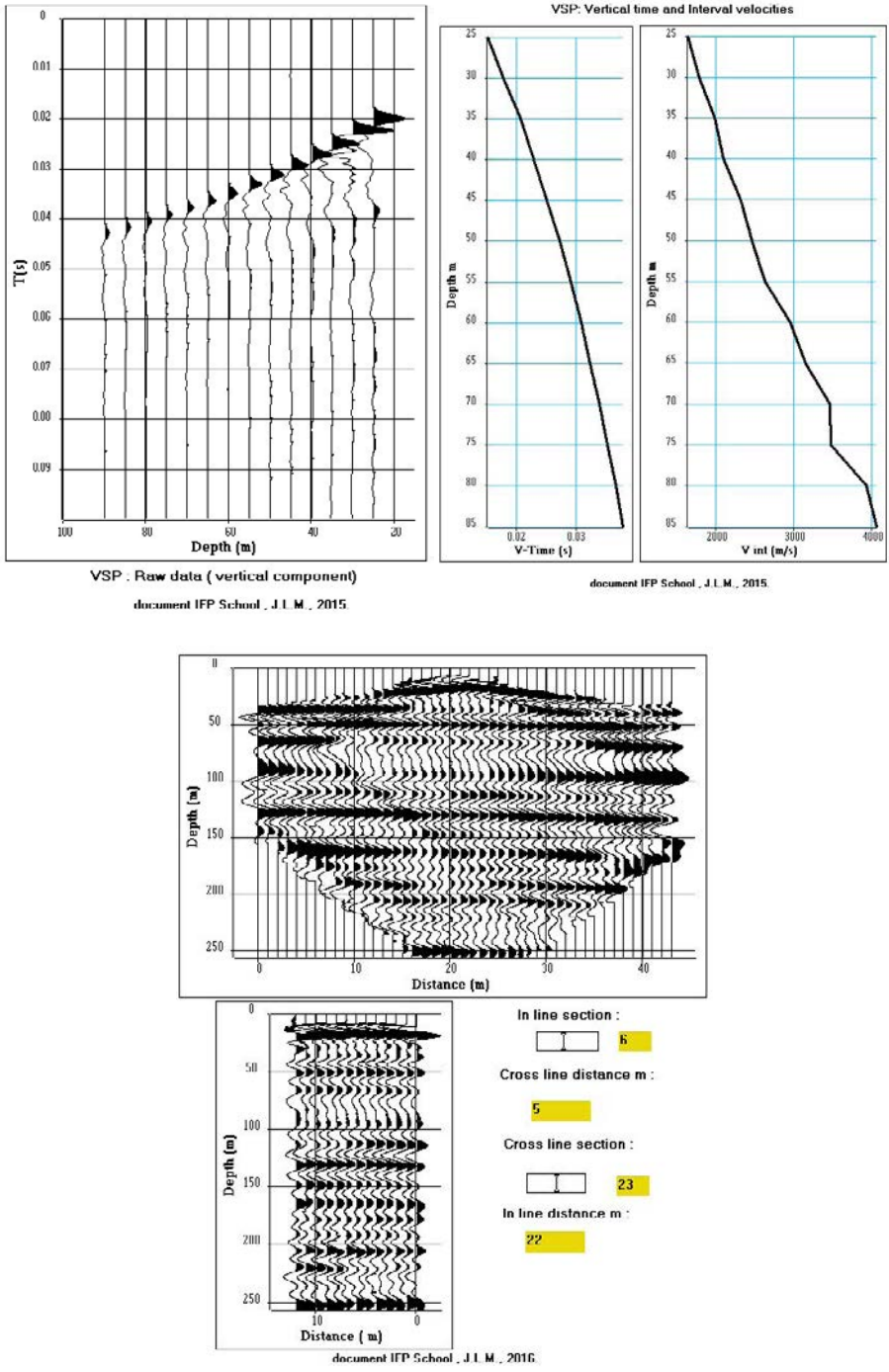

Figure 4.18 *VSP and 3D block in depth. Top: Raw VSP and VSP logs (vertical time and interval velocities); bottom: 3D block in depth.*

4.4 A Hydrogeology example

This example concerns the imaging of a near-surface karstic reservoir at the Hydrogeological Experimental Site of Poitiers. The field case has already been discussed in the "Refraction surveying" chapter.

Preliminary studies led to the selection of the following spreads for 3D imaging. The detonating impulse source was selected to record high frequency data and to reduce the air wave effect. To preserve the high frequency content of the data and to have an accurate picking of the refracted wave, a single geophone per trace was used.

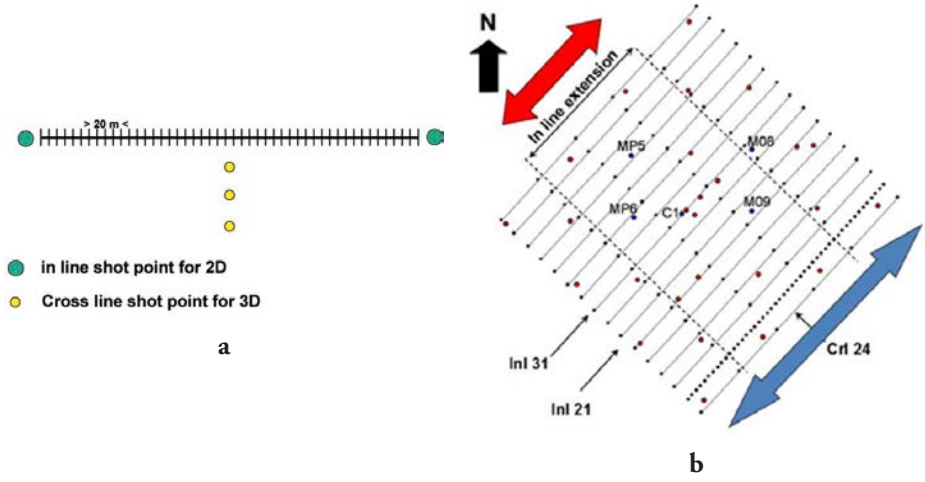

Figure 4.19 *Seismic spreads and field implementation of seismic lines. (a) Seismic spreads - A direct shot and reverse shot are fired in line to obtain 2D seismic images. Several cross-line shots are fired to obtain 3D seismic images. (b) Seismic line implementation: the distance between 2 adjacent lines is 15 m. Red points indicate well locations.*

To avoid spatial aliasing, a 5 m distance between two adjacent geophones was selected. Due to the dimensions of the area, it was not possible to extend the length of the seismic line over 250 m in the in-line direction. Consequently, a 48-channel recorder was used. In the cross-line direction, the extension of the area did not exceed 300 m. As a result, 21 receiver lines were implemented, with a 15 m distance between adjacent lines. For the refraction survey, a direct shot and a reverse shot were recorded per receiver line. For the reflection survey, 3 shot points in the cross-line direction were fired per receiver line. The range of offsets was selected to optimize the quality of the seismic image in the reservoir zone, between 40 and 130 m. The minimum offset distance was chosen as 40 m to reduce the

influence of surface waves. The distance between 2 adjacent shot points in the cross-line direction was chosen to be 10 m. Figure 4.19 shows the selected seismic spreads and the map locating the seismic lines. The red points indicate the location of the wells.

The processing sequence has been described in detail in several publications (Mari and Porel, 2007; and Mari and Delay, 2011), so it is only briefly explained here. Each shot point was processed independently (both in the cross-line direction and in the in-line direction) to obtain a single-fold section with a sampling interval of 2.5 m (half the distance between 2 adjacent geophones) in the in-line direction. The processing of an in-line direct and reverse shot gather enabled a single-fold section with an in-line extension of 240 m to be obtained (indicated by a blue arrow on the seismic line map, Figure 4.19-b) while a cross-line shot gather has provided a single-fold section with an in-line extension of 120 m (indicated by a red arrow on the seismic lines map, Figure 4.19-b).

A 3D seismic refraction tomography (Mari and Mendes, 2012, see also the "Refraction Surveying" chapter) was carried out to map the irregular shape of the top of the karstic reservoir, and to obtain static corrections and a velocity model of the overburden. To add information to the inversion procedure, we used in-line and cross-line cross shots simultaneously, with an offset of 60 m. The shots were selected to ensure that the refracted wave was the first arrival wave, regardless of the source-receiver distance. The picked times of the first seismic arrivals for all shots (in-line and cross-lines shots), the depth map of the top of the reservoir (defined from the wells), and the velocity model obtained by the Plus–Minus method were used as input data for the inversion procedure (see "Refraction surveying" chapter). The inversion results obtained with 3D data emphasize the previously mentioned geological structures, providing a better understanding of their alignments and shape (corridor of fractures). Furthermore, no cavities were detected near the surface.

The processing sequence includes: amplitude recovery, deconvolution, wave separation (SVD method for extracting refracted waves and combining the SVD and F-K methods for filtering surface waves), static corrections (obtained by inversion tomography) and NMO corrections. A VSP was recorded in well C1. VSP data were processed to obtain a time versus depth relationship and a velocity model. The velocity model was used to apply the NMO corrections. The VSP time versus depth law was also used to convert the time sections into depth sections with a 0.5 m depth sampling interval.

For illustration, the elementary cross-spread corresponding to geophone line 11 with a 60 m lateral source offset is shown in Figure 4.20.

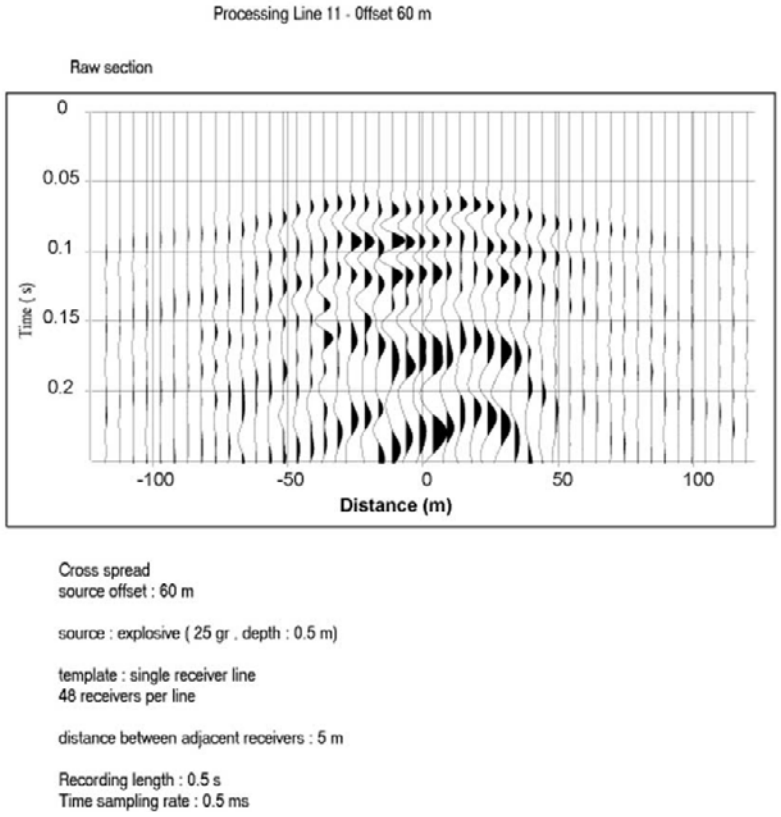

Figure 4.20 *Example of an elementary cross-spread.*

Figures 4.21 and 4.22 show the first steps of the processing of the cross spread recorded on line 11 with a 60 m source offset. After amplitude recovery (Figure 4.21, top left) and deconvolution (Figure 4.21, bottom left), the wave separation procedure is applied as follows:

- Extraction of the refracted wave by SVD filter (Figure 4.21, top right).
- Subtraction of the refracted wave from the initial section to obtain the first residual section (Figure 4.21, bottom right). The residual section shows mainly surface waves with low apparent velocities.
- Extraction of the low apparent velocity events by F-K filter (Figure 4.22, top left).
- Subtraction of the low apparent velocity events from the first residual section to obtain the second residual section (Figure 4.22, bottom left).

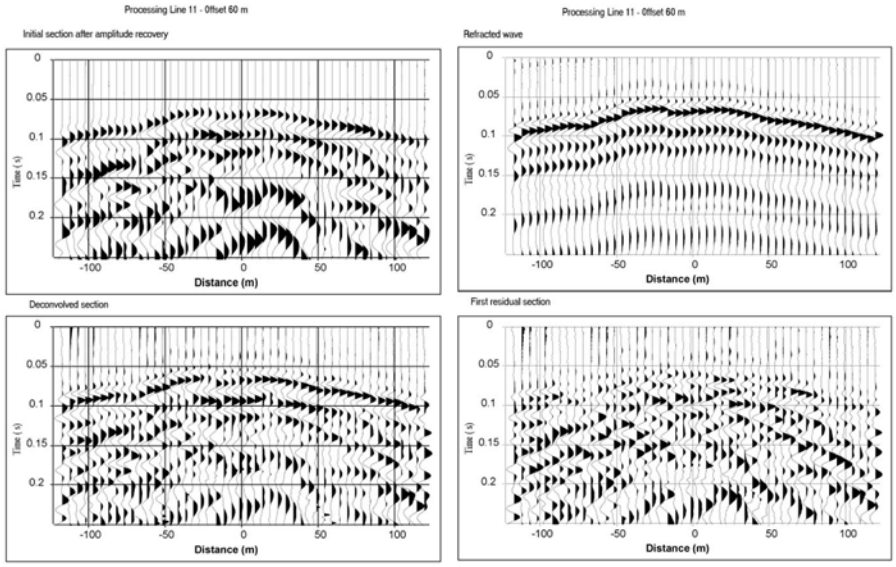

Figure 4.21 *Processing of geophone line 11 with a 60 m source offset; top left: amplitude recovery, bottom left: deconvolution, top right: refracted wave, bottom right: first residual section.*

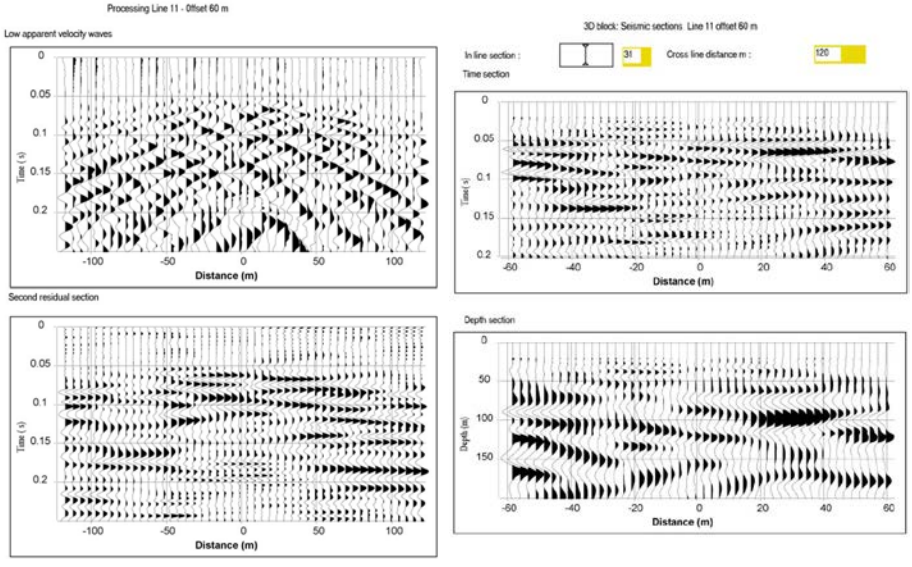

Figure 4.22 *Processing of geophone line 11 with a 60 m source offset; top left: low apparent velocity waves, bottom left: second residual section, top right: time section, bottom right: depth section.*

The second residual section shows high apparent velocity seismic events with a poor lateral continuity. This could be reflected or diffracted waves corrupted by residual noise. The velocity model was used to apply the NMO correction to the residual section to obtain a zero-offset section at normal incidence.

The same processing sequence was applied to the 60 individual shot points to obtain 60 zero offset sections. The 60 sections were merged to create the 3D block. The width of the block in the in-line direction is 120 m. The abscissa zero indicates the location of the source line. The abscissa of the reflecting points varies between –60 m and +60 m in the in-line direction; the distance between two reflecting points is 2.5 m. Due to the geometry of acquisition, the shot point recorded on geophone line 11 with a 60 m source offset becomes the in-line section 31 (Figure 4.22, top right). The VSP time versus depth law measured at well C1 was used to convert the time sections into depth sections with a 0.5 depth sampling interval. The depth conversion of time section 31 is presented in Figure 4.22 (bottom right). In the 30 to 120 m depth interval, it can be noted that the vertical seismic resolution is insufficient to describe the heterogeneities inside the reservoir. The only way to increase the vertical resolution is to apply a deconvolution of the wave number to the depth sections. The result for depth section 31 is presented in Figure 4.23-a (upper part). A significant improvement of the vertical resolution is thus obtained.

After deconvolution, it was assumed that the seismic trace represents the reflectivity function of the geological model. Integration with respect to depth enabled the deconvolved seismic trace to be constrained to obtain an estimate of the interval velocity function versus depth. For this purpose, after deconvolution and integration, a Wiener filter (Mari *et al.*, 2015) was applied to the seismic traces to convert the amplitude sections into velocity. The Wiener filter is designed to obtain an optimum fit between the acoustic velocity log at well C1 and the associated deconvolved and integrated seismic trace (Figure 4.23-b). The Wiener operator thus obtained was applied to all the deconvolved and integrated traces of the 3D block to transform an amplitude block into a 3D pseudo velocity block in depth. The result obtained with the in-line depth section 31 is shown in Figure 4.23-a (bottom). The procedure was validated by measuring correlation coefficients between estimated seismic pseudo velocity logs and acoustic logs at wells MP6, MP5, M8 and M9 (Figure 4.19-b).

The 2D direct and reverse shots were processed in the same way to laterally extend the 3D block. All pseudo-velocity depth sections were merged to create the 3D block. The width of the block in the in-line direction is 240 m, and 300 m in the cross-line direction.

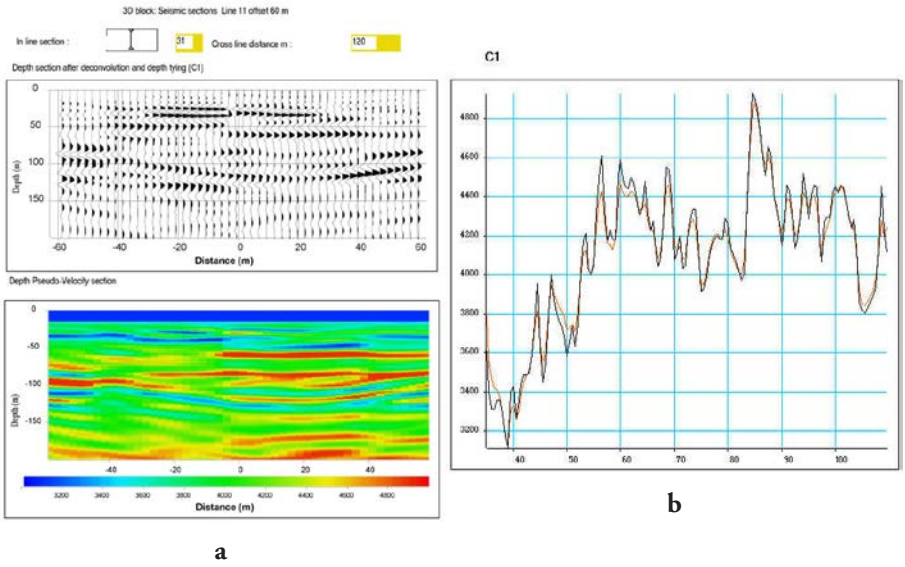

Figure 4.23 *Example of deconvolved and pseudo velocity depth sections (in-line section 31). (a) Depth section after deconvolution and depth tying (top). Depth pseudo velocity section (bottom). (b) Velocity functions at well C1: velocity function derived from acoustic measurement (black curve), velocity function derived from seismic trace (red curve).*

In the in-line direction, the abscissa zero indicates the location of the source line. The abscissa of the reflecting points varies between –120 m and 120 m in the in-line direction. The distance between two reflecting points is 2.5 m. In the cross-line direction, the distance between two reflecting points is 5 m.

The pseudo velocity sections of the 3D block thus obtained were merged with those obtained by refraction tomography (see "Refraction surveying" chapter) to create a 3D extended velocity model from the surface (Figure 4.24). Figure 4.24 (top left) shows the results obtained for the in-line 31 seismic section extracted from the 3D extended velocity model. It also shows the velocity map at a depth of 87 m (Figure 4.24, top right). The 3D velocity model shows the large heterogeneity of the aquifer reservoir in the horizontal and vertical planes. To quantify the porosity variations within this aquifer, the seismic interval velocities were first converted into resistivity values. For this purpose, the empirical relationship between seismic velocity and resistivity proposed by Faust (1953) was used. Resistivity values were then converted into porosity values, using Archie's law (1942). Figure 4.24 (bottom) shows the pseudo velocity and porosity seismic sections for the in-line 21 and cross-line 24.

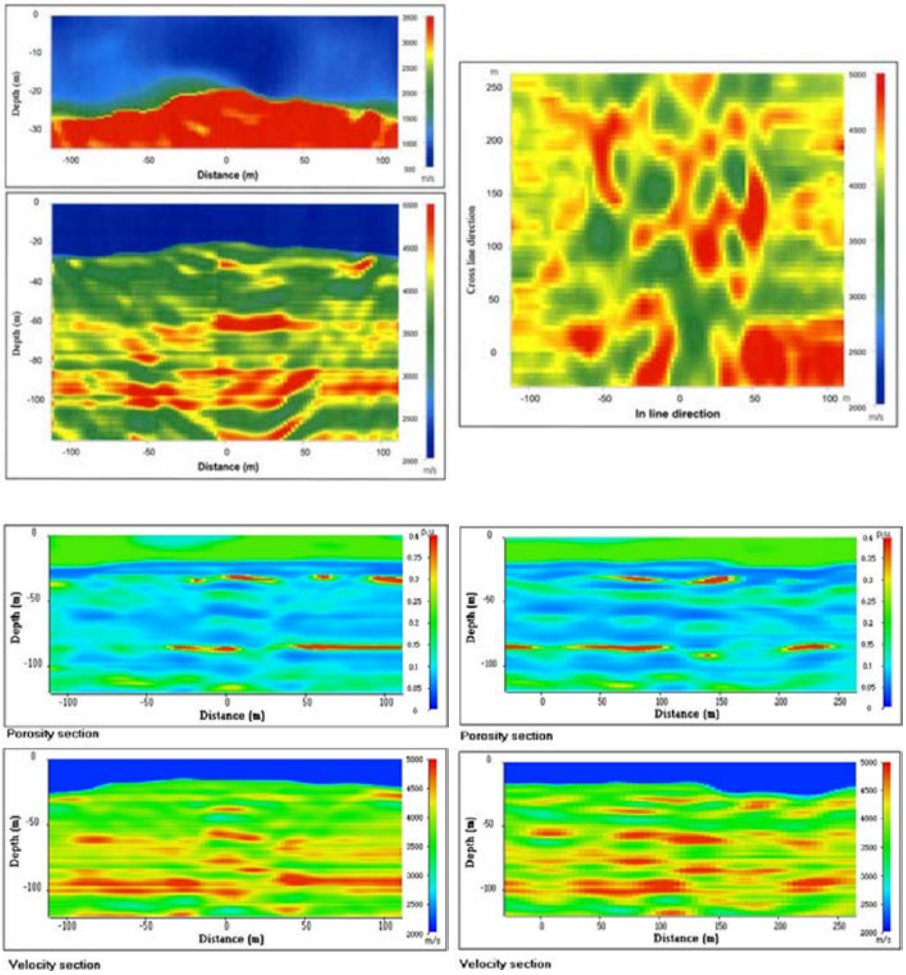

Figure 4.24 *3D seismic processing. Top left: in-line 31 pseudo-velocity section (upper part: close up of 0 to 35 m depth interval). Top right: pseudo-velocity map at 87 m depth. Bottom left: in-line 21 pseudo-velocity and porosity seismic sections. Bottom right: cross-line 24 pseudo-velocity and porosity seismic sections.*

The resulting 3D seismic pseudo-porosity block revealed three high-porosity layers, at depths of 35 to 40 m, 85 to 87 m and 110 to 115 m. The 85 to 87 m layer is the most porous, with porosities higher than 30 %, which represents the karstic part of the reservoir. Figure 4.25 shows the distributions of porous bodies in the 80 to 90 m and 100 to 120 m depth intervals.

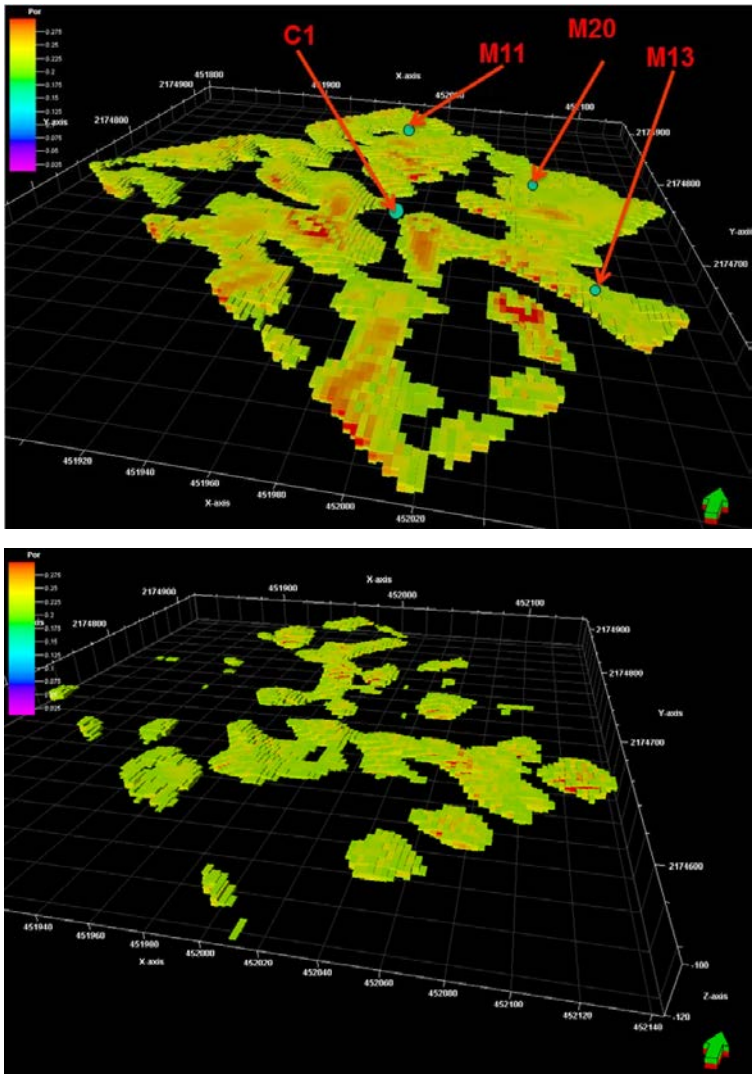

Figure 4.25 *Distribution of karstic bodies. Top: the 80 to 90 m depth interval. Bottom: the 100 to 120 m depth interval.*

The 3D block is composed of elementary cells (2.5 m in the in-line direction, 5 m in the cross-line direction, and 1 m deep), which clearly show the connectivity of the karstic bodies. The local validation of the results obtained by the 3D seismic method was achieved using full waveform acoustic data and VSP, recorded in 11 wells in 2014 and 2015 respectively (Mari and Porel, 2018).

4.5 Conclusion

Seismic reflection technology has been developed for the oil industry. The 3D seismic spread designs require the use of telemetric recording systems. Processing sequences enable high-resolution 3D seismic blocks to be obtained, due to sophisticated algorithms (3D prestack depth migration, full waveform inversion…) that are implemented on high performance computers.

In this chapter we have shown that it is possible to obtain very high-resolution 3D blocks for near surface applications with very basic seismic spreads (48 channels recorders, a single geophone per trace, light seismic source). Near surface studies require specific test phases to define the optimum acquisition parameters (minimum offset, geophone interval). The processing sequence must be carefully adjusted to the field data, especially for the wave separation.

In the near-surface karstic reservoir imaging example (Hydrogeological Experimental Site of Poitiers), we have shown that the velocity distribution obtained by refraction tomography in the first 30m can be merged with the velocities extracted from the amplitude of the reflected events, to obtain a continuous velocity model from the surface up to a depth of 120 m.

The spread, designed for near-surface reflection surveying, can be used for refraction surveying and surface wave analysis. The results obtained using the different methods can be productively combined, which is explored further in the "Hybrid seismic methods" chapter.

References

Anstey N., 1986, Part 1: Whatever happened to ground roll? *The Leading Edge*, 5, 40-45, DOI:10.1190/1.1439239.

Archie G.E., 1942, The electrical resistivity log as an aid in determining some reservoir characteristics, *Petroleum Technology*, 146, 54-62.

Chaouch A., Mari J.L., 2006, 3D land seismic surveys: Definition of Geophysical parameters, Oil & Gas Science and Technology, *Rev. IFP.,* 61 (5), 611-630, DOI: 10.2516/ogst:2006002.

Cordsen A., Galbraith M., Peirce J., 2000, Planning land 3D seismic surveys – SEG Series No. 9, Bob A. Hardage Ed.

Faust, L.Y., 1953, A velocity function including lithologic variation, *Geophysics*, 18, 271-288.

Galbraith M., 2000, 3D seismic survey design: a solution, *First break*, 18 (5), 171-176.

Lansley M., 2000, 3D seismic survey design: a solution, *First break*, 18 (5), 162-166.

Mari J.L., Glangeaud F., Coppens F., 1997, *Signal processing for geologists and geophysicists*, Technip Ed., Paris, ISBN: 2-7108-0752-1

Mari J.L., Porel, G., 2007, 3D seismic imaging of a near-surface heterogeneous aquifer: a case study, *Oil and Gas Science and Technology, Rev IFP* 63, 179-201. DOI: 10.2516/ogst/2007077.

Mari J.L., Delay F., 2011, "Contribution of Seismic and acoustic methods to reservoir model building", in *Hydraulic Conductivity / Book 1*, InTech-Open Access Publisher, ISBN 978-953-307-288-3, DOI: 10.5772/22051.

Mari J.L., Mendes M., 2012, High resolution near surface imaging of fracture corridors and cavities by combining Plus-Minus method and refraction tomography, *Near Surface Geophysics*, 10, 185-195, DOI: 10.3997/1873-0604.201 1052.

Mari J.L., 2015, Signal processing for geologists & geophysicists, e-book, DOI:10.2516/ifpen/2011002. http://books.ifpenergiesnouvelles.fr/ebooks/signal-processing/

Mari J.L., Porel G., 2018, Contribution of seismic and acoustic methods to the characterization of karstic formation, in Mari J.L., Vergniault C., 2018, *Well seismic surveying and acoustic logging*, EDP Sciences, ISBN (e-book): 7598-2263-8, DOI: 10.10051/978-2-7598-2263-8, https://www.edp-open.org/well-seismic-surveying-and-acoustic-logging

Mayne W.H., 1962, Common reflection point horizontal data stacking techniques, *Geophysics*, 27, 927-938, doi: 10.1190/1.1439118

Meunier J., 1998, Land 3D acquisition geometry: what is the cost of ground roll?, 68th annual international meeting, SEG, expanded abstracts, 58-61.

Meunier J., 1999, 3D geometry, velocity filtering and scattered noise, 69th annual international meeting, SEG, expanded abstracts, 1216-1219.

Meunier J., Gillot E., 2000, 3D seismic survey design: a solution, *First break*, 18 (5), 176-179.

Meunier J., 2011, Seismic acquisition from Yesterday to Tomorrow, distinguished instructor series, N° 14, SEG, ISBN 978-1-56080-281-5 (volume), ISBN 978-1-56080-086-06 (series)

Monk D., Yates M., 2000, 3D seismic survey design: a solution, *First break*, 18 (5), 180-183.

Musser J.A., 2000, 3D seismic survey design: a solution, *First break*, 18 (5), 166-171.

Robein E., 2003, *Velocities, Time-imaging and depth imaging, in Reflection seismics, Principles and methods*, EAGE Publications bv, ISBN 90-73781-28-0.

Vermeer G.J.O., Hornman K., 2000, Introduction to a 3D design problem, *First break*, 18 (5), 184-185.

Yilmaz O., 1987, Seismic data processing, SEG, Tulsa.

5

Full waveform inversion

H. Chauris

5.1 Overview

Full Waveform Inversion (FWI) is a processing technique to derive quantitative images of the subsurface from seismic measurements. By quantitative, we mean for example P-wave velocity models expressed in m/s, and not only a structural image of the Earth as a classical stack section would provide. The principle is simple: the optimal model is the one for which the computed shot gathers are reproducing the observed shot data. More details on the formulation are provided in section 5.3. Beyond the apparent simplicity, the practical applicability of FWI is a difficult task. This is a non-linear process; the user should provide an initial model; the quality of the final inverted model depends on the reliability of the low frequency content of the observed data. A proper strategy should be established to iteratively determine the model (typically by successively introducing higher frequencies). One also needs to use the adequate wave equation to generate synthetic wave fields and associated

DOI: 10.1051/978-2-7598-2351-2.c007

shot gathers in order to mimic the physics of wave propagation. Finally, due to the limited data frequency band and limited data acquisition from the surface only, FWI does not necessarily lead to a unique solution. For example, if the user is interested in determining P-velocity and density models, there is an intrinsic trade-off between the two quantities, especially for short offset data. This is not specific to FWI: other imaging techniques suffer from the same effect, but this is visible in the FWI context as FWI is expected to provide quantitative results. A large number of FWI results have been published on real data in seismology, as well as at the exploration scales, at least in the marine case. The use of the technique on land with onshore data, however, has only been proven for a limited number of applications due to the presence of strongly energetic surface waves. While at the geotechnical scale, it has only been tried on a few occasions (among others, Gao *et al.*, 2007; Gélis, 2005; Pérez Solano *et al.*, 2014).

The chapter is organised as follows. We first give a brief overview of the history of Full Waveform Inversion (section 5.2). We then introduce the formalism, limiting the number of equations to the most important ones. We discuss the potential impact as well as the limitations of FWI. This is an important section for anyone who would like to evaluate the potential of FWI on a particular dataset (section 5.4). Finally, we present a few illustrations at the geotechnical scale. For an overview of FWI at the seismological and exploration scales, we refer to Virieux and Operto (2010), and to Fischtner (2010) as well as to three recent didactic papers (Louboutin *et al.*, 2017; Louboutin *et al.*, 2018; Witte *et al.*, 2018).

There are two main elements to consider before applying FWI: the first important aspect is that Full Waveform Inversion considers the *full* wave field (e.g. pressure field or vertical displacement at the receiver position), and does not decompose the data in terms of travel times and amplitude (more details in 5.3). The other important aspect is that FWI can provide high-resolution quantitative results if there is a correct understanding of the main phenomena influencing the wave propagation as well as a proper strategy to iteratively converge towards a meaningful solution. For these reasons, FWI is not an automatic process and is applied after more standard processing such as travel time tomography (Bishop *et al.*, 1985).

5.2 History

This section mainly refers to the exploration scale (imaging of the first few kilometres of the subsurface). It is perhaps surprising that the formalism was not derived until the 1980s, through the work of Tarantola and his group in particular (Tarantola, 1984; Mora, 1987). Imaging is an inverse problem: one seeks a model such that the differences between the modelled (computed) data and the observed data are minimum in the least-squares sense. This is a very standard technique in many physical fields. On the geophysical side, the new aspect discovered in the 1980s was a method to update the model, i.e. how to compute the gradient of the misfit

objective function. Similar expressions existed before, for example proposed by Claerbout (1968) but not necessarily leading to quantitative results. The definitions of the objective function and the associated gradient are detailed in section 5.3. In practice, the applications were limited to small size 2D datasets due to limited computer capabilities (more details on this aspect in section 5.4, "memory and CPU requirements").

New perspectives appeared around 2000, not only because computers were more powerful, but also because Sirgue and Pratt (2004), among others, proposed a practical strategy for the applicability of FWI. This strategy is further discussed in section 5.4 ("how to avoid local minima"). The main idea is to start from low frequency data. Following a few FWI iterations, the inverted model will contain the large-scale structure. Higher frequencies are then progressively introduced and the model is refined accordingly. The strategy of directly considering the full bandwidth may lead to an incorrect solution: it means that the objective function is multimodal (i.e. contains local minima) due to the non-linearity between the data and the model (more details in section 5.4). Spectacular results were obtained by Pratt and his group, especially on synthetic data for which the observed data contain low enough frequencies to enable the use of the increasing frequency strategy. The 2004 EAGE workshop demonstrated the fundamental role played by the low frequencies during the first iterations, and consequently triggered renewed interest in FWI (Billette and Brandsberg-Dahl, 2005).

Since the early 2000s, FWI has been developed from 2D to 3D, from acoustic to elastic and visco-elastic, as well as in anisotropic contexts, from offshore to onshore datasets. It is clear that the development of computer facilities has supported this trend. FWI remains under development, particularly for multi-parameter estimation (i.e. not only pressure velocity models v_p from body waves, but also shear velocity models v_s from surface waves, as well as anisotropy or attenuation parameters). The difficulty is to extract more than one parameter (Operto *et al.*, 2013). Since the 1980s, the challenge has been to incorporate higher frequencies from the data, initially in 2D and now in 3D, as well as more physics (more details in section 5.4).

5.3 Formalism

For reasons of clarity, we limit the number of equations presented in this section, and aim to give a physical interpretation of the different quantities introduced. The objective of FWI is to minimize the least-squares misfit function

$$J(m) = \frac{1}{2}\|d_{\text{calc}}(m) - d_{\text{obs}}\|^2, \tag{5.1}$$

where $m(\boldsymbol{x})$ is the model to be determined, which is a function of the spatial coordinates $\boldsymbol{x} = (x, y, z)$, $d_{\text{obs}}(\boldsymbol{s}, \boldsymbol{r}, t)$ the observed data at source position $\boldsymbol{s}$, receiver

position $\boldsymbol{r}$ and for time t. The calculated data $d_{\text{calc}}(\boldsymbol{s},\boldsymbol{r},t)$ are a function of the m model and are the solution of the wave equation

$$L(m)\,d(\boldsymbol{s},\boldsymbol{x},t) = \delta(\boldsymbol{s}-\boldsymbol{x})\Omega(t), \tag{5.2}$$

$$d_{\text{calc}}(\boldsymbol{s},\boldsymbol{r},t) = d(\boldsymbol{s},\boldsymbol{x}=\boldsymbol{r},t), \tag{5.3}$$

where L is the wave equation operator, d the wave field, $\Omega(t)$ the seismic source wavelet, and δ the dirac distribution. It means that the wave field d is the solution of the wave equation for a point source located at $\boldsymbol{x}=\boldsymbol{s}$ and for a seismic source wavelet. The calculated data are obtained by sampling the wave field d at the receiver position (Eq. (5.3)). The simplest case corresponds to the constant density acoustic wave equation, with m being the pressure velocity model v_p, yielding

$$L(m) = \frac{1}{v_p^2(\boldsymbol{x})}\frac{\partial^2}{\partial t^2} - \Delta. \tag{5.4}$$

The Laplacian operator Δ is the sum of the second-order derivatives in space. There are thus three elements to evaluate the quality of a given model $m(\boldsymbol{x})$:

- Determination of the source wavelet $\Omega(t)$ (Pratt, 1999);
- Choice of the wave equation operator L;
- Resolution of the forward modelling (equations (5.3) and (5.4)) (Louboutin *et al.*, 2017; Louboutin *et al.*, 2018). In section 5.4, we provide more information on this aspect.

The evaluation of $J(m)$ is a first step, but one usually needs to determine a more suitable model. There are a few recent examples of global search methods (e.g. Sajava *et al.*, 2016). For this strategy, the model space is explored with a Monte Carlo approach or with genetic algorithms. Such an approach would be feasible if the number of model unknowns was small, but this is not typically the case: the model space normally contains millions of unknowns as it is finely discretised along the x, y and z-axis. As discussed in section 5.4, the CPU cost for solving a single equation (5.2) is the main limiting factor for a global approach (Raknes *et al.*, 2017). The only practical approach is to use a gradient-based inversion, where the model is iteratively determined. The requirements for this are:

- an initial model, usually determined by a standard tomographic approach (Bishop *et al.*, 1985);
- computation of the gradient of the objective function (Plessix, 2006).

Formally, the gradient of the objective function is written as the derivative of the objective function with respect to the model parameters. It has the same (large) size as the model space. This is not a trivial task: J depends on m through the dependency on d_{calc}, and the relation between d_{calc} and m is given by the wave equation and is clearly non-linear (Eqs. (5.2–5.4)). As mentioned in the introduction, Lailly (1983) and Tarantola (1984) established an efficient way to compute the gradient, with the "adjoint state method" (Plessix, 2006). This approach is related to the

minimization under constraints, with the introduction of Lagrangian multipliers $\lambda(s,x,t)$. In practice, the derivation of the gradient requires three elements:

- computation of the forward wave field d (Eq. (5.2)) for each source;
- computation of the backward residual wave field λ, also for each source. It is obtained by solving the adjoint wave equation (for the constant density acoustic wave equation, the same wave equation applies) for a source term being the residual wave field at the receiver position $d_{\text{calc}} - d_{\text{obs}}$.
- cross-correlation between d and λ, with a summation over all times, but for fixed spatial x positions.

The final gradient is obtained by adding the contribution of all sources. In practice, the derivation of d and λ are very similar: the gradient thus requires two modelling steps. The CPU cost associated to the cross-correlation is much less than that for solving the forward or backward problem.

Once the gradient is computed, the new model is updated with the typical strategy

$$m_{n+1} = m_n - \alpha \frac{\partial J}{\partial m}, \tag{5.5}$$

where the gradient is $\partial J / \partial m$ and $\alpha > 0$ a scalar step length. More advanced methods such as quasi-Newton or Newton approaches take into account the curvature of the objective function (Hessian) for a faster convergence (Nocedal, 1980).

As mentioned before, the user should provide an estimation of the source wavelet. The most popular strategy is to consider the direct arrival between a source and a receiver (Pratt, 1999). In practice, such determination depends on the unknown velocity model in the shallow part: the source wavelet as well as the model itself are together iteratively determined.

By definition, Full Waveform Inversion considers the *full* wave field (e.g. pressure field or vertical displacement at the receiver position) and does not decompose the data in terms of travel times and amplitude. Travel time is a notion associated to high frequency approximation, also known as geometrical optics. FWI is thus considered as a "wave equation approach", in the sense that it takes into account effects related to finite frequencies, such as the diffraction on a scatter. In practice, FWI can partly select data around certain windows, for example to only include a zone around the direct arrivals or to remove ground roll. This means that equation (5.1) is modified according to

$$J(m) = \frac{1}{2} \| M (d_{\text{calc}}(m) - d_{\text{obs}}) \|^2, \tag{5.6}$$

where M is a mask in the data domain. With the adjoint state approach to derive the gradient, only a minor change is needed in the so-called adjoint source.

In the next section, we illustrate the behaviour of FWI on a 2D synthetic dataset and discuss the impact of several factors, such as the initial velocity model and the role of the frequency content of the data.

5.4 Applicability and practical aspects

Below we provide some practical solutions for a number of key issues that users must address when applying FWI to specific datasets (Virieux and Operto, 2009; Operto *et al.*, 2013; Basker *et al.*, 2016; Raknes *et al.*, 2017).

Model parameterization

Defining the model parameterization, i.e. the quantity FWI should determine, is the first issue to be considered. This may seem curious but is in fact essential in the case of multi-parameter estimation. We considered a practical example here: suppose that the model unknowns are the pressure velocity v_p model and the density model ρ. The P-impedance is the product of the density and velocity ($I_p = \rho v_p$). We compared two strategies:

- In the first case, v_p and density ρ were determined by FWI. Then the impedance was deduced from the product of the final v_p and ρ models;
- In the second case, v_p and I_p were determined by FWI. The density model was determined a posteriori by dividing I_p by v_p.

The two approaches do not lead to the same result, as illustrated by Operto *et al.*, 2013. This should not be surprising because for zero-offset data there is a trade-off between a velocity and density contrast associated to diffraction. With larger offsets, the diffractions have different responses. This means that the algorithm converges to different solutions, all in the null space, depending on the initial model.

Choice of wave equation

Selection of the appropriate wave equation is of course critical. It must be sensitive to the model to be determined. For example, if the attenuation factor is of interest, then the wave equation should contain visco-acoustic or visco-elastic terms. If the analysis of surface waves is important, then acoustic modelling is not sufficient and elasticity should be considered. The determination of a v_p model from marine acoustic data is a subtler example. An acoustic framework would usually be sufficient in this situation, unless the data contain converted waves, even if only the pressure is recorded at the receiver position. For pure acoustic data, is there a need to consider density? The amplitudes of the *transmitted* (diving) arrivals are not sensitive to density, whereas this is the not the case for *reflected* waves. Such questions are still not fully solved.

Time versus frequency

Two main approaches are possible to solve the direct problem (Eq. (5.4)) and the inverse problem: either in the time or the frequency domain (Virieux and Operto, 2009; Raknes *et al.*, 2017). Many scientific papers were published on this topic in the 2010s. From a theoretical point of view, the two approaches lead to the same

results if dense frequencies cover the whole spectrum. The Parseval relationship indeed indicates that

$$J(m) = \frac{1}{2}\| d_{\text{calc}}(m)[t] - d_{\text{obs}}[t]\|^2 = \frac{1}{2}\| d_{\text{calc}}(m)[\omega] - d_{\text{obs}}[\omega]\|^2, \qquad (5.7)$$

where the dependency on ω indicates the Fourier transform from time to angular frequency. We omit the dependency on the source and receiver positions. The result is different if one considers only a small number of discrete frequencies. There is currently some consensus that:

- for many frequencies, the most efficient approach is time implementation.
- for a limited number of frequencies in 3D, the time approach is also preferred, followed by a discrete Fourier transform.
- for a limited number of frequencies in 2D, the frequency approach is more suited, but one has to solve a large (sparse) linear system, for example with a LU decomposition. Once this LU decomposition is performed, the imaging is very efficient.

Beyond the time versus frequency approaches, the most important aspect is to avoid local minima.

FWI = migration + tomography?

This title is a reference to a publication by Mora in 1989. For an adequate application of FWI, it is essential to understand how FWI behaves. In particular, FWI has two main "modes", i.e. different methods of updating the long and short wavelength components of the velocity model:

- The *tomographic* mode means that the long wavelengths of the velocity model are updated, with an influence on the kinematics of wave propagation. In practice, this is the difficult part of FWI as this process is non-linear: if one multiplies the velocity model by 10%, then the data, for example reflected waves, are recorded at a different (shorter) time;
- The *migration* mode indicates that if the data, up to a first-order approximation, linearly depend on the short wavelength components of the velocity model. After linearization, the data only contain reflected waves. If the velocity perturbations are increased by 10%, then the recorded pressure or displacement at the receiver is also multiplied by the same factor.

There is no strict limit between the tomographic and migration modes in FWI, but if multiple frequencies are used for the inversion, the migration will dominate and it will be difficult to update the long wavelengths. The linearized version of FWI is called "iterative least-squares migration" (LSM). Standard migration corresponds to the first iteration only.

Avoiding local minima

A standard FWI application, without careful pre-processing or meticulous parameter selection, would not typically lead to the expected solution. The algorithm may easily converge into a *local* minimum, which is possibly far from the *global* minimum (Bunks *et al.*, 1995). To analyse this, it is useful to refer to the tomographic and migration modes explained in the previous section.

Seismic data are oscillatory signals by nature, as the zero-frequency part is not recorded. The FWI misfit function (Eq. (5.1)) evaluates the least-squares distance between calculated and observed data, both being oscillatory signals. If the initial velocity model provides the correct kinematics, then FWI mainly operates in the migration mode and the events are correctly positioned. If the initial kinematics are not correct, then the algorithm will match incorrect phases between the synthetic and observed data. This is known as the cycle-skipping effect: it means that the algorithm converges in a local minimum (Bunks *et al.*, 1995).

We illustrated this effect using a very simple example, representative of what happens in practice. We considered a single trace. The blue trace corresponds to the observed data (Figure 5.1). An incorrect velocity model has an effect on the kinematic (position) and on the dynamic (amplitude) of the events. We studied here the kinematic effect because of the non-linearity. The red trace is the one in the inverted model (Figure 5.1, top). It does not perfectly match the observed trace because of the presence of noise. We then shifted the red trace to mimic the kinematic effect, for half a period and for a period (Figures 5.1, middle and bottom).

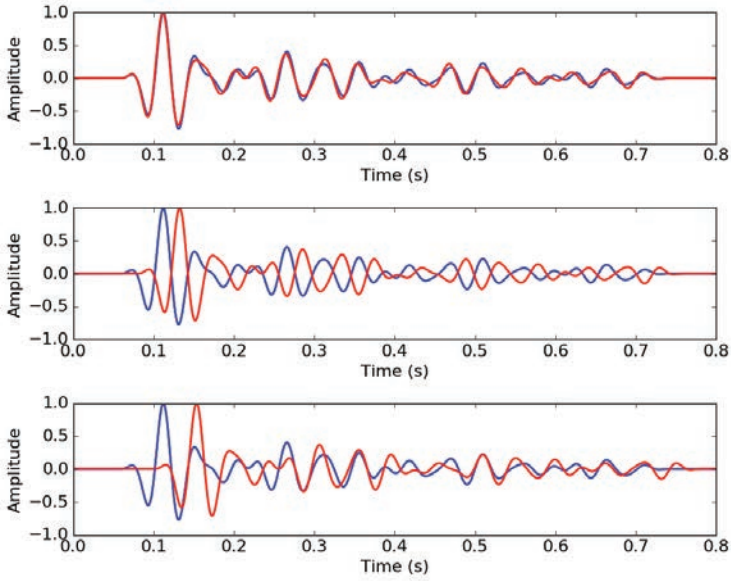

Figure 5.1 *Observed trace (blue) and synthetic trace (red), for different shift values applied to the red trace (from top to bottom: 0, -21 and -42 ms, respectively).*

For each possible shift, we computed the standard least-squares misfit (Eq. (5.1)) between the observed (blue) and synthetic trace (red) (Figure 5.2, blue solid line). The objective function oscillates, with a minimum for zero-shift as expected (blue dot). The shift of half a period corresponds to a local maximum (red dot) as the two signals are out of phase (Figure 5.1, middle), whereas the shift of a period is associated to a local minimum (cyan dot) for which the blue and red traces are mainly in phase. The maximum possible shift to ensure a convergence towards the global minimum (blue dot) is indicated by the red dot. This phenomenon is known as the *cycle-skipping effect*. For the same signals, if the central frequency had been halved, then the shape of the objective function would be within the blue dashed line (Figure 5.2). It means that the basin of attraction is twice as large (Bunks *et al.*, 1995).

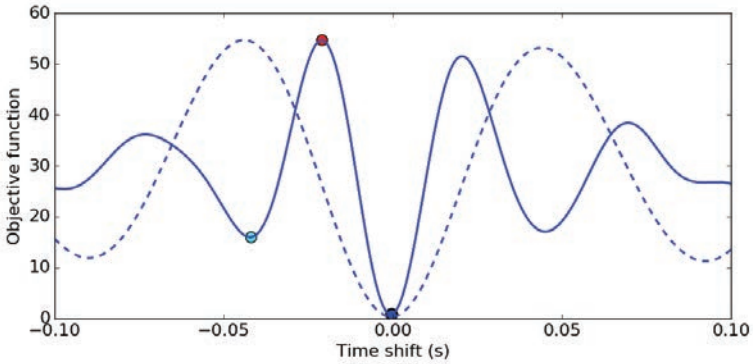

Figure 5.2 *Shape of the objective function for different shift values. The blue, red and cyan dots are associated to the traces in Figure 5.1 (from top to bottom). When the central frequency is divided by two, the objective function has a basin of attraction (dashed line) that is twice as large.*

In conclusion, there are two main strategies to ensure a proper convergence:

- Start with an initial velocity model that is not too far away from the correct solution.
- Use low frequencies at first, then progressively increase the frequency content. Low frequencies have larger basins of attraction than higher frequencies, as illustrated in Figures 5.1 and 5.2. Different authors have proposed practical rules (Sirgue and Pratt, 2004). The current practice is to consider a frequency band $[f_0 - f]$, where f_0 is the minimum reliable frequency and where f increases progressively. The alternative is to let f_0 also increase. Note that for a given frequency band, at least a few non-linear iterations are performed before modifying the frequency range. Then the same process is repeated.

Beyond these two points, the redundancy of the data is an important aspect to constrain the inversion. The *null space* refers to equivalent models associated to the

same misfit value. The reduction of the size of the null space can be achieved by introducing log data or a priori information.

Memory and CPU requirements

FWI is an expensive process, both in terms of memory and CPU requirements. Let's consider a simple case where the forward and backward wave equations are solved with a standard Finite Difference scheme (Virieux, 1986). We applied the constant density acoustic wave equation (Eq. (5.4)). In the simplest case, one first needs to define a regular grid in time and space; the second-order time derivative and Laplacian operator are approximated in 2D by $[+1,-2,+1]/(\Delta t)^2$, $[+1,-2,+1]/(\Delta x)^2$ and $[+1,-2,+1]/(\Delta z)^2$, where Δt, Δx and Δz are the grid increments along the time and space axis. They cannot be chosen arbitrarily and should satisfy the conditions

$$\Delta x = \Delta z \leq \frac{1}{10}\frac{v_{min}}{f_{max}} \tag{5.8}$$

$$\Delta t \leq \frac{1}{\sqrt{\left(\frac{1}{\Delta x}\right)^2 + \left(\frac{1}{\Delta z}\right)^2}}\frac{1}{v_{max}} \tag{5.9}$$

The first equation is the *dispersion* condition: the space discretization should be 10 times smaller than the maximum wavelength v_{min}/f_{max}, obtained for the minimum expected velocity value in the model and for the maximum frequency. This is more restrictive than the Nyquist condition (more than 2 points per wavelength) as this is not a static representation but a dynamic one. If the condition is not satisfied, then numerical dispersion is observed on the signals.

Equation (5.9) is related to the *stability* condition and is a function of the maximum velocity value. If the condition does not hold, the scheme is not stable and does not provide any useful information.

Let's consider an example for a target at 1 km depth, with desired maximum frequencies at 10 Hz and 100 Hz, for typical velocities between 300 m/s to 3000 m/s.

Table 5.1 *2D discretization in space and time for the same extreme velocity values and for two different maximum frequency values, as well as the storage requirement for a single wave field (right column).*

	Δx (m)	Δz (m)	Δt (ms)	Storage (GB)
f_{max} = 10 Hz v_{min} = 300 m/s v_{max} = 3000 m/s	3.0	3.0	0.70	3.2
f_{max} = 100 Hz v_{min} = 300 m/s v_{max} = 3000 m/s	0.3	0.3	0.07	3200

Note that f_{min} does not play a role here. For f_{max} = 100 Hz, the discretization is very fine. Suppose that the image is 1 km deep and 5 km long, with a record up to 1 s. The number of samples can be easily computed. For a simple example, the storage for a single wave field is evaluated in Table 5.1, right column. This is feasible for the 10 Hz case, but not for the 100 Hz. The important aspect is that the storage depends on f_{max}^3 in 2D and f_{max}^4 in 3D (with the introduction of Δy). In practice, the maximum processed frequency is limited because of limited memory and CPU resources.

5.5 Examples

Below we present an example of the capabilities of FWI, as well as its applicability for a 2D synthetic dataset. The choice of synthetic versus real data is driven by the a posteriori control of the results. At the end of the section we discuss the additional difficulties related to real data (Basker *et al.* 2016).

Geophysical context

The synthetic data is inspired from a real data acquisition in the geotechnical context (Deidda and Balia, 2001). It consists of three main parts: an unconsolidated sediment layer with silt and clay in the deeper part, a concrete layer at around 4-5 m depth and a compacted back fill material in the shallow part (Figure 5.3). For the analysis, we use the same synthetic model (with P-wave velocity and density) as presented in Pérez Solano *et al.*, 2014. Despite the apparent relatively simple structure, the difficulty in this model comes from its lateral variations.

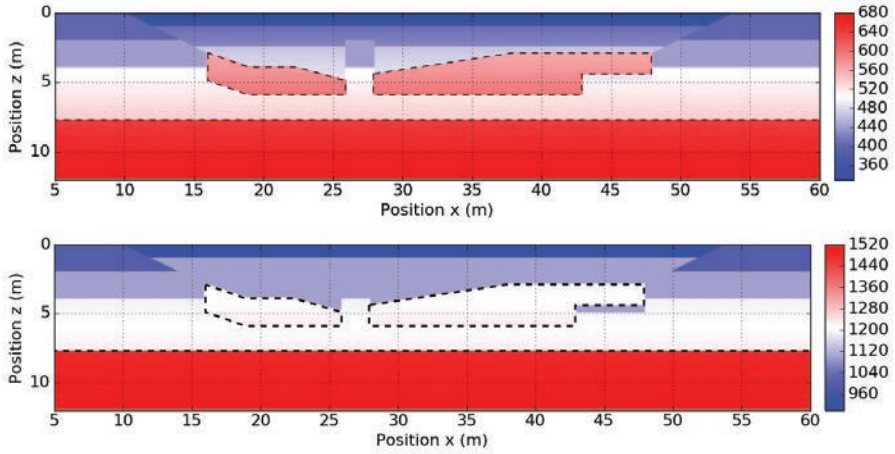

Figure 5.3 *Exact v_p (top, in m/s) and density (bottom, in kg/m^3) models, from (Pérez Solano* et al.*, 2014).*

For simplicity, we have used acoustic modelling. With elasticity, the presence of surface waves largely complicates the imaging strategy (see below in the discussion part) (Brossier *et al.*, 2009). The modelling is based on a staggered grid strategy with a velocity-stress formulation (Virieux, 1986). The particle velocity is converted at the surface into a pressure wave field. The acquisition geometry consists of regular shots every 1 m along the profile and receivers at ±10 m around the source position, knowing that the maximum depth to be investigated is at around 10 m. It means that in this configuration, the interesting information is contained in the reflected waves and not in the transmitted waves for which longer offsets would be needed (see Chapters 2 and 3 on "refraction surface" and "seismic tomography").

Inversion results

For the definition of the initial model (here the v_p and density models), we used a simple gradient model, where the parameters linearly increase with depth (Figure 5.4). This model is consistent with a smooth version of the exact model on the left or right parts, but differs in the central part (Figure 5.3). The only modification brought to this gradient model was the introduction of the shallow layer (first 50 cm) with a dipping interface around x = 12 and 53 m (Figure 5.4).

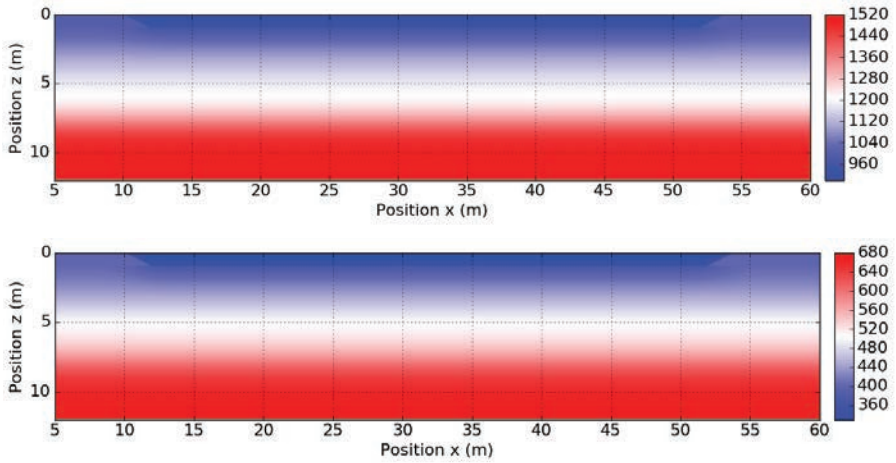

Figure 5.4 *Initial v_p (top, in m/s) and density (bottom, in kg/m^3) models.*

In the first strategy (A), the minimum and maximum data frequencies were 30 and 300 Hz, respectively. All frequencies were inverted simultaneously. Note that the central frequency was about 120 Hz. The non-linear minimization was obtained with a standard quasi-Newton scheme (L-BFGS, (Nocedal, 1980)), for which the last 5 iterations are used to build the inverse of the Hessian to speed up convergence

and more importantly to equalize the contributions with depth (at the first iteration, only the very shallow part is updated). Note that only the P-wave model was updated: the density model remained unchanged, even if the exact density model differs from the initial model (Figures 5.1 and 5.2, bottom). After 30 non-linear iterations, the final model displays some interesting structures, for example around x = 27 m (Figure 5.5). We superimposed the main elements in a dashed black line extracted from the exact model (Figure 5.3). But this final model does not display homogeneous velocities within the cemented structures. The bedrock is not horizontal and its depth is slightly underestimated in the central part. In fact, the FWI algorithm converges to a local minimum as the initial model (Figure 5.4) is too far from the correct one for the frequency range of the data.

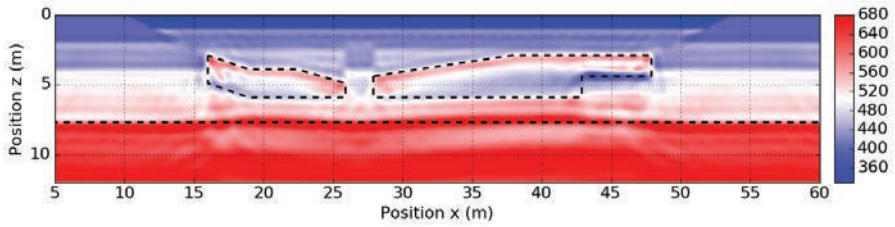

Figure 5.5 *Inverted v_p model (m/s) after 30 iterations, with f_{min} = 30 Hz and f_{max} = 300 Hz. The density model is not updated.*

We thus developed the second strategy (B), consisting of two steps: (1) 15 non-linear inversions with frequencies between 30 and 60 Hz, and then (2) 30 non-linear inversions with frequencies between 30 and 300 Hz as before. The intermediate model after 15 iterations is smooth and contains higher velocities in the cemented structure, even if the limit is not clear (Figure 5.6, top). From that result, we increased the frequency range. The final model (Figure 5.6, bottom) provides a very satisfactory result. The velocity model is much more homogeneous and the main interfaces are correctly positioned. Also, the low (blue) velocity anomaly around x = 45 m and z = 5 m is well retrieved. Note that some oscillations were created to compensate for density contrasts as the density model remains unchanged.

This is clearly visible on vertical sections extracted from the inverted and exact models (Figure 5.7). There is a good agreement between the inverted (blue) and exact (red) velocity models (Figure 5.7, left) and a quantitative match between the impedance models ρv_p (Figure 5.7, right), where v_p is the inverted model and ρ the initial model. For example, for x = 30 m, the velocity jump at 1 m depth is overestimated in v_p and correctly determined in ρv_p. Here, the image mainly comes from the analysis of *reflected* waves; this is why the *impedance* section is preferred compared to the *velocity* section.

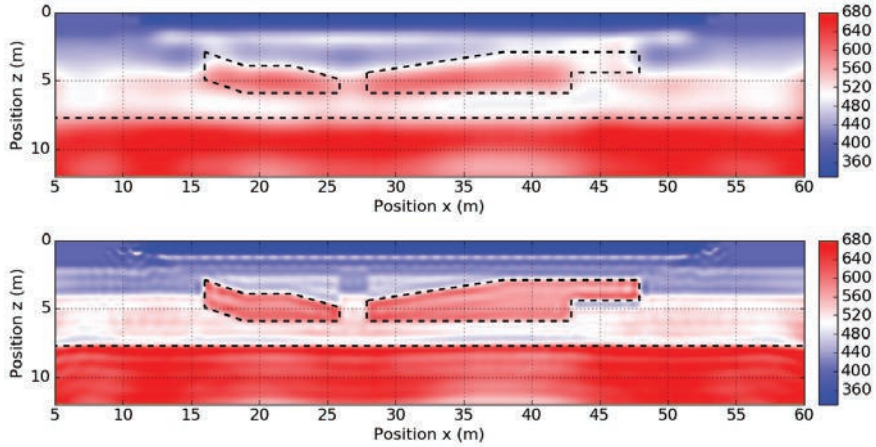

Figure 5.6 *Inverted v_p models (m/s); top: after 15 iterations with f_{min} = 30 Hz and f_{max} = 60 Hz; bottom: after 30 iterations with f_{min} = 30 Hz and f_{max} = 300 Hz, starting from the model on the top. As for Figure 5.5, the density model is not updated.*

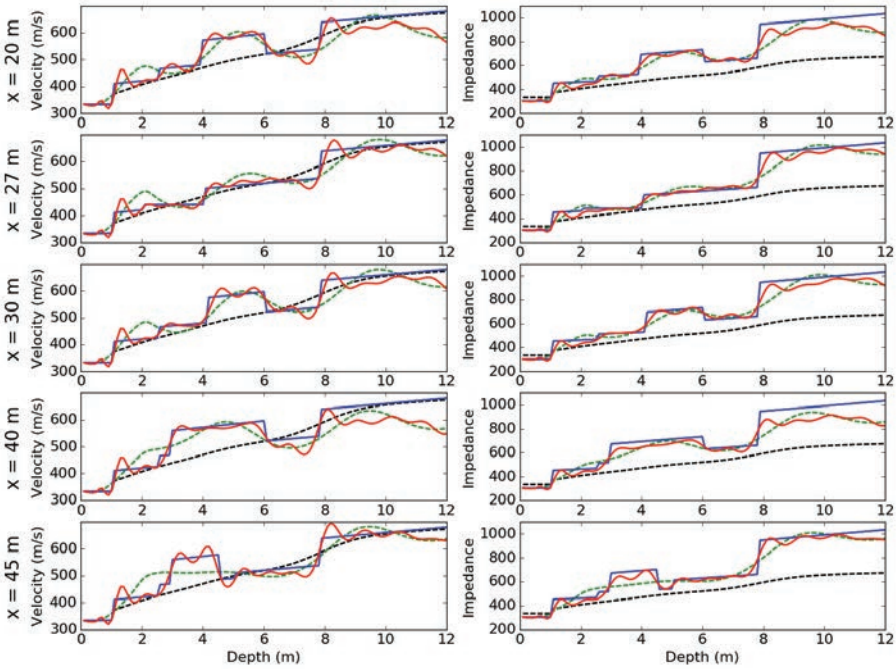

Figure 5.7 *Vertical selections across v_p models (m/s), left, and impedance models ρv_p (in 10^3 kg/s/m^2), right, for x = 20, 27, 30, 40 and 45 m, from top to bottom, respectively. Dashed black line: initial model; dashed green line: intermediate model (Figure 5.6, top); solid red line: inverted model (Figure 5.6, bottom) and solid blue line: exact model. As for Figure 5.5, the density model is not updated.*

The FWI objective function decreases in the two steps (Figure 5.8). Here, we have shown all iterations, even though the L-BFGS algorithm does not consider all of them as real iterations. The reason is that each iteration has the same CPU cost. The objective function is normalized by its maximum value. After the first step (iteration 15), the objective function suddenly increases dramatically, even if the models are the same, simply because the frequency content of the data is modified. Most of the decrease is observed during the first iterations, while the final iterations are still important to retrieve the details in the model.

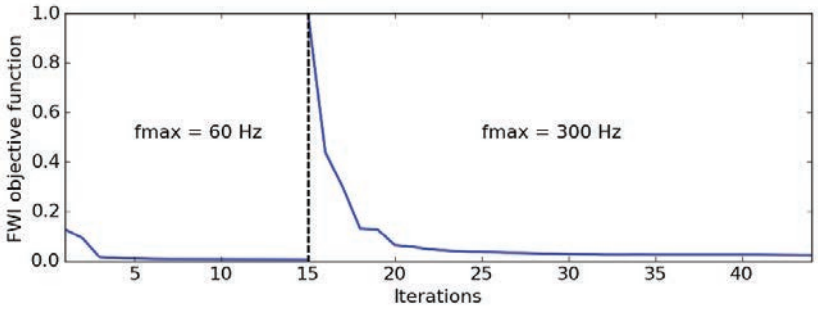

Figure 5.8 *Shape of the FWI objective function (normalised to 1) for the first 15 iterations (with f_{min} = 30 Hz and f_{max} = 60 Hz) and for the subsequent 30 iterations (with f_{min} = 30 Hz and f_{max} = 300 Hz).*

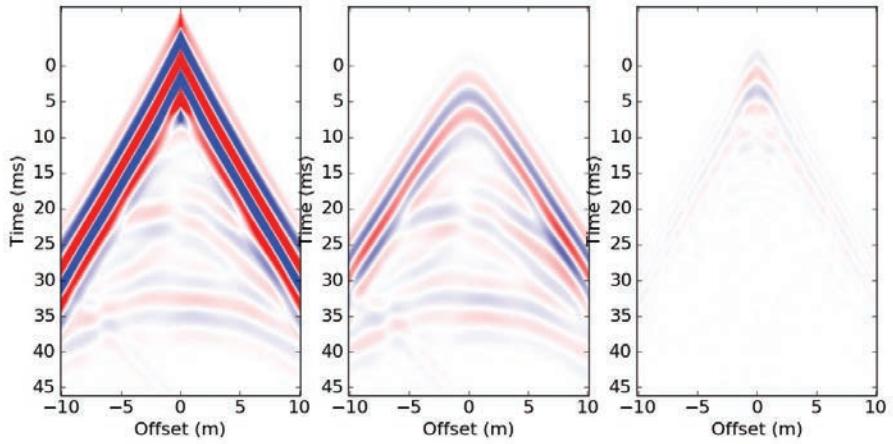

Figure 5.9 *Observed data (left), initial data residuals (middle) and final data residuals (right), all represented at the same scale and for a shot at position x = 32 m. Here the pressure is displayed.*

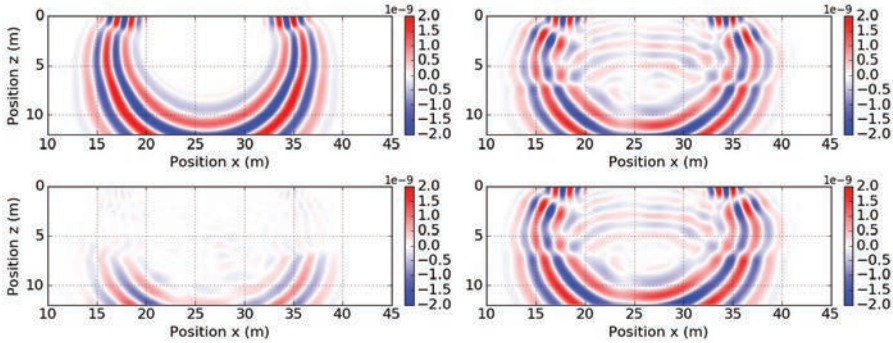

Figure 5.10 *Snapshots (from the same source, the same time and at the same scale); top left: in the initial model (Figure 5.4, top); top right: in the inverted model (Figure 5.6, bottom); bottom right: in the exact model (Figure 5.3, top) and bottom left: differences between the snapshots on the right.*

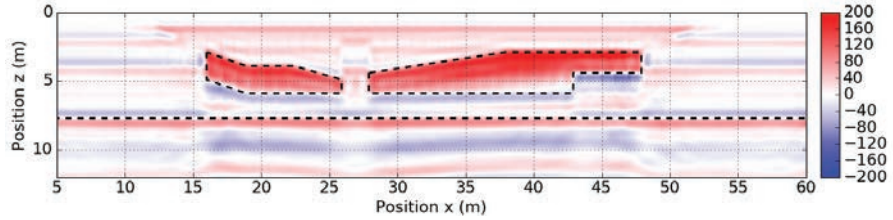

Figure 5.11 *Least-squares migration results (30 iterations), expressed in v_p perturbations (in m/s) and computed in the model from Figure 5.6, top).*

Most of the energy in the shot gather for the shot position at x = 32 m is contained in the first arrival (Figure 5.9, left). As the initial model for the first meter is relatively correct, the initial residuals are related to the first reflection at 1 m depth as well as deeper reflections (Figure 5.9, middle). After inversion, the misfit is largely reduced. Note that in the imaging algorithm, the shallowest part is not updated, indicating that the largest final residuals are associated to the first event (Figure 5.9, right).

It is interesting to analyse the snapshots in the initial, exact and inverted models (Figure 5.10). This is a representation of the wave field for a given propagation time, here t = 22.9 ms. The snapshot for the exact model is not available on real data. After minimization, there is an excellent match between the up-going waves. The down-going waves differ (Figure 5.10, bottom left) as they are not recorded at the surface: the model is not constrained below the deepest reflectors.

Least-squares migration (LSM) is a linearized version of FWI. It only deals with reflected waves and ignores transmitted waves, refracted waves, multiples, etc.

In practice, a pre-processing step should be applied to only select reflected waves from the observed data. We ran LSM in the same initial model as for the second FWI scheme (Figure 5.6, top). Here, the velocity perturbation is updated, not the initial macro-model. It means that the Green's functions are always computed in the same model. They cannot generally be saved in memory as their size depends on the number of sources, the spatial size of the model and the number of time samples. The final result is an oscillatory signal (Figure 5.11), here expressed in terms of velocity perturbations. We used a quantitative LSM approach, but migration algorithms are often qualitative, for a structural interpretation. Here, with the quantitative approach, it is possible to sum the macro-model (initial model, Figure 5.6, top) and the velocity perturbation, yielding a very similar result as the one provided by FWI. The reason for this is that most of the information is contained in the reflected energy, and not in the transmitted waves already explained by the initial model.

Sensitivities

We tested the sensitivity of FWI with respect to the

- acquisition geometry;
- choice of the model parameter to be inverted.

We repeated the same process as in Figure 5.6, except that we selected a source every 5 m, instead of every 1 m. The final FWI is similar (Figure 5.12) and the differences are localized in the shallow part, around 1 to 2 m depth, every 5 m along the *x* axis. These zones with higher (white) velocities are the imprint of the acquisition design: for datasets that are too sparse, the model cannot be properly reconstructed because of aliasing effects (Gray, 2013). These effects would have been even stronger if a mask had not been applied to prevent any updates in the first meter.

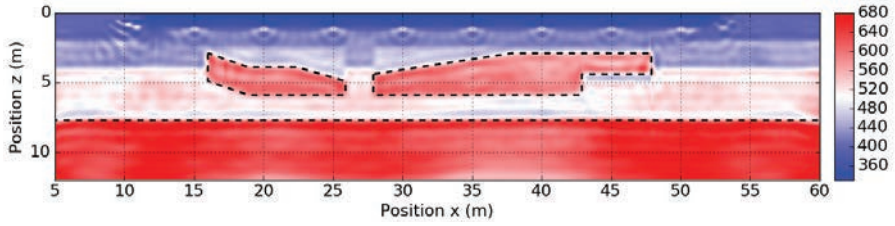

Figure 5.12 *Same as for Figure 5.4, bottom, but for sources every 5 m instead of every 1 m as in all other examples. The differences are mainly visible in the shallow part.*

In the previous example, the velocity was updated, while the density model remained fixed, even if the exact Earth (Figure 5.3) contained both velocity and density variations. We discussed the fact that the best reconstruction was obtained by the impedance (product of velocity by density). Here, we ran FWI for a fixed

velocity (from Figure 5.6, top): only the density model is updated. After 30 non-linear quasi-Newton FWI inversions, the final density model is highly oscillating and tends towards either low or high values (Figure 5.13). The cemented structure cannot be interpreted. As expected, this means that a density model cannot be replaced by a velocity model. Velocity has an influence on the kinematics (event positioning) and dynamics (amplitude) of wave propagation, whereas density only plays a role with regard to amplitude. Thus, a pure density-FWI scheme cannot update an incorrect kinematic part. The objective function did not reach a value as low as before (Figures 5.8 and 5.14). Note that the value of the objective function itself is not very significant; the data residuals should be analysed as in Figure 5.10.

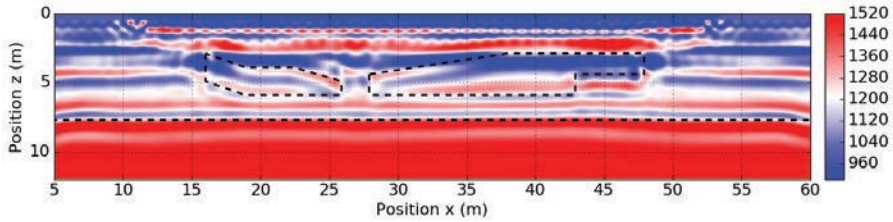

Figure 5.13 *As for Figure 5.6 bottom, except for the density model (in kg/m^3). The velocity model has not been updated (Figure 5.6, top).*

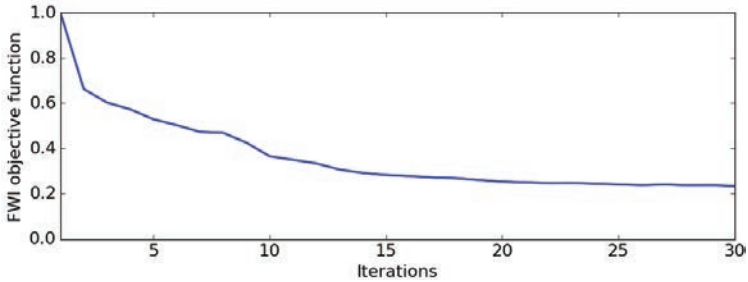

Figure 5.14 *As for Figure 5.8, but where only the density model has been updated.*

Towards applications on real data

Before concluding, we discuss the additional steps required for applications on real data. Most of the published results are related to the marine environment. Water in the shallow part prevents energetic surface waves, which remains a challenging problem for FWI (Brossier *et al.*, 2009).

As FWI is a data misfit approach, the amplitudes play an important role. We discussed the importance of density contrasts in the synthetic example. Diving waves are sensitive to velocities but not to density. This is one of the main reasons why they are

classically used in FWI. In practice, a window is applied around the transmitted waves (direct and diving/refracted) so that only these waves are considered in the FWI, while removing the surface waves and reflected/diffracted waves. This means that large offsets should be recorded. The other reason to consider transmitted waves is that the objective function is more convex than for the reflected waves. This avoids the problem of falling into a local minimum.

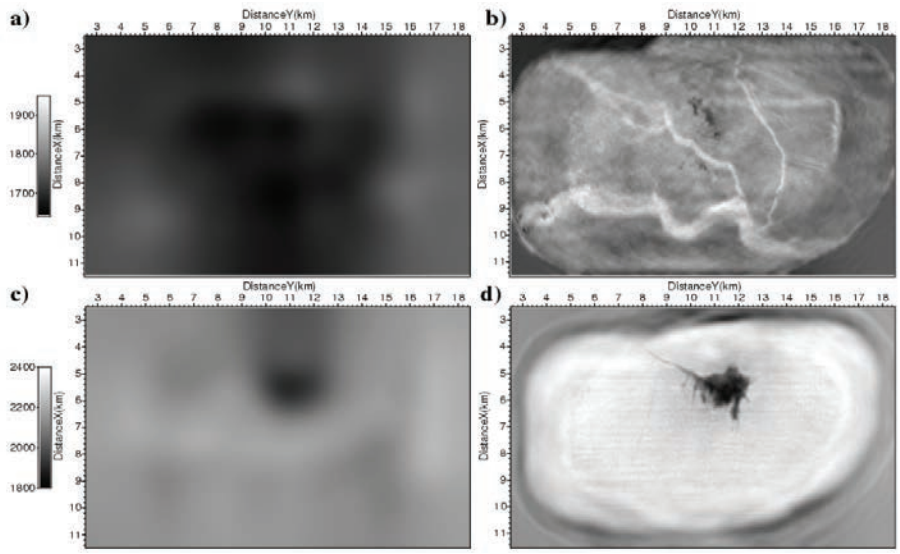

Figure 5.15 *Depth sections in 3D velocity models on the marine Valhall OBC data set, obtained by ray-based reflection tomography (left), followed by FWI (right), for depths z = 150 m (top) and 1050 m (bottom). In the FWI images, channels (top) and the presence of gas (bottom) are clearly visible (Sirgue* et al.*, 2009).*

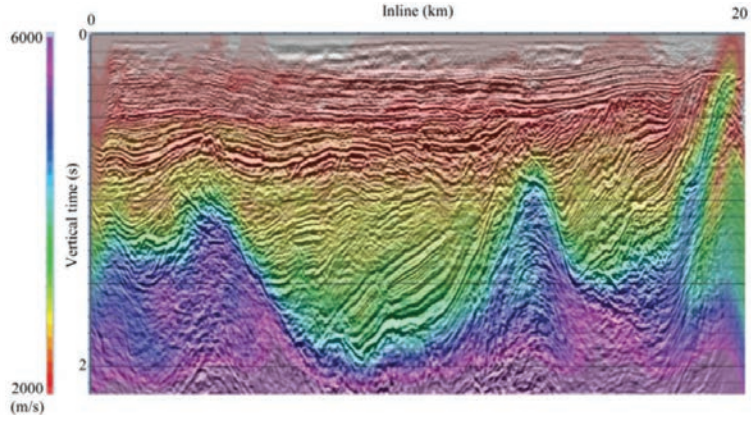

Figure 5.16 *Migrated section superimposed on the FWI velocity model, in a land example (Baeten* et al.*, 2008).*

We present here two examples of impressive FWI results, based on marine (Figure 5.15) and land (Figure 5.16) datasets. In the former, the starting model was obtained by a conventional ray-based reflection travel time tomography (Bishop *et al.*, 1985). FWI was then used to refine the model, leading to clear channels in the shallow part (in white in Figure 5.15-b) and to the presence of gas in the deeper part (in black in Figure 5.15-d). It is possible to see gas leakage along the main faults.

The second example, in a land acquisition context (Inner Mongolia, China), was more challenging due to the presence of highly energetic surface waves (Baeten *et al.*, 2008; Brossier *et al.*, 2009). Here, they were filtered out in a pre-processing step. The initial velocity was derived from travel time tomography and is mainly a 1D model (not represented here). Specific attention was paid to the preservation of energy in the dataset between 1.5 to 2 Hz: this was a crucial step in the FWI construction of the velocity model.

In both cases, the acoustic FWI largely outperforms standard travel time tomography. More work is needed in future to consider higher frequencies and more complex physics.

5.6 Conclusions

Full Waveform Inversion is a technique to obtain seismic quantitative images of the subsurface. However, there are a number of difficulties in terms of its applicability. In particular, a low to high frequency strategy may need to be applied. A carefully considered initial model as well as suitable pre-processing steps must be determined. Finally, the multi-parameter estimation (beyond P-wave estimation) is still an active area of research.

In future, FWI will hopefully become "full": currently, windows are applied to the data to select transmitted waves, for example, or to remove surface waves. These waves contain interesting information on the subsurface (Pérez Solano *et al.*, 2014). The question is to know how to efficiently extract it.

There have been a number of possible alternatives to FWI, for example the Adaptive Waveform Inversion strategy (Warner and Guasch, 2016). Usually, the objective is to remove the cycle-skipping effects or to be able to consider the reflected waves more easily (as in the Reflection Waveform Inversion approach (Zhou *et al.*, 2015)). Another alternative is to split the problem into two parts: the estimation of the macro-model containing the main structures (migration velocity analysis or tomography), and of the model perturbation (migration) (Symes, 2008; Chauris and Cocher, 2017).

Despite larger computation capabilities and memory allocation, FWI can only process limited frequencies in 3D and usually follows a deterministic approach: starting from an initial model, the model is iteratively updated. In future, uncertainties around the final solutions should be properly evaluated, taking into account

uncertainties regarding the data as well as the non-perfect knowledge of the physics of wave propagation through the Earth. On the geotechnical scale, FWI is still in its early development stage, but it has great potential for the future.

References

Baeten G., De Maag J.W., Plessix R.-E., Klaassen R., Qureshi T., Kleemeyer M., Ten Kroode F., Rujie Z., 2013, The use of low frequencies in a full-waveform inversion and impedance inversion land seismic case study, *Geophysical Prospecting*, 61 (4), 701-711, DOI: 10.1111/1365-2478.12010.

Basker B., Rüger A., Deng L., Jaramillo H., 2016, Practical considerations and quality control for an FWI workflow, *The Leading Edge*, 35 (2), 151–156, DOI: 10.1190/tle35020151.1.

Billette F., Brandsberg-Dahl S., 2005, The 2004 BP velocity benchmark.: *67th Annual Conference and Exhibition*, EAGE, Extended Abstracts, B035.

Bishop T.N., Bube K.P., Cutler R.T., Langan R.T., Love P.L., Resnick J.R., Shuey R.T., Spindler D.A., Wyld H.W., 1985, Tomographic determination of velocity and depth in laterally varying media, *Geophysics*, 50 (6), 903-923, DOI: 10.1190/1.1441970.

Brossier R., Operto S., Virieux J., 2009, Seismic imaging of complex on-shore structures by 2D elastic frequency-domain full-waveform inversion, *Geophysics*, 74, WCC105–WCC118, DOI: 10.1190/1.3215771.

Bunks C., Salek F.M., Zaleski S., Chavent G., 1995, Multiscale seismic waveform inversion, *Geophysics*, 60 (5), 1457-1473, DOI: 10.1190/1.1443880.

Chauris H., Cocher E., 2017, From migration to inversion velocity analysis, *Geophysics*, 82 (3), S207–S223, DOI:10.1190/GEO2016-0359.1

Claerbout J.F., 1968. Synthesis of a layered medium from its acoustic transmission response, Geophysics, 33 (2), 264-269, DOI: 10.1190/1.1439927.

Deidda G.P., Balia R., 2001, An ultrashallow SH-wave seismic reflection experiment on a subsurface ground model, *Geophysics*, 66, 1097–1104, DOI: 10.1190/1.1487057.

Fichtner A., 2010, *Full Seismic Waveform Modelling and Inversion*, Springer Verlag.

Gao F., Levander A., Pratt R.G., Zelt C.A., Fradelizio G., 2007, Waveform tomography at a groundwater contamination site: surface reflection data, *Geophysics*, 72, G45–G55, DOI: 10.1190/1.2752744.

Gélis C., 2005. Inversion des formes d'onde élastique dans le domain espace-fréquence en deux dimensions. Application à la caractérisation de la subsurface

dans le cadre de la détection de cavités souterraines. PhD thesis: Université de Nice-Sophia Antipolis.

Gray S.H., 2013, Spatial sampling, migration aliasing, and migrated amplitudes, *Geophysics*, 78 (3), S157-S164, DOI: 10.1190/geo2012-0451.1.

Lailly P., 1983. The seismic inverse problem as a sequence of before-stack migrations, in J. Bednar, ed., *Conference on inverse scattering: Theory and application*, Society for Industrial and Applied Mathematics, 206–220.

Louboutin M., Witte P., Lange M., Kukreja N., Luporini F., Gorman G., Herrmann F.J., 2017, Full-waveform inversion, Part 1: Forward modelling, *The Leading Edge*, 36 (12), 1033–1036, DOI: 10.1190/tle36121033.1.

Louboutin M., Witte P., Lange M., Kukreja N., Luporini F., Gorman G., Herrmann F.J., 2018, Full-waveform inversion, Part 2: Adjoint modelling, *The Leading Edge*, 37 (1), 69–72, DOI: 10.1190/tle37010069.1.

Mora P., 1987. Nonlinear two-dimensional elastic inversion of multioffset seismic data, *Geophysics*, 52 (9), 1211-1228, DOI: 10.1190/1.1442384.

Mora P., 1989. Inversion = migration + tomography, *Geophysics*, 54 (12), 1575-1586, DOI: 10.1190/1.1442625.

Nocedal J., 1980. Updating quasi-Newton matrices with limited storage, *Mathematics of Computation*, 35, 773–782, DOI: 10.1090/S0025-5718-1980-0572855-7.

Operto S., Gholami Y., Prieux V., Ribodetti A., Brossier R., Metivier L., Virieux J., 2013, A guided tour of multiparameter full-waveform inversion with multicomponent data: From theory to practice, *The Leading Edge*, 32 (9), 1040-1054, Doi: 10.1190/tle32091040.1.

Pérez Solano C.A., Donno D., Chauris H., 2014, Alternative waveform inversion for surface wave analysis in 2-D media, *Geophysical Journal International*, 198 (3), 1359–1372, DOI:10.1093/gji/ggu211.

Plessix R.-E., 2006, A review of the adjoint-state method for computing the gradient of a functional with geophysical applications, *Geophysical Journal International*, 167(2), 495–503, DOI: 10.1111/j.1365-246X.2006.02978.x.

Pratt R.G., 1999, Seismic waveform inversion in the frequency domain, Part 1: Theory and verification in a physical scale model: *Geophysics*, 64 (3), 888-901, DOI: 10.1190/1.1444597.

Raknes E.B., Arntsen B., 2017, Challenges and solutions for performing 3D time-domain elastic full-waveform inversion, *The Leading Edge*, 36 (1), 88–93, DOI: 10.1190/tle36010088.1.

Sajeva, A., Aleardi M., Stucchi E., Bienati N., Mazzotti A., 2016, Estimation of acoustic macro models using a genetic full-waveform inversion: Applications to the Marmousi model, *Geophysics*, 81 (4), R173-R184, DOI: 10.1190/geo2015-0198.1.

Sirgue L., Pratt R.G., 2004, Efficient waveform inversion and imaging: a strategy for selecting temporal frequencies: *Geophysics*, 69 (1), 231-248, DOI: 10.1190/1.1649391.

Sirgue L., Barkved O.I., Van Gestel J.P., Askim O.J., Kommedal J.H., 2009. 3D Waveform Inversion on Valhall Wide-azimuth OBC: Session WEM and WAZ Velocity Model Building, *71st EAGE Conference and Exhibition incorporating*, DOI: 10.3997/2214-4609.201400395.

Symes W.W., 2008, Migration velocity analysis and waveform inversion, *Geophysical Prospecting*, 56 (6), 765-790, DOI: 10.1111/j.1365-2478.2008.00698.x.

Tarantola A., 1984, Inversion of seismic reflection data in the acoustic approximation, *Geophysics*, 49 (8), 1259–1266, DOI: 10.1190/1.1441754.

Virieux J., 1986, P-SV wave propagation in heterogeneous media: Velocity-stress finite-difference method, *Geophysics*, 51 (4), 889-901, DOI: 10.1190/1.1442147.

Virieux J., Operto S., 2009, An overview of full waveform inversion in exploration geophysics, *Geophysics,* 74 (6), WCC1–WCC26, DOI: 10.1190/1.3238367.

Warner M., Guasch L., 2016, Adaptive waveform inversion: Theory, *Geophysics*, 81 (6), R429-R445, DOI: 10.1190/geo2015-0387.1.

Witte P., Louboutin M., Lensink K., Lange M., Kukreja N., Luporini F., Gorman G., Herrmann F.J., 2018, Full-waveform inversion, Part 3: Optimization, *The Leading Edge*, 37 (2), 142–145, DOI: 10.1190/tle37020142.1.

Zhou W., Brossier R., Operto S., Virieux J., 2015, Full waveform inversion of diving & reflected waves for velocity model building with impedance inversion based on scale separation, *Geophysical Journal International*, 202 (3), 1535-1554, DOI: 10.1093/gji/ggv228.

6

Hybrid seismic imaging

M. Mendes, J.-L. Mari, M. Hayet

Traditionally, each seismic prospection technique requires the optimization of field layout, equipment and configuration dependent on the target, attempting to record only the proposed seismic wave, with the highest possible quality. Although setup parameters are designed specifically for selected wave types, seismic records are always corrupted by other waves. To isolate a single wave type, data processing methods are applied for the extraction and/or minimization of all other arrivals.

Conversely, this chapter addresses how it is possible to take advantage of several existing wave types, within the same dataset, encouraging the application of hybrid seismic methods. The objective being to obtain a final model that is built with the information produced by different seismic processing sequences, which thus improves significantly the delineation of seismic velocity interfaces and/or the physical parameterization of subsurface geological structures. Thus, the proposed hybrid seismic strategy offers economic and practical benefits because its implementation can be carried out without increasing the costs of seismic data acquisition, while data processing follows standard procedures.

DOI: 10.1051/978-2-7598-2351-2.c008

Here, we focus on two field examples that target shallow structures, the final results of which emphasize the advantage of applying hybrid seismic methods to provide more accurate geophysical models.

The first example presents a refraction-reflection imaging strategy with the capability to evaluate reflectivity information from the acquisition surface. Depending on the minimum offset defined for the survey, standard reflection imaging techniques usually start to image the reflectivity parameter a few meters below the surface, therefore refracted arrivals are used to complete the reflectivity features for the shallowest structures.

The procedure involves three steps:

- construction of a depth velocity model from first arrival times, accomplished iteratively by tomographic inversion,
- construction of a time reflectivity section from the reflected waves of direct and reverse shot gathers by classical reflection seismic processing. Generally, this is the most critical step in the imaging procedure, due to the low fold of reflection data,
- extension up to the surface of the time reflectivity section by converting the shallowest depth velocity model to time reflectivity, associated with velocity contrasts in the subsurface. The time reflectivity sections require a factor scale before being gathered in a final time reflectivity section.

As this hybrid approach has the capability to start imaging from the surface, it is a very useful tool for providing reflectivity information for targets located in the near and/or very near surface, which is often required for the monitoring of civil engineering structures, in environmental engineering studies and even archaeological exploration.

The second example described in this chapter relates to another hybrid seismic strategy for refraction-surface waves imaging. When a compressional wave source is used in surface seismic surveys, more than two-thirds of the total seismic energy generated is usually imparted into Rayleigh waves, the principal component of ground roll. This hybrid seismic technique addresses this issue by combining information about the P-wave velocity provided by the refraction arrivals with the S-wave velocity distribution obtained from the surface wave data, also presented on the same field records.

The velocity-estimation procedures include the following steps:

- construction of a P-wave velocity model from first arrival times accomplished iteratively by tomographic inversion. A large range of initial models are used to estimate the sensitivity and depth of the investigation. The final P-wave velocity model is an average of all models satisfying the picked field data within a predetermined fitting level;
- construction of an S-wave velocity model from the analysis of surface waves in the frequency-phase velocity domain. After field data windowing for the validation of a 1D model hypothesis; the experimental dispersion curve is easily identified in the f-k domain and the location of maxima energy can be picked.

By taking advantage of multi-shot acquisition setups, a stacked dispersion curve can be obtained. The dispersion curve is a diagram of phase velocity versus frequency. S-wave velocity can be obtained by the inversion of dispersion curves, using a global search method with a neighborhood algorithm (NA).

The distribution of both velocities is productively combined to evaluate mechanical properties of the subsurface, which are critical properties for many geotechnical foundation designs, aquifer system characterizations and the time-lapse monitoring of shallow water content.

6.1 Refraction-reflection imaging

The main purpose of this example is to obtain a complete shallow subsurface image for the reflectivity property through the simple and fast processing of refraction survey data.

The refraction survey was carried out near the underground research laboratory of Andra (National Radioactive Waste Management Agency) located in the eastern region of France. The refraction survey, collected by the geophysical company DMT GmbH & Co KG, aimed to estimate the velocity field in the near surface zone (weathering zone) for a reliable evaluation of static corrections. The intention was to improve the processing of a high-resolution 3D seismic survey of 37 km^2, which also covered this region (Figure 6.1).

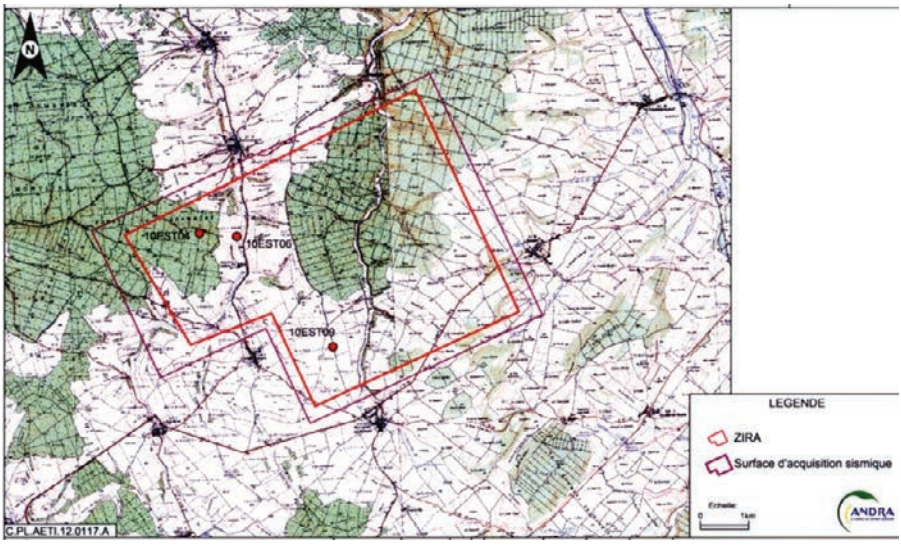

Figure 6.1 *Plan view of the 3D seismic reflection survey area (magenta polygon) with the location of three relevant 2D seismic refraction profiles (red points): 10EST04, 10EST09, 10EST06. Adapted from Mendes* et al. *(2014).*

Several refraction profiles were then implemented with a total spread length of 203 m for each profile. The 10 Hz vertical geophones, 48 in total, were spread with a receiver spacing of 2.5 m for source offsets ranging from 1 to 7.5 m and 5 m for source offsets larger than 7.5 m. The source was a weight dropper (10 kJ) shooting at 3 points: shot point 1 (SP01) with a 1 m offset from geophone 1, shot point 2 (SP02) with a 1 m offset from both geophones 24 and 25, and shot point 3 (SP03) with a 1 m offset from geophone 48. Figure 6.2 shows a diagram of the acquisition spread and the three common shot-gathers of the 10EST04 profile.

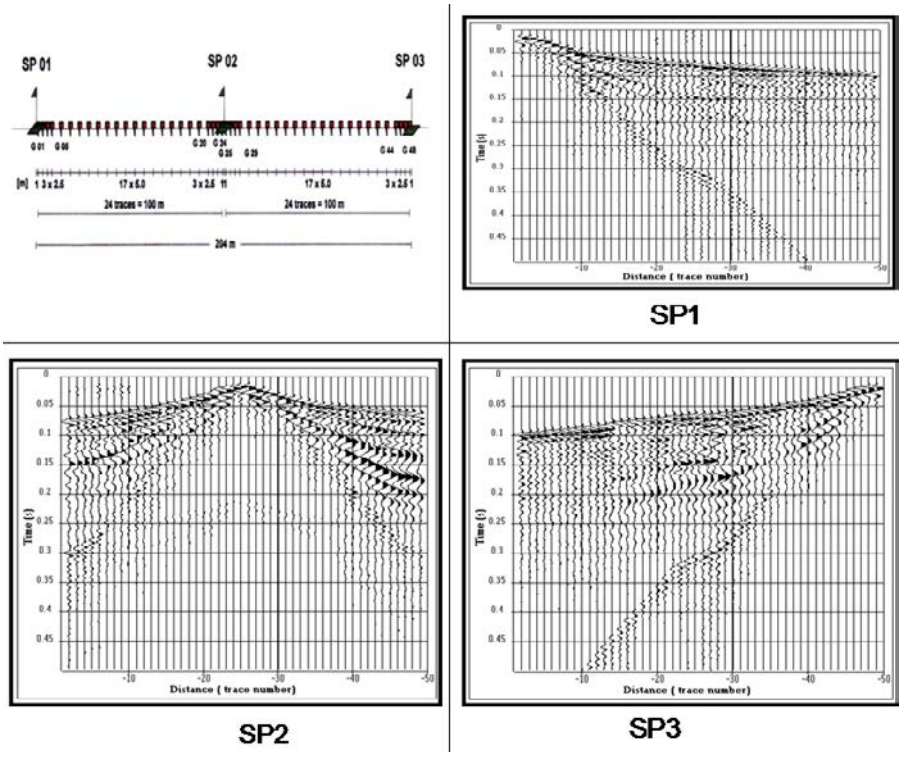

Figure 6.2 *Refraction seismic acquisition: spread and the three-common shot-gathers of the 10EST04 profile. Adapted from Mendes* et al. *(2014).*

Full details describing the acquisition and seismic hybrid processing of this field example are presented in Mendes, Mari and Hayet, 2014 (Mendes *et al.*, 2014). This chapter presents only a brief outline.

The first step was to derive a depth velocity model for the shallowest region from the processing of first arrivals (direct, diving or refracted waves). The Plus-Minus method of refraction interpretation (Hagedoorn, 1959) using the first-arrival time information was used to produce an interval velocity depth model: the weathered

layer presents constant velocity V1 = 1,300 m/s over a bedrock with velocity V2 = 3,250 m/s. This model, along with all available information, was then used to generate the best initial model for tomographic inversion. Tomography was applied to refine the velocity-depth model, which has major benefits when dealing with complex geological setups involving lateral variations. Figure 6.3 shows the advantages of processing by tomographic inversion where strong lateral velocity variations add value to the model. The weathering zone is a heterogeneous shaly mudstone over a compacted limestone.

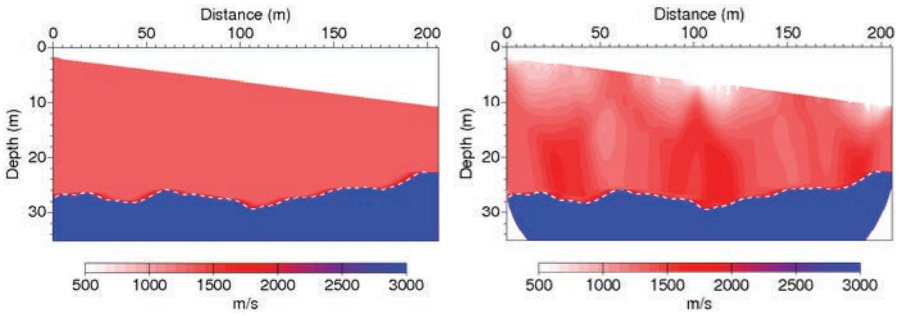

Figure 6.3 *Tomographic inversion for the 10EST04 profile. Left: Input model V1 = 1,300 m/s and V2 = 3,250 m/s provided by the Plus-Minus method. Right: Velocity model generated by tomographic inversion. The result exhibits velocity with strong lateral variations for the heterogeneous shaly mudstone over a bedrock of compact limestone. Adapted from Mendes* et al. *(2014).*

In a second step, only the reflection events were considered for imaging. In this case, processing capable of isolating and enhancing the reflected waves was required, since they derive from data recorded for a refraction survey and the shot-gathers were corrupted by energetic surface waves that arrived simultaneously with the reflected waves.

To obtain a single-fold reflectivity section, shot points 1 and 3 (the end-off shots) were processed according to the following standard sequence:

- amplitude recovery;
- deconvolution by spectrum equalization (12–160 Hz frequency bandwidth);
- wave separation by SVD extraction of refracted waves;
- wave separation by F-K filter, to extract surface waves and convert refracted waves;
- static corrections based on the high-resolution velocity model provided by the tomographic inversion;
- CMP sorting, traces gathered in a common shot-gather are sorted in a common midpoint-gather;

- velocity analysis by velocity scan to produce a velocity model;
- normal move-out (NMO) corrections to flatten the reflected arrivals.

Figure 6.4 illustrates the main evolution of field data during the processing sequence. Special attention was focused on the residual section (Figure 6.4-bottom right), which clearly shows high apparent velocity events associated with reflected waves.

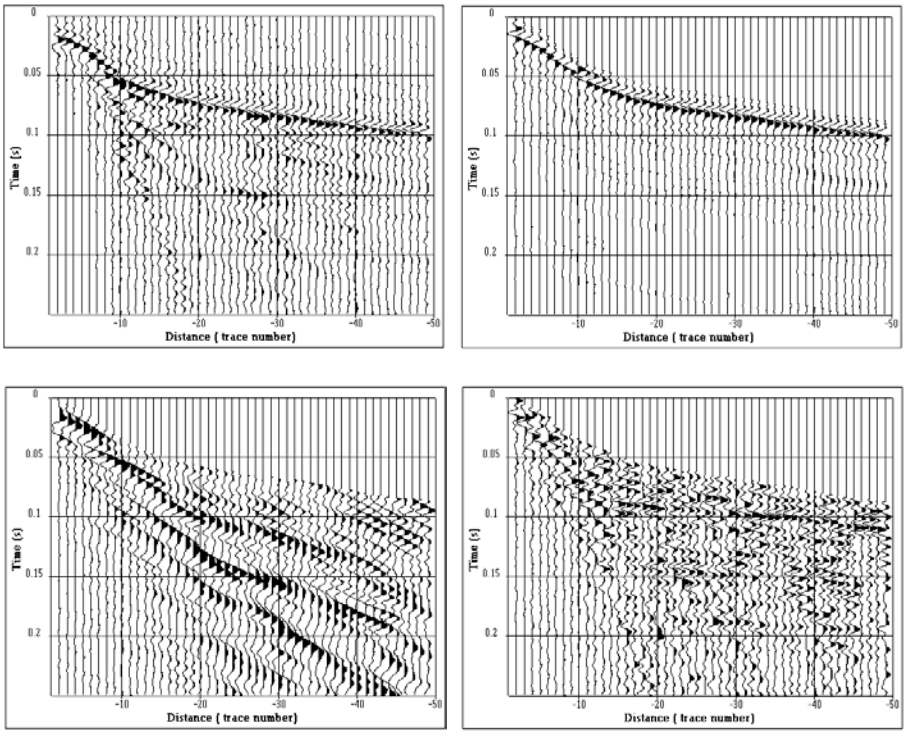

Figure 6.4 *Deconvolution and wave separation for shot point 1 of the 10EST04 profile. Top left: deconvolution by spectrum equalization in the 12–160 Hz frequency bandwidth. Top right: Extraction of direct and refracted waves by SVD filter. Bottom left: Extraction of surface waves (Pseudo Rayleigh waves) by F-K filter. Bottom right: Reflected waves and residual noise. Adapted from Mendes* et al. *(2014).*

Chapter 4 contains more information about the processing sequence, which readers should look through to gain further insight into the method.

The NMO correction produced a single fold section (Figure 6.5 left). We considered the traditional definition for reflectivity, $RZ_i = (Z_{i+1} - Z_i) / (Z_{i+1} + Z_i)$ where Z_i is the acoustic impedance (product of the density by velocity) at cell i and Z_{i+1} is the acoustic impedance at cell i+1. Nevertheless, density was neglected in our reflectivity

coefficient computation. Thus, this reflectivity section displays the reflection coefficients associated to the interfaces, filtered in the seismic frequency bandwidth.

The third and last step of this hybrid approach focuses on extending the reflectivity section upwards through the depth velocity model of the uppermost region, obtained by tomographic inversion. The depth velocity model was converted to time and used to estimate the reflectivity according the definition of $RV_i = (V_{i+1} - V_i)/(V_{i+1} + V_i)$ where V_i is the velocity at cell i and V_{i+1} is the velocity at cell i+1. The section obtained was then filtered in the same frequency bandwidth as defined for the section in the previous processing step.

Before they could be gathered into a single time reflectivity section, the two time reflectivity sections required a scale factor (k): the reflectivity section derived from the velocity model (RV) is related to the reflectivity section derived from acoustic impedance contrasts (RZ) by the equation RZ = kRV. The scale factor was computed by the amplitude ratio between the reflectivity sections in a time-distance window, where the reflected wave on the bottom of the weathering zone is visible. In practice, the time-distance window is defined as follows: time window (between 0.025 s and 0.050 s) for the short offsets (between 0 m and 25 m). Figure 6.5-bottom right shows the final time reflectivity section obtained by gathering the two reflectivity sections also shown in Figure 6.5, where a noticeable reflection at approximately 40 ms is associated with the bottom of the weathering zone.

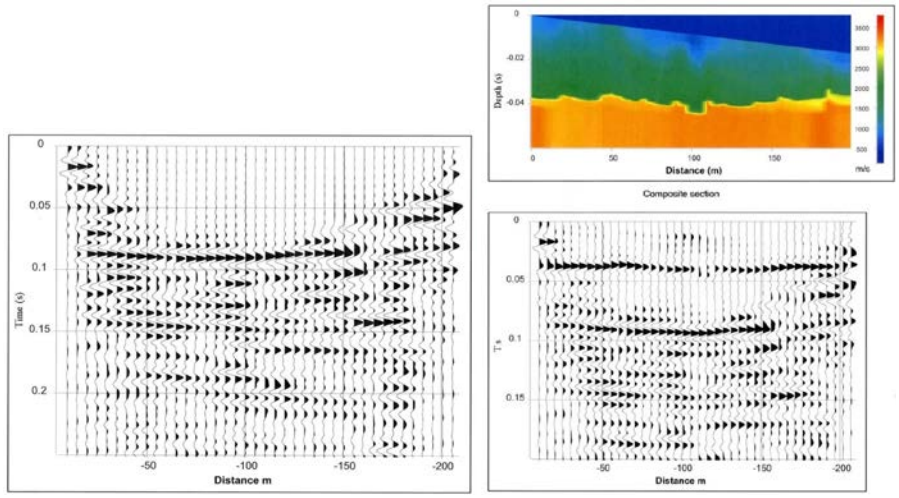

Figure 6.5 *Reflectivity section for 10EST04 profile: Left: Single fold section derived from reflection processing of off-end shots. Bottom right: Upward continuation of single-fold section using reflectivity derived from tomographic velocity model. Top right: Time converted velocity model obtained by tomographic inversion. Adapted from Mendes* et al. *(2014).*

The field data examples illustrate the potential of gathering two sections, extracted from different parts of the seismic wave field, for providing a means to resolve reflectivity and images from the ultra-shallow surface down to deeper structures. This is achieved using a simple seismic data processing method, with data acquired in a rapid and inexpensive manner, for refraction seismic surveying, without increasing the acquisition costs.

6.2 Refraction-surface waves imaging

The main objective of this example is to encourage the processing of P-wave refraction and surface-wave data obtained from a single seismic survey.

The geophysical survey was carried out in Yellowstone National Park (USA), in the Obsidian Pool Thermal Area. The goal of the seismic survey carried out at this site was to study shallow hydrothermal systems, characterize fluid pathways and improve understanding of the depths at which steam separates from liquid water. The area is characterized by extensive CO_2 diffuse degassing and isolated thermal features with water temperatures between 21.9 °C and 84.0 °C. Seismic data were collected in July 2016 along a south-southwest–north-northeast transect, crossing a heat-flow anomaly between 50 and 120 m and a degassing feature between 86 and 96 m.

The equipment and parameters used in the seismic survey were:

- a 5.4 kg sledgehammer source swung onto a metal plate. The plate was hit five times at each position to increase the S/N,
- 10 Geometrics Geode seismographs, with 24-channels in each one,
- 4.5 Hz vertical component geophones spaced every 1 m, obtaining a 239 m long profile,
- 25 shot gathers recorded every 10 m,
- a sampling rate of 0.125 ms and a recording time of 0.75 s, to include the full surface wavefield.

In addition, a GPS survey and airborne LiDAR data collection were carried out to extract the topography.

The following results are extracted from Pasquet and Bodet (2017), who have developed an open-source MATLAB-based package that performs surface wave inversion and profiling (SWIP) to obtain 1D to 2D variations of S-wave velocity.

The first step of the proposed velocity-estimation procedure concerns the P-wave velocity model.

The construction of the P-wave velocity model from the first arrival times was accomplished iteratively by tomographic inversion. A large range of 100 initial models were tested to estimate the sensitivity and depth of investigation. The final P-wave velocity model produced is an average of all models satisfying the picked

field data within a predetermined fitting level; it shows smoothly varying velocities ranging between 100 and 2,000 m/s, with a low velocity layer, approximately 5 m thick, at the surface.

Figure 6.6 shows the layout of the seismic acquisition setup, with 240 geophones and 25 shots, the shot-gather for a source located at 120 m and the final P-wave velocity model obtained from P-wave travel time tomography.

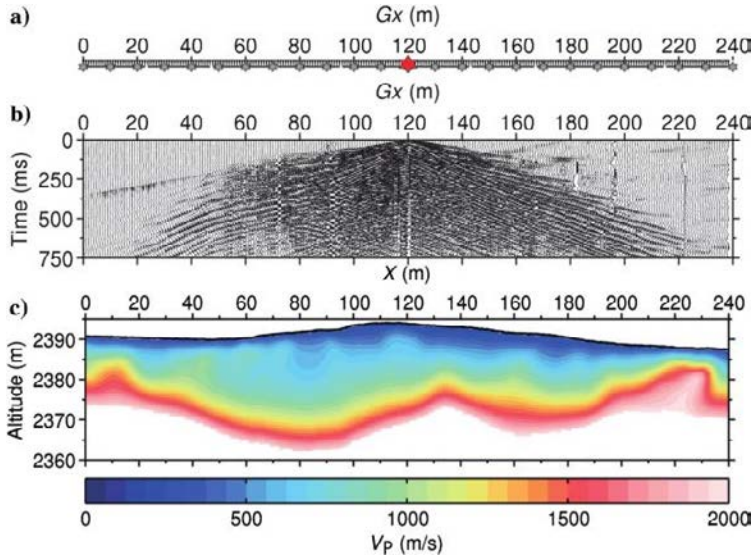

Figure 6.6 *(a) Layout of the seismic acquisition setup, with 240 geophones (gray triangles) spaced every 1 m and 25 shots (gray stars) spaced every 10 m. (b) Example of a shot gather for a source located at 120 m (red star in a). (c) Final P-wave velocity model obtained from P-wave travel time tomography. The topography extracted from airborne LiDAR data is represented with a solid black line. From Pasquet and Bodet (2017).*

The second step of the velocity-estimation procedure is related to the S-wave velocity model extracted from the surface waves. The processing of the surface waves data was carried out using SWIP and readers can find supplementary information about this practical processing sequence in Pasquet and Bodet (2017). Therefore, very few details are provided here and we restrict our comments to the main results only.

After field data windowing for validation of the 1D model hypothesis, the seismic record from its original time–distance domain was transformed into the frequency–phase-velocity domain. This step results in a set of frequency–phase-velocity pairs specifying dispersion curves. The experimental dispersion curves were identified in the f-k domain and the location of maxima energy were picked. The dispersion

curve is a diagram of phase velocity versus frequency and Figure 6.7 shows examples of single dispersion curves from shots located at 0 m, 10 m, 50 m, and 60 m.

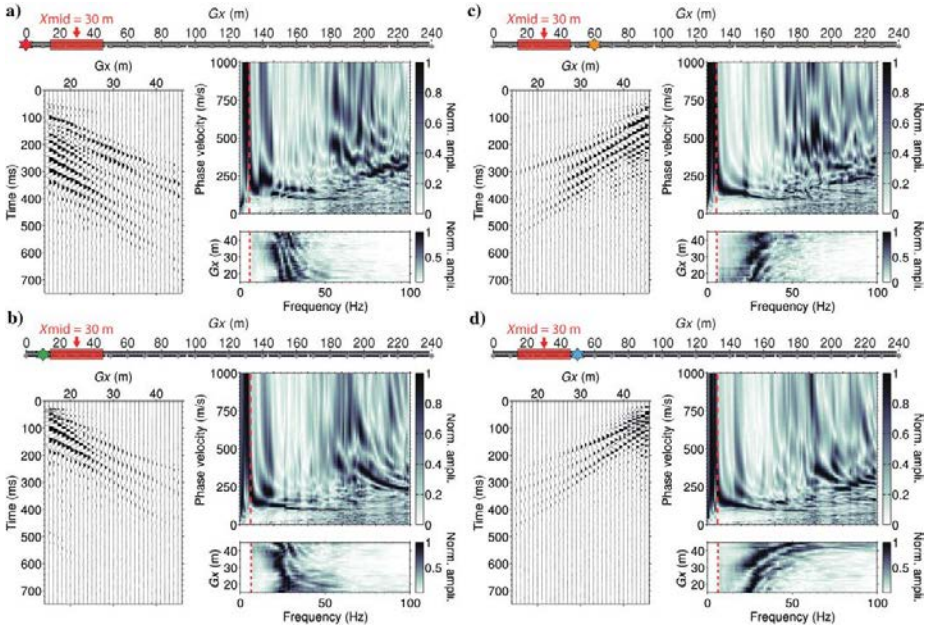

Figure 6.7 *Extraction of single dispersion images for a 31 trace window centered at Xmid=30 m, using shots located at (a) 0 m, (b) 10 m, (c) 50 m, and (d) 60 m. On each inset, windowed shot gathers are on the left, corresponding spectrograms are at the bottom right, and computed dispersion images are at the top right. The dashed red lines on the spectrograms and dispersion images correspond to automatic low-cut frequencies defined from the spectrogram amplitude. From Pasquet and Bodet (2017).*

Through the utilization of multi-shot acquisition setups, a stacked dispersion curve can be obtained, and the S/N ratio improved, as shown in Figure 6.8.

The dispersive events were stacked on the frequency–phase velocity panel, and then the interactive picking of events was conducted. Figure 6.8 presents two examples of stacked dispersion curves with picked events for the fundamental and first modes. The associated uncertainties are also defined.

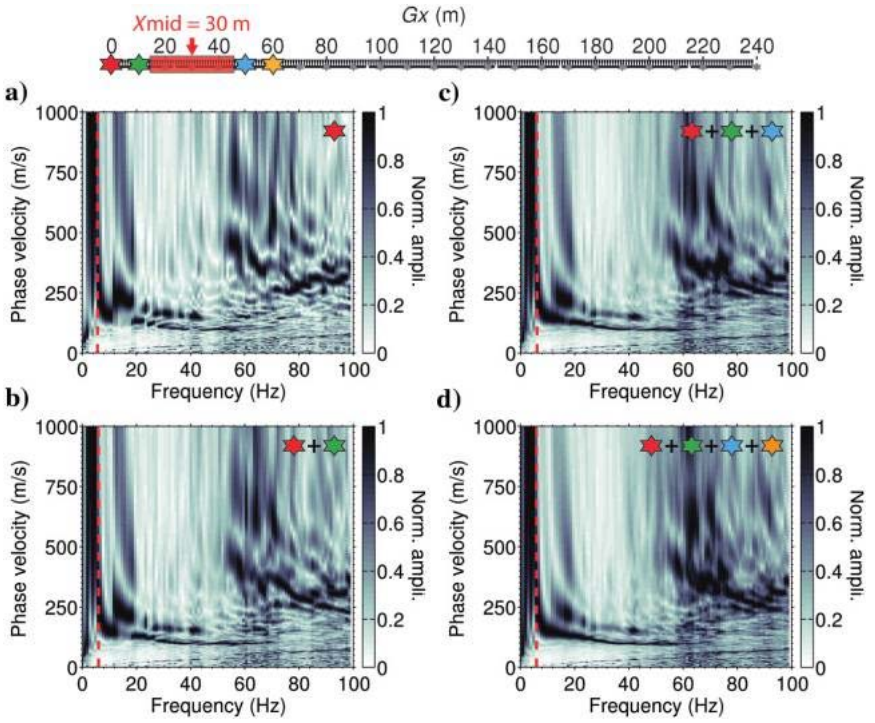

Figure 6.8 *(a-d) Successive stacking of the single dispersion images represented in Figure 6.7-a–d. From Pasquet and Bodet (2017).*

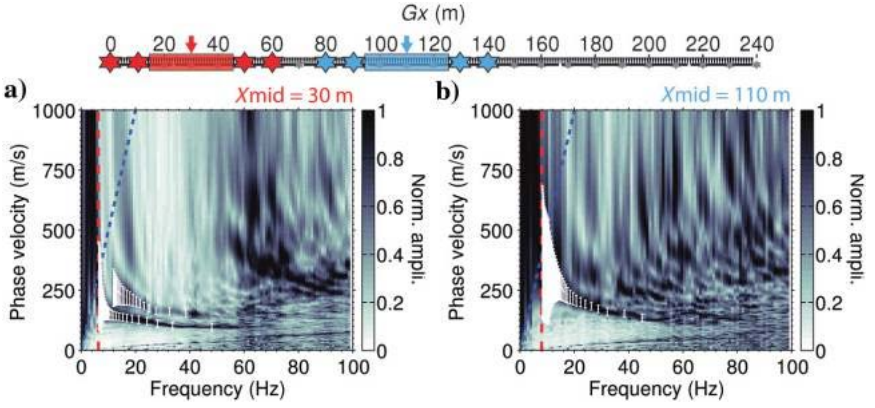

Figure 6.9 *Stacked dispersion images extracted at (a) Xmid = 30 m and (b) Xmid = 110 m with picked dispersion curves (white error bars) of the fundamental (0) and first higher (1) modes. The uncertainty range is defined according to the work-flow described in O'Neill (2003). Dispersion curves are limited to a frequency defined with a spectral amplitude threshold of 2.5% (dashed red line), or up to a wavelength of 50 m (dashed blue line). From Pasquet and Bodet (2017).*

Adjacent dispersion images were displayed during picking to follow the lateral evolution of different modes and to avoid mode misidentification. The fundamental mode was clearly identified all along the line, whereas the first higher mode was only partially shown, as seen in Figure 6.10.

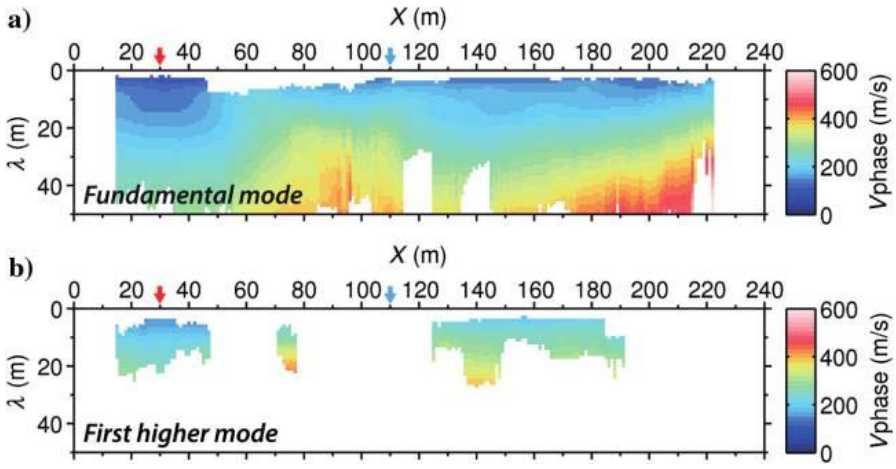

Figure 6.10 *Pseudo-sections of SW phase velocity picked for (a) the fundamental and (b) first higher modes along the line after dispersion stacking, represented as a function of the wavelength λ and the spread mid-point position. From Pasquet and Bodet (2017).*

A model with vertical velocity variation below each extraction window was assumed, therefore, the initial model chosen for the inversion is a one-dimensional stack of 10 homogeneous elastic layers based on a P-wave velocity model and geological information. A neighborhood algorithm (NA) without lateral constraints performs the inversion of the dispersion curves. The results for Xmid = 30 m and Xmid = 110 m are displayed in Figure 6.11.

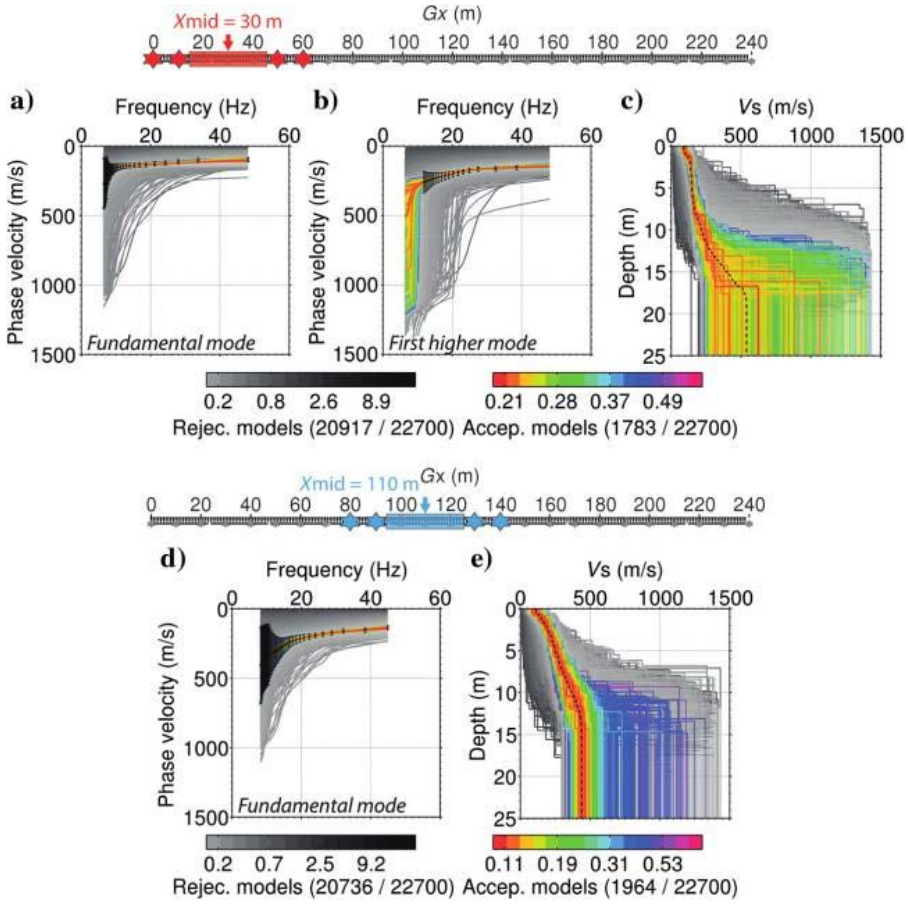

Figure 6.11 *Results of 1D NA inversions of dispersion data (black error bars) at Xmid = 30 m ([a] fundamental and [b] first higher modes) and Xmid = 110 m ([d] fundamental mode). Resulting VS models are represented for (c) Xmid = 30 m and (e) Xmid = 110 m, along with a misfit-weighted velocity structure (dashed black lines) built from the average parameters of all accepted models. Calculated dispersion and corresponding models are represented with misfit-based color and gray scales for accepted and rejected models, respectively. From Pasquet and Bodet (2017).*

After each 1D inversion, models fitting the observed data within the uncertainty were selected. For each extraction window model, a misfit-weighted model was built averaging all accepted models. Once this model had been constructed, its acceptability was evaluated by calculating the theoretical dispersion curves (Figure 6.12).

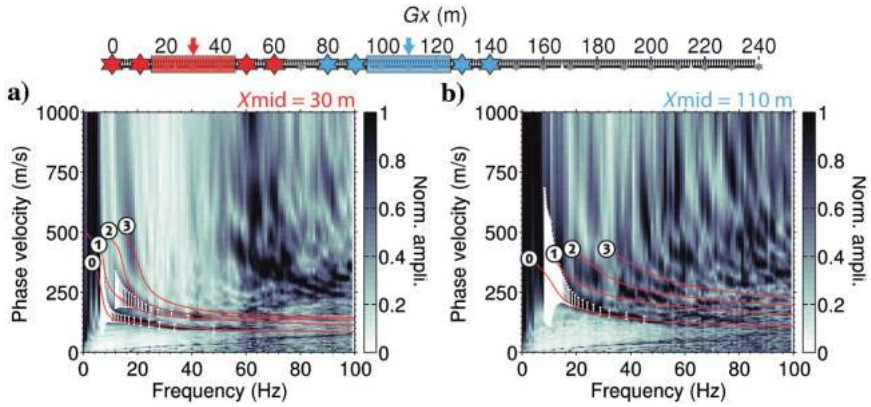

Figure 6.12 *Stacked dispersion images extracted at (a) Xmid = 30 m and (b) Xmid = 110 m with picked (white error bars) and calculated (solid red lines) dispersion curves represented for the fundamental (0), the first (1), second (2), and third (3) higher modes. From Pasquet and Bodet (2017).*

The study of the fitting parameters, for each 1D model provided by the inversion algorithm along the acquisition line, confirmed the good quality of this model. Then, the investigation depth was evaluated for each Xmid position and finally the pseudo-2D section of the S-wave velocity was built with each 1D S-wave velocity model. The final results are shown in Figure 6.13.

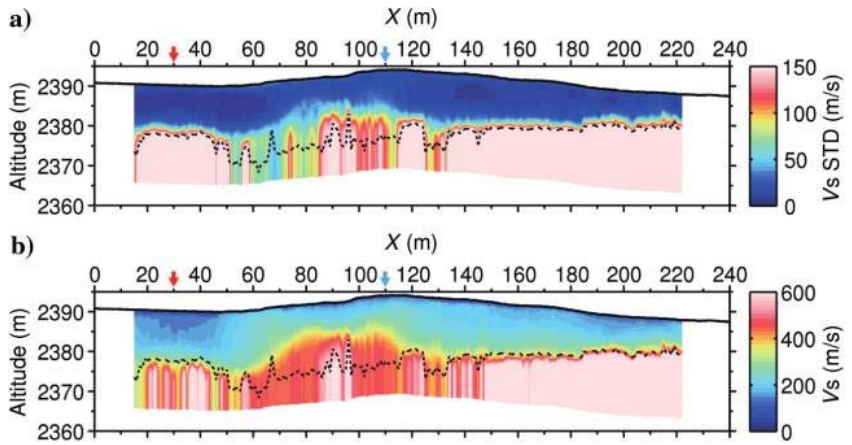

Figure 6.13 *(a) Pseudo-2D section of S-wave velocity standard deviation computed from accepted models at each Xmid position along the line. (b) Pseudo-2D section of average S-wave velocity model computed from accepted models at each Xmid position along the line. The dashed black line corresponds to the depth of investigation estimated with an S-wave velocity model standard deviation threshold of 150 m/s. The topography extracted from airborne LiDAR data is represented with a solid black line. From Pasquet and Bodet (2017).*

The S-wave velocity model is characterized by velocities ranging between 50 and 600 m/s, with higher shallow velocity below the heat-flow anomaly observed between 50 and 120 m. Although the S-wave velocity model has a lower investigation depth than the VP model, it provides more information regarding the lateral variations of the velocities of shallow layers due to the intrinsic smoothing of tomographic inversion and the substantial horizontal component of P-wave travel paths.

SWIP also calculates Poisson's ratio, if P-wave velocity is available. The results, as shown in Figure 6.14, reveal values in the range of 0.3–0.5, typical of non-saturated and saturated media, respectively. For most of the subsurface, Poisson's ratio values are between 0.45 and 0.5 indicating high water content, except in the highest part of the hill observed at depths below the degassing area visible at the surface, which presents a low Poisson's ratio.

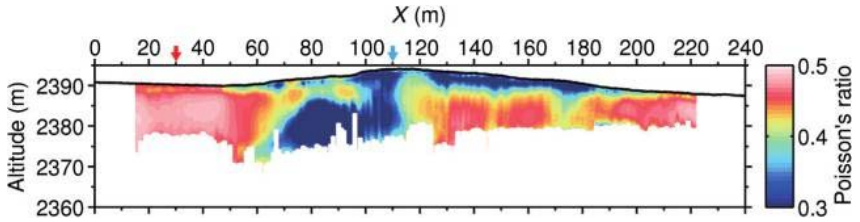

Figure 6.14 *Poisson's ratio computed from P-wave velocity provided by tomography and S-wave velocity from surface wave dispersion inversion and masked below the depth of investigation estimated from S-wave velocity standard deviation. The topography extracted from airborne LiDAR data is represented with a solid black line. From Pasquet and Bodet (2017).*

Finally, this example indicates that the estimated Poisson's ratio is a valuable parameter to clearly highlight gas pathways in the subsurface consistent with degassing observed at the surface.

6.3 Conclusion

This chapter, which describes the handling of different types of waves present within the same dataset, underlines some of the advantages of hybrid seismic imaging strategies to provide efficient, accurate and reliable subsurface models, in terms of geometry and mechanical properties.

In the first field example, the hybrid seismic imaging tool showed that seismic data derived from traditional refraction acquisition is valuable for obtaining information about the reflectivity for targets located in the near and/or very near surface. Based on a three-step procedure, the processing of refraction and reflection waves provided two sections, which after gathering produced an extended time reflectivity section starting from the surface.

The second example describes the use of hybrid seismic refracted and surface waves. The processing of surface waves, extracted from a seismic survey, was performed in the f-k domain with SWIP, an open-source MATLAB-based package. The inversion of the dispersion curves produced pseudo 2D models of S-wave velocity with an estimated depth of investigation of around 10 m. A P-wave velocity model was extracted from the refraction arrivals by a tomography algorithm. The Poisson's ratio was estimated from this information. The distribution of this parameter, more particularly its contrasts, clearly highlights gas pathways in the subsurface consistent with degassing observed at the surface.

The good results obtained in the case studies reveal that it is possible to obtain complementary information from the combination of different wave types from the same seismic survey. Thus, these hybrid seismic methods open up new perspectives for more applications.

References

Hagedoorn G.J., 1959, The Plus–Minus method of interpreting seismic refraction sections, *Geophysical Prospecting*, 7, 158-182.

Mendes M., Mari J.L., Hayet M., 2014, Imaging geological structures up to the acquisition surface using a hybrid refraction-reflection seismic method, *Oil & Gas Science Technology*, 69 (2), 351-361, http://dx.doi.org/10.2516/ogst/2012095.

Pasquet S., Bodet, L., 2017, SWIP: An integrated workflow for surface-wave dispersion inversion and profiling, *Geophysics*, 82 (6), WB47-WB61.

7

Integrated seismic study

Focus on "Cigéo", the French geological repository project

J.-L. Mari and B. Yven

"*Cigéo*" is the French Geological Repository Project dedicated to the disposal of high-level (HL) and intermediate-level long-lived (IL-LL) radioactive waste in a Callovo-Oxfordian argillaceous formation. The area is located in the eastern part of the Paris Basin and has been extensively studied by the French national radioactive waste management agency (Andra) for the past 25 years (Andra, 2005; Andra, 2009; Andra 2016).

In 2010, a zone of interest for a detailed survey, located a few kilometres from the Bure Underground Research Laboratory, was defined. It was chosen to be a site for

DOI: 10.1051/978-2-7598-2351-2.c009

underground facilities (Andra, 2009). A 3D seismic survey (37 km^2) was recorded to verify the geometry and properties of the clay formation and of the underlying and overlying limestone formations. In addition to the 3D seismic campaign, drilling and geophysical borehole measurements, including vertical seismic profiles (VSP), and up-hole investigations were performed to calibrate the 3D seismic blocks and to perform the time-to-depth conversion.

After presenting the geological setting, we describe the survey design and the processing applied to the dataset. We describe a method that could be developed to build a geo-model in depth, using pre-stack time migration, elastic inversion in time and the relationship between P-wave velocity and acoustic impedance. We also show how petro-physical studies could be conducted. 2D and 3D lines are used to illustrate the potential of the proposed procedure for estimating density (ρ), velocity (Vp, Vs), distributions of mechanical (Q factor, dynamic and static moduli) and petro-physical parameters (porosity, specific surface, permeability indicator). This chapter is a review of published literature. The data and parameter values contained in this chapter do not predetermine the use that will be made of them for design and safety analyses.

7.1 Geological setting

The Meuse/Haute-Marne sector is located in the eastern part of the Paris Basin (Figure 7.1). The sedimentary succession shows a simple, monocline structure, dipping towards the centre of the basin (NW) which follows the general structure of the basin.

The sector north of the Haute-Marne and south of the Meuse (Figure 7.1) constitutes a geologically simple area of the Paris Basin, with a succession of layers of limestone, marl and clay rock deposited in ancient ocean. The dip of the layers is low, around 1° to 1.5° towards the north-west. The Callovo-Oxfordian formation was chosen to host the Cigéo underground installation. It comprises 155 million year old clay rock, which is at least 130 meters thick and located at a depth of between 400 and 600 meters. It is referred to herein as the Callovo-Oxfordian argillites (Cox) formation. The selection of this Callovo-Oxfordian formation was based on its depth, low permeability, weak diffusion of solutes, high retention capacities and its significant thickness, which is favourable to the limitation of radionuclide migration from the Callovo-Oxfordian, into the surrounding formations, and then the biosphere, for a time scale of at least several hundred thousand years.

The top of the Cox formation is more carbonate-rich, with interbedded clayey layers and carbonate rock. The Cox is more homogeneous in its central part with a clay-mineral concentration of 45-50%, which corresponds to a maximum of flooding within the area. A detailed study of the spatial variability of the Cox geological and physical properties may be found in Garcia *et al.* (2011). This formation is

embedded by two thick carbonated units: Dogger and Oxfordian. The Dogger (Bathonian, Bajocian) corresponds to the development of carbonate platforms in the Paris Basin (Gaumet, 1997; Purser, 1980, Brigaud, 2014). The clayey formation is separated from the Dogger limestone by a regional paleo-erosion surface. The Bathonian limestone formation is the first aquifer encountered in the Jurassic succession.

Above the Cox, an Oxfordian (Middle and Late) platform was found, developed with reefs and bioclastic facies. The Oxfordian limestone formation is a second Jurassic aquifer. The two aquifers are studied in this work. In the area investigated by seismic surveying, the outcropping formations are Kimmeridgian marls and Kimmeridgian and Tithonian limestone with a thin deposit of Cretaceous. Figure 7.2 gives the geological description of the Jurassic and Triassic series at well EST433 and the location of the interpreted seismic horizons (Landrein *et al.*, 2014; Mari and Yven, 2014).

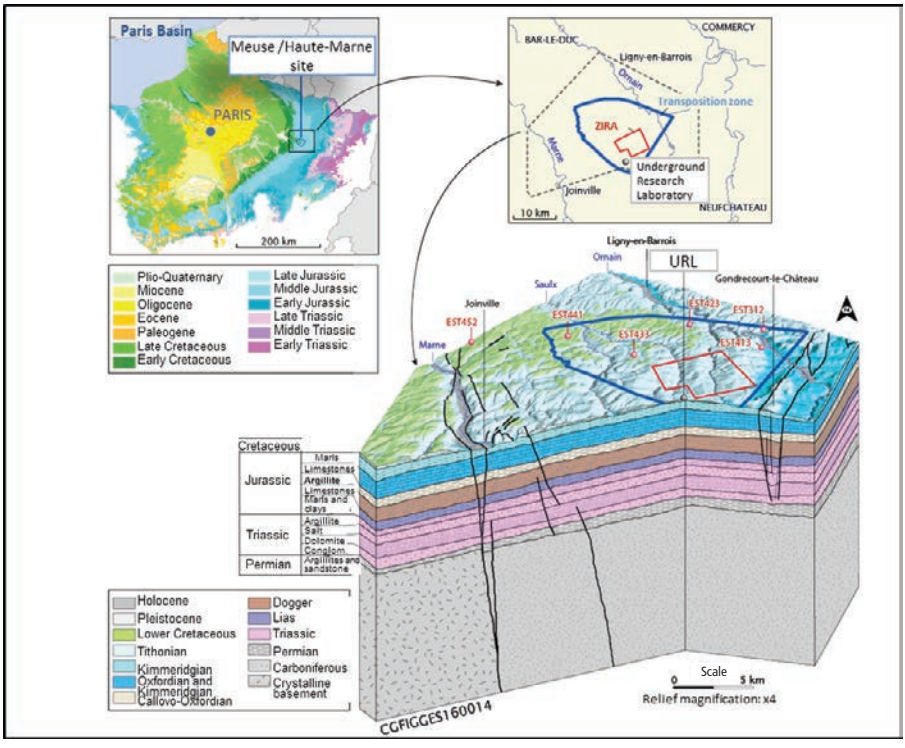

Figure 7.1 *Simplified geological map of the Paris Basin showing the location of the Meuse/Haute-Marne site and Andra's underground research laboratory (URL).*

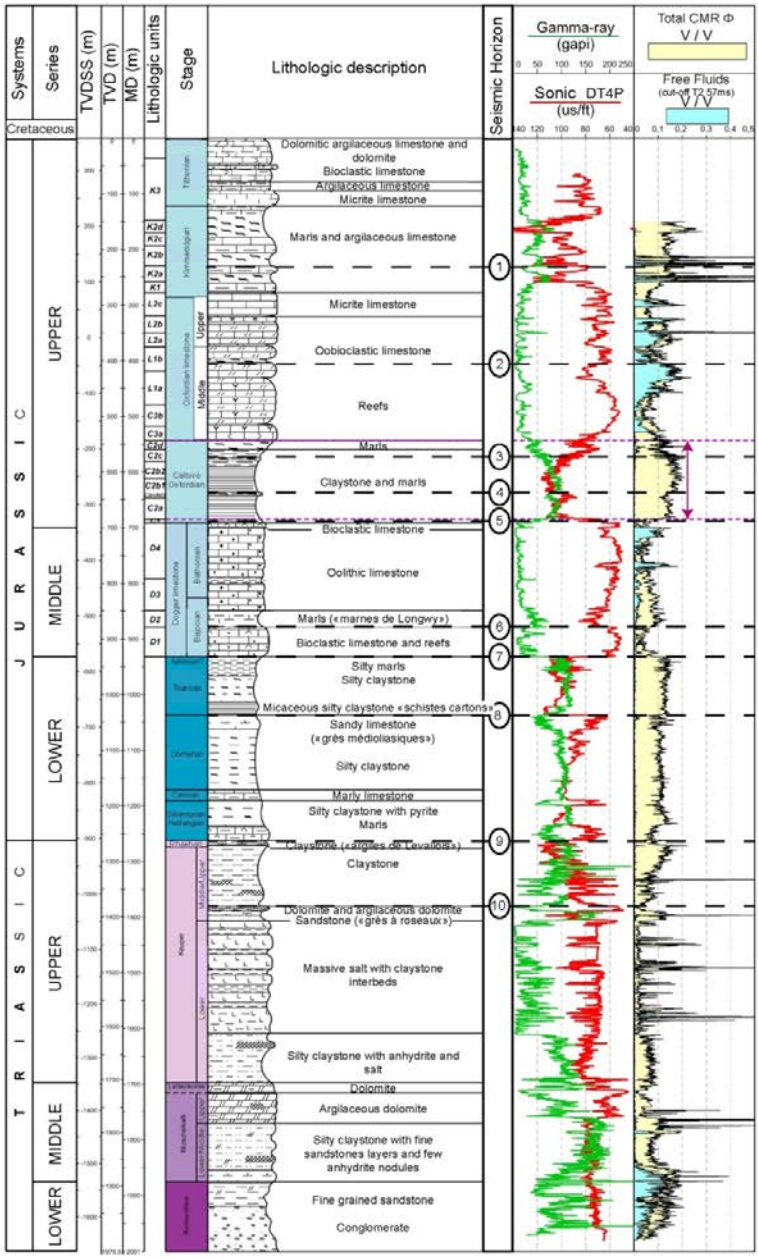

Figure 7.2 *EST 433 geological log and seismic horizons. 1 Top of Kimmeridgian White Limestones, 2 Top of Porous Horizon HP4, 3 Top of Lower Oxfordian (nearly top of target interval), 4 Top of Upper Callovian (RIO), 5 Top of Carbonated Dogger (Base of target interval), 6 Base of Argillaceous limestones and marls, 7 Base of Carbonated Dogger, 8 Top of Domerian, 9 Base of Lias (base of Gryphees limestone), 10 Top of Beaumont dolomite.*

The deformations associated with tectonic plate movements have remained small for the past 150 million years, as in the rest of the Paris Basin (Guillocheau *et al.*, 2000; Megnien, 1980). They are essentially limited to the Gondrecourt and Marne grabens, on the boundary of the sector studied (André *et al.*, 2004; Rocher *et al.*, 2004). The geological and geophysical studies have shown that the Cox layer is regular and virtually flat between these faults. Available data confirms that the region has very low seismicity.

7.2 Seismic designs and processing sequence

Figure 7.3 is a map showing the location of the 2D seismic line 07EST10 crossing the area covered by the 3D survey (in purple) and the location of 2 lines extracted from the 3D block: the in-line 405 (IL405) and the cross-line 217 (XL 217). Although there are no boreholes located in the 3D seismic survey area, additional 2D lines have been recorded to calibrate the 3D seismic data by tying to 3 wells (pink circles) situated outside of the 3D area. Line 07EST10 is an example of the additional 2D seismic lines. Well EST433 is located on the line 07EST10 in the vicinity of the CMP 654 (Common Midpoint).

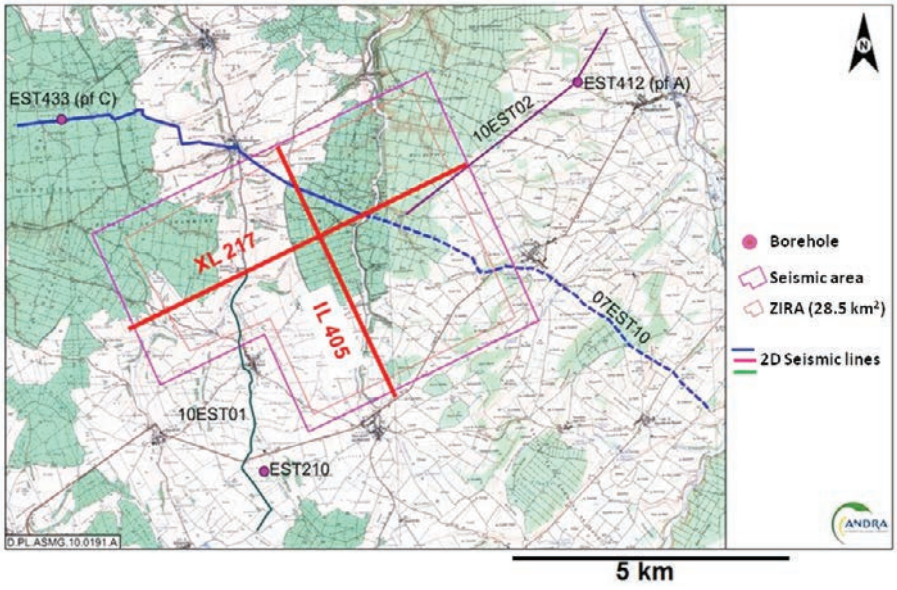

Figure 7.3 *Seismic line implementation and well locations.*

For the 3D seismic acquisition, the active spread (or template) is composed of 12 receiver lines with 120 stations on each line, with a cross-line roll along of

6 receiver lines. The source lines are perpendicular to the receiver lines. The receiver and source line spacings are respectively 80 m and 120 m. The receiver and source point spacings are 20 m. The receiver is an array of 12 geophones. The length of the array equals the receiver interval (20 m). The source is a vibroseis source generating a signal in the 14-140 Hz frequency bandwidth. The bin size is 10 x 10 m^2. The nominal fold is 60. The in-line IL 405 is composed of 544 CMP points. The cross-line XL 217 is composed of 772 CMP points.

For the 2D seismic acquisition, the shot point is located at the centre of the receiver spread composed of 120 stations. The receiver and source point spacings are 25 m. The source is a vibroseis source generating a signal in the 14-140 Hz frequency bandwidth. The bin size is 12.5 m. The nominal fold is 60. The selected part of the 2D line 07EST10 is composed of 727 CMP points.

The main aim of the processing was to apply an amplitude preserving sequence and to accurately image the target zone. Frequencies above 100 Hz were also present in the final data volumes. Andra supplied a geological model (distribution of velocities in depth), which was used to compute a first set of static corrections (Figure 7.4). An up-hole survey consisting of 20 wells was used to calibrate the static correction model. The use of the statics model and a consistent processing approach for both the 2D seismic lines and the 3D seismic volume ensured a good match between them.

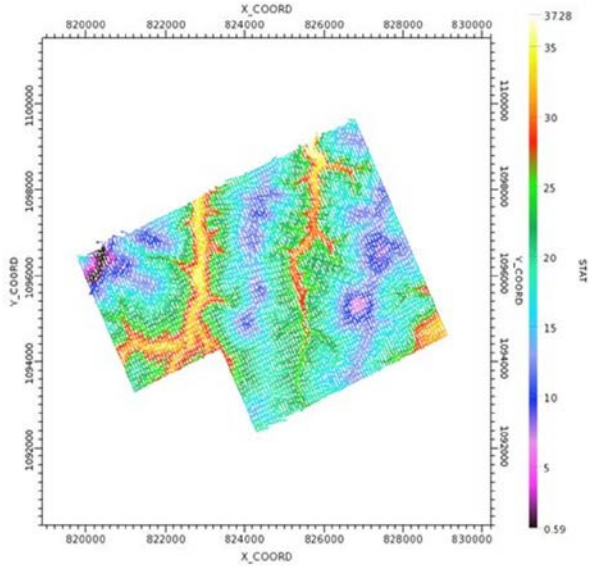

Figure 7.4 *Map of basic static corrections (Andra document).*

Although the area was generally rural, there were high levels of ambient noise, both linear and random. The 3D survey is located in forest and rural areas. In land seismic the variability of receivers is related to geophone coupling with the ground and

to surface conditions. One of the main challenges of the processing was to effectively attenuate the noise and compensate source and receiver coupling as part of an amplitude preserving processing sequence. A methodical multi-domain approach, including shot, common offset and post stack domains, was used to analyse and apply suitable algorithms to progressively attenuate the observed noise. An iterative approach was seen to be the best method to optimize the noise attenuation and the compensation of source and receiver variability. The final pre-PSTM (Pre Stack Time Migration) sequence dedicated to noise attenuation and source-receiver variability compensation proved effective and achieved the aim of creating amplitude-preserved PSTM data.

The main seismic processing sequence steps were:

- data editing,
- minimum phase conversion,
- amplitude compensation (spherical divergence correction),
- surface consistent amplitude compensation (source and receiver),
- de-noise and wave separation on shots,
- statics application (data shifted to floating datum),
- surface consistent deconvolution,
- velocity analysis,
- surface consistent residual statics,
- second pass velocity analysis,
- surface consistent amplitude compensation (source, receiver and offset),
- interpolation and regularization in offset planes and noise attenuation,
- velocity model updating (residual move out),
- QC: 60 fold CMP stack (0-1,400 m offsets) with static to the final datum (450 m MSL),
- pre-stack time migration (time shifted to the final datum: 450 m MSL),
- Q compensation (Q =100),
- Noise attenuation and phase conversion (statistical to zero phase),
- Band pass filter (15, 20-140, 160 Hz).

However, using the processing sequence described, some undulations of the seismic horizons in time were observed on the obtained seismic lines. The undulations, which have no geological meaning, are characteristic of long wavelength static anomalies, which do not degrade the stack but can introduce structural anomalies. They are due to lateral variations in the properties of the weathering or shallow layers (elevation effects, lateral velocity variations, dip) which are negligible at the scale of the recording spread or CMP gather but not negligible at the scale of the seismic line. Short wavelength anomalies are detectable at the spread length and they degrade the CMP stack. They can be compensated for by the residual static correction methods.

In this area of the Paris Basin, the layer of the first 20 meters of variable velocity is the most sensitive layer of the static model. It largely conditions the shapes of

seismic horizons and is the source of the long wavelength static anomalies. The velocities in the first 20 m are sensitive to:

- the nature of the formations affected by the alteration (Valanginian sands, Portlandian limestones or Kimmeridgian marls),
- the geomorphology (difference in velocities observed between plateaus, hillsides and valleys).

To compensate the long wavelength static anomalies, two procedures can be carried out:

- obtain a new set of static corrections based on refraction surveying (weathering shots) and up-hole surveying (VT: vertical times); including all the geological information available (geological maps). The seismic dataset must be completely reprocessed,
- estimate the geological time variation of the seismic horizons. The methodology is based on an a priori knowledge of the structural shape of the geological model. In 3D, a map of LWL static corrections has to be computed, the more appropriate method being a kriging method which allows the filtering of the map of the picked times of a reference horizon into a trend map and a residual map.

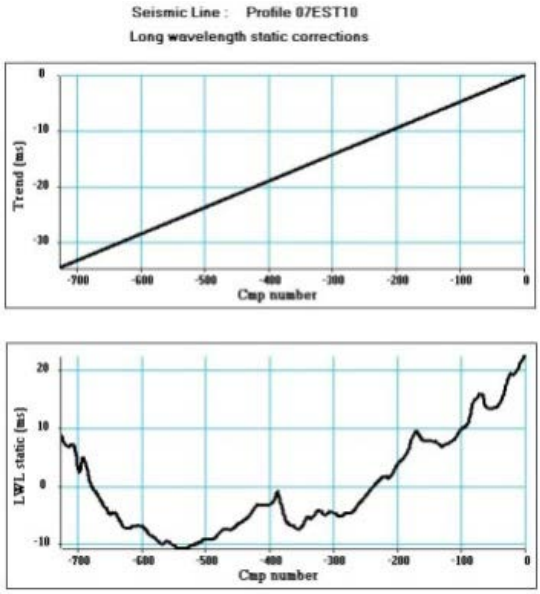

Figure 7.5 *Long wavelength wave static correction - trend and LWL static curve.*

To compensate the long wavelength anomalies, the picked times of major seismic horizons (0.3 – 0.6 s) have been considered as the stack of 2 functions: a trend which represents the geological time variation of the seismic horizon and a residual time function which represents the long wavelength anomaly correlated with

the topographic variations of the floating DP. The residual time function is a long wavelength static correction which is applied on the post-stack migrated sections to compensate the long wavelength LWL static anomalies. Figure 7.5 shows the LWL static curve and the associated trend for the 2D line 07EST10. Figure 7.6 shows the 2D line 07EST10 before and after LWL static compensation.

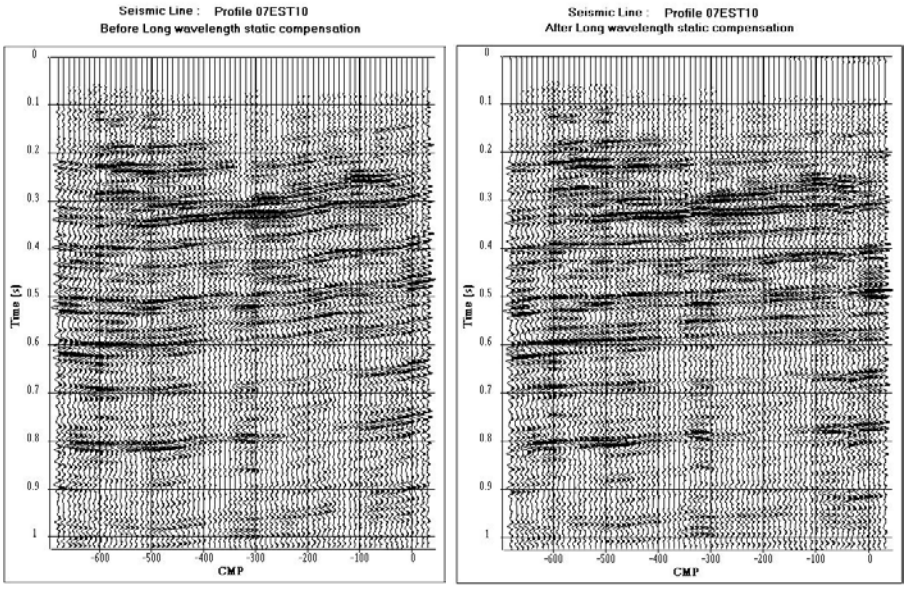

Figure 7.6 *Long wavelength wave static compensation after stack. Left: seismic line before LWL static compensation. Right: seismic line after LWL static compensation.*

During the migration process (Robein, 2003), the data are migrated and sorted into common image gathers (CIG) to update the velocity model before stacking. Each image gather is composed of migrated seismic traces which are functions of time (time migration) and offset or angle. The offset-angle conversion can be carried out during or after the migration process by using the velocity model. The common image gathers after offset-angle conversions are used to perform Amplitude versus Angle analysis (Castagna, 1993; Walden, 1991) and elastic inversion (EI). The small angle amplitudes (near-offset or intercept) migrated stacks relate to changes in acoustic impedance (AI) and can be inverted back to AI using a post-stack inversion algorithm (acoustic inversion). The acoustic impedance is a simple function of P-wave velocity Vp and density ρ(AI = ρ.Vp). The amplitudes of angle migrated stacks relate to changes in elastic impedance EI (θ). They can be inverted back to impedances Ip (Ip = AI = ρ.Vp) and Is (Is = ρ.Vs) using a linearization of Zoeppritz equations for P-wave reflectivity R(θ). The reflectivity R(θ) is a function of the incidence angle (θ) and depends on the variations ΔVp, ΔVs, $\Delta\rho$ of the mechanical parameters (Vp, Vs, ρ) of the two media located on each side of the discontinuity which generates the reflection.

Shuey (1985) proposes the following approximation between the reflectivity R(θ), the elastic impedance EI(θ) and the mechanical parameters:

$$R(\theta) = \frac{1}{2}\frac{\Delta EI(\theta)}{EI(\theta)} = A + B\sin^2(\theta) \quad \text{with} \quad A = \frac{1}{2}\frac{\Delta Ip}{Ip} = \frac{1}{2}\left(\frac{\Delta Vp}{Vp} + \frac{\Delta \rho}{\rho}\right) \qquad (7.1)$$

The coefficient B is called the gradient and can be approximated by:

$$B = \frac{1}{2}\left(\frac{\Delta Vp}{Vp} - \frac{\Delta \rho}{\rho} - 2\frac{\Delta Vs}{Vs}\right) \qquad (7.2)$$

The parameter *A* in equation (7.1) represents the seismic trace as a compressional wave associated with acoustic impedance contrast Ip. The parameters *A* and *B* represent the seismic trace as a shear wave associated with acoustic impedance Is contrasts. If the incidence angle equals 0 (θ=0), the elastic impedance EI(θ) is the acoustic impedance Ip. Equations (7.1) and (7.2) show that the elastic impedance EI(θ) is a function of P-wave velocity *Vp*, S-wave velocity *Vs*, and density ρ. Connolly (1999) shows that the elastic impedance EI(θ) can be written as follows:

$$EI(\theta) = Vp^{(1+\tan^2\theta)}Vs^{-8K\sin^2\theta}\rho^{(1-4K\sin^2\theta)} \quad \text{with} \quad K = \frac{Vs^2}{Vp^2} \qquad (7.3)$$

Such processing is referred to elastic inversion (Shuey, 1985; Connolly, 1999; Whitecombe *et al.*, 2002). A model-based elastic inversion (a priori impedance model obtained from well data), applied to the angle migrated stacks, provides impedance sections (Ip and Is sections). In our field case, three angle migrated stacks have been generated (0-14°, 14-28°, 28-42°) to perform the elastic inversion to compute Ip and Is – sections.

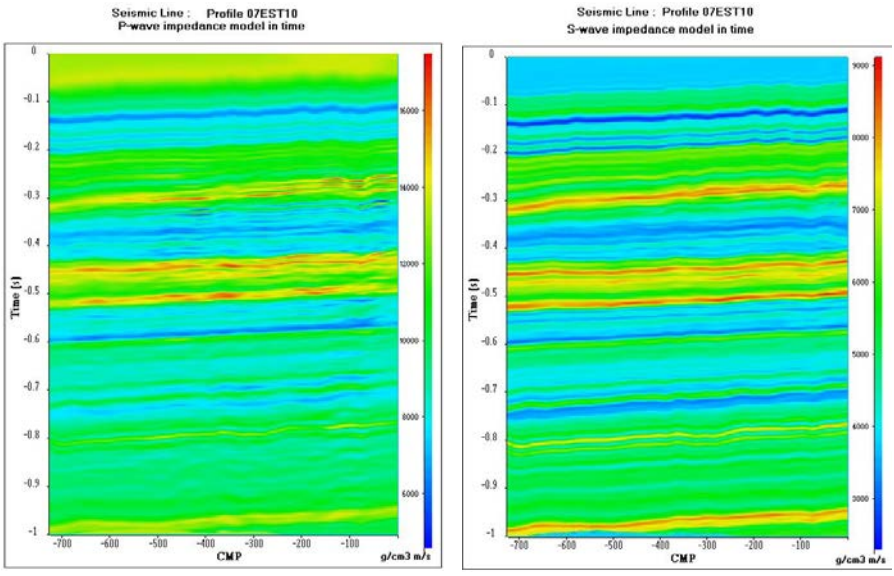

Figure 7.7 *Ip and Is sections for the 07EST10 profile.*

Figure 7.7 shows the Ip and Is - sections associated with the 07EST10 profile.

Figures 7.8 and 7.9 show the results for the profiles extracted from the 3D block: IL405 and XL217. For each profile, we show the PSTM sections before and after LWL static compensation, the Ip and Is – sections.

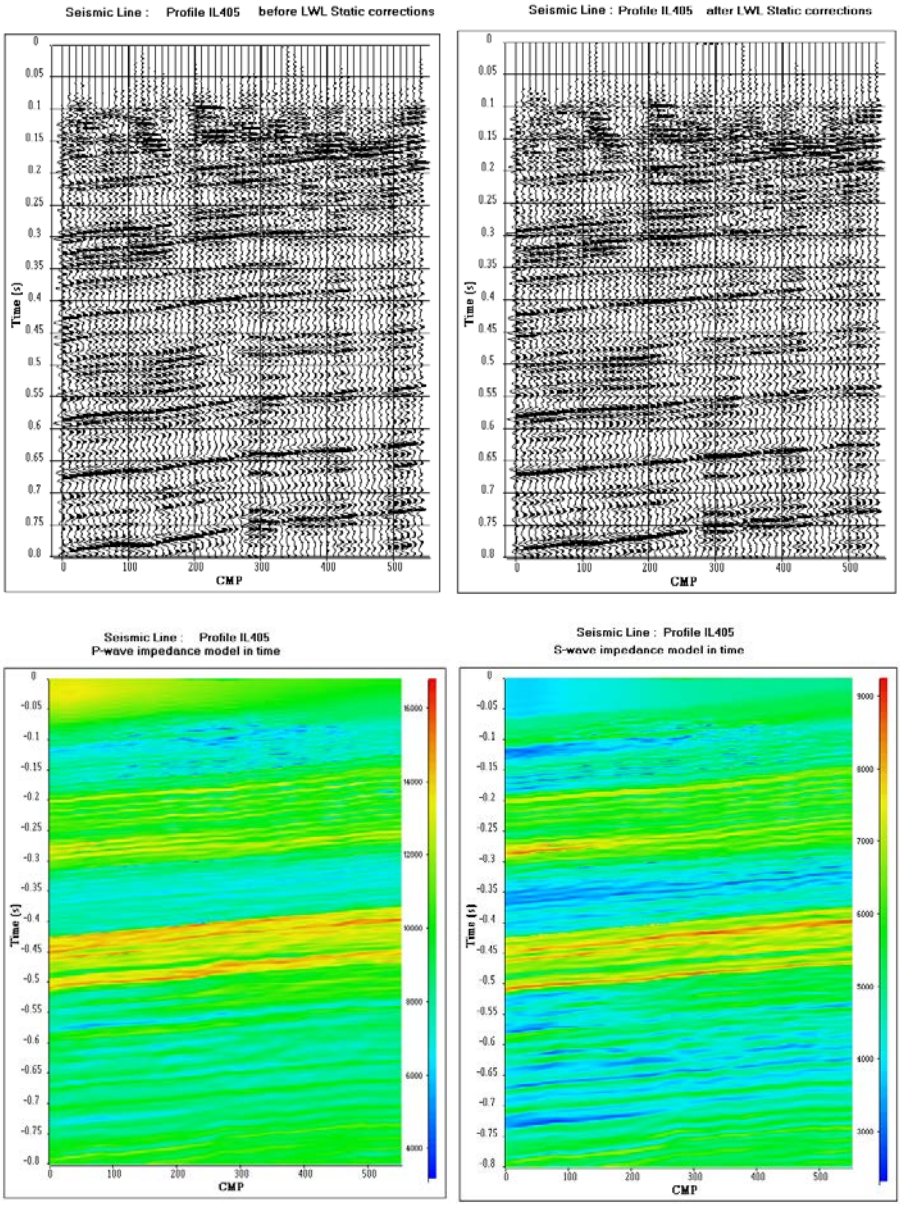

Figure 7.8 *IL 405 profile. Top: PSTM sections before and after LWL static compensation. Bottom: Ip and Is sections.*

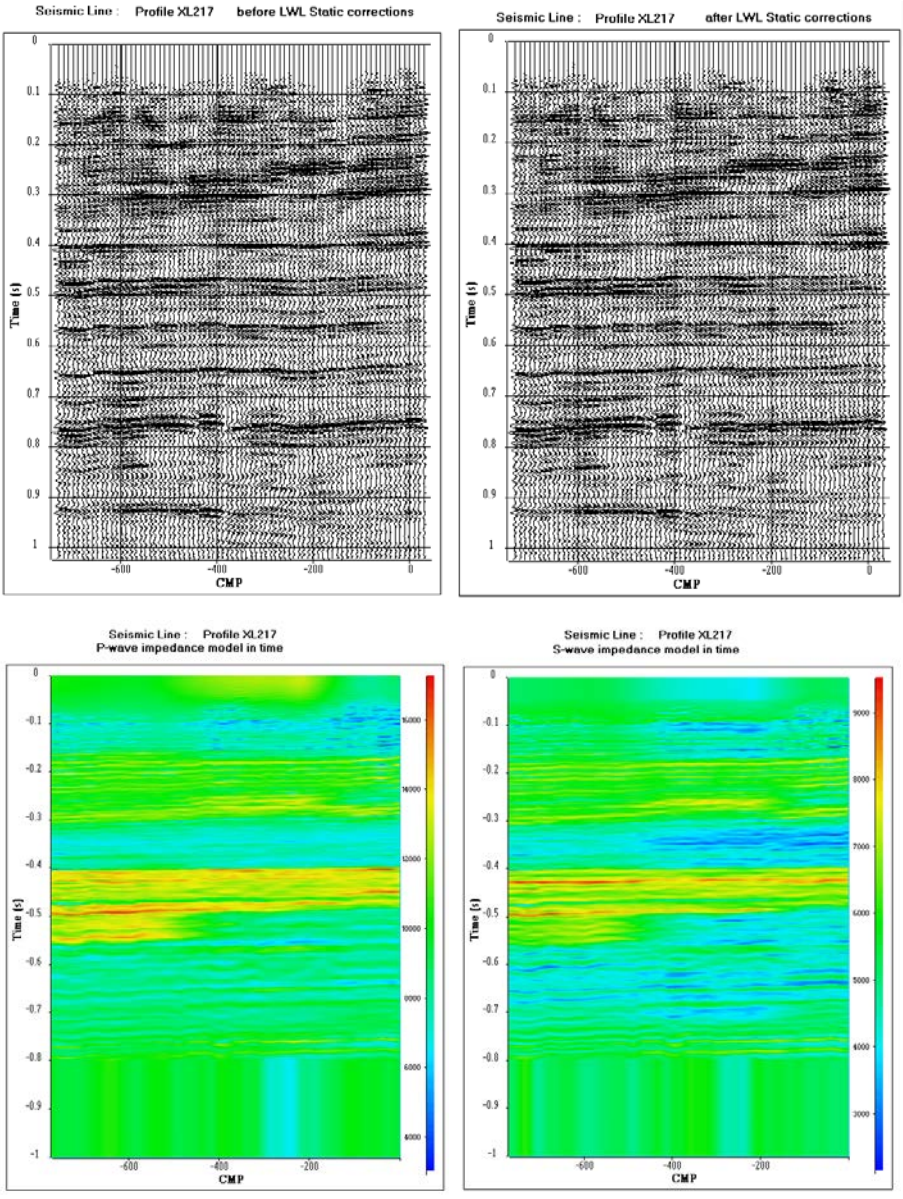

Figure 7.9 *XL 217 profile. Top: PSTM sections before and after LWL static compensation. Bottom: Ip and Is sections.*

7.3 Depth conversion

A geostatistical approach for time-to-depth conversion of seismic horizons is often used in many geo-modelling projects. The more appropriate kriging method for this problem is the Bayesian Kriging method (Sandjivy and Shtuka, 2009). The Bayesian approach provides an excellent estimation, which is more general than the traditional kriging with external drift(s) and fits very well with the requirements for time-to-depth conversion of seismic horizons. For each selected horizon, Bayesian Kriging (BK) provides its estimated depth Z associated with its time t, in agreement with all the calibration points (well tops depth…). BK depth conversion also provides the underlying interval velocity model (trend and residual), and associated quantified uncertainties. The BK depth conversion simultaneously updates the estimated depths of all the seismic horizons.

Figure 7.10 illustrates the time-to-depth conversion of seismic horizons by the BK method, using the UDOMORE depth software developed by Seisquare. The advantage of using the Bayesian Kriging (BK) for estimations compared to other approaches is that we can simultaneously manage the uncertainty on the trend velocity model and the local uncertainty defined by the uncertainty of interpreted time maps and local fluctuations of interval velocities.

The input information required for BK consists of:

- two-way-time (TWT) maps for interpreted horizons,
- well markers for each horizon,
- prior velocity model and associated uncertainty for each layer,
- local uncertainty definition for each time map (picking uncertainty, and spatial variogram definition),
- local uncertainty definition of interval velocity for each layer (local velocity fluctuations around the trend model, and spatial variogram definition).

Like any kriging-based estimation approach, the Bayesian Kriging (BK) provides:

- the estimated variable (estimated depth for each horizon),
- variance of estimation (associated uncertainty of estimated depth).

The advantage of using BK in depth conversion is that it provides the ability to combine the prior knowledge of the velocity model with a certain degree of uncertainty and the well data. All sources of uncertainty (velocity and time) are integrated in a consistent way in a unique probabilistic model used for estimation or simulation.

For each selected horizon, the Bayesian Kriging provides its estimated depth Z associated with its time t. The "Z versus t" data set is interpolated in the whole space (3D block) at the time sampling rate (1 ms) to obtain a time-to-depth conversion model, using the impedance sections to estimate the short wavelength variations of the velocity model.

The time-to-depth conversion procedure is illustrated via the line XL 217 (see location map, Figure 7.3). Ten seismic horizons, numbered 1 to 10, have been picked in time and converted to depth. The 10 seismic horizons are:

1. Top of Kimmeridgian White Limestones
2. Top of Porous Horizon HP4
3. Top of Lower Oxfordian (close to the top of target interval)
4. Top of Upper Callovian (RIO)
5. Top of Carbonated Dogger (base of target interval)
6. Base of Argillaceous limestone and marls
7. Base of Carbonated Dogger
8. Top of Domerian
9. Base of Lias (base of Gryphees limestone)
10. Top of Beaumont dolomite

Figure 7.10 shows the picked times of the 10 seismic horizons (left) and the depth conversion of the 10 horizons (right).

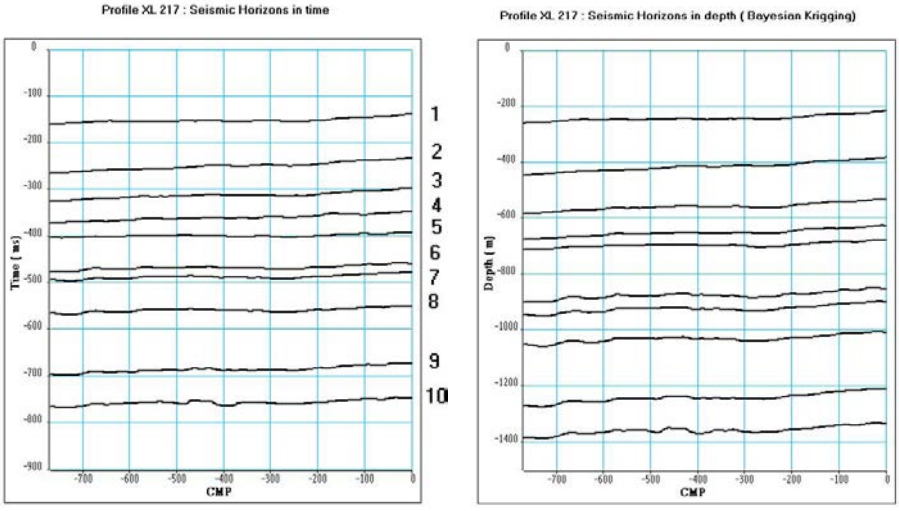

Figure 7.10 *Time-to-Depth of seismic horizons by Bayesian Kriging. Example of the XL 217 profile (left: horizon in time, right: horizons in depth).*

To obtain a high-resolution velocity model, the acoustic impedance Ip obtained by inversion can be used assuming that the P-wave velocity and the density of a formation vary in a consistent way (an increase of velocity is associated with an increase of

density) and a relationship between the two variables exists. The Gardner's relation (Gardner *et al.*, 1974) given by the following equation $\rho = \alpha Vp^{\beta}$ is often used.

The logging data (sonic and density logs) recorded at well Est433 (see map location, Figure 7.3) have been used to compare acoustic impedance *Ip* and velocity *Vp* logs and the relationship given by equation (7.4) has been checked:

$$\mathrm{Log}(\mathrm{Vp}) = \mathrm{Av}.\mathrm{Log}(\mathrm{Ip}) + \mathrm{Bv} \tag{7.4}$$

The coefficients Av and Bv have been computed in a root mean square sense, between the Vp and Ip logs. The results of the minimization have shown that the Vp log and the predicted P-wave velocity from the acoustic impedance log are strongly correlated (Figure 7.11, left). The correlation coefficient and the Taner-Kohler coefficients between the two velocity logs are very high (> 0.98) and a single law can be used whatever the range of acoustic impedance and whatever the geological unit to obtain a high-resolution velocity model in time Vp given by equation (7.4). Consequently a density log can be easily obtained by the ratio Ip to Vp.

The velocity model was integrated in time to obtain a time-depth conversion model (Figure 7.11, right). The time-depth conversion model was used to convert in depth any type of time-seismic sections such as amplitude, instantaneous frequency, Ip and Is, and consequently Vp, Vs and density.

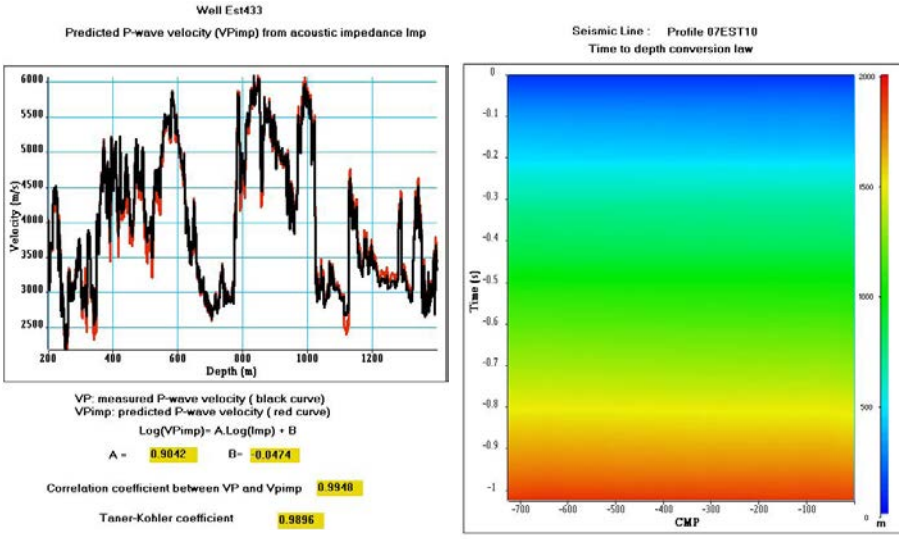

Figure 7.11 *Predicted P-wave velocity model and time-to-depth conversion model.*

The depth conversion is not calibrated in depth. This must be carried out, and it can be performed using the depth conversion of seismic horizons by a geo-statistical method (Omre H. 1987, Sandjivy L. and Shtuka A. 2009) which simultaneously uses Bayesian co-kriging and a multilayer model, and which handles the following sources of uncertainty:

1. Velocity model uncertainty: this relates to regional (trend or low frequency) uncertainty and local uncertainty (high frequency velocity fluctuations that are invisible on the seismic).
2. Time interpretation uncertainty. Even when one considers that interpretation is unbiased and calibrated, there are fluctuations that cannot be observed by the seismic because of limited resolution.
3. Well marker uncertainty.

The depth converted horizons are calibration points for the velocity model extracted from the acoustic impedance distribution. The updated velocity model thus obtained must be consistent with an underlying interval velocity model obtained by the geostatistical method for the time-to-depth conversion of seismic horizons with a resolution comparable to the resolution of the acoustic impedance sections. Some results have already been obtained using seismic lines extracted from the 3D seismic survey recorded on the Zira area (Mari J.L. and Yven B., 2014).

The P-wave velocity distribution Vp and the results of elastic inversion Ip ($Ip = AI = \rho.Vp$) and Is ($Is = \rho.Vs$) are used both to compute the shear wave velocity Vs and the density ρ distributions in depth. The values of densities obtained are realistic for the sedimentary layers present. They vary between 2.25 and 2.70 g/cm^3. In the Callovo-Oxfordian, the highest value of the density is 2.48 g/cm^3.

Figures 7.12 to 7.14 show the results obtained for the 3 profiles: 07EST10, IL405, XL217. For each profile, we show the seismic line after depth conversion, the distribution of P-wave and S-wave velocities in depth, and the distribution of density in depth.

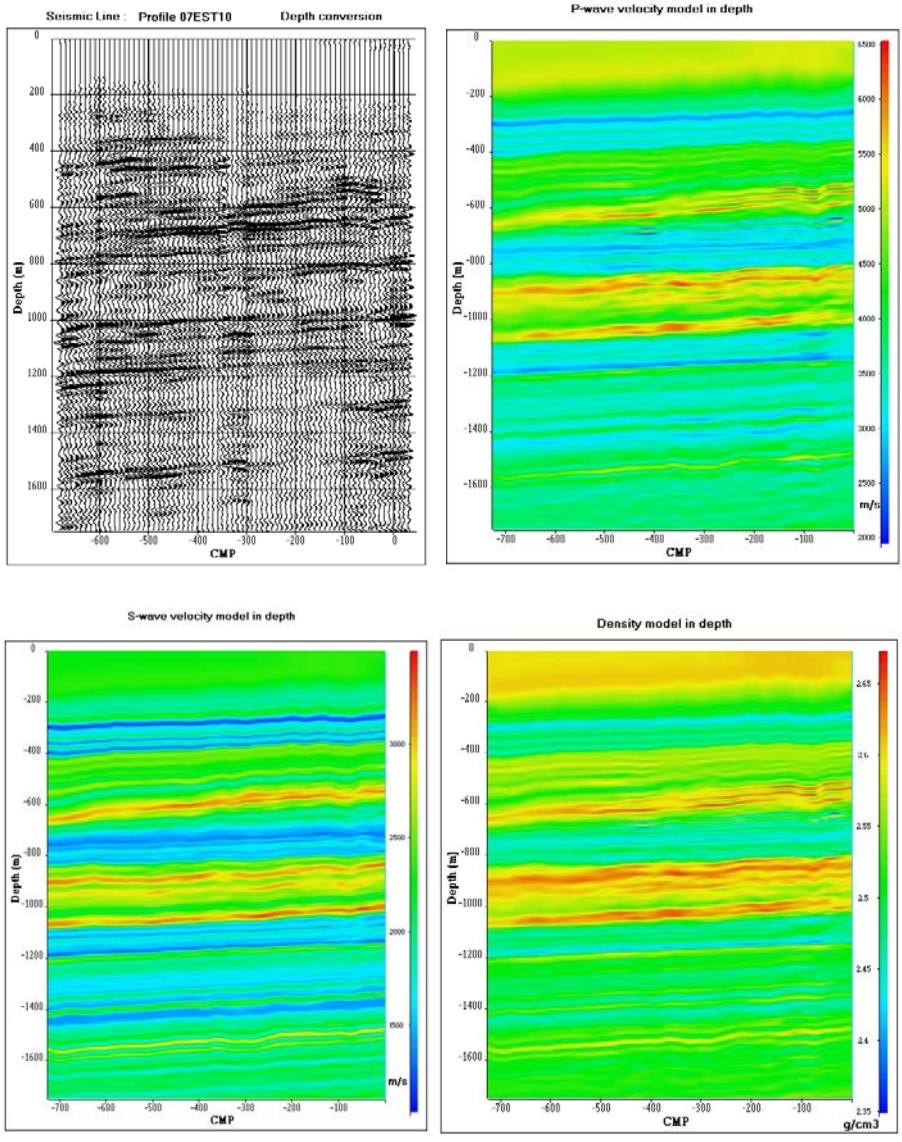

Figure 7.12 *Profile 07EST10. Top: section in depth and P-wave velocity distribution in depth, Bottom: S-wave velocity and density distributions in depth.*

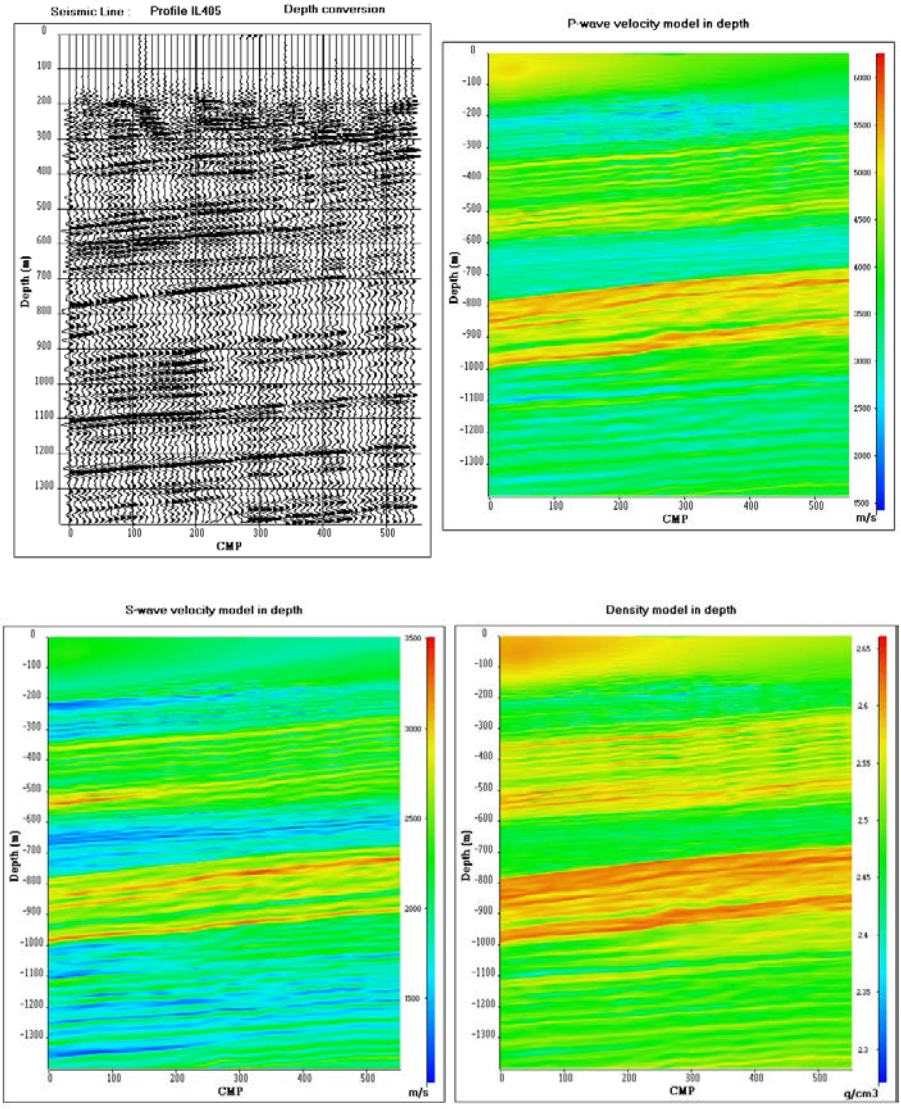

Figure 7.13 *Profile IL405. Top: section in depth and P-wave velocity distribution in depth; Bottom: S-wave velocity and density distributions in depth.*

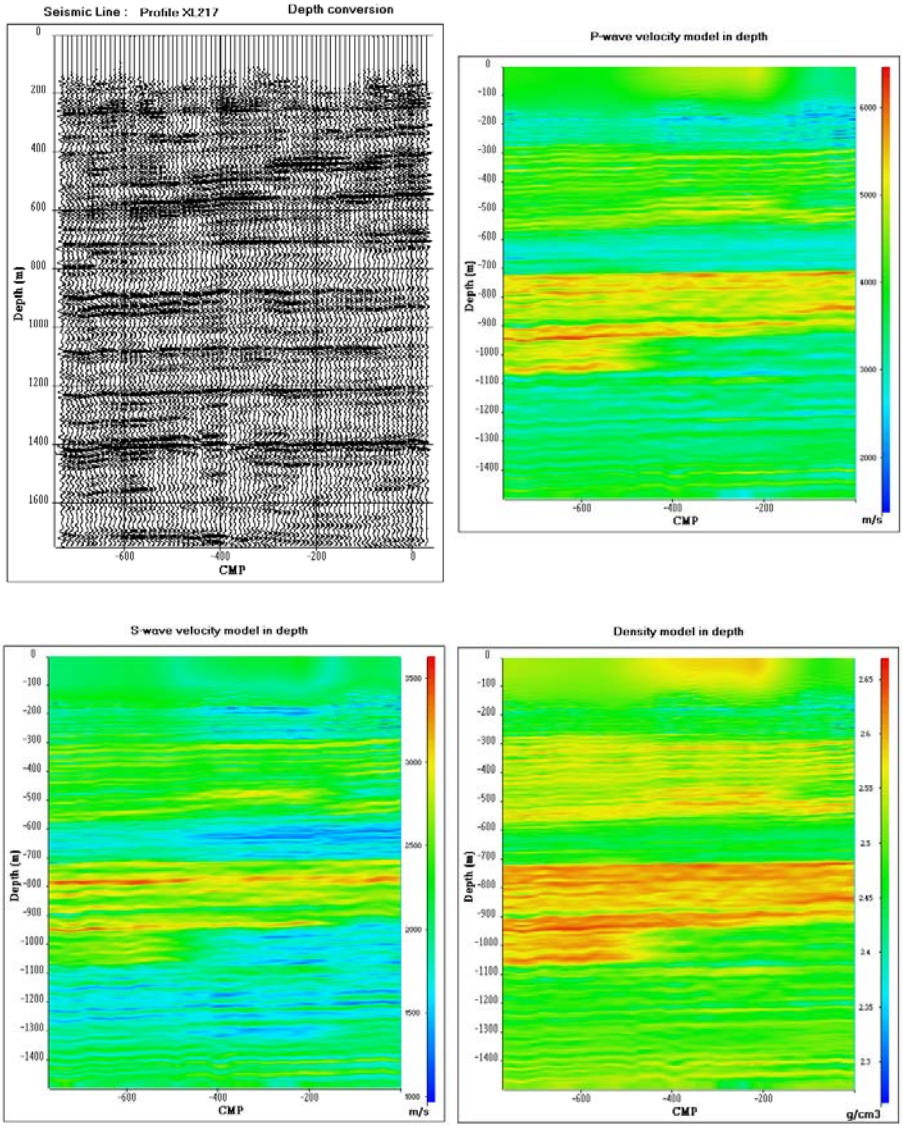

Figure 7.14 *Profile XL217. Top: section in depth and P-wave velocity distribution in depth; Bottom: S-wave velocity and density distributions in depth.*

7.4 Amplitude quality control

A Stochastic Quality Assessment (SQA) workflow has been designed to assess the reliability of the stacked amplitudes and to optimize further modelling of mechanical and hydrogeological properties.

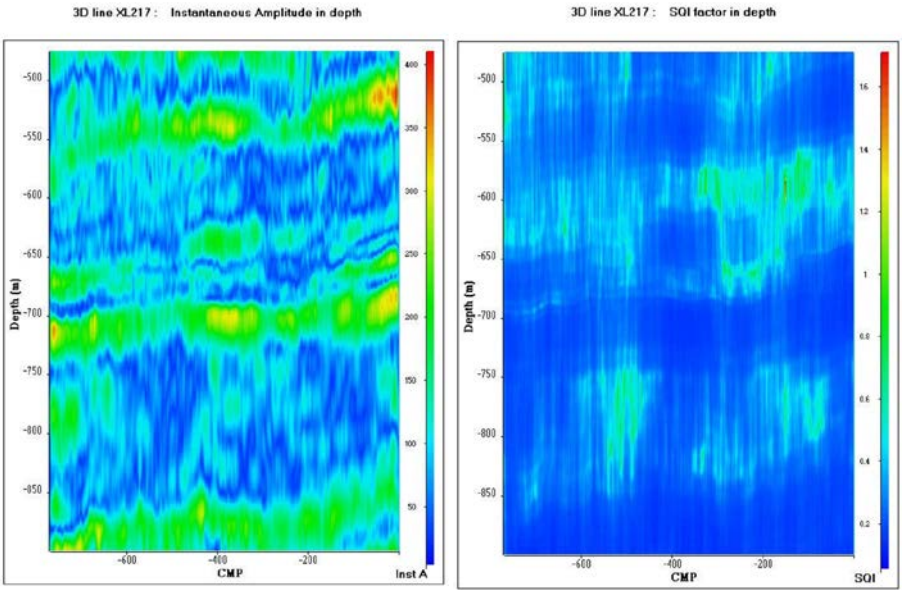

Figure 7.15 *Profile XL217. Instantaneous amplitude (left) and SQI factor (right).*

SQA processing of seismic data works under a mathematical framework known as geostatistics, where the observed (measured) seismic amplitude is considered as a realization of a random function (RF) defined in space and time (Shtuka *et al.*, 2011 and 2009). The added value of using this type of theoretical framework is that it takes into account the spatial correlation between measured seismic amplitudes at different locations using variogram or spatial covariance. Interpretation and modelling of the experimental variogram computed in the offset direction (for fixed time) on pre-stack gather data enables the assessment of the signal and noise content of the seismic measurements in terms of the contributive (signal) and non-contributive (noise) part of the stacking process. The signal/noise interpretation of the variogram is quantified by modelling the experimental variogram accordingly in both horizontal (offset or angle) and vertical (time) directions. SQA handles the global non-stationary behaviour of the gather, by relying only on a local stationarity assumption: local computations and modelling of variogram parameters (sill and ranges) are performed inside a local neighbourhood defined around each sample

location. The variogram model is used to compute the estimated variance of the stacked trace of the gather as the variance of the estimation error: unknown "true" stacked amplitude minus estimated stacked amplitude. The estimation variance is normalized and expressed as a percentage of the stacked amplitude called the Spatial Quality Index (SQI). Low SQI values mean good confidence in the stacked amplitude.

The results shown here were obtained on the XL217 cross-line on the seismic cube (Figure 7.3). Figure 7.15 shows the instantaneous amplitude section (left) and its associated SQI factor (right). The sections are shown in depth. The time-to-depth conversion is discussed later. The quality of seismic instantaneous amplitudes is quantified by their attached SQI values. Blue SQI areas on the seismic section (low SQI values) indicate reliable amplitudes (80 to 90% reliability), green SQI areas indicate less reliable amplitudes (50 to 70% reliability). The more significant processes were analysed in greater detail, confirming that the amplitudes were not adversely affected by the processing.

7.5 Q factor

We present here the methodology developed to estimate the Q factor per layer, using VSP data. It shows how the procedure has been extended to estimate the Q factor of seismic lines.

A number of discussions in the literature use different approaches, which lead to a general form for the frequency dependence of the phase velocity. A synthesis has been carried out by Valera (1993). The resulting expression, which is valid for a relatively large and constant Q, is given by:

$$V(f_1)/V(f_2) = 1 + (1/\pi Q)\cdot \mathrm{Ln}(f_1/f_2) \tag{7.5}$$

Where Q is the constant Q factor, $V(f_1)$ is the propagation velocity at frequency f_1, $V(f_2)$ is the propagation velocity at frequency f_2.

Equation (7.5) can be written as follows:

$$Q = (1/\pi)\cdot(V/\Delta V)\cdot \mathrm{Ln}(f_1/f_2) \tag{7.6}$$

Where $\Delta V = V(f_1) - V(f_2) = \Delta z/\Delta t - \Delta z/(\Delta t + d\Delta t)$ and $V = \Delta z/(\Delta t + d\Delta t) = V(f_2)$

Equation (7.5) shows that the high frequency components of a wave train propagate faster than the low frequency components.

For a VSP, Q is computed from equation (7.6). For 2 geophone positions (Δz apart), ΔV is estimated from the variation Δt of the arrival times of the down-going wave over a distance Δz and from $d\Delta t$ the residual variation of Δt due to the variation of frequency between f_1 and f_2.

Figure 7.16 (top left) shows a VSP recorded in well Est 433 (Figure 7.3) as well as its frequency-wavenumber (f-k) diagram. It is composed of 221 levels, with a depth sampling of 5 m between 112 and 687 m, and a depth sampling of 10 m between 687 and 1,737 m. The source is a vibrator (sweep 14-140 Hz). The time sampling is 1ms and the recording length is 2 s after correlation. The down-going and up-going waves have been separated by f-k filtering. To obtain an estimate of the Q factor per layer, we used the fact that attenuation introduces dissipative dispersion, which can be measured from the frequency-dependent phase velocity of the VSP down-going wave (equation (7.6)). The picked times of the first pick of the first arrival have been used to compute the velocity log versus depth, and to measure the frequency log from the instantaneous frequency VSP section, using the analytic signal computed by the Hilbert transform. The 2 logs are shown in Figure 7.16 (top right). The down-going waves have been filtered with a low frequency band (8-28 Hz). The average value of the instantaneous frequency f_2 of the filtered down-going wave is 21.5 Hz and the associated standard deviation is 2 Hz. A scan procedure in $d\Delta t$, equivalent to a velocity scan, was implemented to estimate the quantity ΔV and the Q factor (equation (7.6)), the search carried out in a realistic Q value domain, such as between 20 and 100 (Mari and Yven, 2018). If the f_1/f_2 ratio is close to a constant, the $V/\Delta V$ ratio is a linear function of Q. For Q ranging from 20 to 100, the $V/\Delta V$ ratio varies from 50 to 250 for an f_1/f_2 ratio of 3.5 (Figure 7.16, bottom left).

Figure 7.16 (bottom left) shows, from top to bottom: the $V/\Delta V$ curve for an f_1/f_2 ratio of 3.5; the $d\Delta t$, ΔV and $V/\Delta V$ curves versus the level of the borehole geophone. The average value of the ΔV curve is 27 m/s and its associated standard deviation is 4 m/s. Figure 7.16 (bottom right, black curve) shows the computed Q factor log. Q values vary between 33 and 96. Due to standard deviation low values of the ΔV curve (4 m/s) and of the f_2 frequency curve (2 Hz), the Q factors can be predicted using constant values for ΔV and f_2. The predicted Q-factor curve is shown in Figure 7.16 (bottom right, red curve) as well as the associated relative uncertainty (10% on average) between the 2 Q-logs. The correlation coefficient between the 2 Q-logs is high (0.94). The correlation coefficient between Q factors and interval velocities is 0.69. The Q factor of the Cox (550-700 m) is estimated at 40, while the Q factors of the Oxfordian and Dogger limestone located directly above and below are higher, ranging from 65 to 90.

The results have been validated on a second well, Est 412 (Figure 7.17), the predicted Q values being estimated from the law defined at well Est 433. The uncertainties between the 2 Q-logs are weak, ranging between 0.5 to 30%. Consequently, the predicted Q log can be applied to surface seismic data if interval velocities $V(f_1)$ and instantaneous frequencies f_1 are measured.

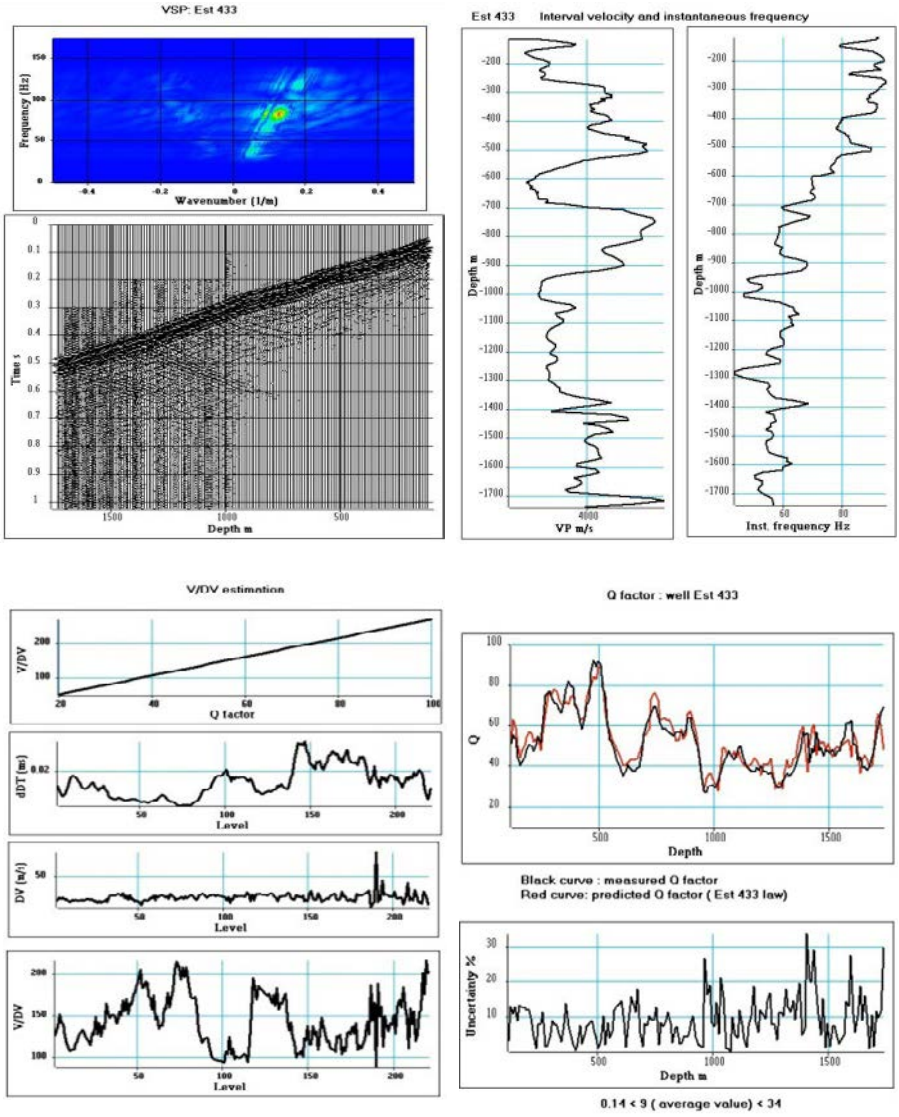

Figure 7.16 *VSP and Q factor at well Est 433. Top left: VSP and its associated f-k diagram; Top right: Velocity (V(f1)) and frequency (f1) logs. Bottom left: V/ΔV estimation: Bottom right: Q factors (measured, predicted) and uncertainties.*

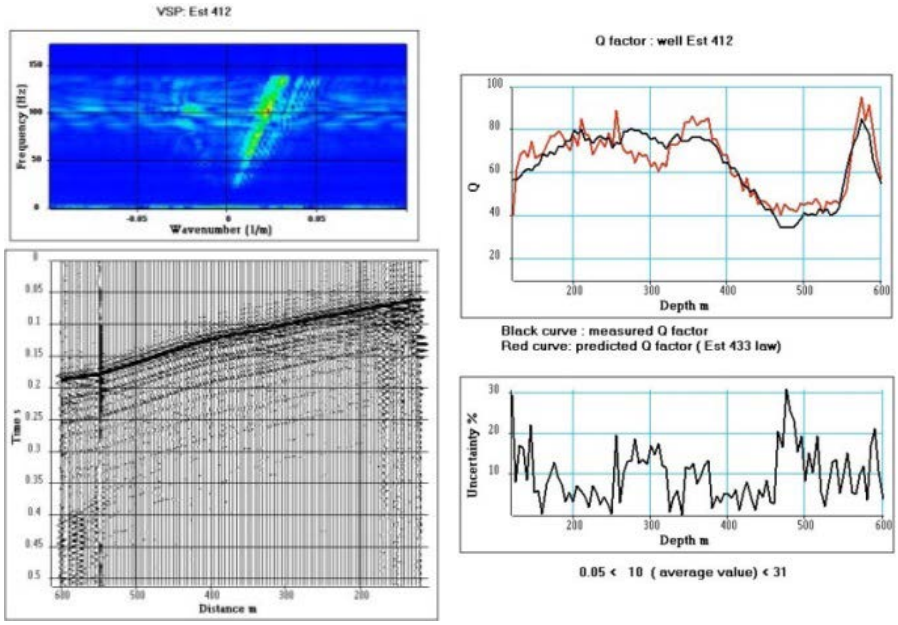

Figure 7.17 *VSP and Q factors with uncertainties at well Est 412.*

For each seismic line in time, the instantaneous frequency section has been computed by analytic signal (Hilbert transform), and then depth converted. The distributions in depth of the instantaneous frequencies and P-wave velocities (Figures 7.12 to 7.14) have been used to predict the distribution of the Q-factor in depth, using equation (7.6) with the constant values for ΔV and f_2 given by the VSP analysis carried out at well Est 433.

The instantaneous frequency section and the Q-factor distribution for the line 07 EST10 are shown in Figure 7.18 (top). Figure 7.18 (bottom) also shows the Q-factor distributions for the lines IL405 and XL 217.

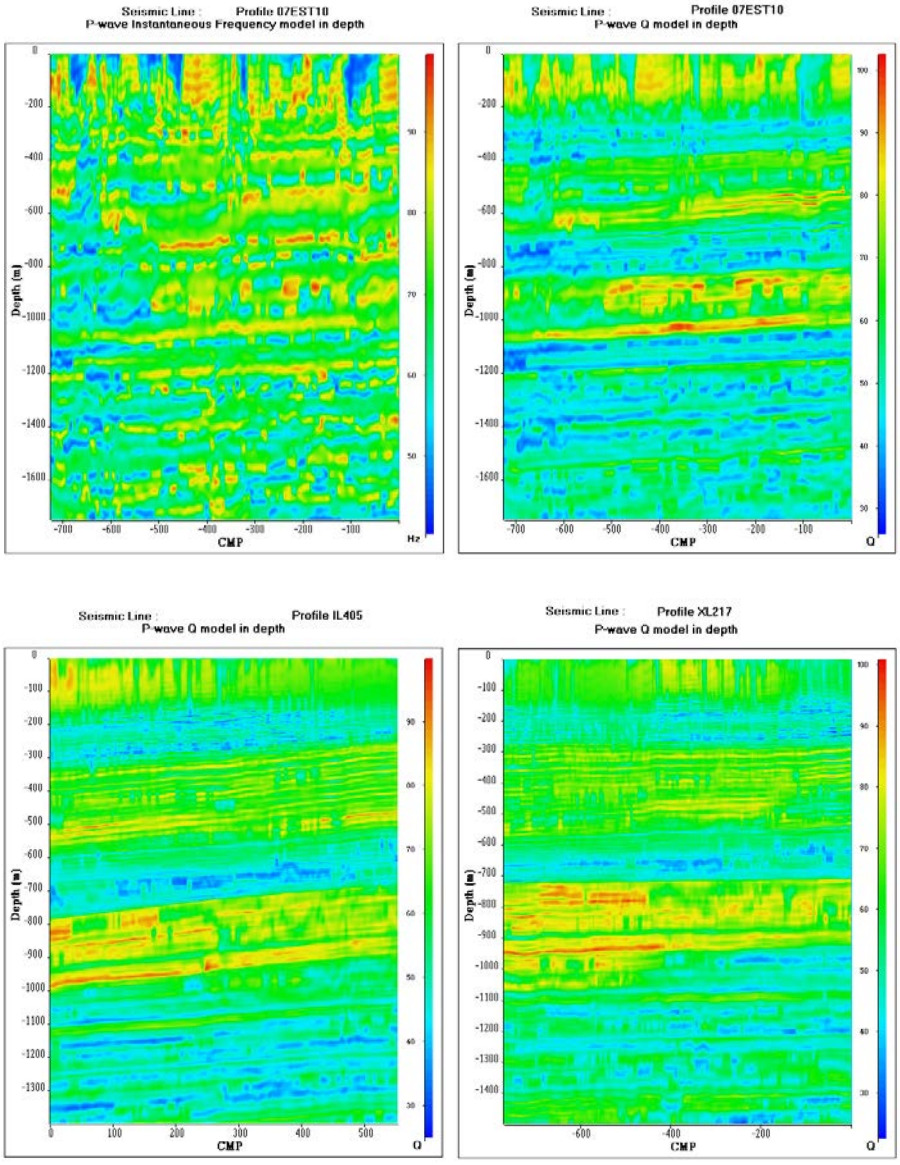

Figure 7.18 *Q models in depth. Top: Profile 07EST10. Instantaneous frequency and Q model. Bottom: Profiles IL405 and XL217. Q models.*

7.6 Mechanical properties

To prepare for the construction and operation of a deep geological disposal facility, the mechanical behaviour of the rock formations must be well understood. One of the parameters studied for this purpose is the Young's modulus. A workflow has been developed to estimate static Young's moduli in claystone and limestone formations on seismic lines.

The P-wave and S-wave velocity (Vp, Vs) distributions and the density ρ_{bulk} distribution obtained by elastic inversion of the seismic data after calibration on well data (VSP and acoustic logs) enable the computation of dynamic mechanical modules, such as the shear modulus (μ), Young's modulus (E), Poisson's ratio (ν). The dynamic Young's modulus is given by the following formula (equation (7.7)):

$$E = \rho_{bulk} V_P^2 \frac{(1-2v)(1+v)}{(1-v)},$$

$$v = \frac{(V_P/V_S)^2 - 2}{2\left[(V_P/V_S)^2 - 1\right]} = \frac{V_P^2 - 2V_S^2}{2\left(V_P^2 - V_S^2\right)} \tag{7.7}$$

The Vp, Vs and ρ_{bulk} distributions for the seismic lines 07EST10, IL405 and XL217 are shown in Figures 7.12 to 7.14 respectively.

Mechanical properties of the Callovo-Oxfordian clay formation were characterized in the laboratory (deformation modulus, compressive strength, tensile strength, etc.) using conventional triaxial or uniaxial compression tests. Samples that were significantly desaturated (Sr < 90%) or damaged were eliminated from the analysis. Finally 39 core samples, selected from the Cox in well Est 433, were used to measure the static Young's moduli ES in the laboratory. At the same depths, logging data (acoustic and density logs) were used to compute the dynamic Young's moduli ED. The results are shown in Figure 7.19 (top left).

A description of methods for determining the relationship between static and dynamic Young's moduli can be found in a number of standard texts. A synthesis is given by Eissa and Kassi (1988). In the laboratory it has been shown that it is possible to predict the static moduli values ES from the dynamic values ED. The appropriate function relating to the high correlation coefficient between measured and predicted static values is the linear function:

$$ES = a.ED + b \tag{7.8}$$

However, Eissa and Kassi (1988) have shown that the value of the static modulus of elasticity can be best predicted from the relationship:

$$Log_{10}(ES) = a.Log_{10}(\rho_{bulk}\, ED) + b \tag{7.9}$$

Equation (7.9) has been used to compute the static Young's modulus using logging data (dynamic modulus computed by equation (7.7)) and core data (static modulus obtained in the laboratory). The coefficients "a" and "b" are evaluated to obtain an optimum fit between the static modulus from core data with the predicted static modulus from logging data (Yven and Mari, 2018). Figure 7.19 (bottom left) shows the static Young's moduli from the laboratory (blue crosses), the dynamic Young's from logs (black crosses), and the predicted static Young's moduli (red crosses). Figure 7.19 (right) shows the associated histograms.

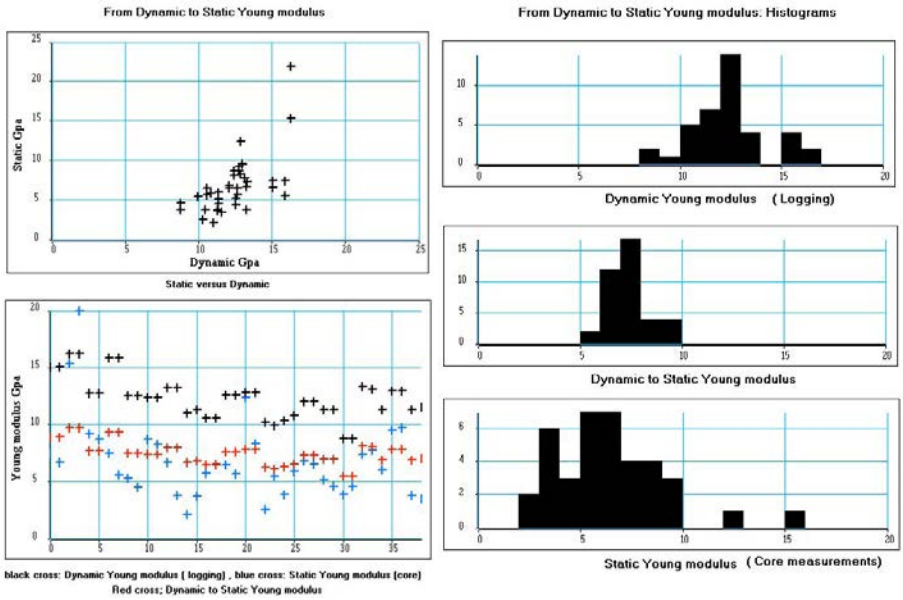

Figure 7.19 *From dynamic to static moduli. Left: static Young's moduli from laboratory (blue crosses), the dynamic Young's moduli from logs (black crosses), and the predicted static Young's moduli (red crosses). Right: histograms.*

Figures 7.20 to 7.22 show the results obtained on the seismic profiles 10EST10, IL405 and XL217 respectively. For each seismic line, we show the distribution of dynamic Young's moduli in depth computed from the Vp, Vs and density distributions obtained by elastic inversion and depth conversion, the distribution of static Young's moduli in depth given by equation (7.9), the static to dynamic ratio distribution in depth, and the histograms of the two sets of moduli. The Static to Dynamic Young's modulus ratio varies between 0.49 to 0.58. The static to dynamic conversion has been carried out with cores from the Cox. In future, the relationship between static and dynamic will be analysed with other boreholes, per each geological unit.

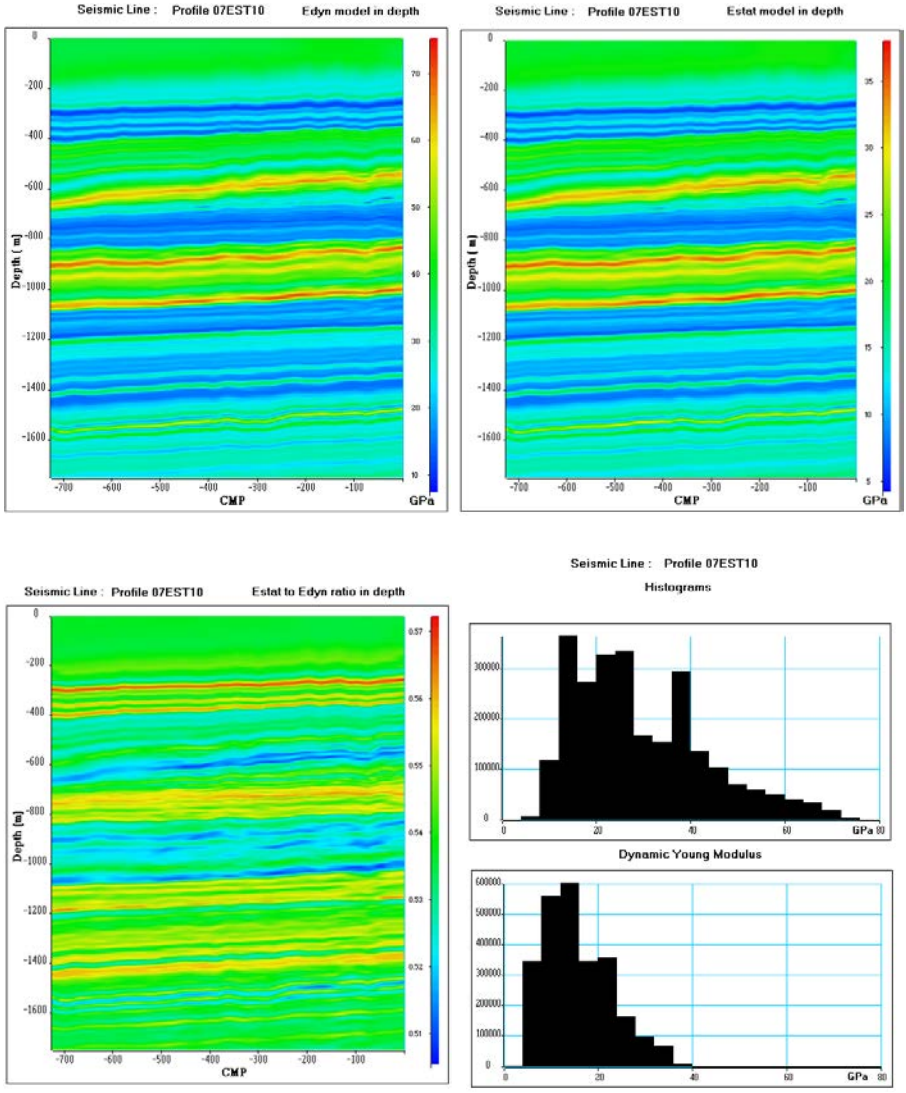

Figure 7.20 *Seismic line 07EST10 - From dynamic to static moduli. Top: distribution of dynamic (left) and static (right) Young's moduli in depth. Bottom: Static to dynamic ratio in depth (left), Histograms of dynamic and static Young's moduli.*

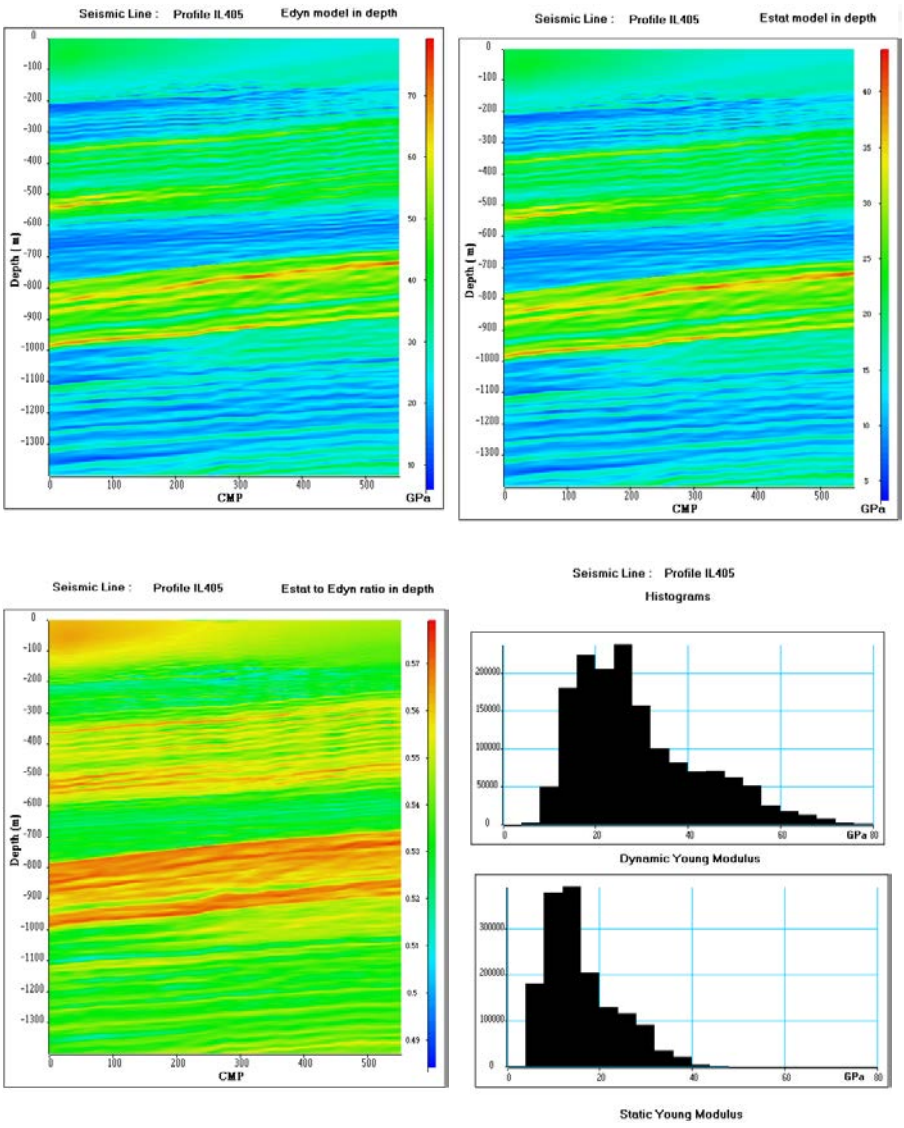

Figure 7.21 *Seismic line IL405 - From dynamic to static moduli. Top: distribution of dynamic (left) and static (right) Young's moduli in depth. Bottom: Static to dynamic ratio in depth (left), Histograms of dynamic and static Young's moduli.*

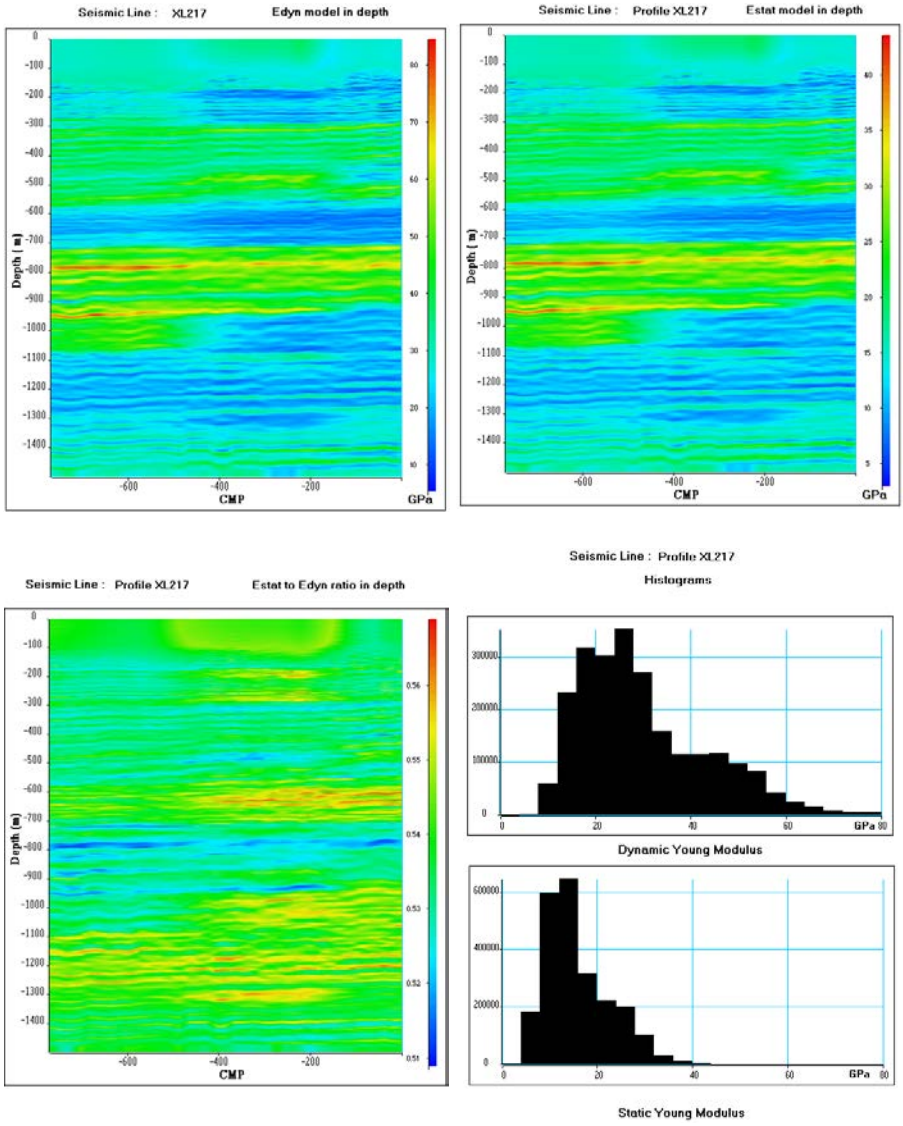

Figure 7.22 *Seismic line XL217 - From dynamic to static moduli. Top: distribution of dynamic (left) and static (right) Young's moduli in depth. Bottom: Static to dynamic ratio in depth (left), Histograms of dynamic and static Young's moduli.*

7.7 Hydrogeological Study

The impedance model (Ip block) can be converted into porosity using an empirical relationship between porosity and acoustic impedance established at well locations. To model porosities, another option is to use porosity at the well locations and interpolate between the wells by means of kriging. Partly due to the small number of wells, this outcome is very smooth and usually seems geologically consistent. More dense information can be integrated to improve the estimation of porosity. As porosity is linked to acoustic impedance, the use of dense seismic acoustic impedance information is relevant. A collocated co-kriging of porosity was thus conducted. The integration of the seismic information was performed using the normalized acoustic impedance as the secondary variable (Bourges *et al.*, 2012). The use of a 3D cube makes it possible to provide 3D imaging of the connectivity of the porous bodies (Mari and Delay, 2011). Core analysis is usually carried out to establish porosity vs. permeability laws (Zinszner and Pellerin, 2007). It has been shown that it is possible to extract new attributes from seismic sections, leading to a better understanding of the distribution of the porous and permeable bodies (Mari and Guillemot, 2012). The attributes are also used to detect the impermeable layers.

At well locations, porosity vs. impedance cross plots were used to define linear laws between the two. The cross plots were obtained using density, acoustic velocity, and porosity (NMR) logs recorded in the wells. Two empirical relationships between porosity and acoustic impedance were used to convert the *Ip* impedance into porosity φ depending on the density ρ of the geological formation. The porosity is expressed in % and the acoustic impedance in (m/s).(g/cm^3). The density sections with a threshold of 2.48 g/cm^3 are used to select the law as follows (equation (7.10)):

- for the carbonated formations: $\rho \geq 2.48$ g/cm^3, $\varphi = 45.1097 - 0.0028\ Ip$,
- for the clayed formations: $\rho < 2.48$ g/cm^3, $\varphi = 26.7678 - 0.0019\ Ip$ (7.10)

Laboratory experiments (Morlier and Sarda, 1971) have shown that the attenuation of a clean formation can be expressed in terms of three structural parameters: porosity, permeability and specific surface. Both theoretical and experimental studies have identified the relation between acoustic attenuation and petrophysical parameters:

$$\delta = (C.S/\varphi).\left(2\pi.k.f.\rho_f/\mu\right)^{1/3} \quad (7.11)$$

With δ: attenuation (dB/cm), f: frequency (Hz), ρ_f: fluid density, μ: fluid viscosity (centipoise)

φ: porosity, S: Specific surface (cm^2/cm^3), C: calibration coefficient and k: permeability (mD).

Fabricius *et al.* (2007) found that the specific surface with respect to grain volume (Sg) is apparently independent from porosity. In an attempt to remove the porosity

effect on Vp/Vs and mimic a reflected φ vs. log (Sg) trend, they proposed the use of the following relationship between porosity φ, Vp/Vs and Sg:

$$\log(Sg.m) = a.\varphi + b.(Vp/Vs) + c \text{ with } Sg = S/(1-\varphi) \tag{7.12}$$

where it should be noted that Sg is multiplied by m to make Sg dimensionless.

In practice, the parameter Ik-Seis (Indicator (**I**) of permeability (**k**) from acoustic or seismic (**Seis**) data) calculated from equation (7.13) is proportional to permeability k (Mari *et al.*, 2018; Benjumea *et al.* 2019).

$$\text{Ik-Seis} = (\varphi.\delta/S)^3/f = (\varphi/SQ)^3/f \tag{7.13}$$

with f: P-wave frequency, Q quality factor, δ: attenuation, S: specific surface and φ: porosity.

The processing of the seismic lines was carried out to estimate the distribution of the velocities (Vp and Vs), the distribution of densities, the instantaneous frequency, the Q-factor (equation (7.6)), the porosity from acoustic impedance (equation (7.10)), the specific surface S (equation (7.12)), and finally the Ik-Seis factor (equation (7.13)). In the domain of seismic frequencies, the Ik-Seis factor can only be seen as a relative indicator, varying from 0 for less porous and permeable bodies, up to 1 for more porous and permeable bodies.

If the porosity distribution is a key point for reservoir characterization, shale content is key both for the reservoir and the seal. Gamma ray logs are a very useful tool that can be computed from seismic data to estimate shale content. After several attempts with different seismic attributes such as P or S-wave velocity, density, seismic mechanical modules such as the shear modulus μ, the matrix shear modulus appeared to be the most sensitive attribute to compute a pseudo gamma ray (Yven and Mari, 2014). The matrix shear modulus μ_{ma} is given by the following formula:

$$\mu_{ma} = \frac{\mu}{1-\beta_B} \tag{7.14}$$

with β_B being Biot's coefficient (1956) defined as follows: $1-\beta_B = (1-\varphi)^{m\varphi}$ and $m\varphi = \frac{3}{1-\varphi}$ with φ the porosity.

The matrix shear modulus is corrected for the effect of porosity and can be converted into pseudo gamma ray (GR-Seis) by using an empirical relationship (polynomial function) between the gamma ray log and the matrix shear modulus established at the well locations.

The proposed procedure was applied on a 3D dataset. The results shown here were obtained on the XL217 cross-line. Figure 7.15 shows the instantaneous amplitude section and its associated SQI factor in depth. The SQI factor is low which means there is good confidence in the seismic amplitude and consequently in the elastic impedance in depth. In the 700-750 m range, one can notice a significant lateral

variation of the seismic amplitude. The amplitude anomaly corresponds to the presence of a porous layer, between CMP 600 and CMP 400 at the top of the Dogger formation. Figure 7.23 (top) shows the specific surface and Ik-Seis distributions in depth. The interpretation is confirmed by a very low value of the specific surface and a high value of the Ik-Seis attribute. The high values of the specific surface are associated with the Callovo-Oxfordian (550-720 m depth interval). The pseudo gamma ray section computed from the Biot Shear modulus is shown in Figure 7.23 (bottom). We noted the lateral variation of the shale content in the Callovo Oxfordian.

7.8 Conclusion

The different steps involved in building a geo-model in depth can be summarized as follows:

- pre-processing must include QC on static corrections for the detection and compensation of long-wavelength anomalies,
- QC on seismic amplitudes and velocity models. Filtering of footprint anomalies. Quantification of amplitude quality (SQI factor) before pre-stack migration and inversion,
- processing: pre-stack time migration. At least three angle migrated stacks must be generated,
- elastic inversion to compute Ip and Is sections,
- computation of an a priori velocity model Vp, assuming that the P-wave velocity Vp and the acoustic impedance Ip of a formation vary in a consistent way and a relationship between the two variables Ip and Vp exists. A single relationship or a relationship per range of impedances or per geological unit can be computed,
- update of the a priori Vp model, using the depth conversion of seismic horizons by a geo-statistical method which simultaneously uses Bayesian co-kriging and a multilayer model and which handles sources of uncertainty: Vp-update,
- depth conversion of the seismic blocks (amplitude, *Vp-update, Ip, Is*) using the updated velocity model Vp-update,
- computation of the density distribution in depth: $\rho = Ip / Vp\text{-}update$,
- computation of the shear velocity distribution: $Vs = Vp\text{-}update \times (Is / Ip)$.

Knowledge of the density (ρ) and velocity (*Vp-update*, *Vs*) distributions allows the computation of mechanical dynamic modules such as the shear modulus, Young's modulus, bulk modulus and the Poisson's ratio. The conversion of dynamic Young's modulus into static Young's modulus was conducted.

We have described a method to build a geo-model in depth, using a 2D seismic line (07Est10) and 3D seismic lines (IL405 and XL-217) as examples.

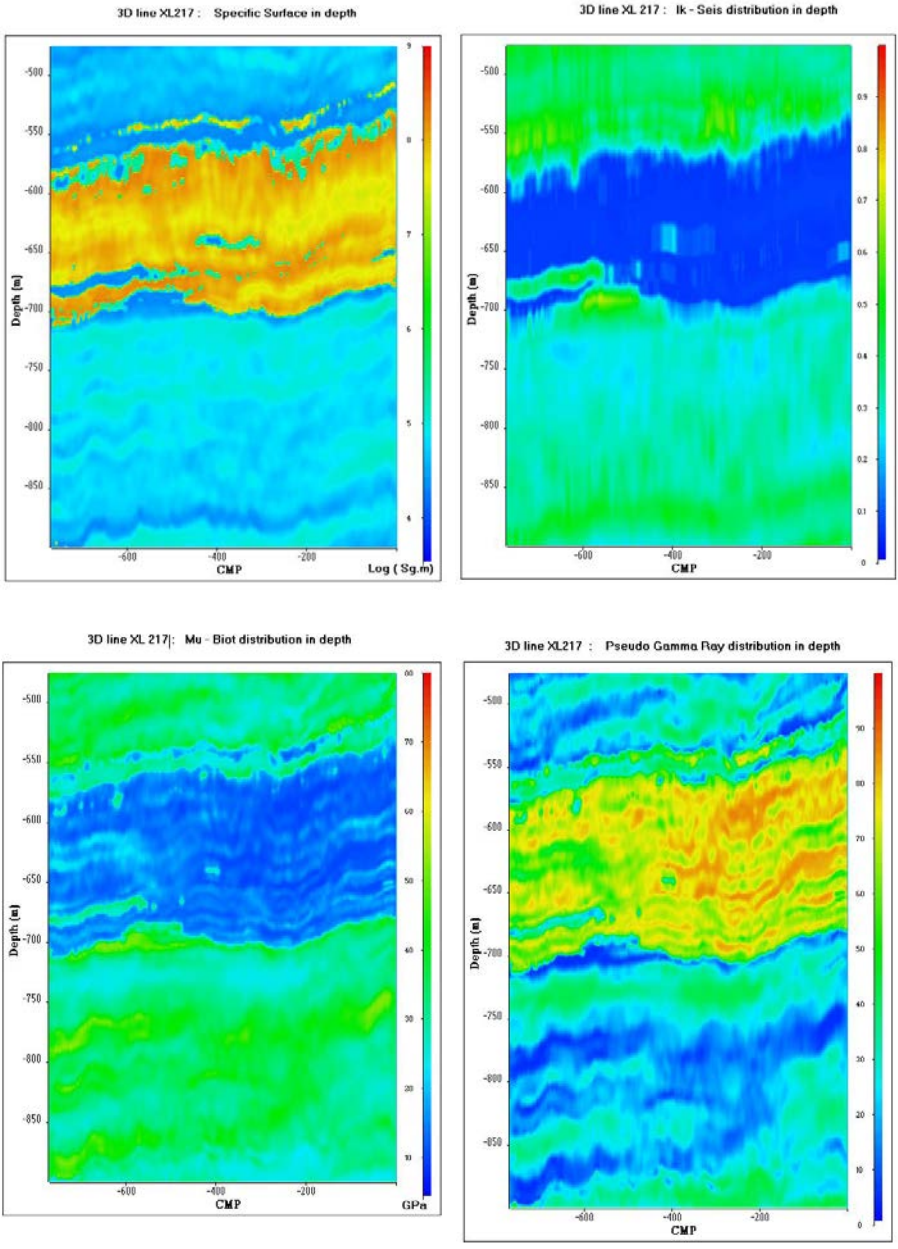

Figure 7.23 *Mechanical and petro-physical parameter. Top: Specific surface and Ik-Seis distribution in depth. Bottom: Shear modulus and pseudo gamma ray distribution in depth.*

We have demonstrated the advantages of geo-statistical processing both to quantify the quality of the seismic amplitude (SQI) and to perform depth conversion (Bayesian Kriging).

The Q factor of geological formations can be obtained from VSP data. We made use of the fact that attenuation introduces dissipative dispersion, which can be measured from the frequency-dependent phase velocity of the VSP down-going wave. The methodology has been extended from well data to surface seismic data. For this purpose, a high-resolution velocity model is required. It is obtained by the elastic inversion of the seismic data and by conversion of acoustic impedance *Ip* into velocity *Vp*. The procedure can be used to build a geo-model in depth defined by mechanical and hydrogeological parameters: velocities (*Vp, Vs*), density, Q factor, porosity, specific surface and index of permeability (Mari and Yven, 2014).

The seismic procedure was extended to calculate a seismic pseudo gamma ray (GR-Seis). A highly porous layer was detected at the top of the Dogger, and lateral variation in shale content can be seen in the Callovo Oxfordian.

Acknowledgements

Many thanks to Andra for granting permission to use the datasets.

References

Andra (2005) Dossier 2005 Argile – Synthèse : Evaluation de la faisabilité du stockage géologique en formation argileuse – décembre 2005.

Andra (2009) Stockage réversible profond - Proposition d'une zone d'intérêt pour la reconnaissance approfondie et de scénarios d'implantation en surface – C RP ADP 09-0035.

Andra (2016) Dossier Option de Sûreté – Partie Exploitation (DOS-EXPL) - CG-TE-D-NTE-AMOA-SR1-0000-15-0060.

André G., Hibsch C., Beaudoin B., Carpentier C., Fourcade S., Cathelineau M., Elion P., 2004. Oxfordian sedimentary dykes: Tectonic and diagenetic implications for the eastern Paris Basin, *Bull. Soc. Geol. Fr*, 175, 6, 595-605.

Benjumea B., Lopez A.I., Mari J.L., Garcia-Lobon J.L., 2019, Petrophysical characterization of carbonates (SE of Spain) through full sonic data, *Journal of Applied Geophysics*, 160, 1-14, https://doi.org/10;1016/J.appgeo.2018.10.024.

Bourges M, Mari J.L., Jeannée N., 2012, A practical review of geostatistical processing applied to geophysical data: methods and applications, *Geophysical Prospecting*, 60, 400-412, DOI: 10.1111/j.1365-2478.2011.00992.x

Brigaud B., Vincent B., Carpentier C, Robin C., Guillocheau F, Yven B, Huret E., 2014, Growth and demise of the Jurassic carbonate platform in the intracratonic Paris Basin (France): Interplay of climate change, eustasy and tectonics, *Marine and Petroleum Geology*, 53, 3-29.

Castagna J.P., 1993, AVO analysis: Tutorial and review: in Castagna, J.P. and Backus M.M. (Eds.), Offset-dependent reflectivity - Theory and practice of AVO anomalies. *Soc. Expl. Geophys., Investigations in Geophysics*, 8, 3-36.

Connolly P., 1999, Elastic impedance, *The Leading Edge*, 18, 438-452.

Eissa E.A., Kazi A., 1988, Relation between static and dynamic Young's moduli of, rocks, *Int. J. Rock Mech. Min. Sci. & Geomech. Abstr*., 25 (6), 479-482.

Fabricius I.L., Baechle G., Eberli G.P., Weger R., 2007, Estimating permeability of carbonate rocks from porosity and Vp/Vs, *Geophysics*, 72 (5), 185-191, DOI: 10.1190/1.2756081.

Garcia M.H., Rabaute A., Yven B., Guillemot D., 2011, Multivariate and spatial statistical analysis of Callovo-Oxfordian physical properties from lab and borehole logs data: Towards a characterization of lateral and vertical spatial trends in the Meuse/Haute-Marne Transposition Zone, *Physics and Chemistry of the Earth*, 36 (17-18), 1469-1485.

Gardner G.H.F., Gardner L.W., Gregory A.R., 1974, Formation velocity and density -- the diagnostic basics for stratigraphic traps, *Geophysics,* 39, 770–7

Gaumet F., 1997. Fondements géologiques pour la modélisation stratigraphique des systèmes carbonates. Le jurassique moyen de l'Angleterre à la Méditerranée. Thèse 3e cycle, Univ. Claude-Bernard, Lyon1, 245.

Guillocheau F., Robin C., Allemand P., Bourquin S., Brault N., Dromart G., Friendenberg F., Garcia J.P., Gaulier J.M., Grodoy B., Hanot F., Lestrat P., Mettraux, M., Naplas, T., Prijac C., Rigollet C., Serrano O., Granjean G., 2000, Meso-Cenozoic geodynamic evolution of the Paris Basin: 3D stratigraphic constraints, *Geodynam. Acta* 13, 189-246.

Landrein P., Vigneron G., Delay J., Lebon P., Page M., 2013, Lithologie, hydrodynamisme et thermicité dans le système sédimentaire multicouche recoupé par les forages Andra de Montiers-sur-Saulx (Meuse), *Bulletin de la Société Géologique de France*, 184 (6), 519-543.

Lebreton F., Morlier P, 1983, A permeability acoustic logging, *Bulletin of the International Association of Engineering Geology*, 1, 101-105.

Mari J.L., Gaudiani P., Delay J., 2011, Characterization of geological formations by physical parameters obtained through full waveform acoustic logging, *J. Phys. Chem. Earth*, DOI:10.1016/jpce.2011.07.11.

Mari J.L, Guillemot D., 2012, Detection of porous and permeable formations: from laboratory measurements to seismic measurements, *Oil & Gas Science*

and Technology _Rev. IFP Energies nouvelles, 64 (4), 703-721, DOI: 10.2516/ogst/2012209.

Mari J.L., Delay F., 2011, Contribution of seismic and acoustic methods to reservoir model building, in Lakshmanan Elango (ed.) Hydraulic Conductivity - Issues, Determination and Applications, InTech, 329-354, ISBN 978-953-307-288-3. Available from http://www.intechopen.com/articles/show/title/contribution-of-seismic-and-acoustic-methods-to-reservoir-model-building

Mari J.L., Yven B., 2014, The application of high resolution 3D seismic data to model the distribution of mechanical and hydrogeological properties of a potential host rock for the deep storage of radioactive waste in France, *Marine and Petroleum Geology*, 53, 133-153, Elsevier, DOI: 10.1016/j.marpetgeo.2013.10.014, http://dx.doi.org/10.1016/j.marpetgeo.2013.10.014

Mari J.L., 2015, Signal processing for geologists & geophysicists, e-book, DOI:10.2516/ifpen/2011002, http://books.ifpenergiesnouvelles.fr/ebooks/signal-processing/

Mari J.L., Lopez A.I, Benjumea B., Garcia-Lobon J.L., 2018, Shape index: a refraction attribute to detect fractures and permeable bodies, paper Th J 12, 80th EAGE annual conference, Copenhagen, Denmark.

Mari J.L., Yven B., 2018, Q factor estimation and validation: a new link between VSP and seismic lines, paper 557, CAJG, 1st Conference of the Arabian Journal of Geosciences, November 12-15 2018, Hammamet, Tunisia.

Megnien, C., 1980, Synthèse géologique du bassin de Paris, Mém. BRGM n°101, n°102, n°103.

Morlier P., Sarda J.P., 1971, Atténuation des ondes élastiques dans les roches poreuses saturées, *Revue de l'Institut Français du Pétrole*, 26 (9), 731-755.

Omre H., 1987, Bayesian kriging merging observations and qualified guesses in kriging. Math. Geol, 19 (1), 25-39.

Purser B.H., 1980, *Sédimentation et diagenèse des carbonates néritiques récents*, Tome 1. Technip, Paris, 366p.

Robein E., 2003. *Velocities, Time-imaging and Depth-imaging in Reflection Seismics*, Principle and Methods, EAGE publications bv, ISBN 90-73781-28-0.

Rocher M., Cushing M., Lemeille F., Lozac'h Y., Angelier J., 2004, Intraplate paleostresses reconstructed with calcite twinning and faulting: improved method and application to the eastern Paris Basin (Lorraine, France), *Tectonophysics,* 387, 1-21.

Sandjivy L., Shtuka A., 2009, Depth conversion and associated uncertainties using consistent velocity model: a probabilistic unified model based on Bayesian approach, paper presented at the 11th International Congress of the Brazilian Geophysical Society, Salvador, Brazil, August 24-28, 2009.

Shuey R.T., 1985, A simplification of Zoeppritz equations, *Geophysics*, 50, 609-614.

Shtuka A., Gronnwald T., Piriac F., 2009, A generalized probabilistic approach for processing seismic data, 79th annual SEG meeting, Expanded Abstracts.

Varela Carlos Lopo, Andre L.R. Rosa, Tadeusz J. Ulrych, 1993, Modeling of attenuation and dispersion, *Geophysics*, 58, 8, 1167-1173.

Walden A.T., 1991. Making AVO sections more robust, *Geophys. Prosp*., 39, 915-942.

Whitcombe D.N., Connolly P.A., Reagan R.L., Redshaw T.C., 2002, Extended elastic impedance for fluid and lithology prediction, *Geophysics*, 67 (1), 63-67.

Wyllie M.R., Gregory R.J., Gardner H.F., 1956, Elastic wave velocities in heterogeneous and porous media, *Geophysics*, 21 (1), 41-70.

Yven B., Mari J.L., 2014, Sedimentology, petrophysics and 3D seismic contributions to the study of the eastern Paris basin formation (France), Doi: 10.3997/2214-4609.20140927, 76th EAGE conference, Amsterdam RAI, The Netherlands.

Yven B., Mari J.L., 2018, Geomechanics: from core and logging to seismic lines, paper 556, CAJG, 1st Conference of the Arabian Journal of Geosciences, November 12-15 2018, Hammamet, Tunisia.

Zinszner, B., Pellerin, F.M., 2007. *A geoscientist's guide to petrophysics*, Éditions Technip, Paris. ISBN 978-2-7108-0899-2.

Synthesis

J.-L. Mari, M. Mendes, H. Chauris

The 7 chapters in this book provide a practical overview of seismic imaging:

Chapter 1 is a brief review of the current state of knowledge in seismic propagation. It introduces the different seismic methods for prospection. Several examples are used to show the different waves, which can be observed on field records and are predicted by the wave equation. The chapter underlines the fact that the acquisition geometry (2D or 3D) and the type of seismic survey (surface or well) must be taken into consideration in the wave identification.

Chapter 2 is dedicated to refraction surveying. Seismic refraction can be used for investigations at all depths, but for various technical reasons it is mostly used in the study of the first 300 metres of the subsurface (spread length, importance of the source energy, …). Refracted P-waves are currently used to obtain a velocity model of the near surface by combining conventional methods such as the T plus – T minus or GRM method and tomography. The refraction method is currently used in hydrogeology and in civil engineering. We have presented 2 applications of the refraction method: the computation of static corrections, and the characterization of a near-surface karstic reservoir.

DOI: 10.1051/978-2-7598-2351-2.c010

For conventional studies, the refraction method requires only the measurement of arrival times of first arrival waves (direct and refracted waves) to provide a geological model. Amplitudes are not commonly used in seismic refraction studies. In the case of an irregular interface, the analysis of the distortion of the head wave arrival allows the detection of wave interferences, which can be associated with the presence of fractures (second field example).

In **chapter 3**, the task of imaging near-surface structures has been addressed with a few seismic tomography approaches. Several seismic field datasets are used to illustrate the ability of tomographic tools.

The first field example concerns a transmission tomographic technique used for inverting first-arrival times, picked from a 3D surface seismic dataset, which was part of a geophysical survey conducted in a karstified dolostone region. Due to the limited azimuthal coverage of the surface data, the tomographic inversion produced a 3D model for the karst aquifer, with significance only in the upper epikarst region (up to 7 m deep). To overcome this image depth limitation, data collected with down-hole receivers were used simultaneously with those from surface geophones, which extended the image depth to the underneath low-permeability volume (up to 28 m deep). This 3D approach revealed a set of elongated furrows at the base of the epikarst and identified heterogeneities deep inside the low-permeability volume that may represent high-permeability preferred pathways for water inside the karst.

In the second field example, the seismic data were collected by triaxial geophones in a cross-well experiment using a reflection tomography procedure, which enabled the imaging of a limestone reservoir at a depth of about 1,850 m. The raw field data were processed like conventional offset VSP data and the information present in the travel time of reflected S-waves was exploited for imaging between the boreholes. The imaging was achieved by time and depth transformations using a VSP-CDP stack, guided by a S-S ray tracing with a velocity model based on previous P and S VSP analysis. Although the reflection tomography did not provide an image with high frequency waveform, it successfully demonstrated the possibility of imaging between two wells from seismic data collected with conventional borehole multi-component sensors and seismic waves generated by a low-energy source.

Finally, through the application of a diffraction tomography approach, based on the Born approximation, we were able to produce quantitative elastic depth images from multi-component offset VSP datasets. One dataset was collected in the North Sea, and another from acoustic and multi-component borehole data collected at two different boreholes in the Paris basin.

The target zone of the North Sea survey, which covered the reservoir area, is a rectangle extending from 50 m to 550 m east of the borehole, with depths from 3,400 m to 4,400 m. Geologists were able to interpret the estimations of three elastic parameters – P and S-wave velocities and density – that were produced by the diffraction tomography. Then, the top of the Brent reservoir could be delineated continuously away from the borehole, while it was also possible to interpret two faults. This chapter also includes a discussion on the assessment of the elastic depth

image quality that should be given directly by the residuals between field data and seismograms computed with the elastic images.

The last example presented in this chapter is based on data from a one-shot seismic survey in the Paris basin. This study includes processed acoustic and multi-component data collected at two different wells with inter-well distances of about 100 m. Only upgoing S-S and S-P reflected events were used for the tomography. The target zone included three sand reservoir levels between depths of 575 and 600 m. Due to insufficient source and receiver coverage of the target zone (because it was only a one-shot survey), the diffraction tomography produced unreliable images with strong artifacts on the upper section, i.e. above 560 m. However, tomography proved capable of producing high-resolution (≈ 3-5 m) images for the reservoir region. The comparison of both density images with a pseudo-density log, produced by a density log convolved with a characteristic signal with the same bandwidth as the density image, is quite satisfactory within the reservoir region.

In conclusion, based on the good results obtained from the field studies, it can be said that seismic tomography has the potential to provide superior images that are capable of addressing the problem of near-surface structure characterization.

Chapter 4 is dedicated to near-surface reflection surveying. After a short review of the design of conventional 2D and 3D surveys, we briefly summarize the main steps of a processing sequence. With two field datasets, we showed that it is possible to obtain very high-resolution 3D blocks for near-surface applications with very light seismic spreads (48 channel recorders, a single geophone per trace, and a light seismic source). Near-surface studies require specific test phases to define the optimum parameters (minimum offset, geophone interval) for the acquisition. The processing sequence must be carefully adjusted to the field data, especially for the wave separation. In the example of the imaging of the near-surface karstic reservoir (Hydrogeological Experimental Site of Poitiers), we showed that the velocity distribution obtained by refraction tomography in the first 30 m can be merged with the velocities extracted from the amplitude of the reflected events to obtain a continuous velocity model from the surface to a depth of 120 m.

Chapter 5 discusses the huge potential of Full Waveform Inversion (FWI) in terms of quantitative seismic image interpretation. In practice, the applicability of the method depends on the quality of the data, as well as on the most appropriate pre-processing (for example to preserve the low frequency data) and on the correct physical understanding of the wave propagation phenomena. In future elastic FWI will replace the acoustic approach, and the technique will be able to extract more than a single parameter (e.g. velocity and attenuation). Also, it may be possible to incorporate higher frequencies. On the exploration scale, FWI is still in its infancy. We hope that this chapter will positively encourage the reader to evaluate for themselves the use of FWI on near-subsurface data sets.

Chapter 6 discusses handling different types of waves present in the same set of experimental data. We have underlined some of the advantages of hybrid seismic imaging strategies to provide efficient, accurate and reliable subsurface models, in

terms of geometry and mechanical properties. In the first field example, the hybrid seismic imaging tool showed that seismic data derived from traditional refraction acquisition is valuable for obtaining information about the reflectivity for targets located in the near and/or very near surface. After first break pickings, a P-wave tomography inversion was performed to obtain a depth velocity model. The processing of reflection events, present in the seismic refraction survey, was carried out by a standard procedure. However, particular attention was focused on isolating the reflection waves. Finally, after a careful adjustment of the results obtained from the processing of refraction and reflection waves, they were gathered to produce an extended time reflectivity section starting from the surface. In the second example, a refraction tomography algorithm has been applied to the first-arrival times picked manually on the shot gathers collected in a hydrothermal area. A P-wave velocity model was obtained that presented values in the range 100 – 2,000 m/s and a low velocity layer at the surface with thickness around 5 m. The processing of surface waves, extracted from the seismic survey, was performed in the f-k domain with SWIP, an open-source MATLAB-based package. The inversion of the dispersion curves produced a set of 1D models of S-wave velocity with an estimated depth of investigation of around 10 m. The final result was a pseudo 2D model obtained by merging all of the best fitting 1D models. The final S-wave velocity model showed strong lateral variations that were not visible on the P-wave velocity model, probably due to strong saturation variations. This information was used to estimate the Poisson's ratio. The distribution of this parameter, more particularly its contrasts, clearly highlights gas pathways in the subsurface that are consistent with the degassing observed at the surface. Thus, these positive results open up new perspectives for several applications of more hybrid seismic methods.

Finally, **chapter 7** presents a field study at a site that has been extensively studied by the French national radioactive waste management agency (Andra). We showed how the integration of seismic data (3D survey and VSP), logging data (acoustic logging), and core measurements, combined with a succession of specific and advanced processing techniques, enabled the development of a 3D high-resolution geological model in depth. We demonstrated the benefit of geostatistical processing, both to quantify the quality of the seismic amplitude (SQI) and to perform depth conversion (Bayesian Kriging). The Q factor of geological formations can be obtained from VSP data. We used the fact that attenuation introduces dissipative dispersion, which can be measured from the frequency-dependent phase velocity of the VSP down-going wave. The methodology has been extended from well data to surface seismic data. For this purpose, a high-resolution velocity model is required. This was obtained from elastic inversion of the seismic data and by conversion of acoustic impedance *Ip* in velocity *Vp*. The procedure can be used to build a geomodel in depth defined by mechanical and hydro-geological parameters: velocities (*Vp, Vs*), density, Q factor, porosity, specific surface, and index of permeability. The seismic procedure was extended to compute a seismic pseudo gamma ray (GR-Seis). A high porous layer was detected at the top of the Dogger and lateral variation of the shale content can be seen in the Callovo-Oxfordian.

Conclusion

J.-L. Mari, M. Mendes

This book provides an overview of seismic imaging. It provides a practical guide, through the use of field examples, to the contribution of seismic methods to reservoir, geotechnical and civil engineering studies. The book is written for students and researchers in geosciences as well as for professionals. We hope that it will positively encourage the reader to evaluate the proposed methodologies for themselves, namely tomography, full waveform inversion, hybrid methods, and integrated approaches, for use on near subsurface datasets.

In each chapter, the reader will find theoretical concepts, practical rules and, above all, actual application examples. For this reason, the book can be used as a text to accompany course lectures or continuing education seminars.

This book aims to promote the exchange of information among geologists, geophysicists, and engineers in geotechnical fields.

DOI: 10.1051/978-2-7598-2351-2.c011

PROfile

Seismic imaging: a practical approach

Jean-Luc Mari and Manuela Mendes

In the geophysics of oil exploration and reservoir studies, the surface seismic method is the most commonly used method to obtain a subsurface model in 2 or 3 dimensions. This method plays an increasingly important role in soil investigations for geotechnical, hydrogeological and site characterization studies regarding seismic hazard issues.

The goal of this book is to provide a practical guide, using examples from the field, to the application of seismic methods to surface imaging.
After reviewing the current state of knowledge in seismic wave propagation, refraction and reflection seismic methods, the book aims to describe how seismic tomography and fullwave form inversion methods can be used to obtain seismic images of the subsurface. Through various synthetic and field examples, the book highlights the benefit of combining different sets of data: refracted waves with reflected waves, and body waves with surface waves. With field data targeting shallow structures, it shows how more accurate geophysical models can be obtained by using the proposed hybrid methods. Finally, it shows how the integration of seismic data (3D survey and VSP), logging data (acoustic logging) and core measurements, combined with a succession of specific and advanced processing techniques, enables the development of a 3D high resolution geological model in depth.
In addition to these examples, the authors provide readers with guidelines to carry out these operations, in terms of acquisition, as well as processing and interpretation.

In each chapter, the reader will find theoretical concepts, practical rules and, above all, actual application examples. For this reason, the book can be used as a text to accompany course lectures or continuing education seminars.

This book aims to promote the exchange of information among geologists, geophysicists, and engineers in geotechnical fields.

978-2-7598-2351-2

edp sciences
www.edpsciences.org

Books of the PROfile collection are intended for the transmission of professional knowledge in different disciplines. They are written by recognized experts in their fields and contribute to the training and information of professionals.